NUMERICAL STUDY OF A LARGE DIAMETER SHAFT IN OLD ALLUVIUM

TAN RWE YUN

NATIONAL UNIVERSITY OF SINGAPORE

2004

NUMERICAL STUDY OF A LARGE DIAMETER SHAFT IN OLD ALLUVIUM

TAN RWE YUN
(B. Eng. (Hons.), NUS)

A THESIS SUBMITTED

FOR THE DEGREE OF MASTER OF ENGINEERING

DEPARTMENT OF CIVIL ENGINEERING

NATIONAL UNIVERSITY OF SINGAPORE

2004

Dedicated to my family and friends

ACKNOWLEDGEMENTS

The author would like to express her gratitude to her supervisors, Associate Professor Harry Tan Siew Ann and Associate Professor Leung Chun Fai for their guidance and encouragement throughout her course of study. The author has learnt much through their mentorship and meaningful discussions, and she deeply appreciated their patience and generosity with time, in spite of their busy schedules.

The author would like to thank Mr Mansour Makvandi and Mr R. Balamurugan, from Econ Corporation Ltd, for their kind assistance in the collection of project information and explanation of technical details of the project. The author is also grateful to Dr Wong Kwong Yan, from Soil Mechanics Pte Ltd, and Ms Teo Li Lin, from CEP Services Pte Ltd, for their support in the compilation of results of instrumentation works. The author is thankful to Mr Ni Qing, a NUS research student, for sharing some of his experimental results on Old Alluvium with her. She is also very appreciative of the support provided by Mr Shen Rui Fu, from the NUS Geotechnical Laboratory.

The author would like to express her heartfelt thanks to Mr Dennis Waterman and Mr Andrei Chesaru, from PLAXIS BV, for clarifying her doubts regarding the use of the PLAXIS and PLAXFLOW programs. The author has also received much encouragement and support from her family and friends, especially Mr Tho Kee Kiat. They have been a source of strength in the course of this project and their kind gestures are greatly appreciated.

TABLE OF CONTENTS

		Page
ACKNOWLEDGEMENTS		**i**
TABLE OF CONTENTS		**ii**
SUMMARY		**v**
NOMENCLATURE		**vii**
LIST OF FIGURES		**xiii**
LIST OF TABLES		**xix**
CHAPTER 1	**INTRODUCTION**	**1**
1.1	Background	1
1.2	Current Issues and Problem Definition	2
1.3	Scope and Objectives	4
CHAPTER 2	**LITERATURE REVIEW**	**8**
2.1	Introduction	8
2.2	Singapore Old Alluvium Formation	8
2.3	Design of Vertical Shafts	19
2.4	Summary	39
CHAPTER 3	**CASE HISTORY**	**55**
3.1	Introduction	55
3.2	General Site Condition and Instrumentation	55

		Page
3.3	Site Investigation	57
3.4	Soil Profile	58
3.5	Excavation Support System and Sequence	58
CHAPTER 4	**THE HARDENING-SOIL MODEL**	**68**
4.1	Introduction	68
4.2	Formulation of Hardening-Soil Model	68
4.3	Determination of Model Parameters	76
4.4	Determination of Hardening-Soil Model Parameters of Old Alluvium	80
CHAPTER 5	**PLAXFLOW**	**100**
5.1	Introduction	100
5.2	Material Models	100
5.3	Material Sets Available in PLAXFLOW	103
5.4	Verification of Axisymmetrical Groundwater Flow	105
CHAPTER 6	**FINITE ELEMENT ANALYSIS**	**113**
6.1	Introduction	113
6.2	Finite Element Model	113
6.3	Finite Element Analysis	117
6.4	Results and Observations	126
6.5	Zone of Influence	133
6.6	Convergence Study	134

		Page
6.7	Limitations of Finite Element Model	135
6.8	Summary	139
CHAPTER 7	**PARAMETRIC STUDIES**	**157**
7.1	Introduction	157
7.2	Influence of Soil Strength	159
7.3	Effect of Hardening-Soil Stiffness Modulus	160
7.4	Influence of Soil Stiffness	161
7.5	Influence of Over-Consolidation Ratio	162
7.6	Influence of Soil Permeability	163
7.7	Influence of Interface Strength	165
7.8	Influence of Grade of Concrete of Circular Shaft Wall	165
7.9	Influence of Grade of Concrete of Ring Wall	166
7.10	Summary	167
CHAPTER 8	**CONCLUSION**	**182**
8.1	Concluding Remarks	182
8.2	Recommendations for Further Research	185
REFERENCES		**186**
APPENDIX A		**197**
APPENDIX B		**200**

SUMMARY

In this research, consolidation finite element analyses are performed to simulate the time-dependent behaviour of a circular shaft excavation in Singapore Old Alluvium. This 70 m deep excavation is conducted for Influent Pumping Shaft 2 at the Changi Water Reclamation Plant. PLAXIS, a finite element package, is used to simulate the excavation process. PLAXFLOW is used in conjunction with PLAXIS to perform axisymmetrical groundwater flow computations.

The outer diameter of the shaft is 42.6 m. The excavation support system consists of a circular diaphragm wall. Internal ring walls are cast against the diaphragm wall after each excavation stage. The Hardening-Soil model is employed to simulate the constitutive behaviour of Old Alluvium. A method proposed by Schanz and Bonnier (1997) to determine the values of parameters for the Hardening-Soil model is critically assessed. Their proposed equations are independently derived and oedometer element tests are simulated using PLAXIS to verify the validity of the method. Schanz and Bonnier's method is found to be suitable for estimating Hardening-Soil model parameters for cohesionless soils with a power for stress-dependency of stiffness that ranges from 0.5 to 0.7.

Laboratory oedometer and triaxial tests conducted on Old Alluvium soil samples are simulated using the Hardening-Soil model to obtain representative soil parameters. The use of equal value for the reference secant stiffness modulus and the reference tangential oedometer stiffness modulus is found to be appropriate for Old Alluvium.

The duration of each excavation and construction stage are carefully considered in the axisymmetrical finite element model. The convergence of the mesh used in the analyses is verified through a convergence study. Significant temperature variations during and after casting of the ring walls are observed. A method to account for these thermal effects in the finite element model is proposed. Hoop strains of the shaft wall usually reflect the excavation sequence and the numerical hoop strains agree well with instrumentation results. It is evident from the finite element analyses that neglecting the thermal effects would lead to an unconservative design for circular shafts with cast in-situ ring walls.

Extensive parametric studies are performed to study the behaviour of such circular shafts in Old Alluvium. The influences of soil strength, soil stiffness, over-consolidation ratio, soil permeability, wall interface strength and stiffness of walls on the maximum hoop force, bending moment, shear and deflection of the shaft wall are investigated.

Keywords: consolidation, finite element analysis, circular shaft, Old Alluvium, Hardening-Soil model, temperature effects.

NOMENCLATURE

A	A linear regression coefficient
B	A linear regression coefficient
c’	Effective cohesion
c_i	Cohesion of interface
$c_{increment}$	Increment of effective cohesion in Hardening-Soil model
c_{soil}	Cohesion of soil
c_u	Undrained cohesion
E	Young’s modulus of elasticity of shaft lining
E’	Effective modulus of elasticity
E_{50}	Stiffness modulus of soil under primary drained triaxial loading
E_{50}^{ref}	Reference stiffness modulus of soil under primary drained triaxial loading
E_{oed}	Stiffness modulus of soil under primary oedometer loading
E_{oed}^{ref}	Reference stiffness modulus of soil under primary oedometer loading
E_{PMT}	Pressuremeter modulus from the first cycle of test
E_r	Pressuremeter unloading-reloading modulus of the second cycle of test
E_u	Undrained stiffness modulus of soil
E_{ur}	Unloading stiffness modulus of soil
E_{ur}^{ref}	Reference unloading stiffness modulus of soil
EA	Axial stiffness
EI	Bending stiffness
$(E_{oed}^{ref})_{input}$	Reference stiffness modulus of soil under primary oedometer loading inputted in Hardening-Soil model
$(E_{oed}^{ref})_{predicted}$	Reference stiffness modulus of soil under primary oedometer loading predicted by (Schanz and Bonnier, 1997)

F_H	Horizontal force
F_T	Tangential Force
F_z	Maximum hoop force at final excavated depth in parametric study
F_{zo}	Maximum hoop force at final excavated depth using basic parameters
f	Yield function
f^c	Cap yield surface of the Hardening-Soil model
$\bar{f}$	Function of stress in the definition of yield function of Hardening-Soil model
g_a, g_l and g_n	Parameters of the Van Genuchten model.
h	Hydraulic head
h_o	Initial hydraulic head
K_{cr}	Critical coefficient of earth pressure at rest distinguishing Mode A from Mode B of yield initiation
K_o	Coefficient of lateral earth pressure at rest
K_o^{nc}	Coefficient of earth pressure at rest for normally consolidation
Ks	Default coefficient of permeability available in PLAXFLOW
k	Coefficient of permeability
k_h	Coefficient of horizontal permeability
k_r	Coefficient of earth pressure for cylindrical shafts
k_{ref}	Relative permeability
k_{sat}	Saturated permeability of soil
k_v	Coefficient of vertical permeability
LI	Liquidity Index
LL	Liquid limit
M	Maximum moment at final excavated depth in parametric study
M_o	Maximum moment at final excavated depth using basic parameters

m	Power for stress-level dependency of stiffness in Hardening-Soil model
m_{input}	Power for stress-level dependency of stiffness inputted in Hardening-Soil model
$m_{predicted}$	Power for stress-level dependency of stiffness predicted by (Schanz and Bonnier, 1997)
m_v	Coefficient of volume compressibility
N	SPT N-value
OCR	Over-consolidation ratio
p	Mean effective stress
P_a	Atmospheric pressure
P_L	Limit pressure
P_p	Isotropic pre-consolidation stress
PI	Plasticity Index
PL	Plastic limit
POP	Pre-overburden pressure
p_o	Initial vertical in-situ stress.
p^{ref}	Reference pressure in Hardening-Soil model
Q	Pumping rate of well
q	Deviatoric stress
q_a	Asymptotic shear stress in Hardening-Soil model
q_c	Cone resistance
q_f	Ultimate deviatoric stress
q_t	Equivalent radial stress acting on circular shaft wall
q_u	Unconfined compression strength
$\bar{q}$	A special stress measure for deviatoric stresses in Hardening-Soil model
R	Radius of circular vertical shaft

R_f	Ratio of ultimate deviatoric stress to asymptotic shear stress in Hardening-Soil model
R_{inter}	Interface strength
R_{tr}	Extent of the plastic zone
R_{vr}	Extent of Mode A and Mode B of yield initiation are present.
RL	Reduced level
r	Radial distance from the centreline of a cylindrical vertical shaft
S	Degree of saturation
S_A	Storativity of Aquifer
S_e	Effective degree of saturation
S_{sat}	Saturated degree of saturation
S_{res}	Residual saturation
T	Temperature
T_A	Transmissivity of aquifer
t	Thickness of shaft lining
V	Maximum shear at final excavated depth in parametric study
V_o	Maximum shear at final excavated depth using basic parameters
W(u)	Well function
w	Water content
z	Depth
z_{ch}	Changeover depth
z_o	Depth of shaft
α	An auxiliary model parameter in Hardening-Soil model
α_c	Coefficient of thermal expansion of concrete
α_r	Radio of radial earth pressure to Berezantzev's active earth pressure
β	An auxiliary model parameter in Hardening-Soil model

δ	Maximum wall deflection at final excavated depth in parametric study
δ_o	Maximum wall deflection at final excavated depth using basic parameters
ε_v^p	Plastic volumetric strain
ε_v^{pc}	Plastic volumetric cap strain
$\dot{\varepsilon}_v^p$	Rate of Plastic volumetric strain
ε_1	Axial strain
ε_1^p	Plastic axial strain
ϕ	Angle of friction
ϕ'	Effective angle of friction
ϕ*	Reduced angle of friction
ϕ_{cv}'	Critical state angle of friction
ϕ_i	Angle of friction of interface
ϕ_m'	Mobilised angle of friction
ϕ_p	Effective pressure head
ϕ_{pk}	Model parameter of Approximate Van Genuchten Model
ϕ_{ps}	Model head parameter of Approximate Van Genuchten Model
ϕ_{soil}	Angle of friction of soil
γ	Unit weight of soil
γ_d	Dry unit weight of soil
γ_{sat}	Saturated unit weight of soil
γ_{unsat}	Unsaturated unit weight of soil
γ^p	Plastic shear strain defined in Hardening-Soil model
$\dot{\gamma}^p$	Rate of plastic shear strain

λ	Earth pressure coefficient for cylindrical shafts
ν'	Effective Poisson's ratio
ν_u	Undrained Poisson's ratio
ν_{ur}'	Effective unloading/reloading Poisson's ratio
σ_a	Datum stress, which equals to 98kPa
σ_h'	Horizontal effective stress
σ_r	Radial earth pressure
σ_{rB}	Berezantzev's radial earth pressure
σ_t	Circumferential stress
$\sigma_{tension}$	Tensile strength of the soil in Hardening-Soil model
σ_v'	Vertical effective stress
σ_{vo}'	In-situ effective overburden pressure
σ_z	Vertical stress
σ_1', σ_2', σ_3'	Principle effective stress
ψ	Angle of dilatancy
ψ_m	Mobilized angle of dilatancy
ΔR	Change in radius
ΔT	Change in Temperature

LIST OF FIGURES

		Page
Figure 1.1	Layout of the Deep Tunnel Sewerage System (DTSS) project (Tan and Weele, 2000)	7
Figure 1.2	Stress paths for soil elements near excavation (Lambe, 1970)	7
Figure 2.1	Geological map of Singapore Island (PWD, 1976)	40
Figure 2.2	A section through Old Alluvium with a selection of morphological features identified (Gupta et al.,1987)	40
Figure 2.3	The Unified Soil Classification System (Dutro et al., 1982)	41
Figure 2.4	Soil distribution of Old Alluvium (Li and Wong, 2001)	41
Figure 2.5	Coefficient of earth pressure at rest of Old Alluvium (Li and Wong, 2001)	42
Figure 2.6	Variation of permeability of Old Alluvium with vertical stress in oedometer tests (Chu et al., 2003)	42
Figure 2.7	Variation of modulus values of Old Alluvium from pressuremeter tests with SPT N-value (Li and Wong, 2001)	43
Figure 2.8	(a) and (b) Stresses acting on a small element of soil at a distance r from centreline of a shaft; (c) and (d) Assumptions on which the computation of earth pressure are based (Terzaghi, 1943)	44
Figure 2.9	(a) Distribution of radial pressure on lining of shaft in sand and distribution of radial stresses on cylindrical section with radius r; (b) Approximate distribution of radial, circumferential and vertical normal stresses along horizontal section at depth z (Terzaghi, 1943)	44
Figure 2.10	Active earth pressure distributions for axial-symmetrical and plane strain problems (Berezantzev, 1958)	45
Figure 2.11	Passive earth pressure distributions for axial-symmetrical and plane strain problems (Berezantzev, 1958)	45

		Page
Figure 2.12	Assumed rupture model for a shaft in cohesionless soil with forces acting on the sliding mass (Prater, 1977)	46
Figure 2.13	Comparison of earth pressure distributions (Wong and Kaiser, 1988)	46
Figure 2.14	Assumed rupture model for a shaft in purely cohesive soil with forces acting on the sliding mass (Prater, 1977)	47
Figure 2.15	Coefficients for active and passive earth pressures on underground cylindrical shafts (Naval Facilities Engineering Command, 1986)	48
Figure 2.16	Modes of yielding: (a) Mode A, $\sigma_t - \sigma_r$ = max; (b) Mode B, $\sigma_v - \sigma_r$ = max; (c) Mode C, $\sigma_t - \sigma_v$ = max (Wong and Kaiser, 1988)	49
Figure 2.17	(a) Ground convergence curve at various depths without gravity effect; (b) Extent of plastic zone and pressure distribution without gravity effect; (c) Pressure distribution from convergence-confinement method with gravity effect (Wong and Kaiser, 1988)	49
Figure 2.18	Model shaft (Fujii et al., 1994)	50
Figure 2.19	(a) Comparison of normalized horizontal earth pressure distributions of sand with relative density = 70%; (b) Comparison of normalized horizontal earth pressure distributions of sand with relative density = 10% (Fujii et al., 1994)	50
Figure 2.20	Model shaft (Ueno et al., 1996)	51
Figure 2.21	Empirical prediction method (Ueno et al., 1996)	51
Figure 2.22	The Relationships between earth pressure and failure mechanism (Fujii et al., 1996)	52
Figure 2.23	Wall failure mechanisms for axisymmetric excavations: (a) Mechanism A; (b) Mechanism B; (c) Mechanism C; (d) Mechanism D (Britto and Kusakabe, 1982)	52
Figure 2.24	Base failure mechanisms for axisymmetric excavations: (a) Mechanism E; (b) Mechanism F (Britto and Kusakabe, 1982)	53
Figure 2.25	Variation of Stability Number with excavation depth to radius ratio (Britto and Kusakabe, 1982)	53

		Page
Figure 2.26	Variation of Stability Number with excavation depth to radius ratio (Britto and Kusakabe, 1983)	54
Figure 2.27	Wall failure mechanisms for support axisymmetric excavations (Britto and Kusakabe, 1984)	54
Figure 3.1	Changi Water Reclamation Plant project site	61
Figure 3.2	Plan view of Influent Pumping Station	62
Figure 3.3	Layout of strain gauges for Influent Pumping Shaft 2 (IPS-2)	63
Figure 3.4	Instrumentation plan for Influent Pumping Shaft 2 (IPS-2)	64
Figure 3.5	SPT N-values at BH 1 and BH 2	65
Figure 3.6	Simplified soil profile at Influent Pumping Station	65
Figure 3.7	Wall dimensions of Influent Pumping Shaft 2 (IPS-2)	66
Figure 3.8	Excavation sequence of vertical shafts at Influent Pumping Station	67
Figure 4.1	Hyperbolic stress-strain relationship in primary loading for a standard drained triaxial test (Schanz et al., 1999)	88
Figure 4.2	Successive yield loci for various values of hardening parameter, γ^p, and failure surface (Schanz et al., 1999)	88
Figure 4.3	Definition of reference tangential oedometer stiffness modulus, E_{oed}^{ref}, in oedometer test results (Brinkgreve, 2002)	89
Figure 4.4	Yield surfaces of hardening-soil model in mean effective stress – deviatoric stress space (Brinkgreve, 2002)	89
Figure 4.5	Representation of total yield contour of the Hardening-Soil Model in principal stress space for cohesionless soil (Brinkgreve, 2002)	90
Figure 4.6	Determination of model parameters using oedometer test (Schanz and Bonnier, 1997)	90
Figure 4.7	Finite element mesh of oedometer test (120 15-node triangular elements)	91

		Page
Figure 4.8	Influence of effective strength parameters on percentage errors of estimated m and E_{oed}^{ref} at p^{ref} of 100 kN/m^2	92
Figure 4.9	Influence of reference pressure on percentage errors of estimated m and E_{oed}^{ref} for cohesionless soils	93
Figure 4.10	Influence of reference pressure on percentage errors of estimated m and E_{oed}^{ref} for cohesive soils	94
Figure 4.11	Determination of m and E_{oed}^{ref} of Old Alluvium soils using method proposed by Schanz and Bonnier (1997)	95
Figure 4.12	Finite element mesh of consolidated undrained triaxial test (120 15-node triangular elements)	96
Figure 4.13	Simulation of oedometer and unconsolidated undrained triaxial test results of Sample 1	97
Figure 4.14	Simulation of oedometer and unconsolidated undrained triaxial test results of Sample 2	98
Figure 4.15	Simulation of oedometer and unconsolidated undrained triaxial test results of Sample 3	99
Figure 5.1	Finite element mesh of aquifer	111
Figure 5.2	Hydraulic head in aquifer after 3970 seconds of pumping	111
Figure 5.3	Comparison between the PLAXFLOW numerical solution and the Theis solution	112
Figure 6.1	Finite element mesh for excavation at Influent Pumping Shaft 2	140
Figure 6.2	Location of thermocouple sensors in ring wall	140
Figure 6.3	Average temperature variation inside ring wall	141
Figure 6.4	Process of setting and hardening of concrete (Mindess and Young, 1981)	141
Figure 6.5	Comparison of measured and predicted hoop strains at Level A and Level B	142
Figure 6.6	Comparison of measured and predicted hoop strains at Level C and Level D	143
Figure 6.7	Comparison of measured and predicted hoop strains at Level E and Level F	144

		Page
Figure 6.8	Comparison of measured and predicted hoop strains at Level G and Level H	145
Figure 6.9	Comparison of measured and predicted hoop strains at Level I and Level J	146
Figure 6.10	Comparison of measured and predicted hoop strains at Level K and Level L	147
Figure 6.11	Comparison between undrained, consolidation and drained analysis on hoop strains at Level A, Level B and Level C	148
Figure 6.12	Comparison between undrained, consolidation and drained analysis on hoop strains at Level D, Level E and Level F	149
Figure 6.13	Comparison between Undrained, Consolidation and Drained analysis on hoop strains at Level G, Level H and Level I	150
Figure 6.14	Comparison between Undrained, Consolidation and Drained analysis on hoop strains at Level J, Level K and Level L	151
Figure 6.15	Plot of plastic points in drained analysis	152
Figure 6.16	Measured and predicted bending moments of diaphragm wall	153
Figure 6.17	Measured and predicted deflections of diaphragm wall	154
Figure 6.18	Variation of stresses in soil continuum at Level D, Level G and Level L	155
Figure 6.19	Influence of mesh density on hoop strains at Level D, Level G and Level L	156
Figure 7.1	Influence of effective angle of friction of soil	169
Figure 7.2	Influence of reference secant stiffness modulus	170
Figure 7.3	Influence of reference tangential oedometer stiffness modulus	171
Figure 7.4	Influence of reference unloading stiffness modulus	172
Figure 7.5	Influence of soil stiffness	173

		Page
Figure 7.6	Influence of over-consolidation ratio of Old Alluvium soils	174
Figure 7.7	Influence of soil permeability	175
Figure 7.8	Influence of permeability on the variation of hoop strains with time	176
Figure 7.9	Plot of plastic points where permeability multiplier = 1	177
Figure 7.10	Plot of plastic points where permeability multiplier = 100	177
Figure 7.11	Influence of interface strength	178
Figure 7.12	Influence of grade of concrete of diaphragm wall	179
Figure 7.13	Influence of grade of concrete of hoop stress of diaphragm wall	180
Figure 7.14	Influence of grade of concrete of ring wall	181

LIST OF TABLES

		Page
Table 2.1	Classification of Old Alluvium (Li, 1999)	13
Table 2.2	Fines content of different OA soil types (Li and Wong, 2001)	13
Table 2.3	Geotechnical properties of Old Alluvium (Sharma et al., 1999)	14
Table 2.4	Effective stress parameters of different zones of Old Alluvium (Li and Wong, 2001)	16
Table 3.1	Depth of strain gauges in Influent Pumping Shaft 2	57
Table 4.1	Hardening-Soil Model parameters for oedometer element tests	78
Table 4.2	Soil Parameters determined using Schanz and Bonnier's method	81
Table 4.3	Hardening-Soil Model Parameters of Old Alluvium Samples	83
Table 5.1	Van Genuchten model parameters for Hypres Soil Classification System (Brinkgreve et al, 2003)	107
Table 5.2	Approximate Van Genuchten model parameters for Hypres Soil Classification System (Brinkgreve et al, 2003)	107
Table 5.3	Van Genuchten model parameters for USDA Soil Classification System (Brinkgreve et al, 2003)	108
Table 5.4	Approximate Van Genuchten model parameters for USDA Soil Classification System (Brinkgreve et al, 2003)	108
Table 5.5	Van Genuchten model parameters for Staring Soil Classification System (Brinkgreve et al, 2003)	109
Table 5.6	Approximate Van Genuchten model parameters for Staring Soil Classification System (Brinkgreve et al, 2003)	110
Table 6.1	Excavation and construction sequence of IPS-2	119
Table 6.2	Date of casting of ring walls	120

		Page
Table 6.3	Correlations used for determination of soil parameters	121
Table 6.4	Proposed soil parameters I	122
Table 6.5	Proposed soil parameters II	122
Table 6.6	Material properties of excavation support system	122
Table 6.7	Properties of flexible plate	123
Table 6.8	Equivalent stresses acting on diaphragm wall	126
Table 6.9	Location of strain gauges	127

CHAPTER 1 INTRODUCTION

1.1 Background

Excavation and tunnelling projects are often found in many metropolitan and build-up areas where there is a need to exploit underground space. Circular excavations are often carried in the construction of underground storage tanks, hydraulic and power facilities, manholes, inspection or access chambers and service entrances. As such, circular vertical shafts are often employed as the retaining systems for these excavations and adopted as the starting and ending sections for underground tunnelling and pipe jacking projects.

According to Xanthakas (1994), there are two major structural benefits of using circular enclosures for deep excavations. Interior lateral bracings are not required and wall embedment may be reduced or eliminated below the final excavation level under certain conditions. Powderham (1999) recognised that a complete elimination of interior bracing would maximise space for construction activities while Ariizumi et al. (1999) highlighted savings in construction cost and time where a cylindrical retaining structure is employed. The two basic functions of an excavation support system are to provide stability at every stage of the excavation and to control movements in the adjacent ground. Hence, the design of a circular vertical shaft involves the structural design of the shaft lining for stability as well as to ensure the soil movements induced by the shaft construction and excavation satisfy the stringent serviceability requirements imposed by the regulating authorities. As lateral soil stresses acting on cylindrical walls are resisted by axial thrusts in the circular shaft linings, hoop compression of a circular vertical shaft has to be considered in the design, in addition

to the moments and shearing forces that would have occurred in the retaining wall adopted in a two-dimensional excavation.

1.2 Current Issues and Problem Definition

The Government of Singapore initiated the Deep Tunnel Sewerage System (DTSS) project as a long-term solution to the country's needs in wastewater collection, treatment and disposal. Hulme and Burchell (1999) reported that the cross-island deep tunnels constructed in this project would intercept wastewater flows in existing gravity sewers, upstream of the pumping stations, and route the wastewater flows by gravity to two new centralised sewage treatment plants. The new sewage treatment plants are located at the south-eastern and south-western coastal regions of the Singapore island and they are extended in phases to replace the existing treatment plants. All the existing sewage pumping stations and the six treatment plants will be phased out eventually.

Two large cross-island deep tunnel systems are constructed in the DTSS project. According to Tan and Weele (2000), the North Tunnel System consists of the North Tunnel and the Spur Tunnel, as shown in Figure 1.1. The completed tunnels connect to the Influent Pumping Station at the Changi Water Reclamation Plant. The North Tunnel is approximately 38.5 km in length and its final diameters range from 3.6 m to 6 m. The Spur Tunnel is 9.6 km in length and it discharges into the North Tunnel. The South Tunnel System has a length of approximately 20 km and it connects to the influent pumping station at the Tuas Wastewater Treatment Plant. Both the wastewater treatment plants are located on reclaimed land. Treated effluent will be discharged into the Straits of Singapore through deep sea outfall systems.

Three circular influent pumping shafts are constructed for the Influent Pumping Station of the Changi Water Reclamation Plant. A 70-m deep multi-stage cylindrical excavation is carried out for Influent Pumping Shaft 2 of the Influent Pumping Station over a period of eight months. A circular concrete diaphragm wall is adopted as the excavation support system. If the excavation were conducted instantaneously, the soil would strain in an undrained condition. On the other hand, the soil would strain in a drained condition if this excavation were performed at an infinitely slow rate. In reality, the soil will be partially drained as the actual excavation was carried out over a finite period. Yong et al (1989) have shown that consolidation phenomenon results in additional movements and changes in loads acting on a retaining system. Thus, effects of consolidation cannot be neglected.

Lambe (1970) considered the changes in stress experienced by two elements, one at the retained side of the excavation and one beneath the excavation. Figure 1.2 shows the stress paths undertaken by the two soil elements. He recognised that an excavation is an unloading process, as shown by the total stress path and it affects the boundary pore pressure inside the excavation. Lambe (1970) has also highlighted the complicated interrelationship between the wall movement and stress on a retaining wall as the horizontal stress in a soil element on the retained side of the excavation can vary, depending whether the wall moves outward or inward.

Thus, in view of the complexity of an excavation problem, the finite element approach is employed to understand the behaviour of the cylindrical excavation for Influent Pumping Shaft 2 of the Influent Pumping Station. Finite element analysis is an invaluable tool for evaluating the performance of an excavation support system as the

excavation and construction sequence can be accounted for and the soil and structure can be considered interactively, thus, enabling the loads acting on the retaining wall and movements of the wall to be accurately examined. However, the main challenge of conducting finite element analysis is the selection of a suitable soil constitutive model and the determination of representative model parameters.

Hence, the detailed investigation of this multi-level excavation in Old Alluvium would first require a careful examination of the soil constitutive model and the determination of its parameters that are representative of the soil conditions at the project site. Field observations taken during the excavation form the basis for this research and the primary emphasis of this study is directed towards measuring the hoop strains in the circular diaphragm wall of Influent Pumping Shaft 2. Finite element analysis is carried out to simulate the excavation and construction process in this project and to provide insights on the design of such deep circular excavations in Old Alluvium.

1.3 Scope and Objectives

The time-dependent behaviour of an excavation for the Changi Water Reclamation Plant is studied in this research. Cylindrical vertical shafts are adopted as the excavation support system for the underground Influent Pumping Station of the Changi Water Reclamation Plant. PLAXIS, a finite element package, is used to simulate the excavation process. PLAXFLOW, another finite element package developed by PLAXIS BV, is utilised in conjunction with the PLAXIS program to perform axisymmetrical groundwater flow computations for the finite element calculations. The PLAXFLOW program is compatible with the PLAXIS program for deformation and stability analysis. Consolidation finite element analyses will be performed to identify

the key influences that affect the time-dependent response of the cylindrical retaining system.

The main objectives of the study are:

a) To determine representative constitutive model parameters for Old Alluvium soils at the project site.

b) To create a finite element model to simulate the response of the excavation support system for the Influent Pumping Shaft 2 (IPS-2) of the Influent Pumping Station.

c) To perform a parametric study to examine the influence of various key parameters on the behaviour of the excavation support system.

This thesis is divided into eight chapters, each of which deals with different aspects of the study. In Chapter 1, the general background, scope and objectives of the research programme are described. Chapter 2 summarises previous studies on the composition, classification and geotechnical properties of the Old Alluvium formation, earth pressures acting on circular vertical walls, observations from centrifuge tests, stability issues concerning unsupported and supported axisymmetrical excavations and numerical studies. The general site information, soil investigation and instrumentation works, and the construction sequence for the Influent Pumping Station excavation project are described in Chapter 3.

Chapter 4 provides a preview of basic characteristics of the Hardening-Soil model and presents the results of determination of some Hardening-Soil model parameters for Old Alluvium using some oedometer and triaxial tests. Material models supported by the

PLAXFLOW program are described in Chapter 5 and a validation exercise is performed to assess the performance of the program in axisymmetrical transient groundwater flow calculations. Chapter 6 presents the results of finite element analysis for the excavation at Influent Pumping Shaft 2 and a discussion on the measured and predicted hoop strains, bending moments and displacements of the circular retaining wall is made. The influence of various parameters on the response of the circular shaft is studied in Chapter 7. Finally, Chapter 8 summarises the conclusions drawn from the preceding chapters.

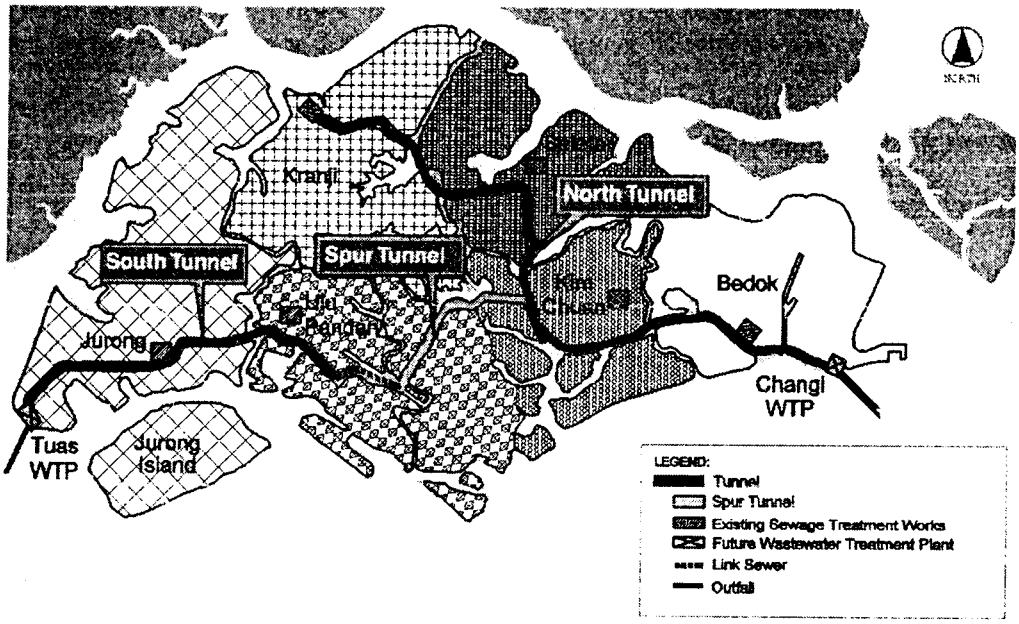

Figure 1.1 Layout of the Deep Tunnel Sewerage System (DTSS) project (Tan and Weele, 2000)

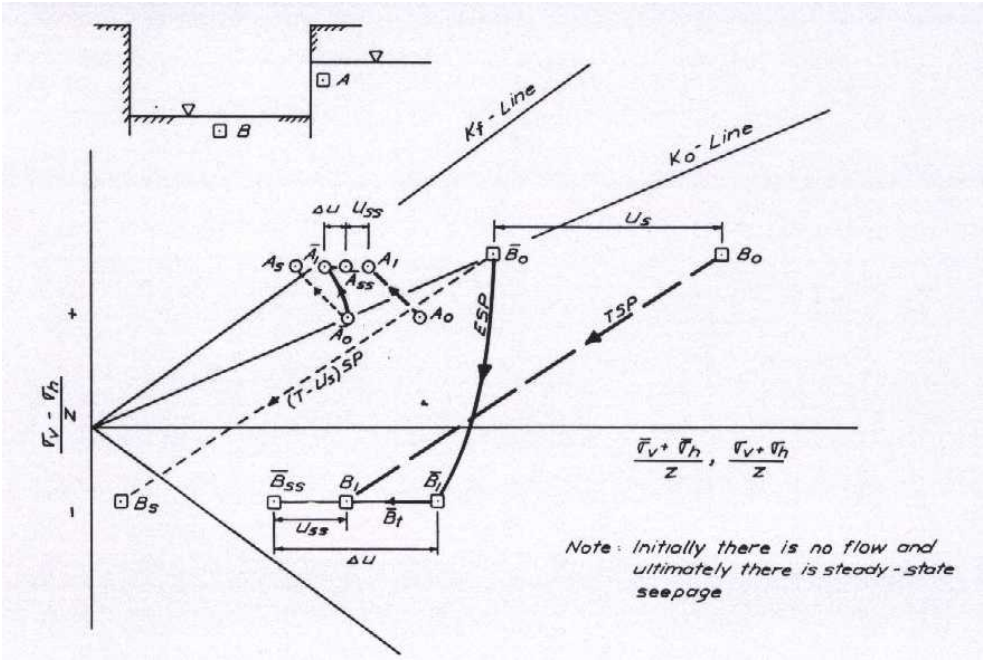

Figure 1.2 Stress paths for soil elements near excavation (Lambe, 1970)

CHAPTER 2 LITERATURE REVIEW

2.1 Introduction

In this chapter, previous studies on the composition, classification and geotechnical properties of the Old Alluvium formation are summarised. Theories of earth pressures acting on circular shaft walls based on soil plasticity considerations, limit equilibrium methods, convergence-confinement method are discussed. Finally, observations from centrifuge tests, stability issues concerning unsupported and supported axisymmetrical excavations and numerical studies carried out by other researchers will be presented in the later part of this chapter.

2.2 Singapore Old Alluvium Formation

The Republic of Singapore consists of a main island and many outlying islands totalling some 620 square kilometres in area. The geology of Singapore is shown in Figure 2.1, as collated by PWD (1976). Nine geological formations have been identified to describe the stratigraphy of Singapore. They are the Sajahat Formation, Gombak Norite, Palaeozoic Volcanics, Bukit Timah Granite, Jurong Formation, Old Alluvium, Huat Choe Formation, Kallang Formation and Tekong Formation. In particular, the Old Alluvium Formation will be of interest in this research.

The Old Alluvium Formation is an extension of a deposit found in southern Johore of Malaysia and it exists as an extensive sheet in the offshore zone to the east of Singapore. PWD (1976) reported that the Old Alluvium could be found lying to the north and north-east of the Kallang River Basin between the central granite and the granite at Changi. Similar Old Alluvium deposits, which lie against the Jurong

Formation, can be found in the north-west region of the Singapore island in the Buloh Besar area. Pitts (1984) highlighted that the area of Old Alluvium in the north-west region of the main island of Singapore is approximately 12 km^2 but the main area of Old Alluvium is in the eastern part of the island, where it occurs as a virtually uninterrupted sheet, either at the surface or buried under younger deposits. The geology and engineering properties of the Old Alluvium are documented in several publications and they are discussed in the following sections.

2.2.1 Age and Thickness of Old Alluvium

There is no direct evidence indicating the age of the Old Alluvium Formation in Singapore as no fossils, pollen or organic material has been found. Gupta et al. (1987) reported that the absence of organic materials could be due to the post-depositional oxidation in a high-energy environment. Alexandar (1950) stated that Old Alluvium is of Pleistocene age but Burton (1964) believed that the deposition of Old Alluvium could extend back to late Pliocene. Aleva et al. (1973) suggested that the Old Alluvium in Singapore could be deposited during the time of Upper Tertiary to Pleistocene age as the characteristics, stratigraphy and environments of deposits of Old Alluvium in Singapore appeared to correlate well with the Alluvial Complex in Singkep and Bangka of Indonesia.

The maximum recorded depth of the Old Alluvium in Singapore is 149 m. PWD (1976) had considered the height of nearby hills and proposed a possible thickness of 195 m for Old Alluvium. Gupta et al. (1987) questioned the 149 m depth reported by PWD (1976) as they believed that it is difficult to differentiate Old Alluvium from the weathered products of the bedrock. The quartzites, quartz sandstones and argillites of

the Sajahat Formation and Bukit Timah Granite are usually similar to the weathered products of Old Alluvium. Thus, a problem of identification would occur. Gupta et al. (1987) believed that Old Alluvium is at least 50 m thick and the top of the formation has been eroded as Old Alluvium can be found up to an elevation of 35 m on local hills. As the determination of preconsolidation pressure using an oedometer is difficult, an approximate method of utilising the ratio of undrained cohesive strength to the effective overburden pressure was used by Pitts (1986) to estimate the overburden thickness of two Old Alluvium samples in the eastern part of Singapore. Pitts (1986) assumed that the water table in the river valley was high during the deposition of the Old Alluvium sediments and he adopted the submerged unit weight of Old Alluvium in the computations. Estimated heights of overburden removal at Bedok and Tampines ranged from 55 m to 59 m and 60.5 m to 65.6 m respectively. Hence, he suggested that the Old Alluvium could have been over 100 m thick.

2.2.2 Composition of Old Alluvium

Old Alluvium is a highly variable formation. Dames and Moore (1983) reported that its vertical variability is usually gradational with intermediate soil types and considerable lateral variability is evident. PWD (1976) mentioned that Old Alluvium consists of clayey coarse angular sand with stringers of subrounded pebbles up to 40 mm in diameter. Tan et al. (1980) reported that poorly-graded clayey sands and sand-clay mixtures are characteristic soils of Old Alluvium. Thin beds of clay and silt occurring at different depths can be found in the formation. Cross-bedding, cut and fill structures, elastic dykes, fine-grained beds, which occur as small lenticular bodies, are also present in Old Alluvium. Tan et al. (1980) believed that the occurrence of cut and

fill structures, lenses in sediments and poor sorting of the deposits is the result of a rapid environment of deposition of Old Alluvium.

Gupta et al. (1987) categorised the Old Alluvium Formation into four contextual classes, which include (i) pebbles, (ii) coarse sand with fine pebbles, (iii) medium to coarse sand and (iv) clay and silt. The four classes contain distinctive sedimentary structures and can be recognized as definite morphological features. Figure 2.2 shows a section through the Old Alluvium Formation where the morphological features are identified. The pebble beds of the formation consist of clast supported pebbles with coarse sand and fines. The pebbles are mostly made up of quartz, vein quartz, quartzite and cryptocrystalline silica and they have an average pebble size of approximately 20 mm. Fresh alkali feldspar pebbles may be found occasionally. The sand grains are mostly subangular and they have similar composition as the pebbles. No unequivocal signs of tilting of the beds have been found in Old Alluvium. Faulting is rarely found and it is mainly restricted to small-scale displacements of the fill of clay in-filled channels.

2.2.3 Weathering and Classification of Old Alluvium

Burton (1964) classified the Old Alluvium Formation into three zones on the basis of extent of weathering. They are the weathered zone, mottled zone and intact zone. The weathered zone is located at the upper part of the formation and it is almost completely weathered. The colour of the weathered zone, which is stained with oxides of iron, is often reddish-yellow or brownish yellow in colour. The weathered zone may pass downwards abruptly into a non-stained zone of partial straining or mottling. The white, cream or grey colour of the fresh material in the mottled zone is variegated by yellow,

purple, red, pink or brown patches that can be associated with a fluctuating groundwater table. The mottled zone then merges gradually into the uncoloured intact zone.

Li (1999) proposed a classification of the Old Alluvium into three zones, OAI, OAII and OAIII, according to the SPT-N values. OAI contains Old Alluvium soils with SPT N-values smaller than 25. OAII has Old Alluvium soils with N-values that range from 25 to 100 while soils with N-values greater than 100 fall into the category of OAIII. Table 2.1 summarises the classification proposed by Li (1999). Sharma et al. (1999) and Li and Wong (2001) adopted this classification of Old Alluvium in their research. Li and Wong (2001) categorised the different soil types of Old Alluvium using the Unified Soil Classification System (USCS) shown in Figure 2.3. It can be seen in Figure 2.4(a) that 71% of Old Alluvium comprises of SC and SM soils. CL and CH soils make up 14% and 7% of the formation respectively and the remaining 8% of Old Alluvium consists of soils with fines less than 12%. It is evident from Figure 2.4 that Old Alluvium becomes more sandy with depth as the percentage of soils with fines less than 12% increases from 8% for OAI to 21% for OAIII. The decrease in clay content implies a decrease in degree of weathering with depth. Table 2.2 lists the fine contents of different Old Alluvium soils. The fines content of SC and SM soils typically ranges from 20% to 30%.

Table 2.1 Classification of Old Alluvium (Li, 1999)

Zone	OAI	OAII	OAIII
Approximate Depth (m)	0.6 to 8	8 to 13	13 and below
SPT-N Value	Smaller than 25	26 to 100	Greater than 100
Colour	Yellowish, reddish or greyish brown	Yellowish brown to light grey or greenish grey	Light grey to greenish grey
Composition	Clayey and silty sand, clayey silt	Clayey and silty sand	Clayey and silty sand
Consistency	Loose to medium dense for sands; medium stiff to very stiff for clays	Medium dense to very dense for sands; very stiff to hard for clays	Very dense to moderately strong

Table 2.2 Fines content of different OA soil types (Li and Wong, 2001)

Soil Types	Fines Contents (%)	
	Average	Standard Deviation
CH	84.0	14.0
CL	67.0	14.0
SC & SM	24.0	7.8
Soils With Fines Lesser Than 12%	8.3	2.5

2.2.4 Geotechnical Properties of Old Alluvium

2.2.4.1 Index Properties and Atterbreg Limits

Tan et al (1980) observed that the water content, w, of the sandy and clayey soils of Old Alluvium ranges from 15% to 25% and 20% to 40% respectively. Sharma et al. (1999) reported that there is a decrease in water content with depth and they associated this trend with the infiltration of rainwater into the zone of aeration, which is usually located in the OAI zone. Sharma et al. (1999) found that the bulk unit weight of Old Alluvium does not vary significantly with depth and across the three zones of Old Alluvium classified by Li (1999). An average bulk unit weight of 20.5 kN/m^3 is

obtained. In contrast, due to increasing confinement at greater depths, the dry density of Old Alluvium increases with depth, as shown in Table 2.3.

Sharma et al. (1999) reported that the average values of liquid limit decrease with increasing depth but there is no significant variation of average plastic limit values with depth. The smaller Plasticity Index for deeper soils indicates a smaller percentage of fine-grained particles. It has been demonstrated by Sharma et al. (1999) that there are more clay than silt in Old Alluvium. They plotted the results of Atterberg limit tests on the plasticity chart and found that most data points fell above or on the A-line.

Table 2.3 Geotechnical properties of Old Alluvium (Sharma et al., 1999)

Zone	OAI	OAII	OAIII
Water Content (%)	22.0	18.2	16.3
Bulk Unit Weight (kN/m^3)	20.3	20.7	20.3
Dry Unit Weight (kN/m^3)	16.6	17.6	17.8
Specific Gravity	2.65	2.64	2.64
Liquid Limit (%)	55	49	38
Plastic Limit (%)	23	20	19
Plasticity Index (%)	32	28	19
Average Undrained Shear Strength (kPa)	100	195	362
Effective Cohesion (kPa)	1.9	8.4	30.3
Effective Angle of Friction (^{o})	36.1	35.9	35
Horizontal Permeability (x 10^{-8} m/s)	18.8	6.4	3.4
Compression Index	0.2	0.1	0.07
Recompression	0.025	0.020	0.015

2.2.4.2 Undrained Shear Strength and Effective Stress Parameters

The SPT N-values of Old Alluvium generally increases with depth. Orihara and Khoo (1998) related the undrained shear strength, c_u, of Old Alluvium soil samples to their SPT N-values. Their data fell between c_u = 4 N-value (kPa) and c_u = 12.5 N-value (kPa) and they recommended the use of c_u = 6 N-value (kPa). Li and Wong (2001)

reviewed the results of 174 unconsolidated undrained (UU) triaxial tests and found that the undrained shear strength of Old Alluvium can be estimated using c_u = 5.4 N-value (kPa). They also established that the undrained shear strength of Old Alluvium decreases with increasing Liquidity Index as follows:

$$c_u = 172.21\ e^{-4.6LI}\ (kPa) \quad (2.1)$$

where LI represents the Liquidity Index.

Sharma et al. (1999) demonstrated that the undrained shear strength of Old Alluvium, c_u, decreases with increasing water content, w, implying that the undrained shear strength generally increases with depth. The effective angle of friction, ϕ', obtained from several consolidated undrained triaxial tests on the three zones of Old Alluvium, does not vary significantly with depth and it falls within a range of 35^o to 35.6^o. On the other hand, the effective cohesion, c', increases with depth and Sharma et al. (1999) associated this trend with the cementation of soil grains due to high overburden pressure and the effects of aging in the deeper zones. Poh et al. (1987) studied the particle size distributions from numerous samples of Old Alluvium and concluded that the cohesion of Old Alluvium is contributed by layers in the western part of the formation and by cementation in the eastern part of the formation.

Li and Wong (2001) obtained similar effective stress parameters from consolidated undrained triaxial tests. By examining the results of consolidated drained triaxial tests, deduced that the effective angle of friction obtained from consolidated drained triaxial tests are slightly smaller than that obtained from consolidated undrained triaxial tests. Table 2.4 lists the effective stress parameters recommended by Li and Wong (2001).

Table 2.4 Effective stress parameters of different zones of Old Alluvium (Li and Wong, 2001)

	OAI		OAII		OAIII	
	c' (kPa)	ϕ' (^{o})	c' (kPa)	ϕ' (^{o})	c' (kPa)	ϕ' (^{o})
Consolidated Undrained Test	1.9	36.1	8.3	35.9	30.3	35.1
Consolidated Drained Test	0	34	0	34.8	Insufficient Data	
Recommended	0	35	5	35	25	35

2.2.4.3 Over-consolidation Ratio

According to Dames and Moore (1983), there is strong evidence of over-consolidation in Old Alluvium. Over-consolidation ratios of 4 to 5 are obtained based on in-situ and laboratory tests. However, Sharma et al. (1999) found that the over-consolidation ratio of Old Alluvium is usually less than 2, implying that this formation is lightly consolidated. Li and Wong (2001) proposed an approximate relationship correlating the over-consolidation ratio, OCR, of Old Alluvium to the SPT N-value and effective in-situ overburden pressure.

$$OCR = 0.146 \left[\frac{N P_a}{\sigma_{vo}'} \right]^{1.25} \quad (2.2)$$

where N, P_a and σ_{vo}' represent the SPT N-value, atmospheric pressure and the in-situ effective overburden pressure, respectively

2.2.4.4 Coefficient of Earth Pressure At Rest

Li and Wong (2001) attempted to correlate the coefficient of earth pressure at rest, K_o, of Old Alluvium to the SPT N-value and proposed the following relationship:

$$K_o = 0.163 \left[\frac{N P_a}{\sigma'_{vo}} \right]^{0.625} \quad (2.3)$$

where N, P_a and σ_{vo}' represent the SPT N-value, atmospheric pressure and the in-situ effective overburden pressure, respectively. It can be observed from Figure 2.5 that the data points are very scattered.

2.2.4.5 Permeability

Pfeiffer (1972) reported that the coefficient of permeability of the weathered zone of Old Alluvium falls within the range of 10^{-8} to 10^{-10} m/s while Orihara and Khoo (1998) mentioned that the coefficient of permeability of Old Alluvium, obtained from in-situ rising head permeability tests, falls within the range of 10^{-7} to 10^{-9} m/s. Dames and Moore (1983) recommended an overall design value of 10^{-7} m/s for the permeability of Old Alluvium. Table 2.3 summarises the coefficient of horizontal permeability, k_h, of Old Alluvium provided by Sharma et al. (1999). Although there are insufficient data to determine the magnitude of vertical permeability, k_v, Sharma et al. (1999) believed that the vertical permeability of Old Alluvium would be smaller than the horizontal permeability by a factor of 2 to 5.

Li and Wong (2001) clarified that laboratory oedometer tests measure the coefficient of vertical permeability of soils whereas in-situ tests provide the coefficient of horizontal permeability. The coefficient of permeability obtained from oedometer tests ranges from 10^{-8} to 10^{-10} m/s while those measured in the field vary from 10^{-6} to 10^{-9} m/s, which is approximately 100 times of those determined from oedometer tests. Li and Wong (2001) believed that the in-situ tests would yield more reliable results as compared to laboratory tests as a larger volume of soil is tested and sampling disturbance is avoided. Li and Wong (2001) reported that there is no clear trend of decrease in coefficient of permeability with increasing fines content of Old Alluvium

soils.

Chu et al. (2003) performed oedometer tests on some Old Alluvium soil samples in the eastern part of Singapore. Load increments that increased gradually from 70 to 2260 kPa were used. Figure 2.6 shows the variation of permeability with vertical pressure for some cohesive and granular Old Alluvium samples. Chu et al. (2003) concluded that the coefficient of permeability is in the order of 10^{-10} m/s even for granular Old Alluvium soils.

2.2.4.6 Stiffness Characteristics

Sharma et al. (1999) examined the results of several pressuremeter tests to determine the undrained stiffness to undrained shear strength ratio, $\frac{E_u}{c_u}$. A significant scatter ranging from 40 to 400 for $\frac{E_u}{c_u}$ ratio is obtained. The average value for the $\frac{E_u}{c_u}$ ratio is found to be 170. Similar studies were conducted by Dames and Moore (1983), which recommended a value of 250 for the $\frac{E_u}{c_u}$ ratio of Old Alluvium. Li and Wong (2001) correlated the undrained stiffness moduli, E_{PMT} and E_r, obtained from pressuremeter tests to the corresponding SPT N-values. E_{PMT} is the pressuremeter modulus from the first cycle of test whereas E_r is the unloading-reloading modulus of the second cycle. It can be observed from Figure 2.7 that E_{PMT} is approximately 0.74 N-values (MPa) and E_r is roughly 3.72 N-values (MPa). The $\frac{E_r}{E_{PMT}}$ ratio of Old Alluvium ranges between 3 to 8, but no clear relationship with the SPT N-value can be determined. Orihara and

Khoo (1998) had performed similar studies earlier and concluded that E_{PMT} and E_r can be determined using E_{PMT} = 1 N-values (MPa) and E_r = 2 N-values (MPa) respectively.

2.3 Design of Vertical Shafts

According to Terzaghi (1943), vertical shafts are excavations of large cylindrical holes that are at least several feet in diameter. The basic functions of an excavation support system are to provide stability at every stage of the excavation and to minimise movements in the adjacent ground. Thus, the design of an underground vertical shaft includes the design of shaft lining to ensure structural stability of the shaft and an assessment of wall deflections and soil movements due to the excavation and construction of the vertical shaft.

Earth pressure on a circular vertical wall was studied by many researchers, for example, Terzaghi (1943), Berezantzev (1958), Prater (1977), Abel (1979), Lade et al. (1981), Wong and Kaiser (1988), Fujii et al (1994), Hagiwara et al. (1994), Fujii et al (1996), Ueno et al (1996) and Imamura et al. (1999). These researchers have proposed various design approaches and theories based on soil plasticity considerations, limit equilibrium methods assuming hypothetical failure lines, convergence-confinement method and centrifuge tests. These design methods of determination of earth pressure acting on a cylindrical vertical shaft lining are reviewed. The assumptions made in these approaches and their limitations are discussed. Research studies on the stability of unsupported and supported cylindrical excavations and numerical analyses are also examined.

2.3.1 Determination of Earth Pressure on Shaft Linings

2.3.1.1 Terzaghi's Method

Terzaghi (1943) proposed an approximate solution for determining the earth pressure acting on a vertical shaft with an infinite depth by considering the effect of gravity. The limit equilibrium state of a downward-sliding cylindrical block of yielded ground was considered and the minimum supported pressure required to prevent this mode of failure would be the earth pressure acting on the shaft lining. Figure 2.8 shows the stresses acting on the sides of a small soil element at a distance r from the centreline of a vertical shaft and the assumptions made for the computation of earth pressure. Terzaghi (1943) assumed that the stress difference between the radial and circumferential stresses in an annulus around a vertical hole causes yielding and circumferential stress of a soil element is taken to be equal to the vertical stress.

Westergaard (1940) derived a solution for the radius of the zone of plastic equilibrium at any depth below the ground surface, on the assumption of coefficient of earth pressure of unity. Terzaghi (1943) considered the stress states of the soil element near a vertical shaft using Mohr's Circle and applied Westergaard's solution to cohesionless soil. He suggested that both the radial and circumferential stresses in the plastic zone increase with radial distance from the shaft and this stress condition is known as ring action. The lateral earth pressure acting on a shaft wall would be smaller than the active Rankine earth pressure due to the ring action, as shown in Figure 2.9. The boundary between the plastic and elastic zone around a vertical shaft is indicated by a break in the stress curves, as shown in Figure 2.9. Terzaghi (1943) deduced that the rate of increase of radial stress on the shaft wall would decrease as the depth of shaft increases. He has neglected the effect of principal stress rotation near the shaft wall

due to non-zero shear stresses. Thus, he proposed the use of a reduced friction angle, ϕ^*, for the Mohr-Coulomb failure criterion.

$$\phi^* = \phi' - 5^o \qquad \text{for } 30^o < \phi' < 40^o, \; c = 0 \tag{2.4}$$

The theory proposed by Terzaghi (1943) is based on an assumption that the depth of shaft is infinity. However, part of the radial pressure exerted by the soil around the lower part of the shaft is transferred to the soil beneath the bottom of the shaft by shear stresses. According to Terzaghi (1943), the stress relief due to this pressure transfer is significant at a distance approximately equals to the width of plastic zone above the bottom of the shaft. If a shaft is constructed in sand, the width of plastic zone is small. Hence, the pressure on the lining at the bottom of the shaft in sand is similar to that on the lining of a shaft with infinite depth. However, the depth of stress transfer extends over a large part of the depth of a shaft in clay. Hence, Terzaghi (1943) expected that the earth pressure on a shaft in clay is smaller than the computed pressure and his proposed method would not predict the earth pressure on vertical shafts in clay accurately.

Terzaghi (1943) also recognised that the method of construction would affect the magnitude and distribution of the earth pressure. However, his method does not account for construction effects due to the lack of computational resources. According to Prater (1977), the disadvantage of Terzaghi's method lies in its unrealistic prediction of the shape of the plastic zone, which increases in radius with depth reaching a limiting value asymptotically.

2.3.1.2 Berezantzev's Method

Berezantzev (1958) applied Sokolovski's (1954) "step-by-step" method of computation for limit equilibrium plain strain problem to solve an axial-symmetrical equilibrium problem. The state of stress around a cylindrical shaft is described by two differential equations of equilibrium, presented in Equations 2.5 and 2.6, and two conditions of limit equilibrium. Berezantzev (1958) used the Mohr Coulomb's failure criterion as one of the conditions of limit equilibrium, as shown in Equation 2.7. He also made assumptions of equal principal stresses, listed in Equation 2.8, to render the problem statically determinate.

$$\frac{\partial \sigma_r}{\partial r} + \frac{\partial \tau_{rz}}{\partial z} + \frac{\sigma_r - \sigma_t}{r} = 0 \qquad (2.5)$$

$$\frac{\partial \tau_{rz}}{\partial r} + \frac{\partial \sigma_z}{\partial z} + \frac{\tau_{rz}}{r} = \gamma \qquad (2.6)$$

$$\frac{1}{\cos\phi}\frac{\sigma_1 - \sigma_3}{2} - \tan\phi\frac{\sigma_1 + \sigma_3}{2} = c \qquad (2.7)$$

$\sigma_2 = \sigma_1$ (active state); $\sigma_2 = \sigma_3$ (passive state) (2.8)

where σ_1, σ_2, σ_3, σ_r, σ_z, σ_t, τ_{rz}, r, z, c and ϕ are the three principal stresses, radial stress, vertical stress, circumferential stress, shear stress, radial distance from the centre line of shaft, depth from top of shaft, cohesion and angle of friction, respectively.

A numerical analysis is required to obtain a family of slip lines for each different case of shaft conditions. The failure surfaces predicted by Berezantzev (1958) could be approximated by the surface of a cone. This method would predict a lower active earth pressure and a higher passive earth pressure as compared with problem of plane deformation. Figures 2.10 and 2.11 show the active and passive earth pressures obtained for both axial-symmetrical and plane strain problems. The earth pressures for

an axial-symmetrical problem are represented by solid lines whereas the dotted lines indicate the pressures for a case of plane deformation.

2.3.1.3 Prater's Method

Prater (1977) extended Coulomb's theory to axially symmetrical conditions and derived solutions of earth pressure acting on circular vertical shaft linings in both cohesionless soils and soils in an undrained, unconsolidated state that exists immediately after loading. Determination of earth pressure on shaft lining in soils in the undrained "$\phi = 0$" condition has not been dealt with by earlier researchers.

In the computation of earth pressure acting on a shaft in cohesionless soils, Prater (1977) approximated the failure surface predicted by Berezantzev (1958) by a cone, as shown in Figure 2.12, and performed a limit equilibrium analysis assuming the Mohr-Coulomb failure criterion at the failure surface. He introduced a tangential force F_T that has a radial outward component F_H in his derivation and proposed a coefficient of earth pressure for cylindrical shafts, k_r. In order to obtain realistic results, Prater (1977) suggested that an earth pressure coefficient λ, which is adopted for the computation of F_T, should fall between the coefficient of earth pressure at rest and the coefficient of active earth pressure, in contrast to the tacit assumption of unity for the earth pressure coefficient λ made by Berezantzev (1958).

Prater's theoretical solution for shafts in cohesionless soils leads to a conclusion that no earth pressure is exerted on the shaft lining below a certain depth of the lining whereas the limit equilibrium theory proposed by Berezantzev (1958) does not give this result. According to Wong and Kaiser (1988), this deficiency may be attributed to

the fact that the magnitude of the tangential force F_T is not limited. Figure 2.13 shows a comparison of the earth pressure distributions acting on a circular shaft in cohesionless soil using the methods proposed by Terzaghi (1943), Berezantzev (1958) and Prater (1977).

Prater (1977) proposed an approximate solution for earth pressure exerting on shafts in soils in undrained "$\phi = 0$" condition using the assumed mode of failure as shown in Figure 2.14 and setting the earth pressure coefficient λ equals to the coefficient of earth pressure at rest, which has a magnitude of unity. A critical depth where no support is theoretically required can be determined by equating the earth pressure coefficient for the circular shaft k_r to zero.

One of the shortcomings of this approach, as elaborated by Wong and Kaiser (1988), was that this design method does not account for the influence of horizontal arching. The effect of yield propagation, the influence of the extent of the plastic zone and the related stress redistribution are also not considered in this approach.

2.3.1.4 NAVFAC Design Method 7.01

The coefficients for active and passive earth pressures on vertical shafts of unlimited depth in granular soils recommended by the Naval Facilities Engineering Command (1986) are shown in Figure 2.15. Naval Facilities Engineering Command (1986) highlighted that rigid bracing at the top of a shaft in sand, which is relatively shallow with a depth less than twice the diameter, may prevent the development of active pressures. Thus, horizontal pressures may be as large as the earth pressures at rest.

For a vertical shaft in clay, Naval Facilities Engineering Command (1986) proposed that no support is required up to a depth of $\frac{2c_u}{\gamma}$ and the ultimate horizontal earth pressure on the shaft lining can be computed. Naval Facilities Engineering Command (1986) reported that the initial earth pressure on the shaft in stiff clay is very small. However, the pressure may increase to several times the overburden pressure over a period of time due to the swelling pressure if the lining is adequately rigid.

2.3.1.5 Wong and Kaiser's Method

Wong and Kaiser (1988) applied the convergence-confinement method (CCM) to the design of circular vertical shafts by considering the effects of horizontal and vertical arching. The convergence-confinement method is usually used to model circular, horizontal underground openings and it is formulated to predict the interrelationship between displacements and stresses in the ground near the opening. Wong and Kaiser (1988) combined plasticity or limit equilibrium techniques with the convergence-confinement method in a two-dimensional "hole-in-a-plate" model to model the behaviour of a vertical shaft. This approach allows most relevant design factors, such as in-situ soil stresses, soil strength, soil stiffness and construction details, to be included in the analysis.

Wong and Kaiser (1988) recognised that the analysis of a circular vertical shaft is a three-dimensional problem in nature and its behaviour is affected and dominated by gravitational forces near the ground surface. Hence, all the three radial, vertical and tangential stress components have to be considered. Excavation of a circular vertical shaft can be simulated by a stress relief, which causes adjacent soil to deform both horizontally and vertically. Excessive stress relief induces yielding and permanent

plastic deformations. The stress relief during excavation leads to stress redistribution near the opening and results in horizontal and vertical arching. A design method to calculate the support pressure of a circular vertical shaft wall by considering the horizontal arching and vertical arching independently is proposed.

When horizontal arching is uncoupled from vertical arching, only equilibrium in the horizontal plane is considered. A soil element adjacent of the shaft lining is subjected to in-situ stresses before excavation. Excavation is modelled by progressively reducing the support pressure, leading to an increase in differences between the stress components. Wong and Kaiser (1988) reported that the onset of plasticity and the mode of yield initiation are dependent on the coefficient of earth pressure at rest and the strength parameters of the soil. Figure 2.16 shows the possible modes of yielding due to a vertical shaft excavation. Wong and Kaiser (1988) found that the mode of failure initiation of a purely frictional, elastic perfectly plastic material with a linear Mohr-Coulomb failure criterion could be determined as follows:

$$\frac{(N+1)}{2N} < K_o < \frac{(N+1)}{2} \qquad \text{(Mode A: } \sigma_t - \sigma_r\text{)} \tag{2.9}$$

$$K_o < \frac{(N+1)}{2N} \qquad \text{(Mode B: } \sigma_v - \sigma_r\text{)} \tag{2.10}$$

$$K_o > \frac{(N+1)}{2} \qquad \text{(Mode C: } \sigma_t - \sigma_v\text{)} \tag{2.11}$$

$$\text{where } N = \frac{\sigma_1}{\sigma_3} = \tan^2\left(\frac{\pi}{4} + \frac{\phi}{2}\right) \tag{2.12}$$

Wong and Kaiser (1988) also studied that the soil response due to excavation in purely cohesive soils. The mode of failure initiation of cohesive materials can be found using the following equations.

$$\left(1-\frac{q_u}{2p_0}\right) < K_o < \left(\frac{q_u}{2p_o}+1\right) \quad \text{(Mode A: } \sigma_t - \sigma_r\text{)} \tag{2.13}$$

$$K_o < \left(1-\frac{q_u}{2p_0}\right) \quad \text{(Mode B: } \sigma_v - \sigma_r\text{)} \tag{2.14}$$

$$K_o > \left(\frac{q_u}{2p_o}+1\right) \quad \text{(Mode C: } \sigma_t - \sigma_v\text{)} \tag{2.15}$$

where q_u is the unconfined compression strength of cohesive soil and p_o is the initial vertical in-situ stress.

Wong and Kaiser (1988) concluded that Mode C of yield initiation is seldom of practical significance. Hence, they only studied Mode A and Mode B of failure initiation. The boundary between Mode A and Mode B of yield initiation is defined by a critical coefficient of earth pressure at rest, K_{cr}, given by Equation 2.16 for purely frictional soils and Equation 2.17 for purely cohesive soils.

$$K_{cr} = \frac{(N+1)}{2N} \quad \text{(Frictional soil)} \tag{2.16}$$

$$K_{cr} = \left(1-\frac{q_u}{2p_o}\right) \quad \text{(Cohesive soil)} \tag{2.17}$$

Wong and Kaiser (1988) illustrated that different types of yielding would be induced if sufficient deformations due to radial stress relief were permitted. For a soil with a coefficient of earth pressure at rest larger than K_{cr}, yield initiation of Mode A would initially occur around the shaft wall, according to Equations 2.9 and 2.13. The extent of the plastic zone is represented by R_{tr}. However, further radial stress relief would cause both Mode A and Mode B of yield initiation to be evident and the extent of this zone, which is smaller than R_{tr}, is denoted by R_{vr}. Thus, after the propagation of

yielding, the plastic zone consists of a region between R_{vr} and R_{tr} where Mode A exists alone and a region, near the shaft, where both Mode A and Mode B occur simultaneously. Similarly, for a soil with coefficient of earth pressure at rest smaller than K_{cr}, Mode B of yielding initiates at the wall. After further propagation of yielding, the plastic zone contains a region when Mode B exists along and a region, near the vertical shaft, where both Mode A and Mode B of yield initiation are present.

The corresponding wall displacement induced by stress relief can be determined after the relationship between the support pressure and the extent of plastic zone has been established. The relationship between the support pressure, the extent of the plastic zone and the wall displacement is known as the ground convergence curve. In order to obtain a closed form solution for the ground convergence curve where only horizontal arching is considered, it is assumed that solutions for plane strain condition provide a reasonable estimation. Hence, in design, once the ground convergence curves for a specific wall elevation are derived, the pressure distribution and extent of plastic zone due to horizontal arching can be obtained by imputing a specific wall displacement based on the serviceability criteria into the ground convergence curves.

The effect of vertical arching is elaborated by Wong and Kaiser (1988). For each mode of yield initiation, the plastic flow occurs along the slip surfaces where ultimate strengths have been reached. The direction and shape of these yield surfaces are different for each mode, as shown in Figure 2.16. When the shear resistances along the yield surfaces have been fully mobilised, the soil mass tends to slide along these surfaces towards the shaft under its own weight. As a result, a support pressure has to be applied to the wall of the vertical shaft in the area where gravity dominates in order

to prevent instability. This phenomenon is known at the “gravity effect”. Vertical arching may develop if sufficient vertical movement is allowed. It is apparent from Figure 2.16 that gravity effects are more dominant in Mode A and Mode B than Mode C of yield initiation.

Although Wong and Kaiser (1988) had identified the presence of two sets of slip surfaces in the inner zone around the shaft wall and only one set in the outer zone if radial stress relief is permitted, the gravitational support pressure arises only at the inner zone with two sets of slip surfaces. Owing to the close proximity of the state of stress in the outer zone to the failure zone, Wong and Kaiser (1988) suggested that the gravitational support pressure, due to the effects of vertical arching, can be calculated based on the maximum extent of the two zones using the plastic equilibrium approach. In the design of a vertical shaft, the two pressure distributions due to horizontal and vertical arching are determined and they form an envelope of the required support pressure for the specified wall displacement. The pressure envelope at the bottom of the vertical shaft is adjusted according to Panet and Guenot (1982) for the reduced pressure caused by face effects. Figure 2.17 provides an illustration of this design approach. The design pressure envelope can be obtained by multiplying the pressure envelope by an appropriate load factor.

Some limitations of this method have been discussed by Wong and Kaiser (1988). As a two-dimensional plane strain “hole-in-plate” model is employed in the simulation of horizontal arching, shear stresses between horizontal layers are neglected. According to Terzaghi (1943), the neglect of these shear stresses could result in an underestimation of the extent of the plastic zone and an unconservative support

pressure. The influence of pore pressure is not considered in this design method. However, Wong and Kaiser (1988) mentioned that the effect of pore pressure could be easily implemented. Volumetric changes during the dissipation of pore pressure can cause significant deformations and changes in soil pressure. These time-dependent processes may govern the shaft design but they are not assessed in this approach.

2.3.1.6 Centrifuge Tests

Recently several researchers have performed centrifuge model experiments to understand the behaviour of circular vertical shafts and to obtain insights on the distribution of earth pressures on the shafts linings. Terzaghi (1943) and Berezantzev (1958) proposed theoretical methods that consider only rigid perfectly plastic soils and hence, the influence of a static soil-structure interaction was not accounted for. Wong and Kaiser (1988) proposed a relationship between earth pressures acting on shaft linings and their displacements but the effect of wall stiffness was not examined in their study. Effects of soil-structure interaction and the real stress-strain behaviour of the soil can be investigated through centrifuge experiments. These centrifuge tests are usually conducted in dry sand.

Fujii et al. (1994) investigated the influence of relative density of dry Toyoura sand and the effect of angle of wall friction on the earth pressure acting on circular vertical shafts. The model vertical shaft consisted of two aluminium semi-cylinders, as shown in Figure 2.18. One of the semi-cylinders was allowed to move horizontally to produce the change of earth pressure from an at-rest state to the active state. Uniform horizontal movement was achieved from the top to the bottom of the model shaft. The model shaft was then roughened with sand paper to model different angles of wall friction.

Fujii et al. (1994) compared their observed active earth pressures with the theoretical earth pressure derived by Berezantzev (1958). It is apparent from Figure 2.19 that Berezantzev's method generally underestimates the earth pressure below a certain depth. The earth pressures on vertical shaft in loose sand seem to be smaller than the earth pressures on vertical shaft in dense sand. Two-dimensional Rankine earth pressures would overestimate the measured earth pressures on the vertical shaft and the differences between the experimental and Rankine active earth pressures increase at greater depths. Fujii et al. (1994) associated this difference to the redistribution of stress at greater depths due to arching effects that occur with the movement of shaft lining. It can be observed from Figure 2.19 that the experimental earth pressures increase substantially near the bottom of the model shaft. Lade et al. (1981), Ueno et al. (1996) and Fujii et al. (1996) also reported similar trends. Fujii et al. (1994) suggested that this increase in earth pressures might be due to the complexity in modelling the bottom condition of the prototype. The measured active earth pressures are only slightly affected by the wall friction of the shaft.

Ueno et al. (1996) modelled some circular vertical shafts in dry Toyoura sand, as shown in Figure 2.20, and they established a prediction method of earth pressures acting on the shafts by considering the influence of stiffness of the shaft linings. They defined an apparent Young's modulus, $\frac{Et}{R}$, to represent the stiffness of shafts according to an elastic thin tube theory proposed by Roark and Young (1975). This elastic thin tube theory is only applicable for a tube with a thickness that is smaller than a tenth of its radius. Ueno et al. (1996) normalised the radial earth pressure, σ_r, with the product of the dry unit weight of sand and the radius of the shaft, $\gamma_d R$, and they found that there is no observable influence of the shaft radius on the normalised

radial earth pressure, $\frac{\sigma_r}{\gamma_r R}$. Thus, the radial earth pressure tends to be in proportion to both the dry unit weight of the soil and the radius of the shaft.

Ueno et al. (1996) observed that the normalised radial earth pressure, $\frac{\sigma_r}{\gamma_r R}$, increases with increasing apparent Young's modulus, $\frac{Et}{R}$. Hence, they concluded that the stiffness of shafts is an important factor influencing the magnitude of earth pressure acting on the shafts. The concept of an empirical prediction method proposed by Ueno et al. (1996) is demonstrated in Figure 2.21. The soil at the section shallower than a changeover depth, z_{ch}, is assumed to be at its at-rest condition as the deformations of shafts are found to be small at shallow depth. The changeover depth can be obtained from:

$$\frac{z_{ch}}{R} = 6.6 \times 10^{-5} \frac{Et/R}{\sigma_a} - 0.32 \qquad (2.18)$$

where z_{ch}, R, t, E and σ_a represent the changeover depth, the radius of the shaft, the thickness of the shaft, the Young's modulus of the shaft and a datum stress which equals to 98kPa, respectively

Ueno et al. (1996) assumed that the radio of radial earth pressure to Berezantzev's active earth pressure, α_r, is constant along the depth of the shaft from the changeover depth. The ratio of radial earth pressure to Berezantzev's active earth pressure, α_r, is found to be proportional to the apparent Young's modulus of the shaft and this relationship is given as:

$$\alpha_r = 1.15 \times 10^{-4} \frac{Et/R}{\sigma_a} + 1 \quad (2.19)$$

Ueno et al. (1996) also assumed that the stress distribution due to vertical arching only appears at the deepest one-third of the depth of the shaft. They recommended a value of 5 for α_r, for the deepest one-third of the shaft. Thus, the radial earth pressure along the depth of a shaft can be expressed according as:

$$\sigma_r(z) = \begin{cases} K_o \gamma_d z & (z \le z_{ch}) \\ \alpha_r \sigma_{rB}(z) & (z_{ch} \le z \le 2/3\, z_o) \\ 5\sigma_{rB}(z) & (2/3\, z_o \le z \le z_o) \end{cases} \quad (2.20)$$

where $\sigma_r(z)$, $\sigma_{rB}(z)$, K_o, γ_d, z_o, z_{cd} and z represent the variation of radial earth pressure with depth, the variation of Berezantzev's radial earth pressure with depth, coefficient of earth pressure at rest, dry unit weight of the soil, total depth of shaft, changeover depth and depth of shaft at which the pressure is computed, respectively

Fujii et al. (1996) studied the failure mechanism of a deep circular shaft at active state by constructing a model shaft made of two semi-cylinders in air-dried Toyoura sand and allowing one semi-cylinder to move horizontally. They observed that the failure line extends from the bottom of the shaft to the surface and the failure pattern occurs more locally along the shaft lining, in comparison to a two-dimensional plane-strain model. Thus, Fujii et al. (1996) concluded that three-dimensional nature and horizontal arching effects are apparent. Fujii et al. (1996) showed that the active failure mechanism of a circular shaft is dependent on its prototype depth or, specifically, the stress levels in the soil by comparing the shape of failure surfaces of shafts with prototype depths of 5 m, 10 m and 20 m. The failure surface of a shaft with a prototype depth of 5 m is a triangular wedge, which corresponds to the Rankine's pattern of slip

surface. The failure surface of shafts with prototype depths of 10 m and 20 m develops approximately along the shaft as a rigid block at the upper portion. At greater depths, the failure surface is approximately logarithmic spiral.

The relationship between the earth pressure and the failure mechanism of a shaft with a prototype depth of 20 m is shown in Figure 2.22. The failure mechanism can be divided into three zones. Region A shows the failure mechanism of a triangular wedge, which is typical of a two-dimensional failure mechanism according to Rankine's theory. The annular region in B is a rigid block that slides vertically down, approximately along the shaft lining. This displacement leads to compression of the lower annular region in C. Region C shears plastically and moves inward radially. This movement may explain the observation of increased earth pressure in region C.

Imamura et al. (2000) investigated the failure mechanism of an axisymmetrical shaft, with a prototype depth of 50 m, at active state and they recommended a prediction method of earth pressures based on centrifuge experiments. Based on the results obtained by Fujii et al. (1996), Imamura et al. (2000) concluded that a unique failure mechanism exists for shafts with prototype depths ranging from 10 m to 50 m. The failure region extends to a distance approximate 30% of the shaft diameter from the shaft lining. The measured surface settlements were also found to increase significantly within a distance of 30% of shaft diameter from the shaft lining, regardless of the strain levels of the shaft movements. Imamura et al. (2000) suggested that the zone of failure of shafts, up to 50 m in depth, is approximately 35% of the shaft diameter from the shaft lining, regardless of stress levels, after consideration of surface and sub-surface movements reported by earlier researchers.

In contrast to Lade et al. (1981), Fujii et al. (1994), Ueno et al. (1996) and Fujii et al. (1996), Imamura et al. (2000) confirmed that the active earth pressure on a circular vertical shaft is constant and agrees well with the earth pressure computed using Berezantzev's formula. Based on the experimental results, they proposed a prediction method of earth pressures on the shafts, which are influenced by the strain levels of the wall.

2.3.2 Stability of Axisymmetrical Excavations

Britto and Kusakabe (1982) presented analytical upper bound solutions for the failure of unsupported axisymmetrical excavations. They treated the soil as a rigid plastic material, satisfying Tresca yield criterion and possessing an uniform undrained shear strength. Britto and Kusakabe (1982) assumed that failure of an axisymmetrical excavation took place in an undrained condition and obtained solutions that enable the velocity fields of the upper bound mechanisms to satisfy incompressibility condition. One of the solutions is applicable to regions, around circular excavations, that behave as rigid blocks with no radial velocity and hence, their movements are always vertical. The other solution is applicable to regions that undergo plastic shearing and the radial movements are accompanied by circumferential straining. Figures 2.23 and 2.24 illustrate the possible wall failure mechanisms and base failure mechanisms respectively.

The expressions of stability number of the different wall and base failure mechanisms have been derived by Britto and Kusakabe (1982) and the variation of the stability number with excavation depth to radius ratio is plotted in Figure 2.25. It is apparent that the stability number generally increases with increasing excavation depth to radius

ratio and Britto and Kusakabe (1982) associated this phenomenon to the increased arching effecting in the circumferential direction as the radius is decreased. It can be observed from Figure 2.25 that Mechanism A is the critical failure mode for shafts with excavation depth to radius ratio greater than 2 whereas Mechanism D is most critical for shafts with excavation depth to radius ratio smaller than 2. Britto and Kusakabe (1982) concluded that the width of the plastic zone for Mechanism A is 40% of the excavation depth from the excavation. The base failure mechanisms that Britto and Kusakabe (1982) had considered are not relevant to practical situations, as the mobilisation of shear strength is unlikely to extend to the ground surface. Nevertheless, the width of the plastic zone of critical base failure mechanism, Mechanism E, is found to be dependent on the radius and depth of the excavation and would increase linearly with both. Britto and Kusakabe (1982) suggested that the extent of the plastic zone would give an indication of the settlement influence zone.

Britto and Kusakabe (1983) further studied the stability of undrained unsupported axisymmetrical excavation in a soil with an undrained shear strength that increases linearly with depth. Using the most critical wall failure mechanism suggested by Britto and Kusakabe (1982), Britto and Kusakabe (1983) minimised the expression of the stability number and proposed a stability chart for different cases of undrained shear strength, as shown in Figure 2.26. Britto and Kusakabe (1983) reported that the critical failure mechanism would change with the conditions of the shear strength and result in three different failure mechanisms. The width of the plastic zone is also found to be approximately 40% of the excavation depth for a wide range of shear strength conditions.

The stability of supported excavations has been considered by Britto and Kusakabe (1984). They assumed the soil to behave as a Tresca material with an uniform undrained shear strength and considered two mechanisms, with rigid lateral support and slurry support, as shown in Figure 2.27. Britto and Kusakabe (1984) proved that using a rigid lateral support has no influence on the failure mechanism unless the length of the support is adequate to prevent horizontal movement at the bottom of the excavation. In comparison, slurry support is useful even for small support length. Thus, the base failure mode is more critical than the wall failure mode when the support approaches a certain depth. Britto and Kusakabe (1984) determined stability numbers for base failure from centrifuge tests and finite element analyses and they proposed stability charts for rigid supported and slurry supported axisymmetical excavations for both wall and base failures.

2.3.3 Numerical Studies

Some researchers employ numerical methods in the design of circular shafts. Chen and Chen (1997) made used of the RIDO program and an elastio-plastic soil constitutive model to analyse the behaviour of three 70 m diameter and 90 m deep cylindrical tanks at the south-western region of Taiwan. The 1.2 m thick diaphragm walls of the underground tanks are modelled as axisymmetrical and considered as beam elements on elastic foundation. Generally, the analytical wall displacements agreed well to the measured wall displacements and Chen and Chen (1997) suggested that higher measured wall displacements may be due to non-true circle effects. Chen and Chen (1997) had shown that the hoop stresses experienced by the diaphragm walls can be predicted reasonably well from the average wall displacements using the cylindrical thin-plate theory.

Mikhail et al. (1999) compared the different methods of computing earth stresses acting on vertical shafts. The classical Rankine's active earth pressure theory, apparent earth pressure envelope (AEP), theoretical methods proposed by Terzaghi (1943), Berezantzev (1958) and Prater (1977) and a numerical method are considered. Numerical analyses were performed using the FLAC program, which is a two-dimensional finite difference program. Mikhail et al. (2000) had shown that Rankine's active earth pressure theory and AEP method do not account for soil arching around circular enclosures and hence, they were unsuitable for such structures. Although the theoretical methods consider soil arching effects, the influence of construction, soil stiffness and stress state are not accounted for. Thus, these methods are not conservative for actual shaft constructions. As the numerical finite difference method can account for soil stresses and stiffness, the actual construction sequence and wall stiffness, it is found to be more appropriate to estimate the earth pressures acting on circular shafts.

Three-dimensional undrained finite element analysis were performed by Bloodworth and Houlsby (1999) to model the interaction between a masonry building and the ground during the construction of 4 m-diameter and 15 m-deep access shaft that is 5 m from the building. A three-dimensional finite element modelling procedure developed by the Oxford University is used in the study. Bloodworth and Houlsby (1999) observed that the presence of the building would affect the settlements of the ground as the weight of the building would increase settlements further, in addition to the shaft construction.

2.4 Summary

Theoretical methods proposed by Terzaghi (1943) and Berezantzev (1958) consider only rigid perfectly plastic soils and soil-structure interaction was not studied. Although Wong and Kaiser (1988) proposed a relationship that considers the effects of in-situ soil stresses, soil strength, soil stiffness and construction details, the effects of wall stiffness and consolidation of soils were not investigated. While centrifuge tests have the capability to model the actual stress strain behaviour of soils and deformations, it is difficult to create a centrifuge model that is truly representative of the Old Alluvium soils and to model the multi-level excavation and construction sequence of the Influent Pumping Shaft 2. Reviews on numerical methods shown that they are appropriate to simulate the actual excavation sequence and to account for the effects of soil stress and material stiffness. Hence, in order to investigate the effects of soil-structure interaction and consolidation effects, the use of finite element analysis, with an advance soil constitutive model, is proposed to simulate the excavation at Influent Pumping Shaft 2.

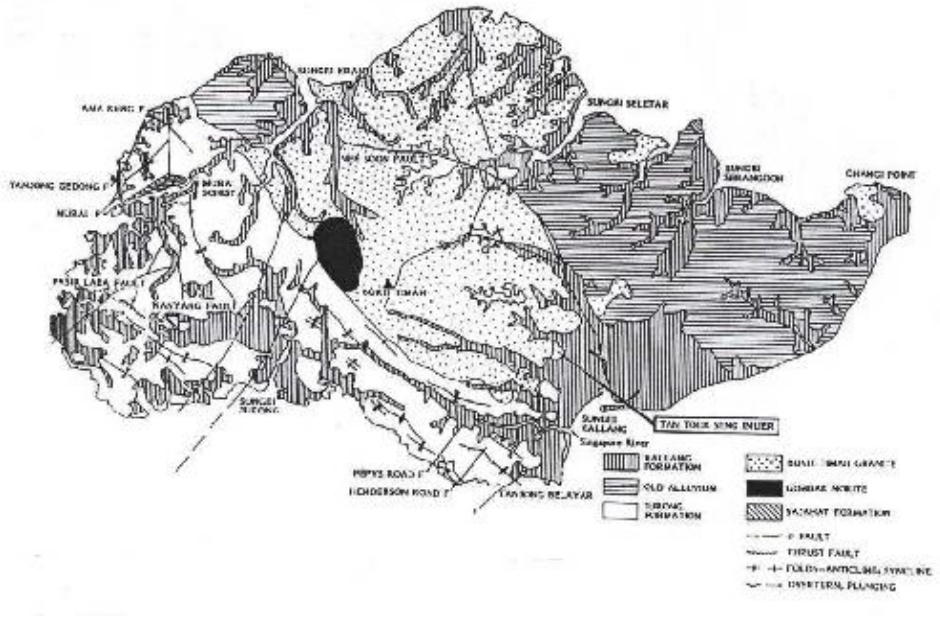

Figure 2.1 Geological map of Singapore Island (PWD, 1976)

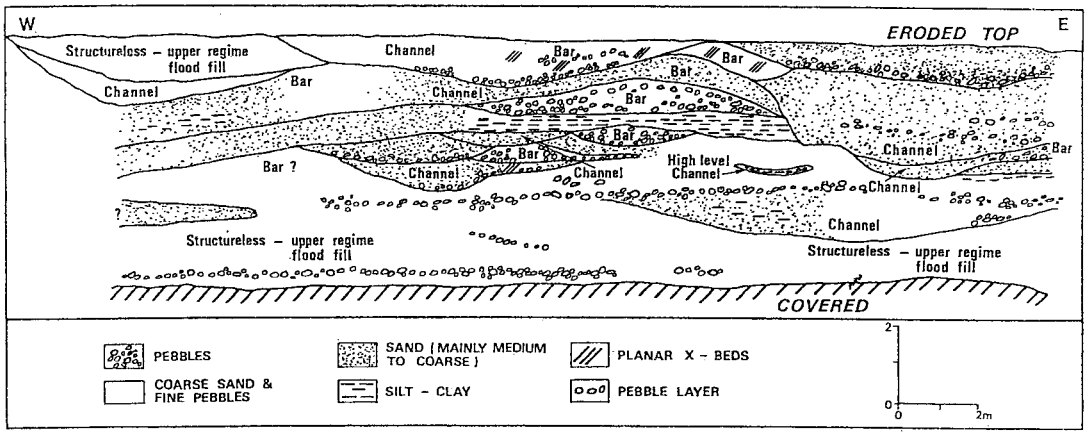

Figure 2.2 A section through Old Alluvium with a selection of morphological features identified (Gupta et al.,1987)

MAJOR DIVISIONS			GROUP SYMBOLS	TYPICAL NAMES
COARSE-GRAINED SOILS More than half of material is larger than no. 200 sieve size.	GRAVELS More than half of coarse fraction is larger than no. 4 sieve size.	Clean gravels	GW	Well-graded gravels, gravel-sand mixtures, little or no fines.
			GP	Poorly graded gravels, gravel-sand mixtures, little or no fines.
		Gravels with fines	GM	Silty gravels, gravel-sand-silt mixtures.
			GC	Clayey gravels, gravel-sand-clay mixtures.
	SANDS More than half of coarse fraction is smaller than no. 4 sieve size.	Clean sands	SW	Well-graded sands, gravelly sands, little or no fines.
			SP	Poorly graded sands, gravelly sands, little or no fines.
		Sands with fines	SM	Silty sands, sand-silt mixtures.
			SC	Clayey sands, sand-clay mixtures.
FINE-GRAINED SOILS More than half of material is smaller than no. 200 sieve size.	SILTS AND CLAYS	Low liquid limit.	ML	Inorganic silts and very fine sands, rock flour, silty or clayey fine sands, or clayey silts, with slight plasticity.
			CL	Inorganic clays of low to medium plasticity, gravelly clays, sandy clays, silty clays, lean clays.
			OL	Organic silts and organic silty clays of low plasticity.
		High liquid limit.	MH	Inorganic silts, micaceous or diatomaceous fine sandy or silty soils, elastic silts.
			CH	Inorganic clays of high plasticity, fat clays.
			OH	Organic clays of medium to high plasticity, organic silts.
Highly organic soils			Pt	Peat and other highly organic silts.

Figure 2.3 The Unified Soil Classification System (Dutro et al., 1982)

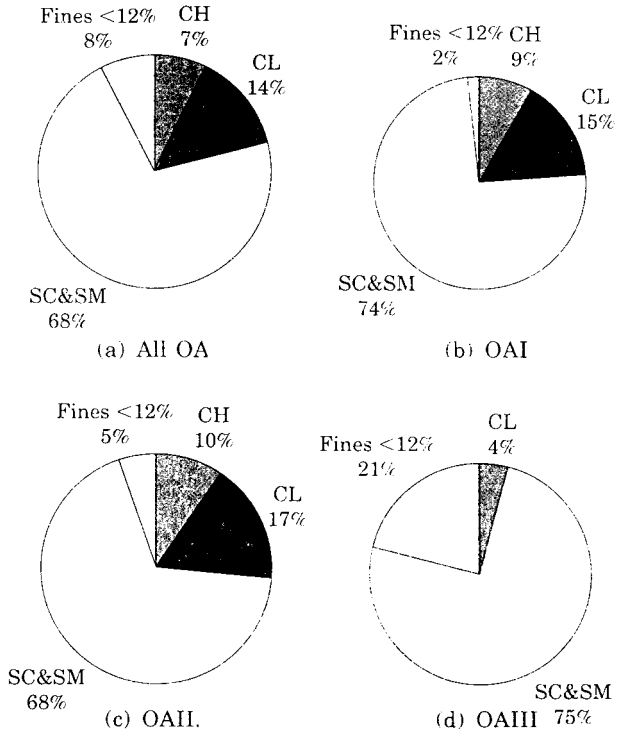

Figure 2.4 Soil distribution of Old Alluvium (Li and Wong, 2001)

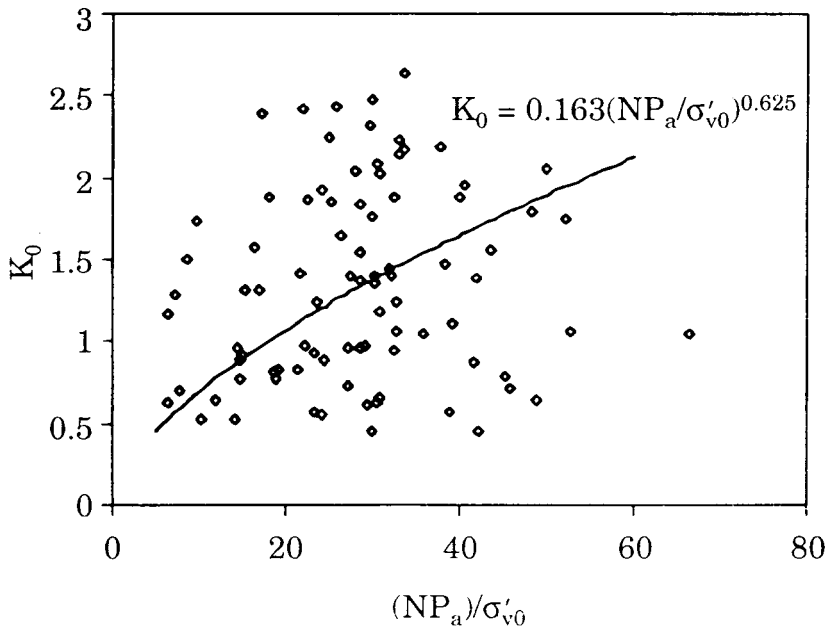

Figure 2.5 Coefficient of earth pressure at rest of Old Alluvium (Li and Wong, 2001)

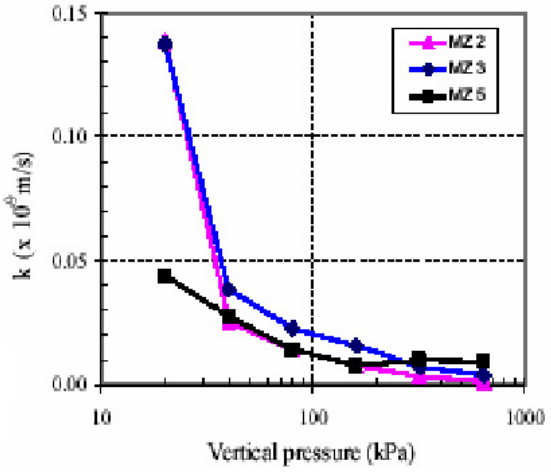

Figure 2.6 Variation of permeability of Old Alluvium with vertical stress in oedometer tests (Chu et al., 2003)

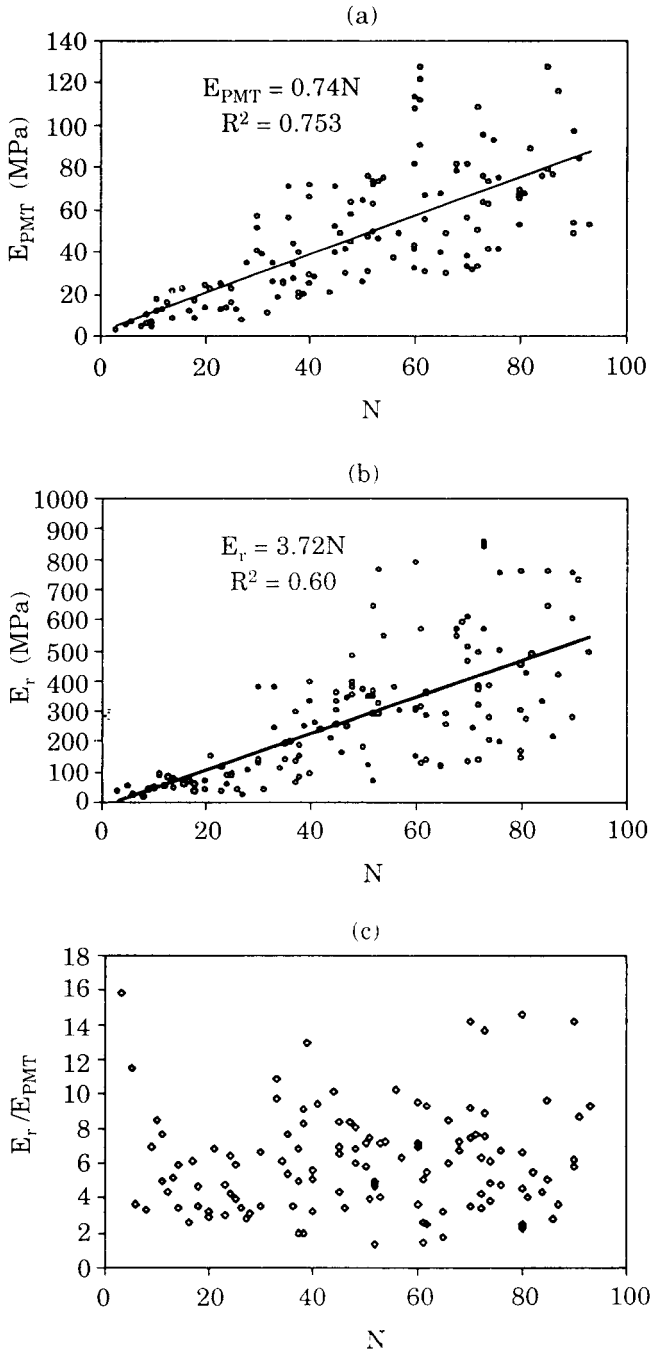

Figure 2.7 Variation of modulus values of Old Alluvium from pressuremeter tests with SPT N-value (Li and Wong, 2001)

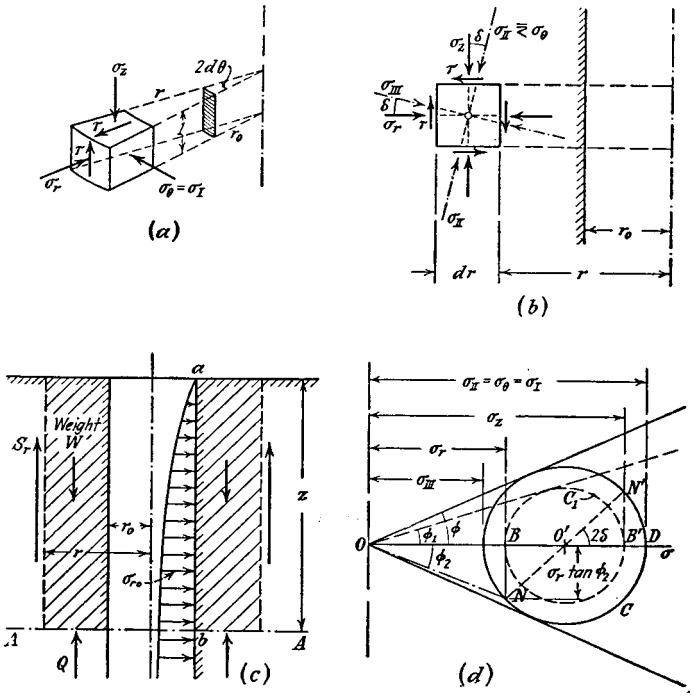

Figure 2.8 (a) and (b) Stresses acting on a small element of soil at a distance r from centreline of a shaft; (c) and (d) Assumptions on which the computation of earth pressure are based (Terzaghi, 1943)

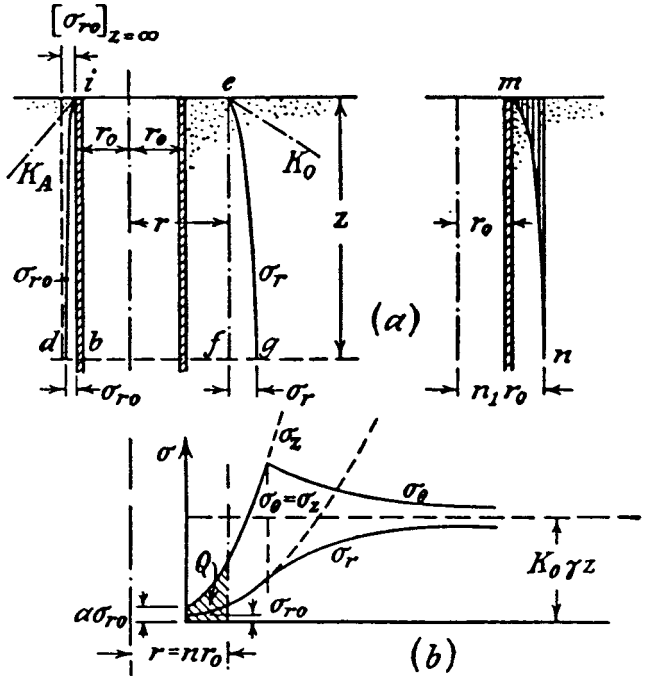

Figure 2.9 (a) Distribution of radial pressure on lining of shaft in sand and distribution of radial stresses on cylindrical section with radius r;
(b) Approximate distribution of radial, circumferential and vertical normal stresses along horizontal section at depth z (Terzaghi, 1943)

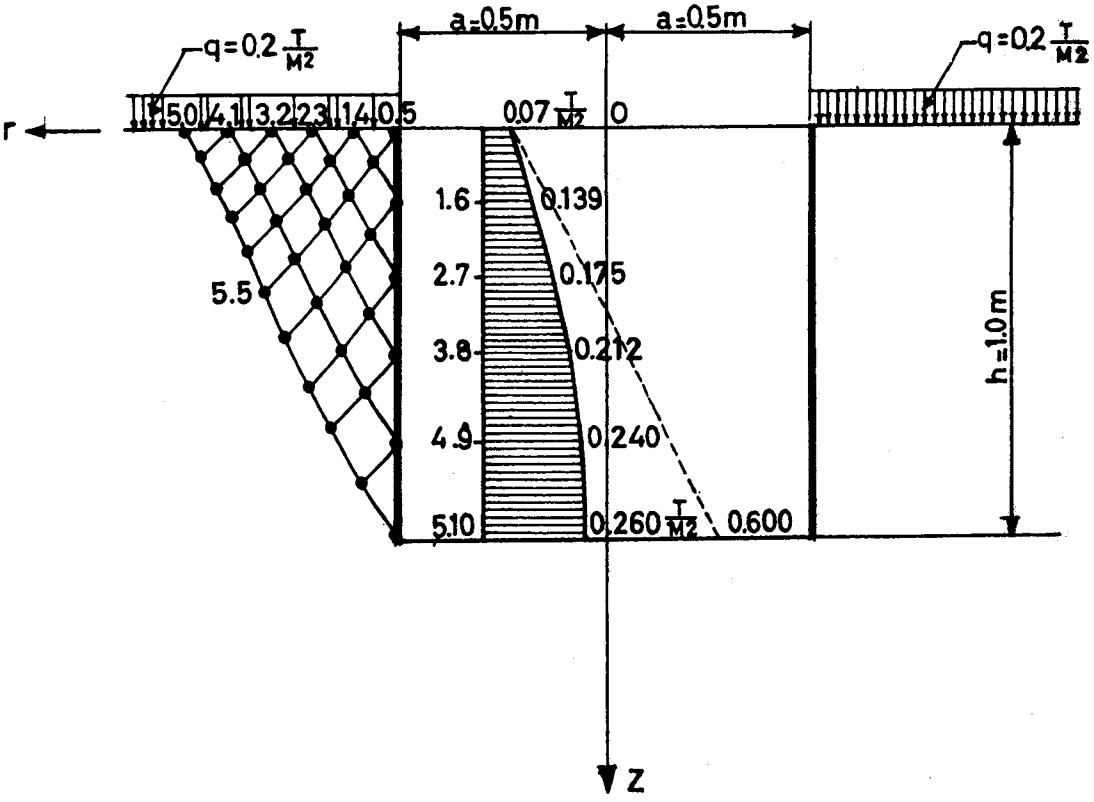

Figure 2.10 Active earth pressure distributions for axial-symmetrical and plane strain problems (Berezantzev, 1958)

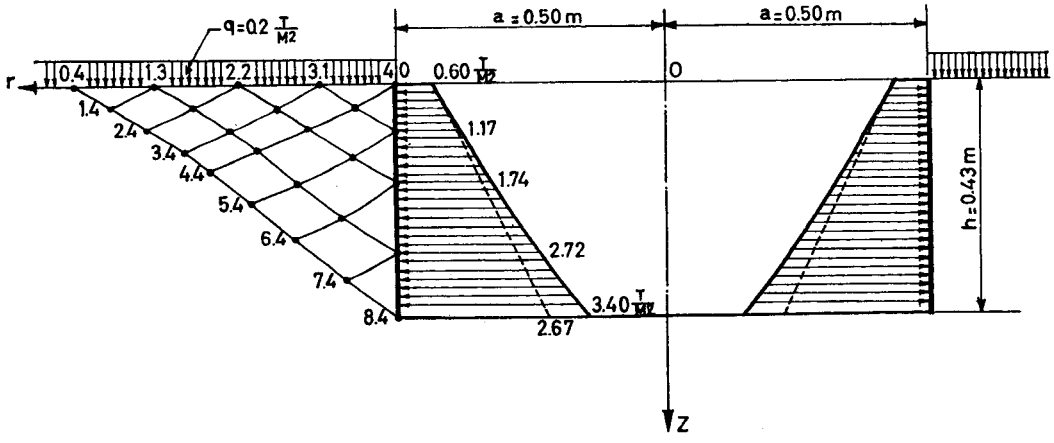

Figure 2.11 Passive earth pressure distributions for axial-symmetrical and plane strain problems (Berezantzev, 1958)

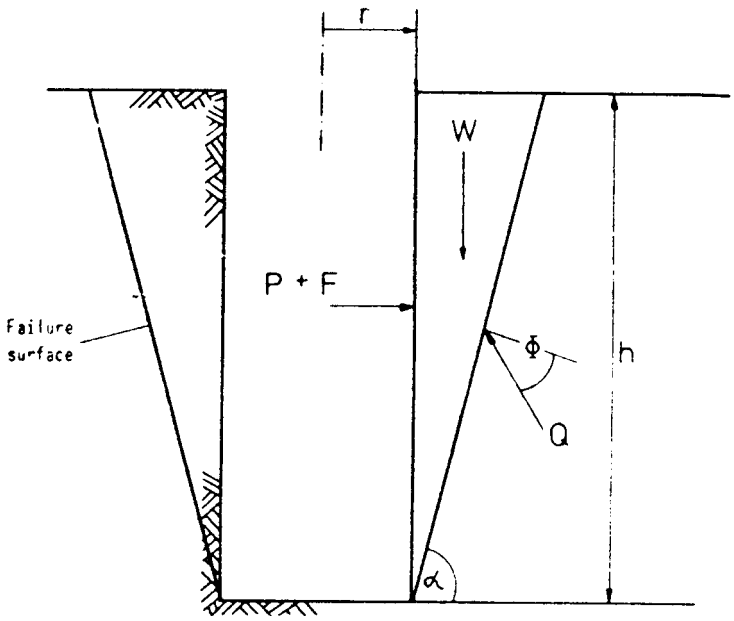

Figure 2.12 Assumed rupture model for a shaft in cohesionless soil with forces acting on the sliding mass (Prater, 1977)

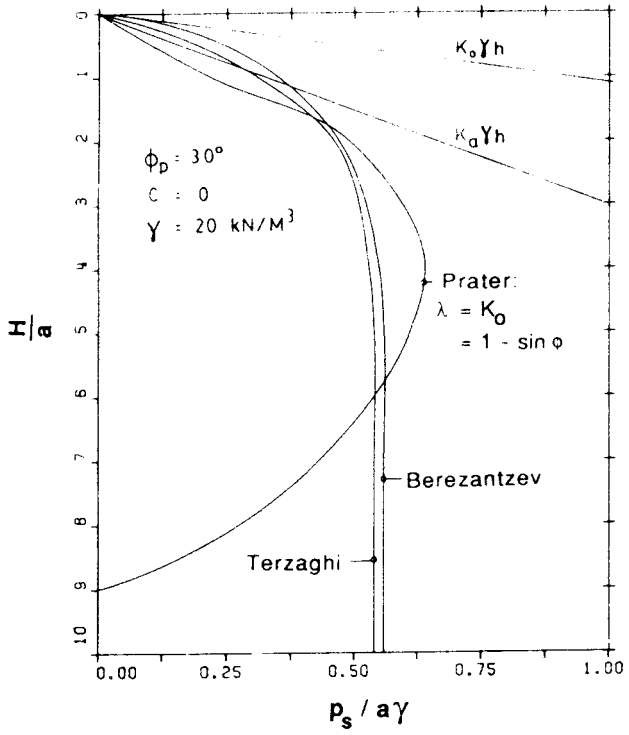

Figure 2.13 Comparison of earth pressure distributions (Wong and Kaiser, 1988)

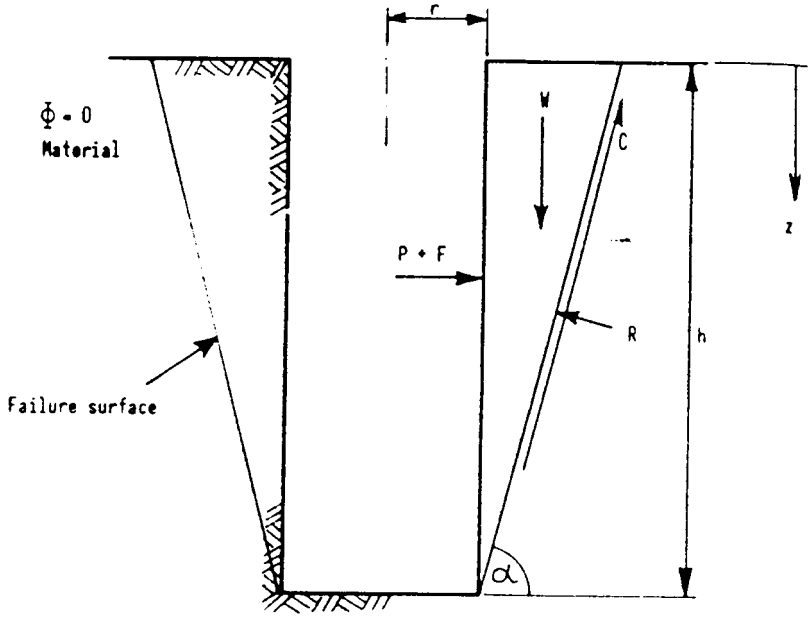

Figure 2.14 Assumed rupture model for a shaft in purely cohesive soil with forces acting on the sliding mass (Prater, 1977)

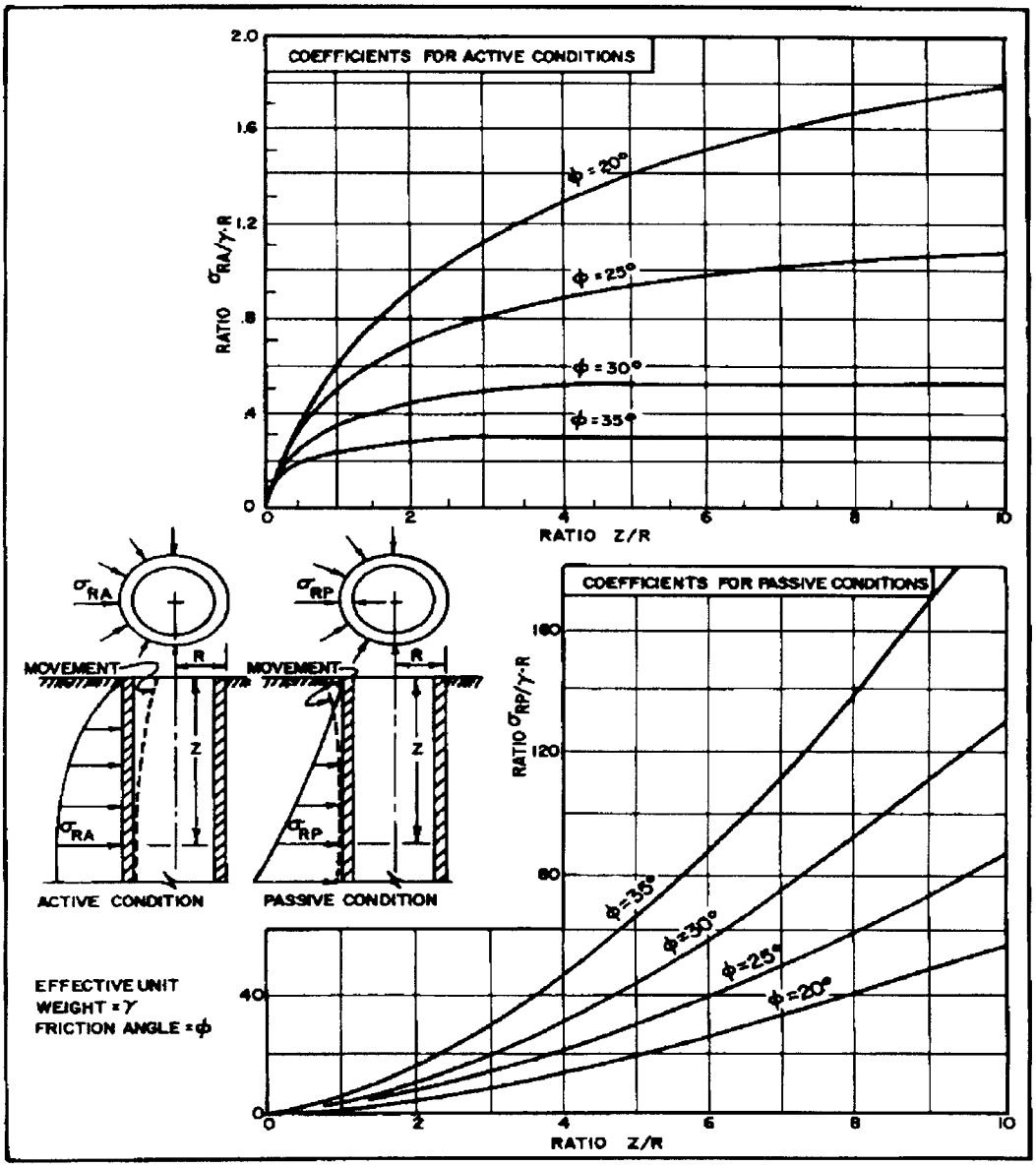

Figure 2.15 Coefficients for active and passive earth pressures on underground cylindrical shafts (Naval Facilities Engineering Command, 1986)

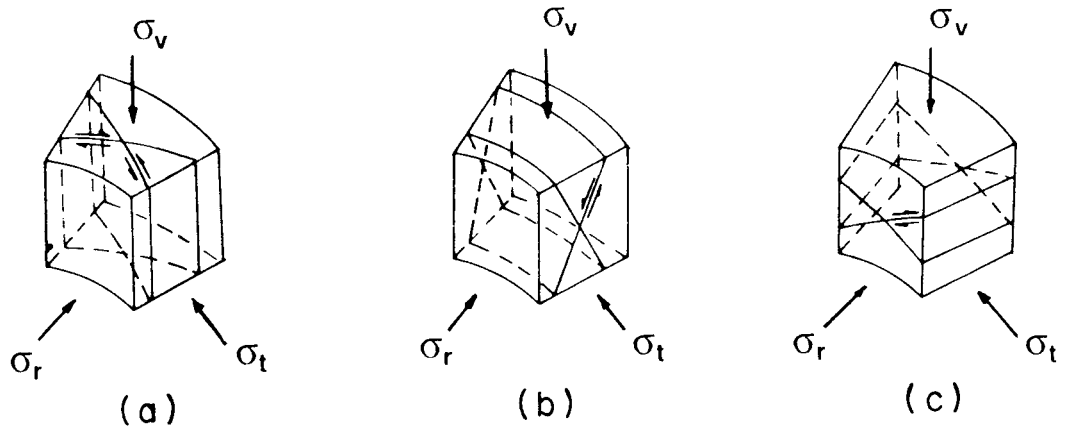

Figure 2.16 Modes of yielding: (a) Mode A, $\sigma_t - \sigma_r$ = max; (b) Mode B, $\sigma_v - \sigma_r$ = max; (c) Mode C, $\sigma_t - \sigma_v$ = max (Wong and Kaiser, 1988)

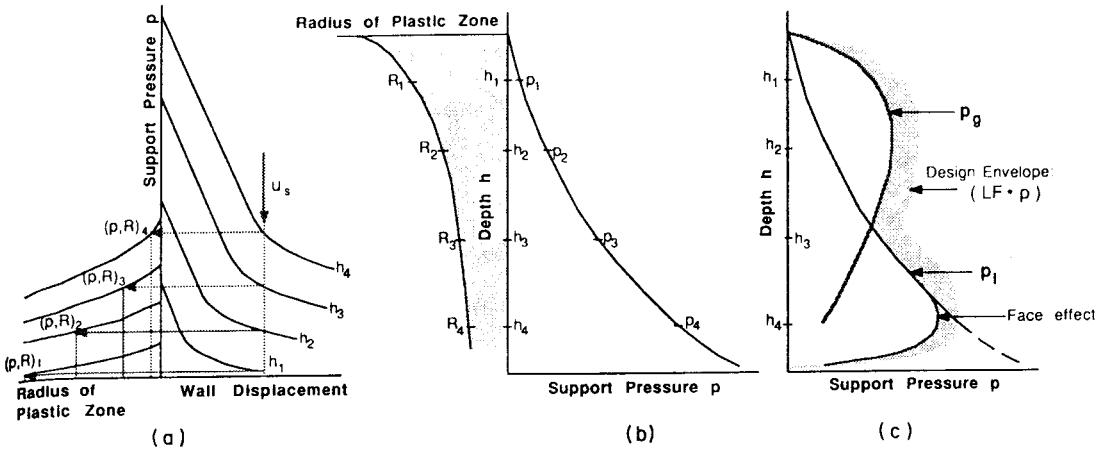

Figure 2.17 (a) Ground convergence curve at various depths without gravity effect; (b) Extent of plastic zone and pressure distribution without gravity effect; (c) Pressure distribution from convergence-confinement method with gravity effect (Wong and Kaiser, 1988)

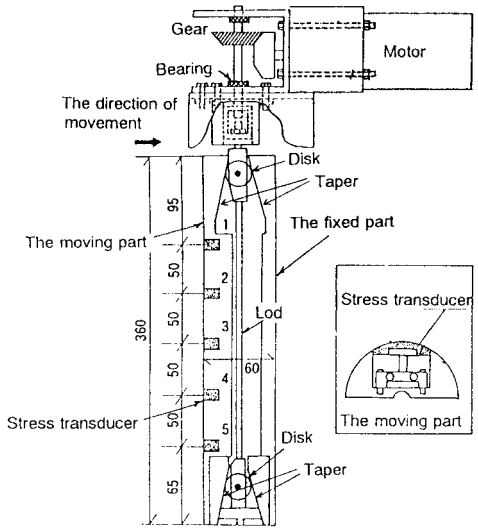

Figure 2.18 Model shaft (Fujii et al., 1994)

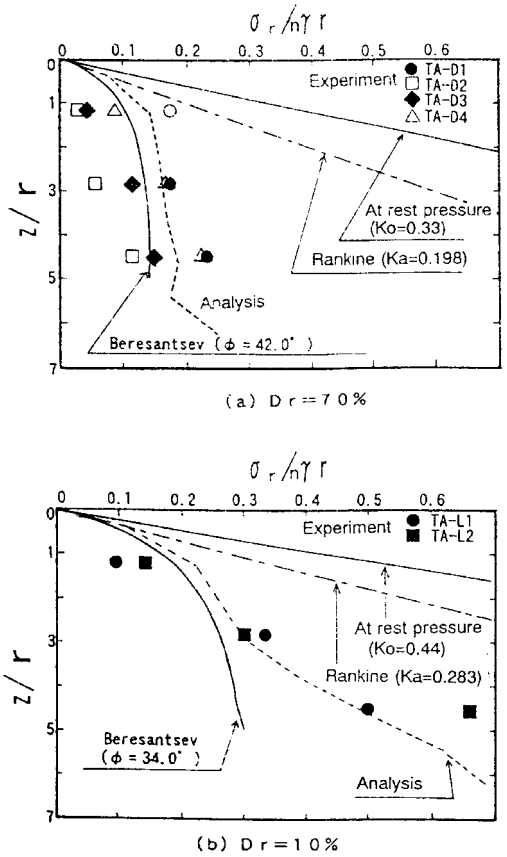

Figure 2.19 (a) Comparison of normalized horizontal earth pressure distributions of sand with relative density = 70%; (b) Comparison of normalized horizontal earth pressure distributions of sand with relative density = 10% (Fujii et al., 1994)

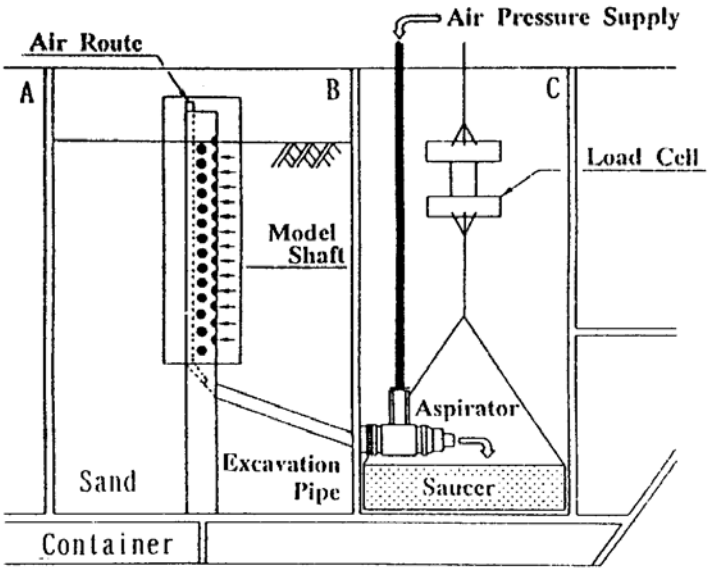

Figure 2.20 Model shaft (Ueno et al., 1996)

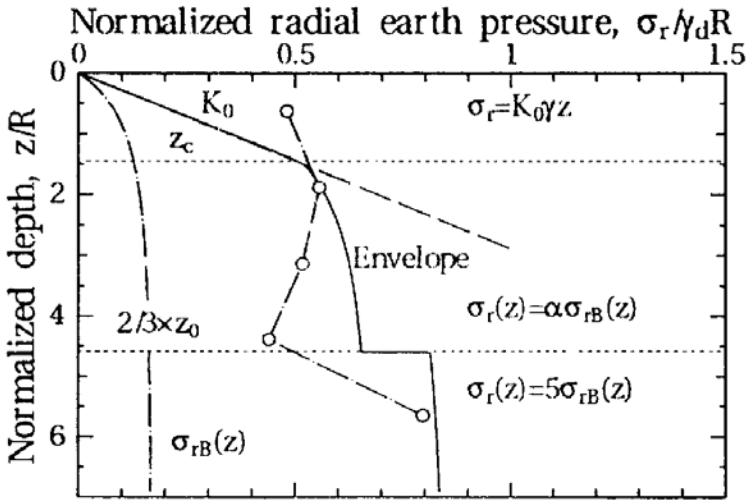

Figure 2.21 Empirical prediction method (Ueno et al., 1996)

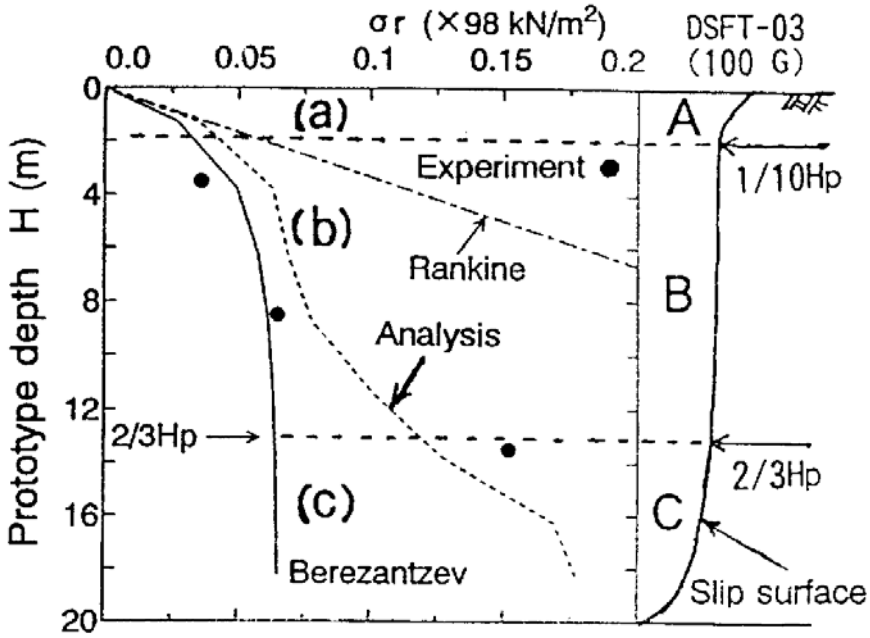

Figure 2.22 The Relationships between earth pressure and failure mechanism (Fujii et al., 1996)

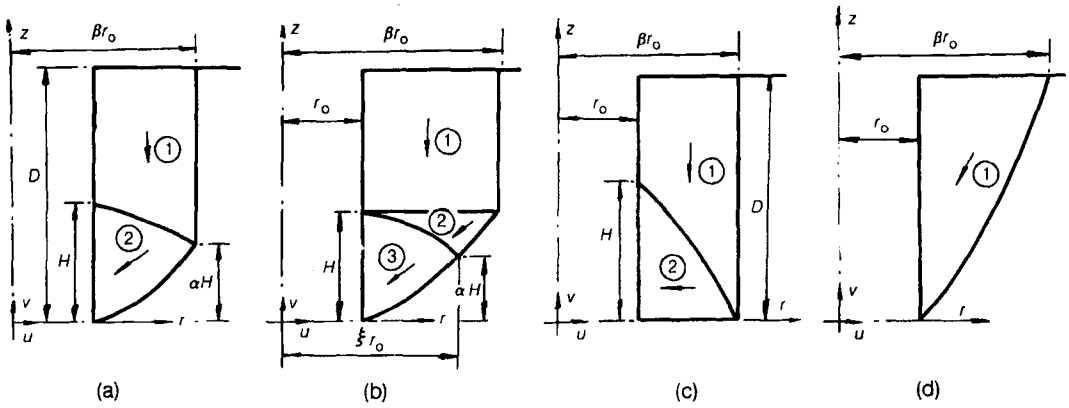

Figure 2.23 Wall failure mechanisms for axisymmetric excavations: (a) Mechanism A; (b) Mechanism B; (c) Mechanism C; (d) Mechanism D (Britto and Kusakabe, 1982)

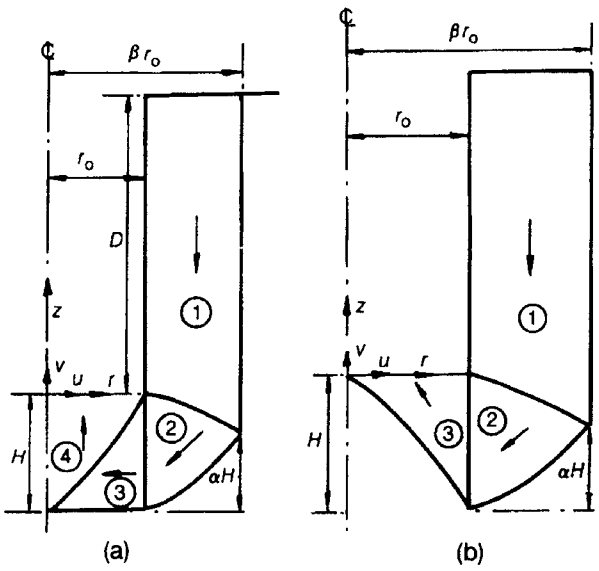

Figure 2.24 Base failure mechanisms for axisymmetric excavations: (b) Mechanism E; (b) Mechanism F (Britto and Kusakabe, 1982)

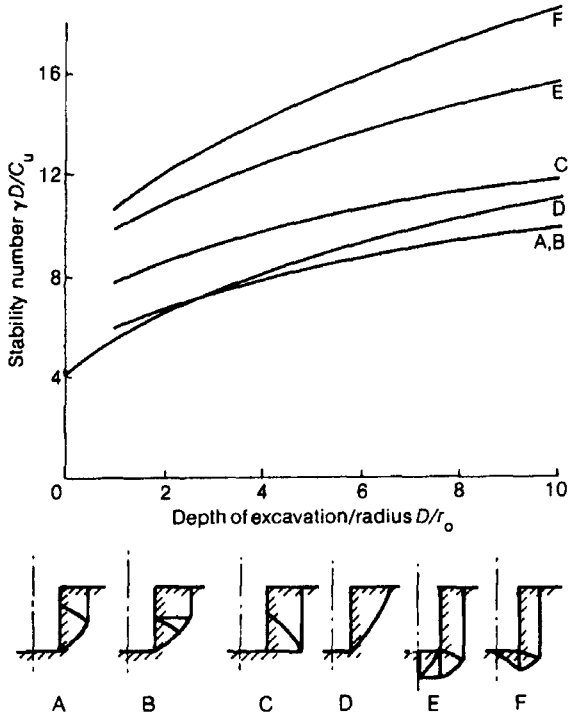

Figure 2.25 Variation of Stability Number with excavation depth to radius ratio (Britto and Kusakabe, 1982)

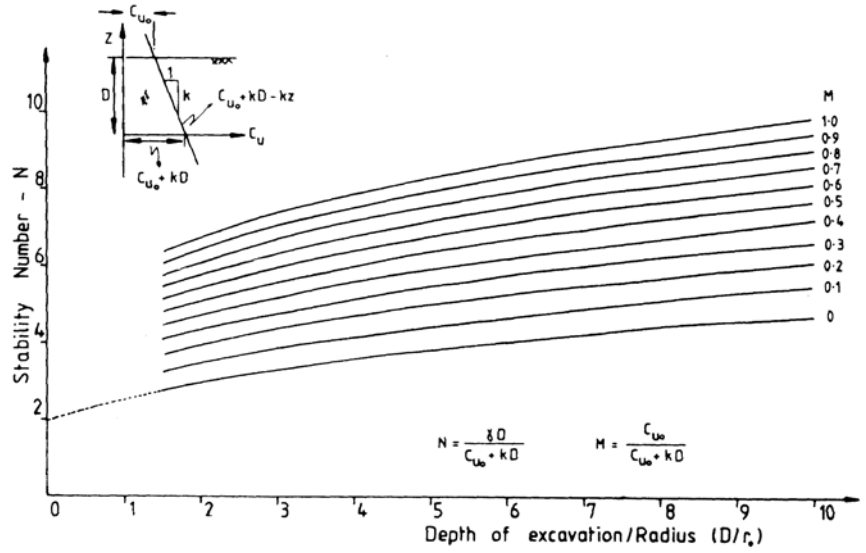

Figure 2.26 Variation of Stability Number with excavation depth to radius ratio (Britto and Kusakabe, 1983)

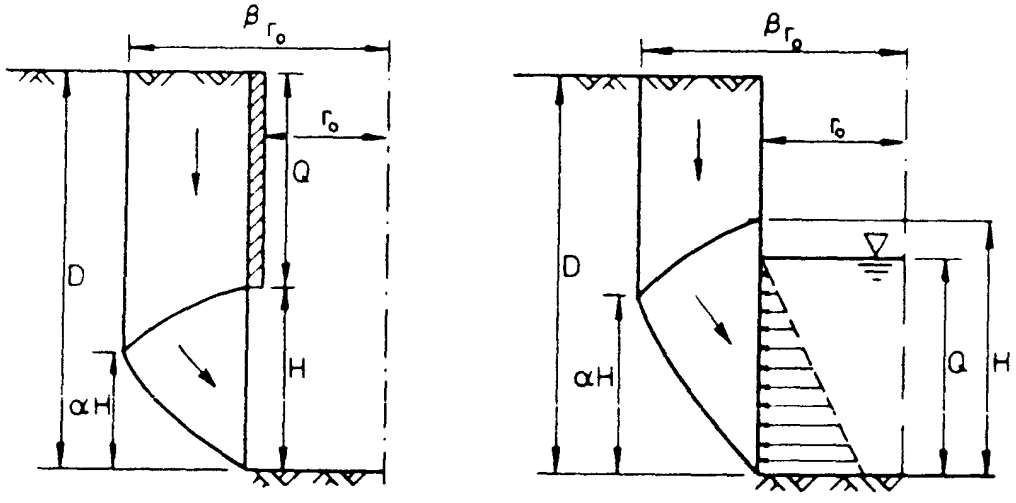

Figure 2.27 Wall failure mechanisms for support axisymmetric excavations (Britto and Kusakabe, 1984)

CHAPTER 3 CASE HISTORY

3.1 Introduction

The main emphasis of this research is directed towards the finite element analysis of a cylindrical shaft excavation in Old Alluvium in Singapore. The excavation project considered in this research is conducted for the underground Influent Pumping Station of the Changi Water Reclamation Plant of the Deep Tunnel Sewerage System (DTSS) project. The Influent Pumping Station consists of three circular vertical shafts, namely, the Coarse Screen Shaft (CCS), the Influent Pumping Shaft 1 (IPS-1), and the Influent Pumping Shaft 2 (IPS-2) respectively. The excavation conducted at the Influent Pumping Shaft 2 (IPS-2) will be examined, as it is the first shaft to be excavated and the most intensively instrumented shaft at the project site. In this chapter, the general site condition, soil investigation and instrumentation works are presented. The excavation support system and excavation sequence adopted for the excavation of the three vertical shafts of the Influent Pumping Station will also be discussed.

3.2 General Site Condition and Instrumentation

The Influent Pumping Station of the Changi Water Reclamation Plant is located at Tanah Merah Coast Road. According to Tan and Weele (2000), the Changi Water Reclamation Plant is located on reclaimed land, southeast of the Singapore Changi Airport. Figure 3.1 gives the plan layout of the entire Changi Water Reclamation Plant project site. It is evident from Figure 3.1 that a cut-off wall is constructed around the project site of the Changi Water Reclamation Plant. The plan view of the Influent Pumping Shafts and Coarse Screen Shaft is shown in Figure 3.2. The centre of the Influent Pumping Shaft 2 is 61 m away from the centre of the Influent Pumping Shaft

1 and the nearest distance between the retaining walls of the two vertical shafts is 18.4 m. The centre of Coarse Screen Shaft is 62.9 m away from the centre of Influent Pumping Shaft 2, with a minimum distance of 23.8 m between the walls of the two vertical shafts.

Influent Pumping Shaft 1 and Shaft 2 are 42.6 m in diameter and have a depth of 73.5 m while the Coarse Screen Shaft is 35.8 m in diameter and 69.5 m in depth. As the construction and excavation of such a large scale underground circular vertical shafts is unprecedented in Singapore, a comprehensive instrumentation programme is implemented to ensure structural stability of the vertical shafts and to monitor any excessive ground movements induced by the excavation and other construction works. The instrumentation consists of ground inclinometers, wall inclinometers, pneumatic piezometers, water standpipes and settlement markers, installed around the influent pumping shafts. Vibrating wire spot-weldable strain gauges are installed on the steel reinforcements of the shaft walls to monitor their hoop and flexural strains that developed during the excavation and construction works. The measurement of these instruments is conducted in a regular basis. This is to ensure that timely remedial works can be performed before structural stresses and ground movements exceed the allowable limits. The layout of strain gauges in the diaphragm wall of Influent Pumping Shaft 2 is shown in Figure 3.3. Twelve elevations of strain gauges are installed at panels S4, S12 and S20 of the diaphragm wall. The instrumentation plan of Influent Pumping Shaft 2 is presented in Figure 3.4. Table 3.1 summarises the elevations of the strain gauges in Influent Pumping Shaft 2

Table 3.1 Depth of strain gauges in Influent Pumping Shaft 2

Level of Strain Gauge	Depth of Strain Gauge Below Final Ground Surface (m)
A	4.0
B	10.0
C	16.0
D	21.0
E	28.0
F	34.0
G	41.0
H	46.0
I	52.0
J	58.0
K	63.0
L	70.0

3.3 Site Investigation

Site investigation work was carried out at the project site before the execution of the construction works. The study of the subsoil condition is essential to determine the soil stratigraphy and geotechnical properties at the site for design and analytical purposes. The site investigation was carried out from 13 May to 28 June 2000. Fifteen boreholes were drilled at the project site using rotary drilling machines and fourteen piezocone penetration tests were conducted. However, only two of the boreholes, BH 1 and BH 2, were located at the vicinity of the three influent pumping shafts. The records of BH 1 and BH 2 are included in the Appendix. Both the boreholes, BH 1 and BH 2, were terminated at a depth of 75.45 m. Standard penetration tests were performed in the two boreholes. Water standpipes were also installed at the project site to monitor the groundwater conditions. Figure 3.5 shows the SPT-N values at BH 1 and BH 2. A permeability test was performed at a clayey sand layer.

3.4 Soil Profile

The sub-surface stratigraphy and groundwater conditions can be interpreted based on the information and soil classification obtained from the boreholes and water standpipes. The original ground surface was at a Reduced Level (RL) of 105 m. The simplified soil profile at the location of the Influent Pumping Station is shown in Figure 3.6. The soil profile is obtained from the soil classification at BH 1 and BH 2. Six uniform soil strata have been identified. The yellowish-reddish brown Backfill layer is approximately 2 m thick and consists of soft sandy silt with clay and rock fragments. A Reclaimed Sand layer can be found under the Backfill. The 15.4 m-thick reclaimed soil layer consists of medium dense fine to coarse sand and is underlain by the Old Alluvium formation. Medium dense to very dense silty sands and clayey sands are characteristics soils of the Old Alluvium formation at this location. The Old Alluvium Formation at the project site can be classified into four different soil layers, as shown in Figure 3.6. The groundwater table lies in approximately 5 m below the ground surface.

3.5 Excavation Support System and Sequence

The existing ground surface at the site was lowered to a Reduced Level of 103 m, prior to the construction of the Changi Water Reclamation Plant. Temporary concrete guide walls, which are 0.5 m thick and 1.2 m deep, were built before the retaining wall. The guide walls were constructed using Grade 20 concrete and they served as a reference for the shaft wall alignment and initial verticality. 1.2 m thick circular concrete diaphragm walls were adopted to support the excavation works for all the three circular vertical shafts. The excavation at Influent Pumping Shaft 1 and Influent Pumping Shaft

2 were carried out to a depth of 70 m below the final ground surface level while a 66 m deep excavation was conducted for the Coarse Screen Shaft.

The retaining walls of Influent Pumping Shaft 1 and Shaft 2 were terminated at a depth of 73.5 m below the final ground surface level while the walls of the Coarse Screen Shaft was terminated at a depth of 69.5 m below the final ground surface level. Both the Influent Pumping Shaft 1 and Shaft 2 have an external wall diameter of 42.6 m whereas the Coarse Screen Shaft has an external diameter of 35.6 m. Internal concrete ring walls of 1.6m thick were cast in lifts, against the diaphragm walls after each excavation stage. Grade 55 and Grade 35 concrete were specified for the diaphragm walls and ring walls, respectively. The average 28-day strength of the diaphragm walls is measured to be 68.7 N/mm^2 while that of the ring walls is 62 N/mm^2. The dimensions of the diaphragm wall and elevations and casting sequence of the internal ring walls of Influent Pumping Shaft 2 are presented in Figure 3.7.

The excavation at the Influent Pumping Shaft 2 was first carried out at the project site. The Coarse Screen Shaft, which is 62.9 m from the Influent Pumping Shaft 2, was excavated 46 days after the start of excavation for the Influent Pumping Shaft 2. The excavation at the Influent Pumping Shaft 1 was then carried out 73 days later. The Influent Pumping Shaft 1 is at a distance of 61.0 m away from the Influent Pumping Shaft 2. Figure 3.8 summarises the time taken and the depth of each excavation stage of the three vertical shafts.

The excavation for the Influent Pumping Shaft 2 was carried out in eight stages as follows:

Stage 1: The shaft was first excavated to a RL of 89.0 m. Internal ring walls were constructed in 5 lifts, from RL 102.0 m to 90.5 m.

Stage 2: Excavation was carried out to a RL of 81.0 m. Internal ring walls were constructed in 3 lifts, from RL 88.0 m to 82.5 m.

Stage 3: Excavation was carried out to a RL of 71.4 m. Internal ring walls were constructed in 3 lifts, from RL 80.0 m to 73.0 m.

Stage 4: Excavation was carried out to a RL of 63.4 m. Internal ring walls were constructed in 4 lifts, from RL 73.0 m to 65.0 m.

Stage 5: Excavation was carried out to a RL of 54.5 m. Internal ring walls were constructed in 3 lifts, from RL 63.0 m to 56.0 m.

Stage 6: Excavation was carried out to a RL of 47.1 m. Internal ring walls were constructed in 4 lifts, from RL 56.0 m to 48.5 m.

Stage 7: Excavation was carried out to a RL of 39.3 m. Internal ring walls were constructed in 4 lifts, from RL 48.5 m to 41.0 m.

Stage 8: This was the last excavation stage, which was carried out to a RL of 33.0 m.

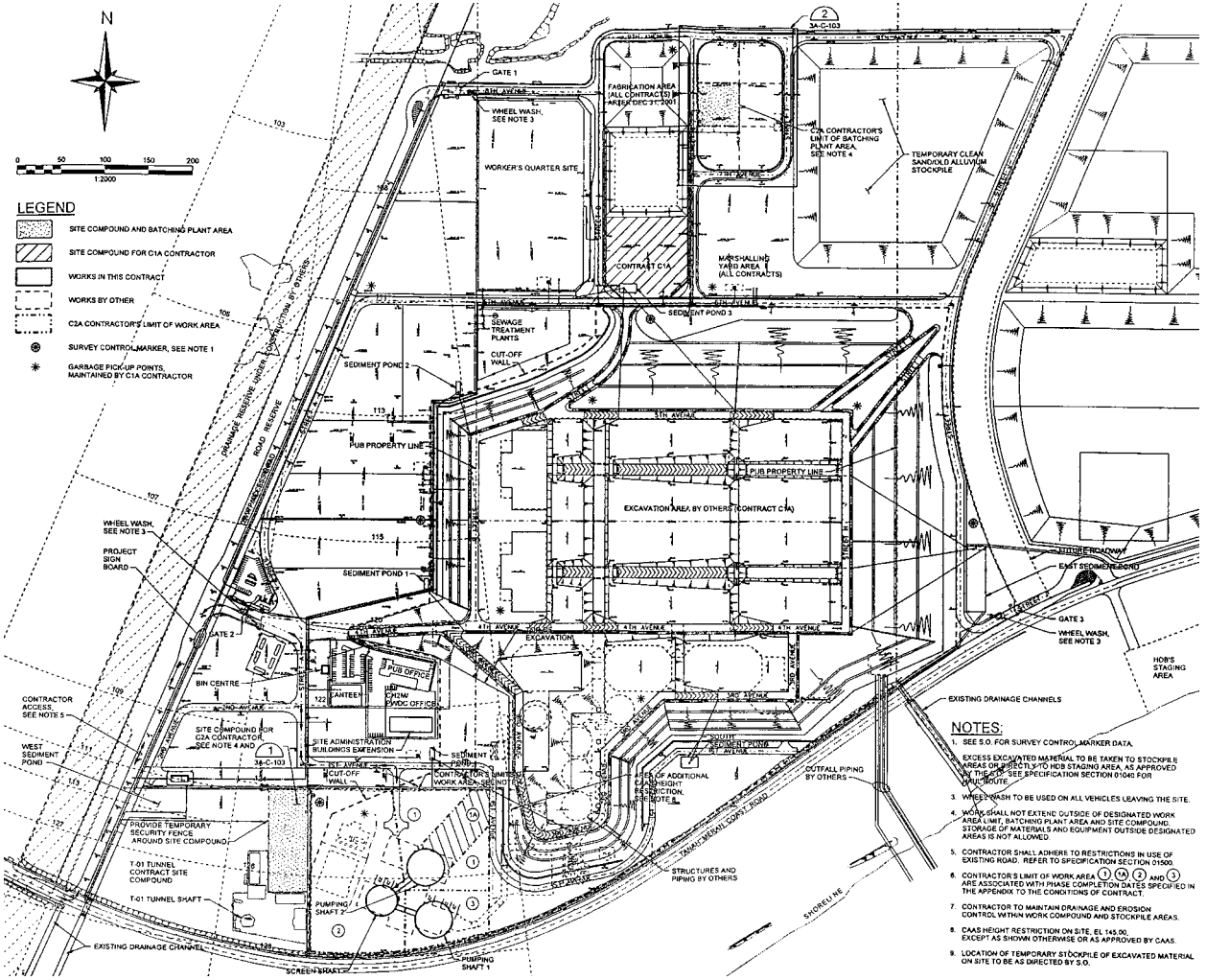

Figure 3.1 Changi Water Reclamation Plant project site

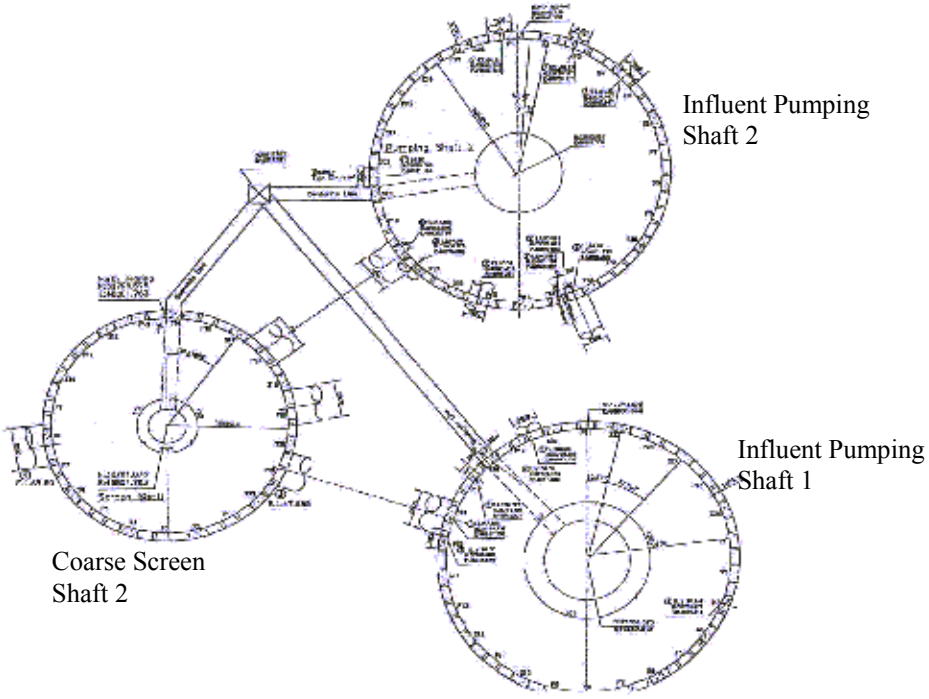

Figure 3.2 Plan view of Influent Pumping Station

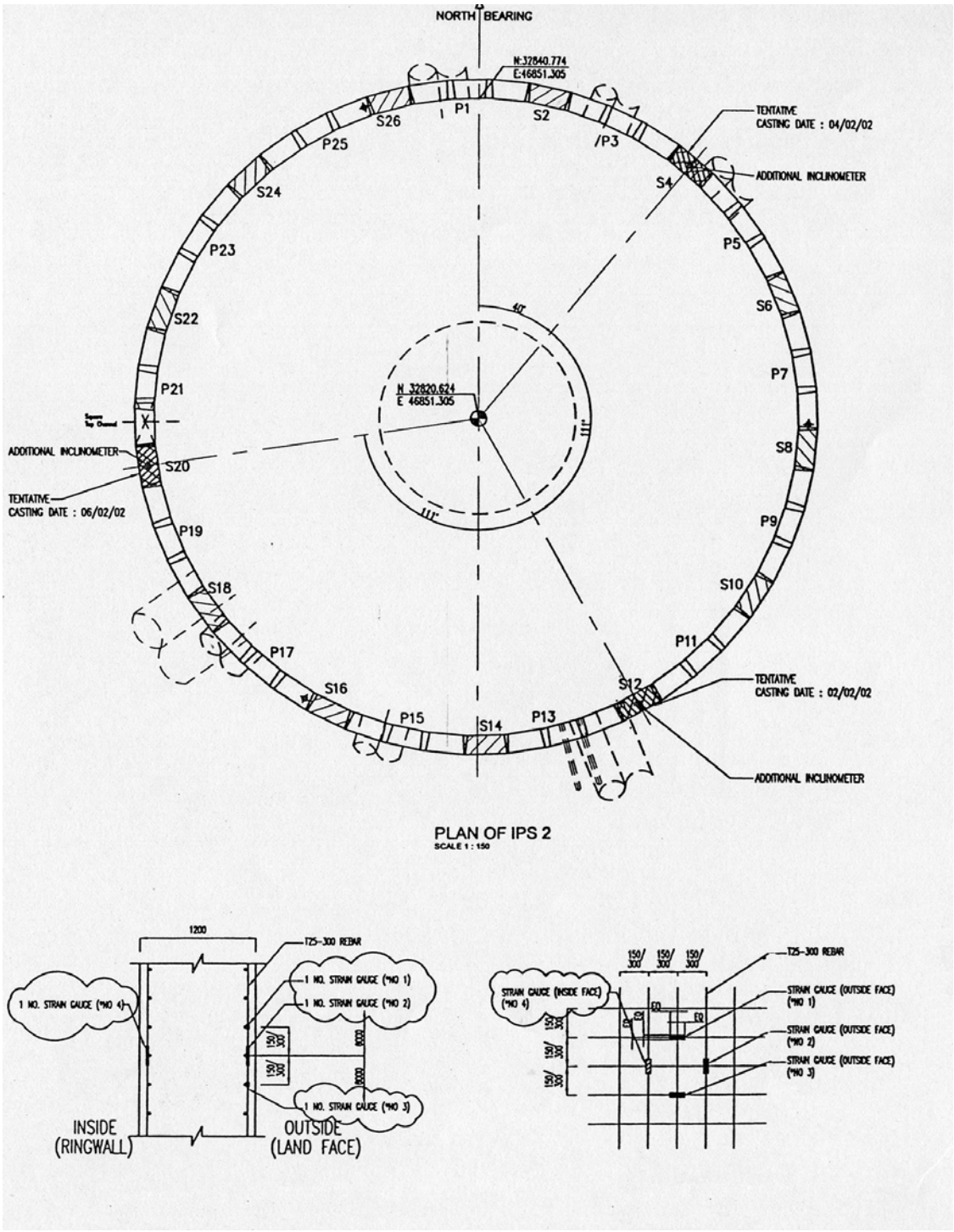

Figure 3.3 Layout of strain gauges for Influent Pumping Shaft 2 (IPS-2)

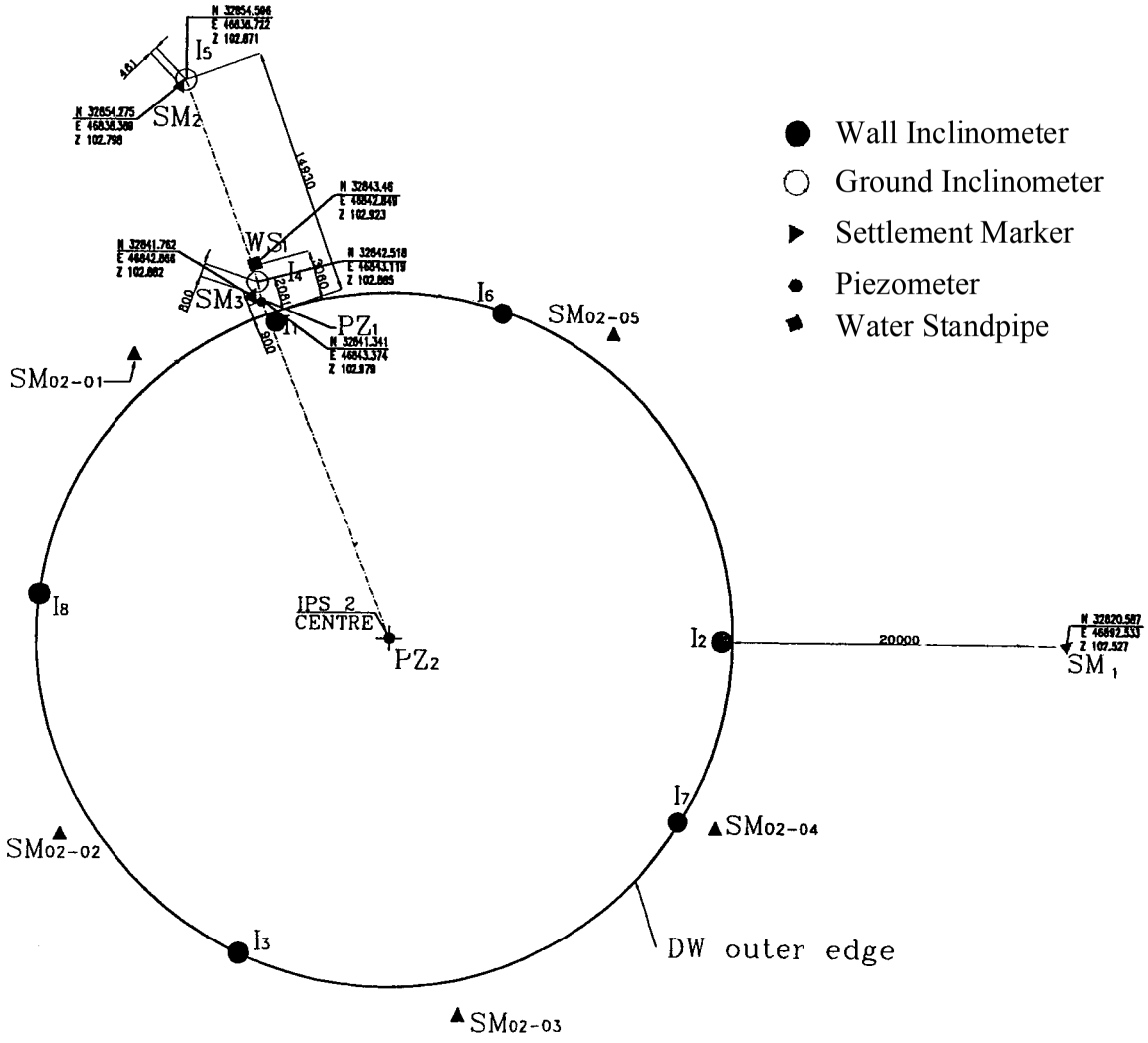

Figure 3.4 Instrumentation plan for Influent Pumping Shaft 2 (IPS-2)

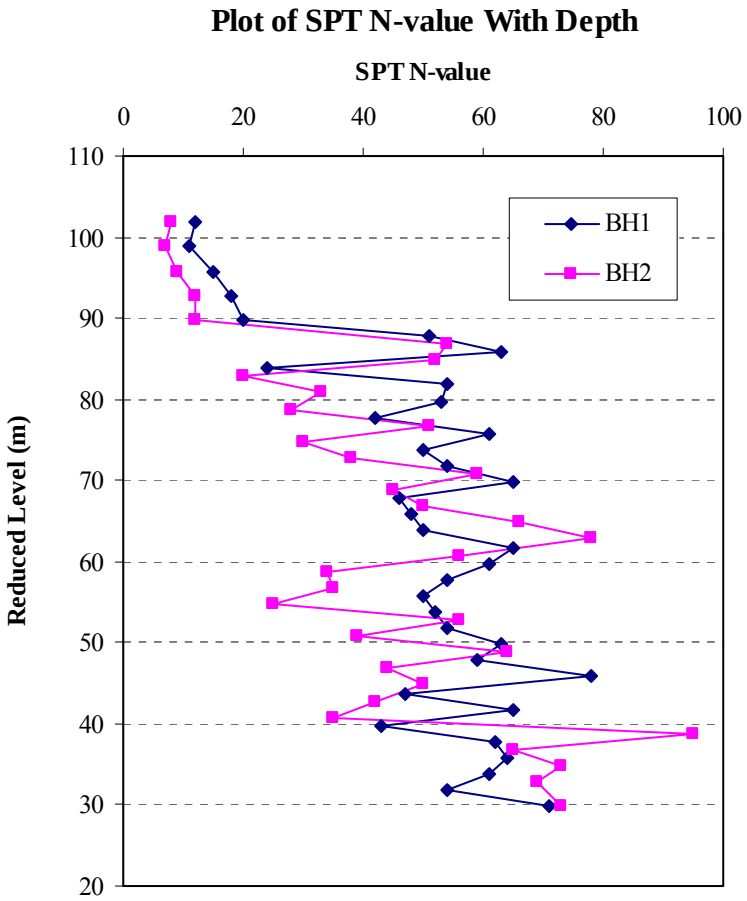

Figure 3.5 SPT N-values at BH 1 and BH 2

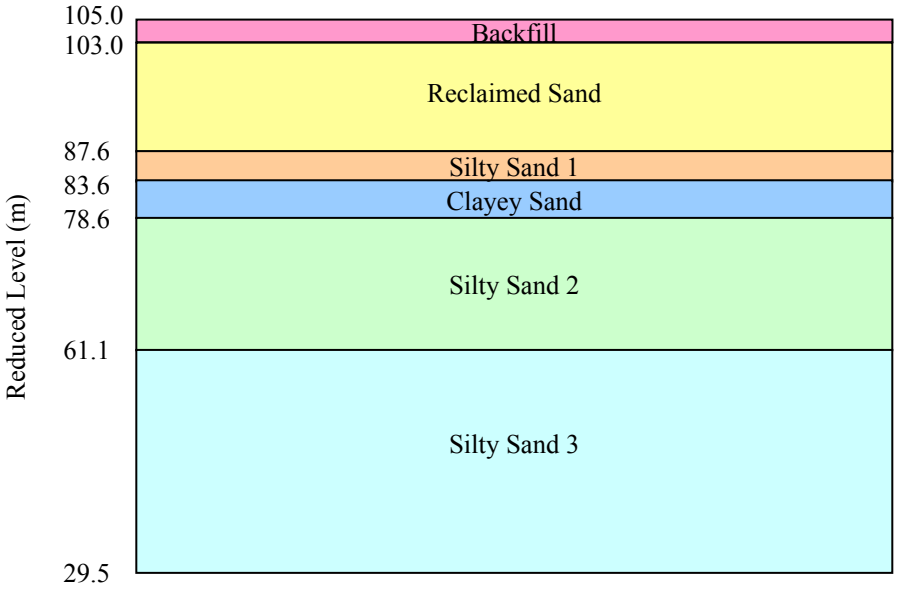

Figure 3.6 Simplified soil profile at Influent Pumping Station

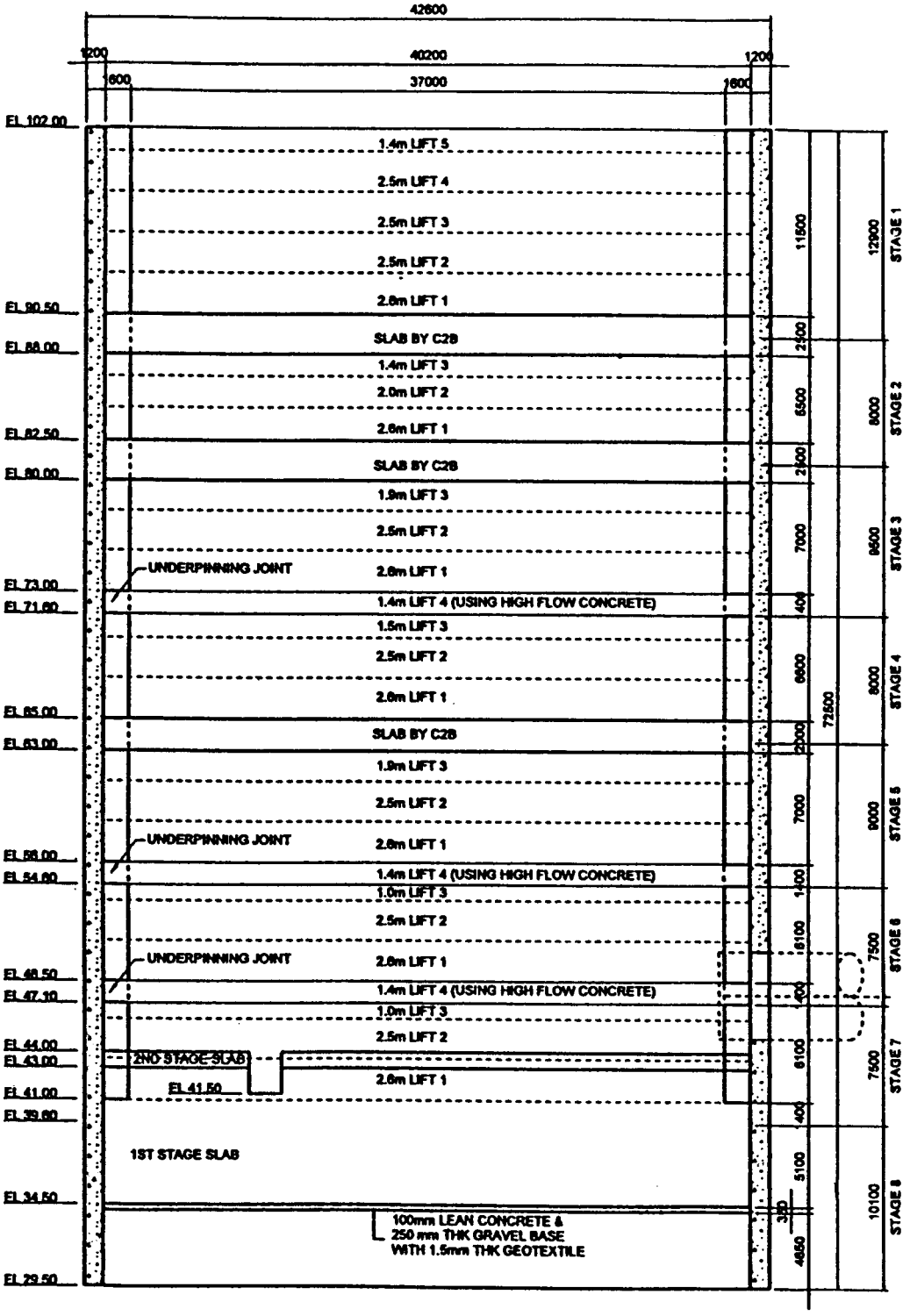

Figure 3.7 Wall dimensions of Influent Pumping Shaft 2 (IPS-2)

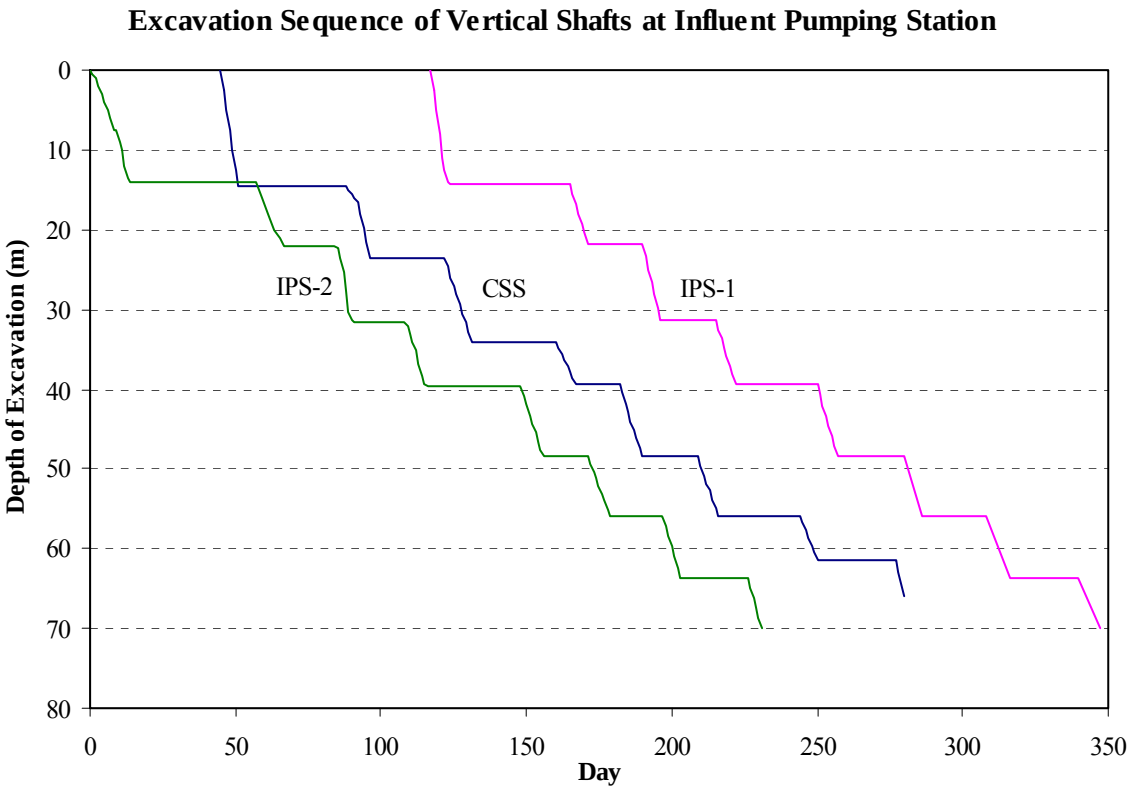

Figure 3.8 Excavation sequence of vertical shafts at Influent Pumping Station

CHAPTER 4 THE HARDENING-SOIL MODEL

4.1 Introduction

The Hardening-Soil model is an advanced constitutive model to simulate the behaviour of different types of soil, including both stiff soils and soft soils. This model is formulated in the framework of classical theory of plasticity and accounts for both shear hardening and compression hardening. The Hardening-Soil model is selected to simulate the behaviour of Old Alluvium soils at the Influent Pumping Station project site. In this chapter, the basic characteristics of the Hardening-Soil model are presented. Schanz and Bonnier (1997) proposed a method for determining the model parameters of the Hardening-Soil model. The derivation and the validity of their proposed method are investigated in the present study. Lastly, the results of some laboratory oedometer and triaxial tests conducted on Old Alluvium are simulated using the Hardening-Soil model to obtain insights on the behaviour of the constitutive model and to estimate some representative soil parameters of Old Alluvium near the project site.

4.2 Formulation of Hardening-Soil Model

4.2.1 Hyperbolic Relationship For Standard Drained Triaxial Test

According to Schanz et al. (1999) and Brinkgreve (2002), the basic idea for the formulation of the Hardening-Soil model is the hyperbolic relationship between the deviatoric stress, q, and the vertical strain, ε_1, in primary triaxial loading. A soil sample would show a decreasing stiffness and develop irreversible plastic strains during primary deviatoric loading. Kondner and Zelasko (1963) reported that the observed relationship between the deviatoric stress and the axial strain in a drained triaxial test

could be reasonably approximated by a hyperbola. The hyperbolic relationship between the deviatoric stress and the axial strain is described by Equation 4.1. Failure of soil is defined according to the Mohr-Coulomb failure criterion and involves the soil strength parameters, c' and ϕ'. The failure criterion is satisfied when the ultimate deviatoric stress is reached and plastic yielding occurs. The ultimate deviatoric stress, q_f and the quantity, q_a, are defined in Equations 4.2 and 4.3. Figure 4.1 shows the hyperbolic stress-strain relationship in primary loading for a drained triaxial test.

$$\varepsilon_1 = \frac{q_a}{2E_{50}} \frac{q}{1 - q/q_a} \qquad \text{for } q < q_f \tag{4.1}$$

$$q_f = \frac{6\sin\phi'}{3 - \sin\phi'} (c'\cot\phi' - \sigma_3') \tag{4.2}$$

$$q_a = \frac{q_f}{R_f} \tag{4.3}$$

where E_{50} is the confining stress dependent secant stiffness for primary loading in standard drained triaxial test and R_f is the failure ratio relating the ultimate deviatoric stress to the asymptotic shear stress in Hardening-Soil model, as shown in Figure 4.1. A failure ratio of 0.9 is recommended by Brinkgreve (2002).

The stress dependency of soil stiffness is considered in the Hardening-Soil model. The amount of stress dependency is defined according to a power law using the power m. It is apparent from Equation 4.1 that the secant modulus, E_{50}, from a drained triaxial test is employed to model the non-linear stress-strain behaviour of soil under primary deviatoric loading. According to Schanz and Bonnier (1997), the secant modulus is not directly related to the Young modulus as strain consists of both elastic and plastic components when the soil is under virgin loading. The magnitude of the secant

modulus, E_{50} is computed for 50% mobilisation of the ultimate deviatoric stress. Equation 4.4 gives the stress dependency relationship of the secant modulus.

$$E_{50} = E_{50}^{ref} \left(\frac{c' \cos \phi' - \sigma_3' \sin \phi'}{c' \cos \phi' + p^{ref} \sin \phi'} \right)^m \quad (4.4)$$

where E_{50}^{ref} is a reference secant stiffness modulus corresponding to the reference stress, p^{ref}. The secant stiffness, E_{50}, is dependent on the minor principal stress, σ_3', which corresponds to the effective confining pressure in a triaxial test. In PLAXIS, compressive stresses and forces, including pore pressures, are taken to be negative. It will be explained in the following section that the reference secant stiffness modulus, E_{50}^{ref}, would control the magnitude of plastic strains that originate from the shear yield surface.

An unloading soil stiffness, as shown in Figure 4.1, is used to model unloading and reloading stress paths. The actual unloading stiffness is dependent on the minor principal stress, σ_3', and the stress dependency relationship of the unloading stiffness is defined as:

$$E_{ur} = E_{ur}^{ref} \left(\frac{c' \cos \phi' - \sigma_3' \sin \phi'}{c' \cos \phi' + p^{ref} \sin \phi'} \right)^m \quad (4.5)$$

where E_{ur}^{ref} is the reference unloading stiffness modulus corresponding to the reference stress, p^{ref}.

4.2.2 Shear Yield Surface, Hardening Law and Flow Rule

The shear yield function, f, of the Hardening-Soil model can be expressed as follows:

$$f = \bar{f} - \gamma^p \quad (4.6)$$

$$\bar{f} = -\frac{1}{E_{50}} \frac{q}{1 - q/q_a} - \frac{2q}{E_{ur}} \quad (4.7)$$

$$\gamma^p = -(2\varepsilon_1^p - \varepsilon_v^p) \cong -2\varepsilon_1^p \quad (4.8)$$

where $\bar{f}$ is a function of stress and γ^p is the plastic shear strain, which is used as a parameter for shear hardening; ε_1^p is the plastic axial strain and ε_v^p is the plastic volumetric strain. Shear hardening is a phenomenon of having irreversible plastic strains due to primary deviatoric loading.

Although the plastic volumetric strains of hard soils, ε_v^p, are not equal to zero, Schanz et al. (1999) argued they are relatively small, in contrast to the plastic axial strains, ε_1^p. Hence, approximation of the plastic shear strain in Equation 4.8 is generally acceptable. The shear yield function that is equal to zero, for a given constant value of the hardening parameter, γ^p, can be plotted in the mean effective stress – deviator stress space by means of a yield locus. Figure 4.2 presents the shape of successive yield loci for soils with m = 0.5. It can be observed that the failure surface of the Hardening-Soil model is not fixed in the stress space, but can expand due to plastic straining. The failure surfaces would approach the Mohr-Coulomb failure criterion, as listed in Equation 4.2.

The Hardening-Soil model employs a linear flow rule between the rates of plastic shear strain, $\dot{\gamma}^p$, and plastic volumetric strain, $\dot{\varepsilon}_v^p$ as follows:

$$\dot{\varepsilon}_v^p = \sin \psi_m \, \dot{\gamma}^p \quad (4.9)$$

where ψ_m is the mobilized angle of dilatancy.

The mobilized angle of dilatancy can be determined according to Equation 4.10 proposed by Schanz and Vermeer (1996). They extended the stress-dilatancy theory proposed by Rowe (1962) and Rowe (1971) in the derivation of Equation 4.10. The mobilised angle of friction, ϕ_m, is computed using Equation 4.11, which can be determined using a Mohr circle.

$$\sin \psi_m = \frac{\sin\phi_m' - \sin\phi_{cv}'}{1 - \sin\phi_m' \sin\phi_{cv}'} \tag{4.10}$$

$$\sin \phi_m = \frac{\sigma_1' - \sigma_3'}{\sigma_1' + \sigma_3' - 2c \cot \phi'} \tag{4.11}$$

where ϕ_m', ϕ_{cv}' and ϕ' are the effective mobilised angle of friction, critical state angle of friction and effective ultimate angle of friction, respectively.

In PLAXIS, the critical state angle of friction is calculated from the ultimate angle of friction and ultimate angle of dilatancy using Equation 4.12. Thus, it is sufficient for the user to input soil parameters for the ultimate angle of friction and ultimate angle of dilatancy.

$$\sin \phi_{cv}' = \frac{\sin\phi' - \sin\psi}{1 - \sin\phi' \sin\psi} \tag{4.12}$$

where ϕ' and ψ are the ultimate angle of friction and ultimate angle of dilatancy, respectively.

4.2.3 Cap Yield Surface In Hardening-Soil Model

The plastic volumetric strain that occurs during isotropic compression cannot be obtained from the shear yield surfaces, as shown in Figure 4.2. Thus, a cap yield surface, f^c, is implemented in the Hardening-Soil model to account for these plastic

volumetric strains due to isotropic compression. The cap yield surface is close to the elastic region in the direction of the mean effective stress axis and is defined as:

$$f^c = \frac{\bar{q}^2}{\alpha^2} + p^2 - P_p^2 \tag{4.13}$$

where α is an auxiliary model parameter that relates to the coefficient of earth pressure at rest for normally consolidation, K_o^{nc}. $\bar{q}$ denotes the special stress measure for deviatoric stresses and p is the mean effective stress. P_p is the isotropic pre-consolidation stress and it determines the magnitude of the cap yield surface. The isotropic pre-consolidation stress can be computed by assigning an over-consolidation ratio, OCR, or a pre-overburden pressure, POP, into the Hardening-Soil model. Over-consolidation ratio is a ratio of the maximum vertical stress experienced by the soil to its present vertical stress whereas pre-overburden pressure is defined as the difference between the greatest vertical stress and the present vertical stress experienced by the soil. A hardening law, relating the isotropic pre-consolidation stress to the volumetric cap strain, ε_v^{pc}, is presented in Equation 4.14. Compression hardening is the occurrence of irreversible plastic strains due to primary consolidation in isotropic and oedometer loading. The volumetric cap strain is the plastic volumetric strain that occurs during isotropic compression.

$$\varepsilon_v^{pc} = \frac{\beta}{1-m}\left(\frac{P_p}{p^{ref}}\right)^{1-m} \tag{4.14}$$

where β is a model constant that relates to the reference tangential stiffness in primary oedometer loading, E_{oed}^{ref}, corresponding to the reference stress, p^{ref}.

Hence, the tangential stiffness modulus in primary oedometer loading will control the cap yield surface. The magnitude of the oedometer stiffness is also stress dependent

and the Hardening-Soil model considers the amount of stress dependency according to a power law using the power m. The actual tangential oedometer stiffness depends on the magnitude of the major principal stress, σ_1', which is the vertical stress in an oedometer test.

$$E_{oed} = E_{oed}^{ref} \left(\frac{c' \cos\phi' - \sigma_1' \sin\phi'}{c' \cos\phi' + p^{ref} \sin\phi'} \right)^m \quad (4.15)$$

where E_{oed}^{ref} is the reference tangential oedometer stiffness modulus corresponding to the reference stress, p^{ref}. The reference oedometer stiffness, as shown in Figure 4.3, will control the amount of plastic strains that originate from the cap yield surface.

Figure 4.4 illustrates the shear and cap yield surfaces of the Hardening-Soil model in the mean effective stress – deviatoric stress space. The elastic region can be further reduced by means of a tension cut-off. The total yield contour of the Hardening-Soil model in principal stress space for a cohesionless soil is presented in Figure 4.5. Both the shear locus and the yield cap have the hexagonal shape of the classical Mohr Coulomb failure criterion. The shear yield locus would expand up to the ultimate Mohr Coulomb failure surface while the cap yield surface expands as a function of the pre-consolidation stress.

4.2.4 Input Parameters of Hardening Soil Model

Failure in the Hardening-Soil model is defined according to the Mohr Coulomb failure criterion. Thus, the failure parameters include the effective cohesion, c', the effective angle of friction, ϕ', and the angle of dilatancy, ψ. The basic parameters for soil stiffness are the power for stress-dependency of stiffness, the reference secant stiffness

modulus and the reference tangential oedometer stiffness modulus corresponding to the reference stress, p^{ref}.

In order to simulate the logarithmic stress dependency, which is typical for soft clays, the power for stress-dependency is taken to be equal to 1. Janbu (1963) found that the power for stress-dependency for Norwegian sands and silts are approximately 0.5. The reference secant stiffness modulus, E_{50}^{ref}, the reference tangential oedometer stiffness modulus, E_{oed}^{ref}, and the reference unloading stiffness modulus, E_{ur}^{ref}, can be inputted independently into the Hardening-Soil model. Schanz and Vermeer (1998) suggested the reference secant stiffness modulus, E_{50}^{ref}, is approximately equal to the reference tangential oedometer stiffness modulus, E_{oed}^{ref}, for sands. By default, PLAXIS assigns a value of thrice the reference secant stiffness modulus, E_{50}^{ref}, to the reference unloading stiffness modulus, E_{ur}^{ref}.

Advanced parameters of the Hardening-Soil model include the effective unloading Poisson's ratio, ν_{ur}', the reference stress, p^{ref}, the coefficient of earth pressure at rest for normally consolidation, K_o^{nc}, and the failure ratio, R_f. The failure ratio, R_f, is assigned a default value of 0.9, which can be changed to a suitable value representative of the soil considered. Over-consolidation ratio, OCR, or pre-overburden pressure, POP, are required to define the isotropic preconsolidation stress, P_p. The tensile strength of the soil, $\sigma_{tension}$, and increment of the effective cohesion, $c_{increment}$, are two other soil parameters of this constitutive model.

4.3 Determination of Model Parameters

Schanz and Bonnier (1997) proposed a method for determining some model parameters of the Hardening-Soil model using one-dimensional oedometer test results. In their approach, the results of vertical strain and normalised vertical stress of an oedometer test are plotted in logarithmic scale, as shown in Figure 4.6. Schanz and Bonnier (1997) suggested that the vertical strain and normalised vertical stress of the loading oedometer test are related according to Equation 4.16. The reference tangential oedometer stiffness modulus, E_{oed}^{ref}, and the power for stress-dependency of stiffness, m, can be obtained from the linear regression coefficients, A and B, using Equations 4.17 and 4.18.

$$\ln \varepsilon_1 = A \ln \frac{\sigma_1}{p^{ref}} + B \tag{4.16}$$

$$m = 1 - A \tag{4.17}$$

$$E_{oed}^{ref} = \frac{1}{A} \frac{p^{ref}}{e^B} \tag{4.18}$$

where ε_1 and σ_1 are the vertical strain and applied stress of an oedometer test, respectively and p^{ref} represents the reference pressure that normalises the vertical stress of oedometer test.

4.3.1 Verification of Schanz and Bonnier's Equations

The stress dependency relationship of the oedometer stiffness modulus is found to be crucial in the derivation of Equations 4.16 to 4.18. Since Schanz and Bonnier (1997) considered compressive stresses as positive stresses, in contrast to Brinkgreve (2002), Equation 4.19 is employed, in place of Equation 4.15, in the derivation of Equations 4.16 to 4.18. Equations 4.16 to 4.18 are independently derived by the author and the

derivation is presented in the Appendix. It is evident from the derivation that an assumption of zero effective cohesion is made by Schanz and Bonnier (1997)

$$E_{oed} = E_{oed}^{ref} \left(\frac{c' \cos \phi' + \sigma_1' \sin \phi'}{c' \cos \phi' + p^{ref} \sin \phi'} \right)^m \quad (4.19)$$

where E_{oed} and E_{oed}^{ref} are the actual tangential oedometer stiffness modulus and the reference tangential oedometer stiffness modulus respectively that corresponds to the reference pressure, p^{ref}, c' and ϕ' are the effective cohesion and effective angle of friction, respectively.

4.3.2 Verification Using Oedometer Element Tests

One-dimensional oedometer element tests are simulated using PLAXIS to verify the validity of the method proposed by Schanz and Bonnier (1997). The oedometer test is modelled by means of an axisymmetric geometry of unit dimensions, as shown in Figure 4.7. The finite element mesh consists of 120 15-node triangular elements. Since the soil weight is not taken into consideration, the dimension of the finite element mesh would not influence the results and the computed stresses and strains of the element test would be uniformly distributed over the geometry. The range of soil parameters used in the simulation of oedometer tests with Hardening-Soil model is summarised in Table 4.1.

Table 4.1 Hardening-Soil Model parameters for oedometer element tests

Unsaturated Unit Weight, γ_{unsat} (kN/m^2)	0
Saturated Unit Weight, γ_{sat} (kN/m^2)	0
Effective Cohesion, c' (kN/m^2)	0 - 30
Effective Angle of Friction, ϕ' (^{o})	25 - 40
Angle of Dilatancy, ψ (^{o})	0
Effective Unloading Poisson's Ratio, ν_{ur}'	0.2
Reference Secant Stiffness Modulus, E_{50}^{ref} (kN/m^2)	10000
Reference Tangential Oedometer Stiffness Modulus, E_{oed}^{ref} (kN/m^2)	10000
Reference Unloading Stiffness Modulus, E_{ur}^{ref} (kN/m^2)	30000
Reference pressure, p^{ref} (kN/m^2)	20 - 500
Power For Stress-Dependency of Stiffness, m	0.5 – 1
Failure Ratio, R_f	0.9

The performance of the method suggested by Schanz and Bonnier (1997) is measured by means of percentage errors in the estimation of the power for stress-dependency of stiffness, m, and the reference tangential oedometer stiffness modulus, E_{oed}^{ref}. The percentage errors are determined according to Equations 4.20 and 4.21. It is evident that an underestimation of the parameters would yield a positive percentage error and an overestimation would give a negative percentage error.

$$\text{Percentage Error in m} = \left(\frac{m_{input} - m_{predicted}}{m_{input}} \right) x\,100\% \tag{4.20}$$

$$\text{Percentage Error in } E_{oed}^{ref} = \left(\frac{\left(E_{oed}^{ref}\right)_{input} - \left(E_{oed}^{ref}\right)_{predicted}}{\left(E_{oed}^{ref}\right)_{input}} \right) x\,100\% \tag{4.21}$$

where m_{input}, and $(E_{oed}^{ref})_{input}$ are the values of power for stress-dependency of stiffness and the reference tangential oedometer stiffness modulus inputted into the Hardening-Soil model. Their predicted values determined using Equations 4.17 and 4.18 are denoted by $m_{predicted}$ and $(E_{oed}^{ref})_{predicted}$ respectively.

Figure 4.8 presents the percentage errors of the estimated power for stress-dependency of stiffness and the estimated reference tangential oedometer stiffness modulus as the effective cohesion and effective friction angles of the soil are varied. A reference pressure of 100 kN/m^2 is adopted. It is apparent that both percentage errors generally increase as the actual power for stress-dependency of stiffness increases from a value of 0.5 to 1. This holds true even for soils with zero effective cohesion although the effective cohesion is neglected in the derivation of Schanz and Bonnier's equations. When the input effective cohesion of the soils is zero and the effective angle of friction is varied, the power for stress-dependency of stiffness is overestimated by 1.36% to 14.36% as the input power for stress-dependency of stiffness varies from 0.5 to 1. However, the method proposed by Schanz and Bonnier (1997) produces a greater deviation in the prediction of the reference tangential oedometer stiffness modulus as the reference tangential oedometer stiffness modulus is underestimated by 0.46% to 50.74%. It is observed from Figure 4.8 that the percentage errors in estimating the parameters increase tremendously when the effective cohesion is significant, as compared to the percentage errors obtained for cohesionless soils

The influence of using various values of reference pressure, p^{ref}, for cohesionless soils is illustrated in Figure 4.9. The reference pressure is varied from 20 kN/m^2 to 500 kN/m^2. It is evident from Figure 4.9 that using different values of reference pressure would not affect the performance of Schanz and Bonnier's method in the prediction of the power for stress-dependency of stiffness, m. However, accuracy in the estimation of the reference tangential oedometer stiffness modulus, E_{oed}^{ref}, is enhanced when a higher reference pressure is adopted. Figure 4.10 summarises the effects of employing different reference pressure for soils with significant effective cohesion. It can be

deduced that the use of different reference pressure would not enhance the prediction of the power for stress-dependency of stiffness and the reference tangential oedometer stiffness modulus.

In conclusion, the method proposed by Schanz and Bonnier (1997) would produce reasonable estimation of the power for stress-dependency of stiffness and the reference tangential oedometer stiffness modulus for cohesionless soils with a power for stress-dependency of stiffness that ranges from 0.5 to 0.7. The accuracy of determining the reference tangential oedometer stiffness can be improved by using a higher reference pressure. This method would not be applicable for cohesive soils as the effective cohesion is neglected in the fundamental derivation of Schanz and Bonnier's equations. The results from finite element oedometer tests further confirmed that this method is not appropriate for cohesive soils. Figures 4.8 and 4.9 would serve as a guide for correcting the estimated parameters using the method proposed by Schanz and Bonnier (1997).

4.4 Determination of Hardening-Soil Model Parameters of Old Alluvium

One-dimensional oedometer tests and consolidated undrained (CIU) triaxial tests are performed on some samples of Old Alluvium by Mr Ni Qing, a fellow research student, near the project site of the Influent Pumping Station of the Changi Water Reclamation Plant, in the eastern area of the Singapore Island. The method proposed by Schanz and Bonnier (1997) is employed to estimate the power for stress-dependency of stiffness, m, and the reference tangential oedometer stiffness modulus, E_{oed}^{ref}, of these Old Alluvium soil samples. The vertical strains and normalised vertical stresses of the four oedometer tests are plotted in logarithmic scale as shown in Figure

4.11. The four samples comprise of silty sands and clayey sands. It is evident that the power for stress-dependency of stiffness, m, of these Old Alluvium samples ranges from 0.49 to 0.63. The estimated range of the power for stress-dependency of stiffness, m, is typical of sandy soils reported by Janbu (1963). The estimated values of power for stress-dependency of stiffness and the reference tangential oedometer stiffness modulus of these soil samples are listed in Table 4.2.

Table 4.2 Soil Parameters determined using Schanz and Bonnier's method

Sample Number	Soil Type	Depth of Sample (m)	Reference pressure, p^{ref} (kN/m^2)	Estimated Power For Stress-Dependency of Stiffness, m	Estimated Reference Tangential Oedometer Stiffness Modulus, E_{oed}^{ref} (kN/m^2)
1	Silty Sand	12.25	100	0.60	6383
2	Clayey Sand	6.30	100	0.49	11950
3	Clayey Sand	27.50	100	0.59	10166
4	Clayey Sand	6.25	100	0.63	5594

Results of laboratory oedometer and triaxial tests conducted on three Old Alluvium soil samples are simulated using the Hardening-Soil model to obtain insights on the behaviour of the constitutive model and to estimate some representative soil parameters of Old Alluvium near the project site. The Mohr Coulomb constitutive model is also used to simulate the laboratory tests. According to Brinkgreve (2002), the Mohr-Coulomb model is an elastic perfectly-plastic constitutive model with a fixed yield surface that is fully defined by model parameters and is not affected by plastic straining. The soil stiffness required for the Mohr Coulomb model is obtained from the secant modulus at 50% mobilisation of the ultimate deviatoric stress of the soil

samples during consolidated undrained triaxial tests. All the consolidated undrained triaxial tests were carried out at effective cell pressures that are approximately equal to the in-situ vertical stress of the soil samples.

One-dimensional oedometer element tests and consolidated undrained triaxial element tests are modelled using PLAXIS. The finite element meshes used for the calibration of oedometer tests and triaxial tests are shown in Figures 4.7 and 4.12, respectively. Similar to the finite element mesh for oedometer tests, the finite element mesh for triaxial element tests is also modelled by means of an axisymmetric geometry of unit dimensions, which represent a quarter of the soil specimen. The finite element mesh consists 120 15-node triangular elements. The soil weight is not taken into account. Figures 4.13, 4.14 and 4.15 present the experimental and numerical results of the oedometer tests and consolidated undrained triaxial tests. The properties of these soil samples are listed in Table 4.3.

Table 4.3 Hardening-Soil Model Parameters of Old Alluvium Samples

Soil Parameters	Sample 1	Sample 2	Sample 3
Unsaturated Unit Weight, γ_{unsat} (kN/m^2)	0	0	0
Saturated Unit Weight, γ_{sat} (kN/m^2)	0	0	0
Effective Cohesion, c' (kN/m^2)	0	0	0
Effective Angle of Friction, ϕ' (^{o})	39.0	43.0	37.0
Angle of Dilatancy, ψ (^{o})	10.0	6.0	2.5
Effective Unloading Poisson's Ratio, ν_{ur}'	0.2	0.2	0.2
Reference Secant Stiffness Modulus, E_{50}^{ref} (kN/m^2)	6150	12400	9900
Reference Tangential Oedometer Stiffness Modulus, E_{oed}^{ref} (kN/m^2)	6150	12400	9900
Reference Unloading Stiffness Modulus, E_{ur}^{ref} (kN/m^2)	59500	45700	69730
Reference pressure, p^{ref} (kN/m^2)	100	100	100
Power For Stress-Dependency of Stiffness, m	0.60	0.49	0.59
Failure Ratio, R_f	0.9	0.9	0.9
$\frac{E_{oed}^{ref}}{E_{50}^{ref}}$	1.0	1.0	1.0
$\frac{E_{ur}^{ref}}{E_{50}^{ref}}$	9.7	3.7	7.0
Effective Stiffness Modulus In Mohr Coulomb Model, E' (kN/m^2)	11661	9735	10313

From the simulation of laboratory oedometer and triaxial tests, it can be concluded that Schanz and Vermeer (1998)'s suggestion of adopting the reference secant stiffness modulus, E_{50}^{ref}, equal to reference tangential oedometer stiffness modulus, E_{oed}^{ref}, is realistic for these Old Alluvium soil samples. The ratio of the reference unloading stiffness modulus to the reference secant stiffness modulus, $\frac{E_{ur}^{ref}}{E_{50}^{ref}}$, is found to be highly variable for Old Alluvium soils and it ranges from 3.7 to 9.7. Values of the reference tangential stiffness modulus estimated from the method proposed by Schanz and Bonnier (1997) is found to be within 4% of the calibrated reference tangential stiffness modulus.

It is apparent from the experimental and numerical oedometer test results, presented in Figures 4.13 to 4.15, that the one-dimensional loading and unloading processes can be better simulated using the more advanced Hardening-Soil model as compared to the simpler Mohr Coulomb model. The better agreement with experimental results when using the Hardening-Soil model is not unexpected as the loading and unloading stress paths are characterised by different loading and unloading soil stiffness parameters and stress-dependency of stiffness is considered by the constitutive model while the Mohr Coulomb model employs the same stiffness modulus for both loading and unloading stress changes and does not account for stress dependency of soil stiffness.

Examination of the experimental consolidated undrained triaxial test results shows that Old Alluvium is dilative in nature. The tendency of the sample to dilate is manifested in the decrease of excess pore pressure and increase of shear strength during undrained deviatoric shearing. It can be observed from Figures 4.13 to 4.15 that the analytical stress paths of the soils during undrained deviatoric shearing predicted by both the Hardening-Soil model and the Mohr Coulomb model are similar and increase of shear strength in dilative soils can be simulated by both constitutive models. However, discrepancies between the numerical and experimental stress paths are evident. As both the Hardening-Soil and Mohr Coulomb constitutive models are mathematical laws for simulating soil behaviour, they do not replicate real soil behaviour due to the complexity in the behaviour of real soil and shortcomings present in these mathematical models. Sampling disturbance and experimental errors may also have contributed to the discrepancies between the numerical and experimental results. Nevertheless, the essential phenomenon in the stress paths, such increase of shear strength during shearing, can be described by these mathematical models.

The prediction of deviator stress and excess pore pressures using the two constitutive models under undrained triaxial condition are also presented in Figures 4.13 to 4.15. It is evident that the Hardening-Soil model provides a better prediction of the excess pore pressures generated during undrained shearing. There are rather substantial discrepancies between the experimental and numerical development of deviatoric stress with vertical strain predicted by both constitutive models. For the Hardening-Soil model, the development of deviator stress with increasing vertical strain under drained primary triaxial loading condition can be described by a hyperbolic relationship. However, it is apparent from Figures 4.13, 4.14 and 4.15 that the relationship between the predicted deviatoric stress and vertical strain during undrained shearing is not purely hyperbolic in the Hardening-Soil model for dilative soils. This is likely to be influenced by the dependencies present in the constitutive model, such as soil dilatancy, plasticity and compression cap yielding, as well as other limitations present in the constitutive law in simulating real soil behaviour. It can be observed from Figures 4.13, 4.14 and 4.15 that both the Hardening-Soil and Mohr Coulomb models are able to predict the stress-strain relation during undrained shearing at low axial strains. However, the Mohr Coulomb model would over-predict the axial strain at peak deviator stress.

Some of the limitations of Hardening-Soil model have been discussed by Brinkgreve (2002) and Vermeer (2003). This constitutive model cannot simulate hysteretic and cyclic loading and cyclic mobility as it is an isotropic hardening model and the elastic region defines by the Hardening-Soil model is found to be larger than the realistic region for triaxial compression. Due to shear hardening, this constitutive model has a drawback of predicting fully elastic behaviour for soils with power for stress-

dependency of stiffness of 1 under oedometric loading condition. According to Vermeer (2003), this shortcoming is not serious for hard soils but it is very significant for soft soils. Effects of creep and stress relaxation are also not accounted for in the Hardening-Soil model. The softening behaviour of the soils after approaching the peak deviator stress cannot be accounted for in most constitutive models, including the Hardening-Soil and Mohr Coulomb models. Since the failure of soil have to be designed for and the softening regime of the deviator stress-strain relationship is hardly attained for real construction and excavation projects, realistic modelling of the softening regime is not required for general geotechnical purposes. As with the case of the Hardening-Soil model, the Mohr Coulomb model is also unable to account for creep, hysteretic and cyclic loading and cyclic mobility phenomenon in real soils.

As the Old Alluvium formation present at the project site consists of mostly stiff soils, secondary compression is not significant. Hysteretic and cyclic loadings are unlikely to occur in the excavation problem considered in this research. Hence, these shortcomings of the Hardening-Soil model are unlikely to cause unrealistic prediction of the response of the circular shaft examined in this research. Although the Hardening-Soil model can provide a better estimation for most experimental results, usage of this advance model is not recommended when soil information is inadequate. Input parameters for the Mohr Coulomb model can be easily derived but the methods for determining the Hardening-Soil model parameters are not as established. Despite having fewer input parameters, many geotechnical problems have been analysed successfully using the Mohr Coulomb model, such as those reported by Yong et al. (1989) and Tan and Tan (2004). Nevertheless, the Hardening-Soil constitutive model is selected to simulate the behaviour of soil at the project site as it is found to be suitable

for stiff soils and is able to account for stress dependency of soil stiffness, shear hardening and compression hardening.

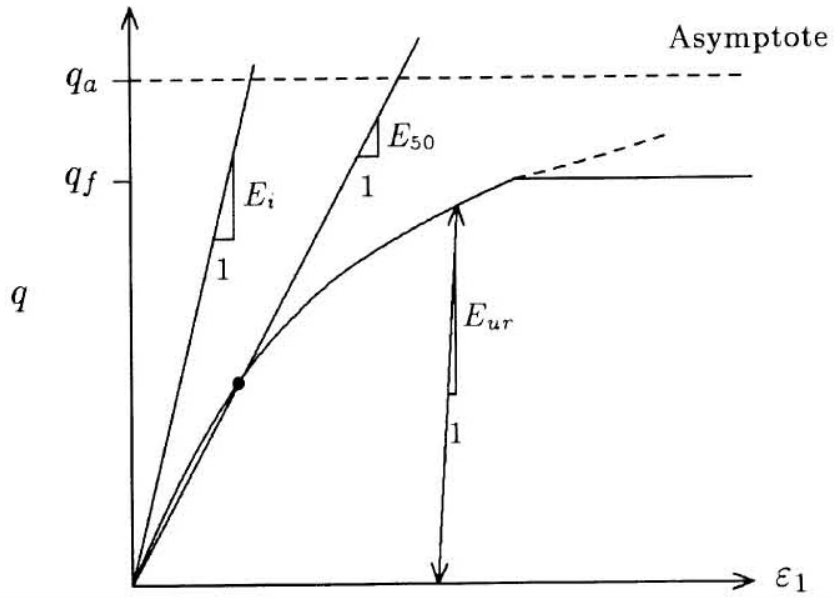

Figure 4.1 Hyperbolic stress-strain relationship in primary loading for a standard drained triaxial test (Schanz et al., 1999)

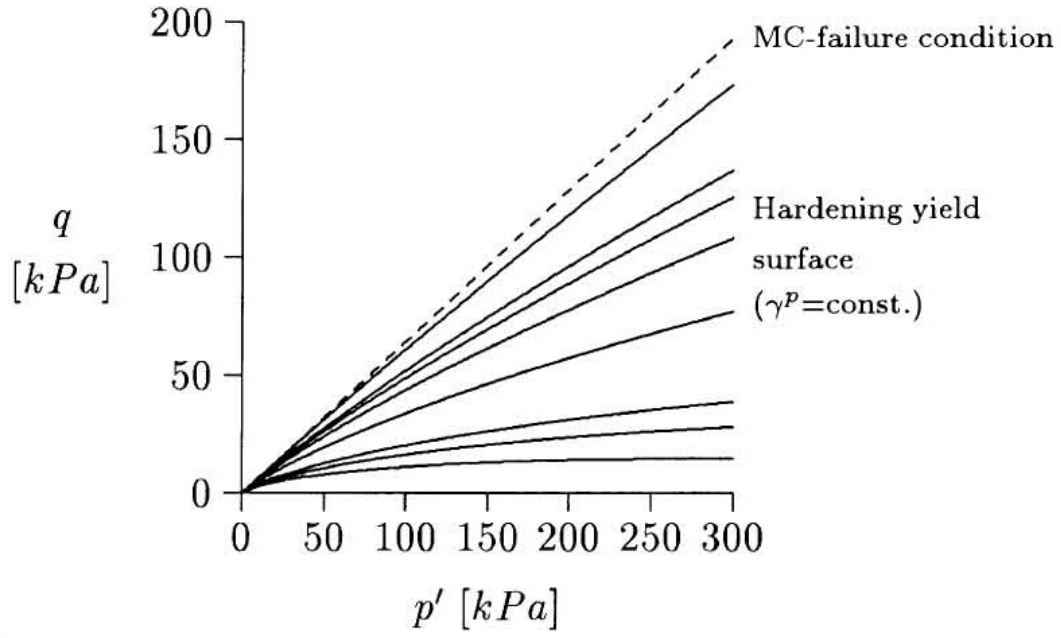

Figure 4.2 Successive yield loci for various values of hardening parameter, γ^p, and failure surface (Schanz et al., 1999)

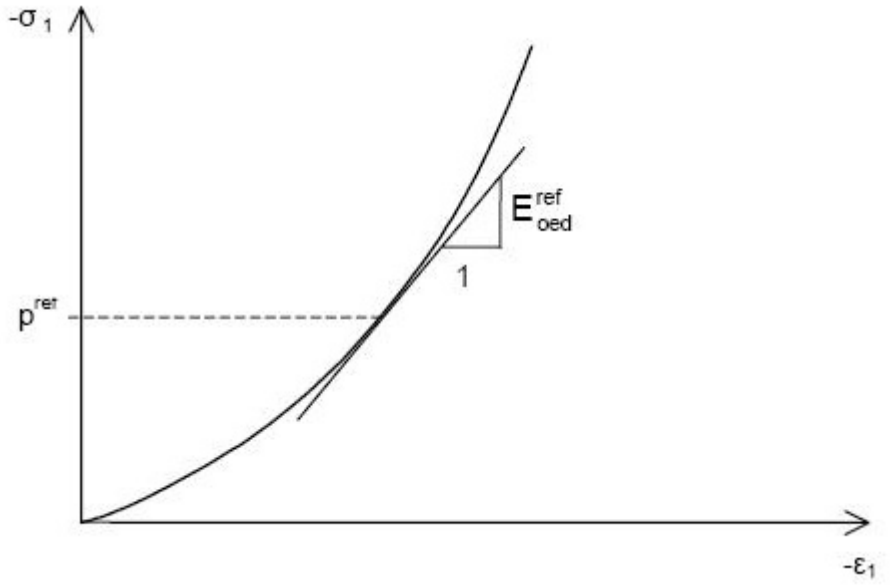

Figure 4.3 Definition of reference tangential oedometer stiffness modulus, E_{oed}^{ref}, in oedometer test results (Brinkgreve, 2002)

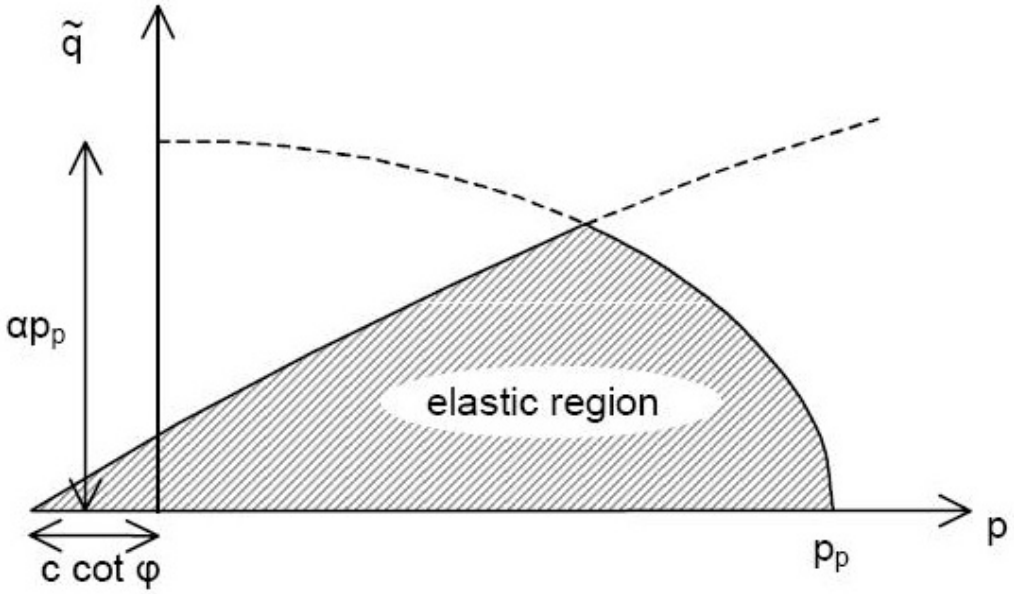

Figure 4.4 Yield surfaces of hardening-soil model in mean effective stress – deviatoric stress space (Brinkgreve, 2002)

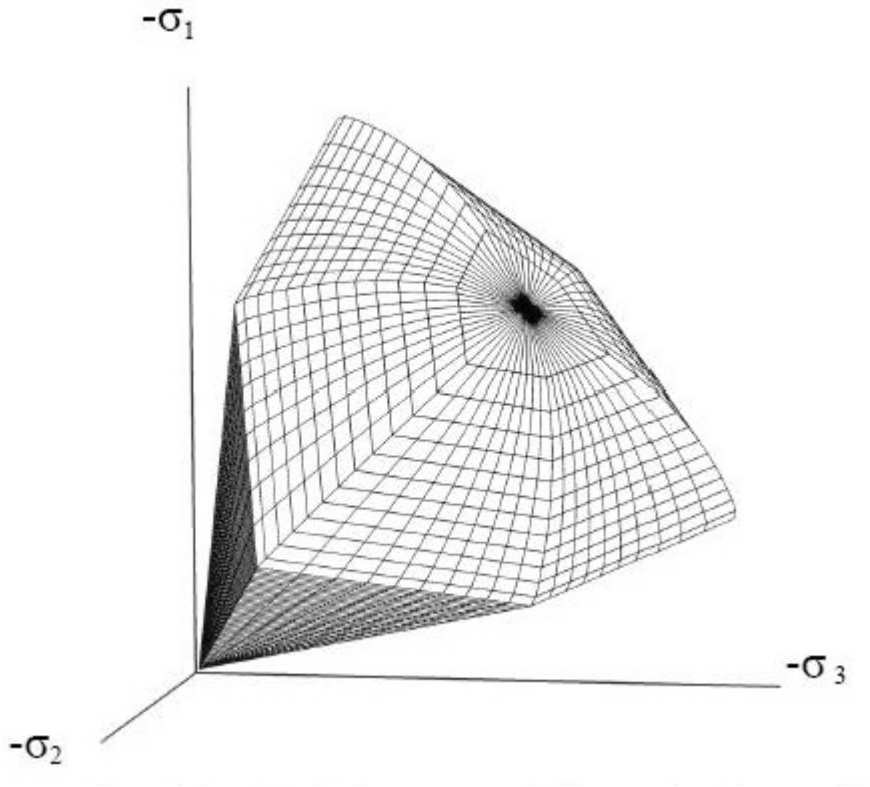

Figure 4.5 Representation of total yield contour of the Hardening-Soil Model in principal stress space for cohesionless soil (Brinkgreve, 2002)

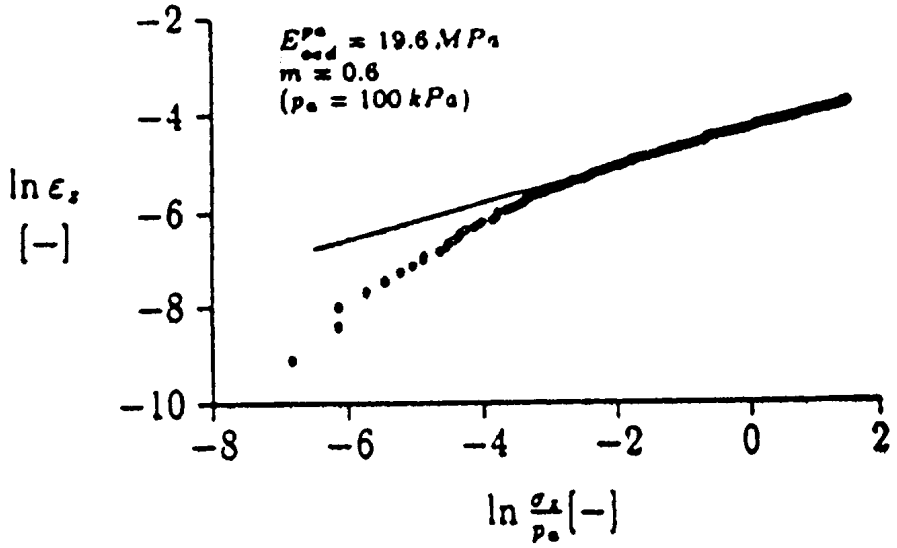

Figure 4.6 Determination of model parameters using oedometer test (Schanz and Bonnier, 1997)

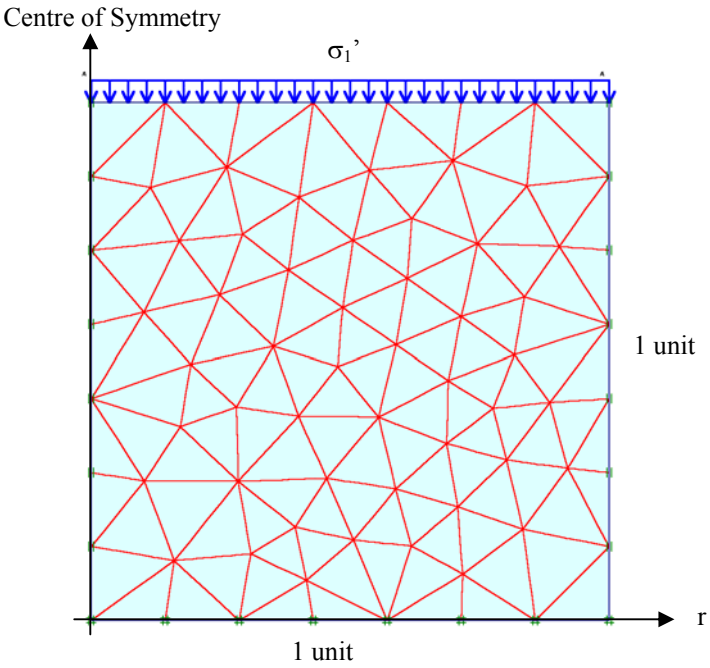

Figure 4.7 Finite element mesh of oedometer test (120 15-node triangular elements)

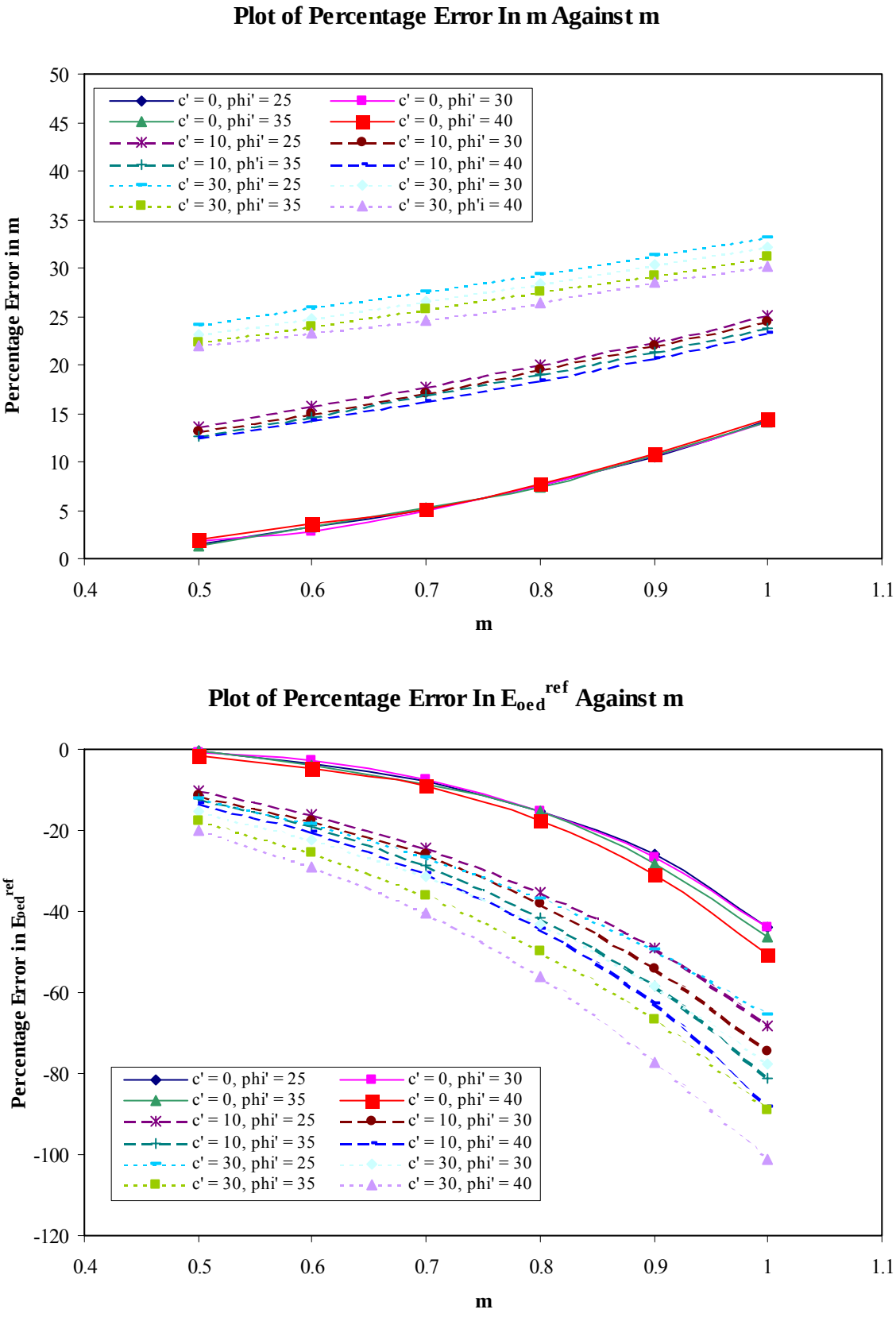

Figure 4.8 Influence of effective strength parameters on percentage errors of estimated m and E_{oed}^{ref} at p^{ref} of 100 kN/m^2

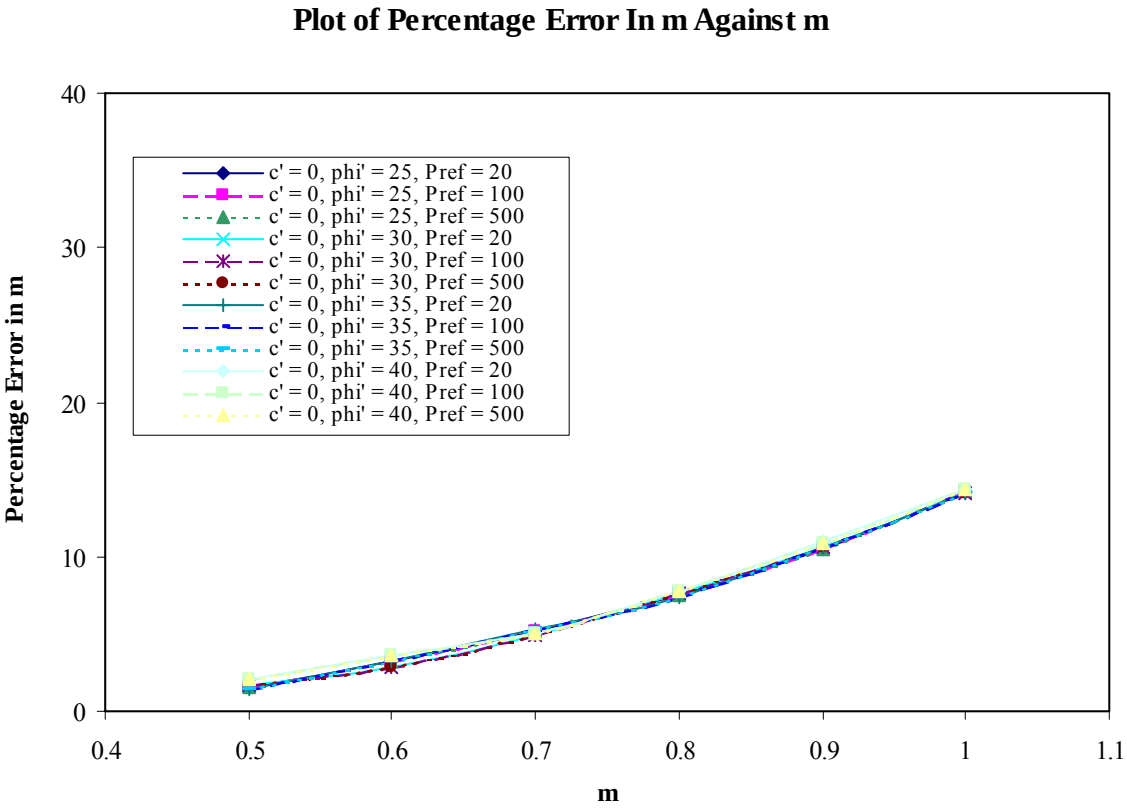

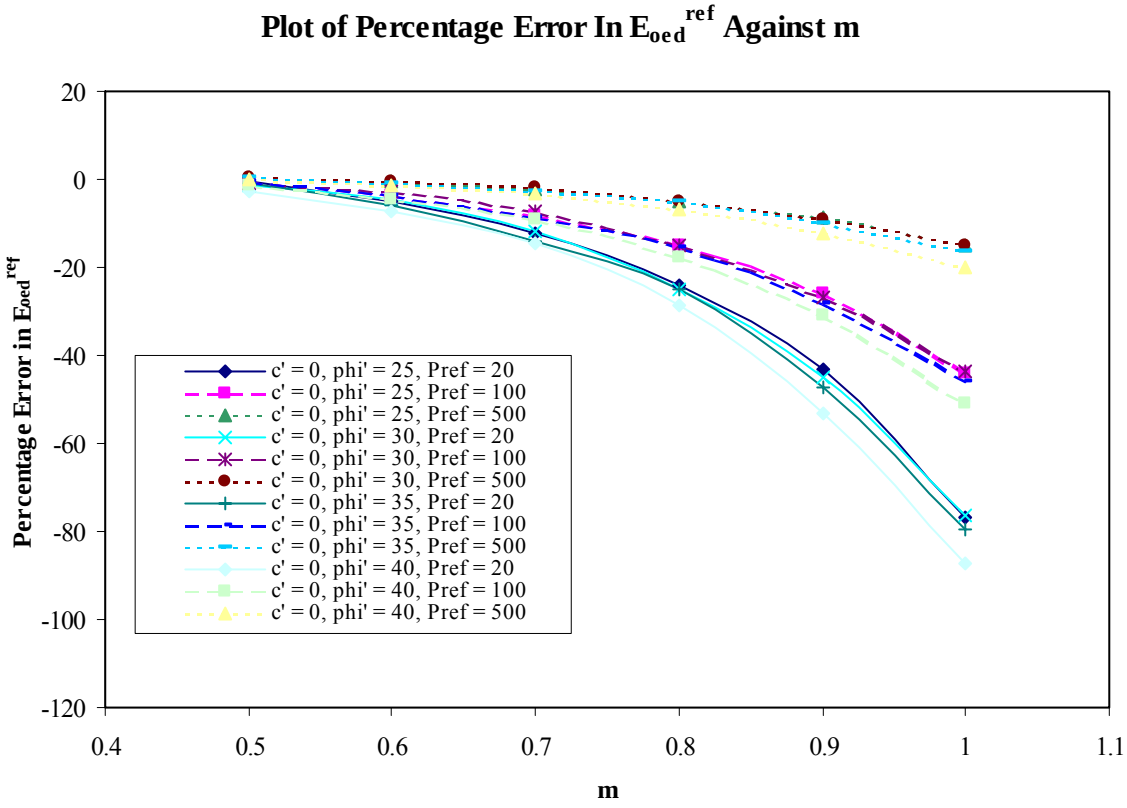

Figure 4.9 Influence of reference pressure on percentage errors of estimated m and E_{oed}^{ref} for cohesionless soils

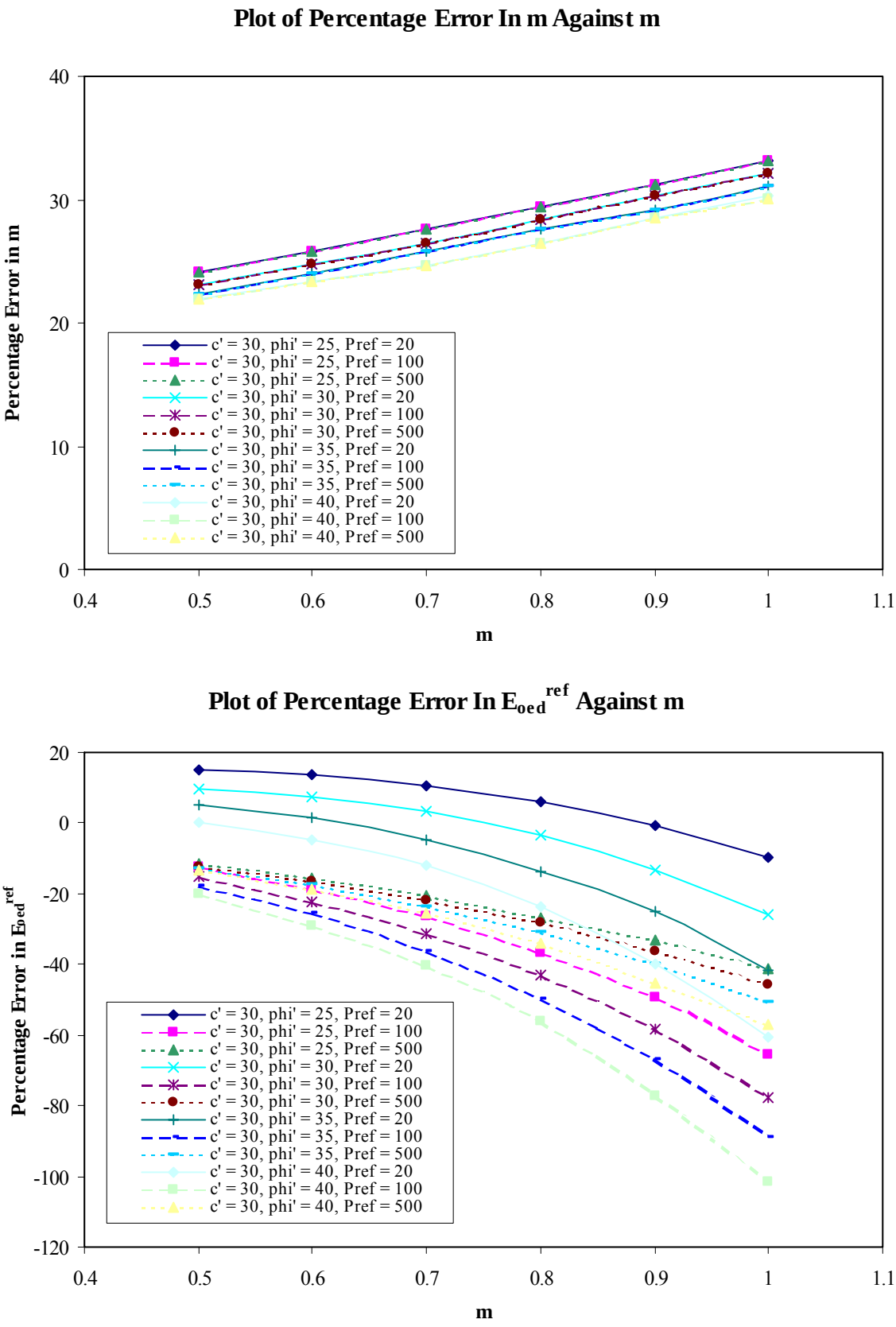

Figure 4.10 Influence of reference pressure on percentage errors of estimated m and E_{oed}^{ref} for cohesive soils

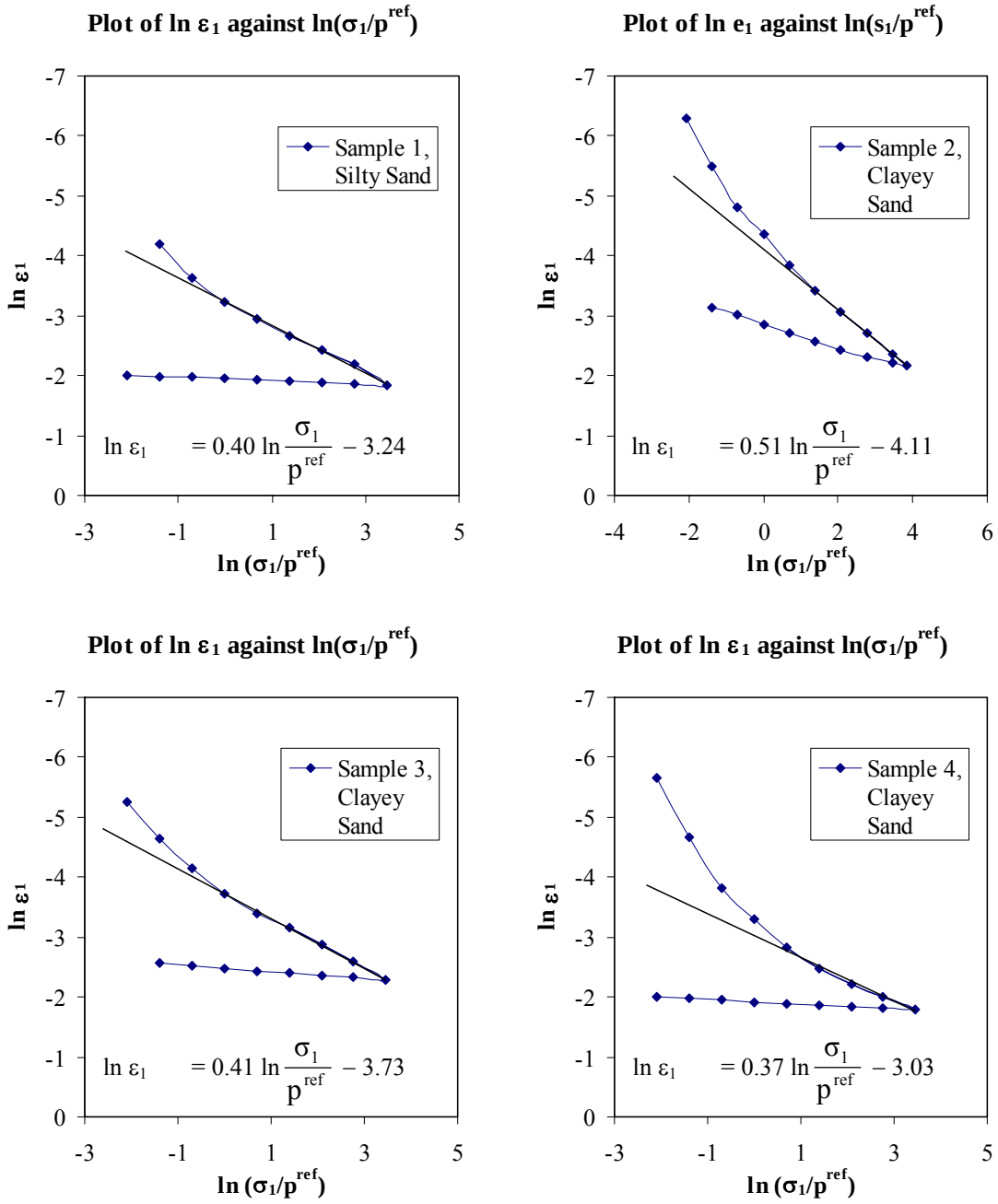

Figure 4.11 Determination of m and E_{oed}^{ref} of Old Alluvium soils using method proposed by Schanz and Bonnier (1997)

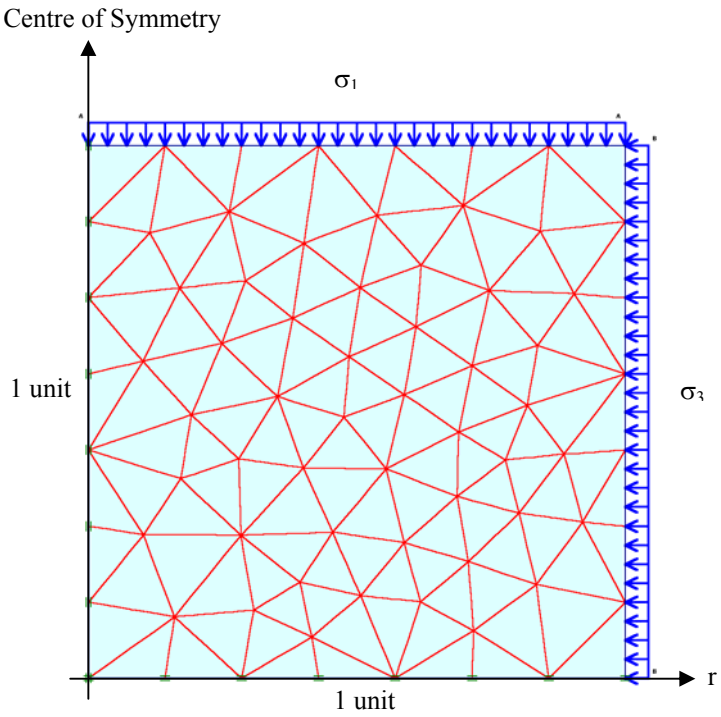

Figure 4.12 Finite element mesh of consolidated undrained triaxial test (120 15-node triangular elements)

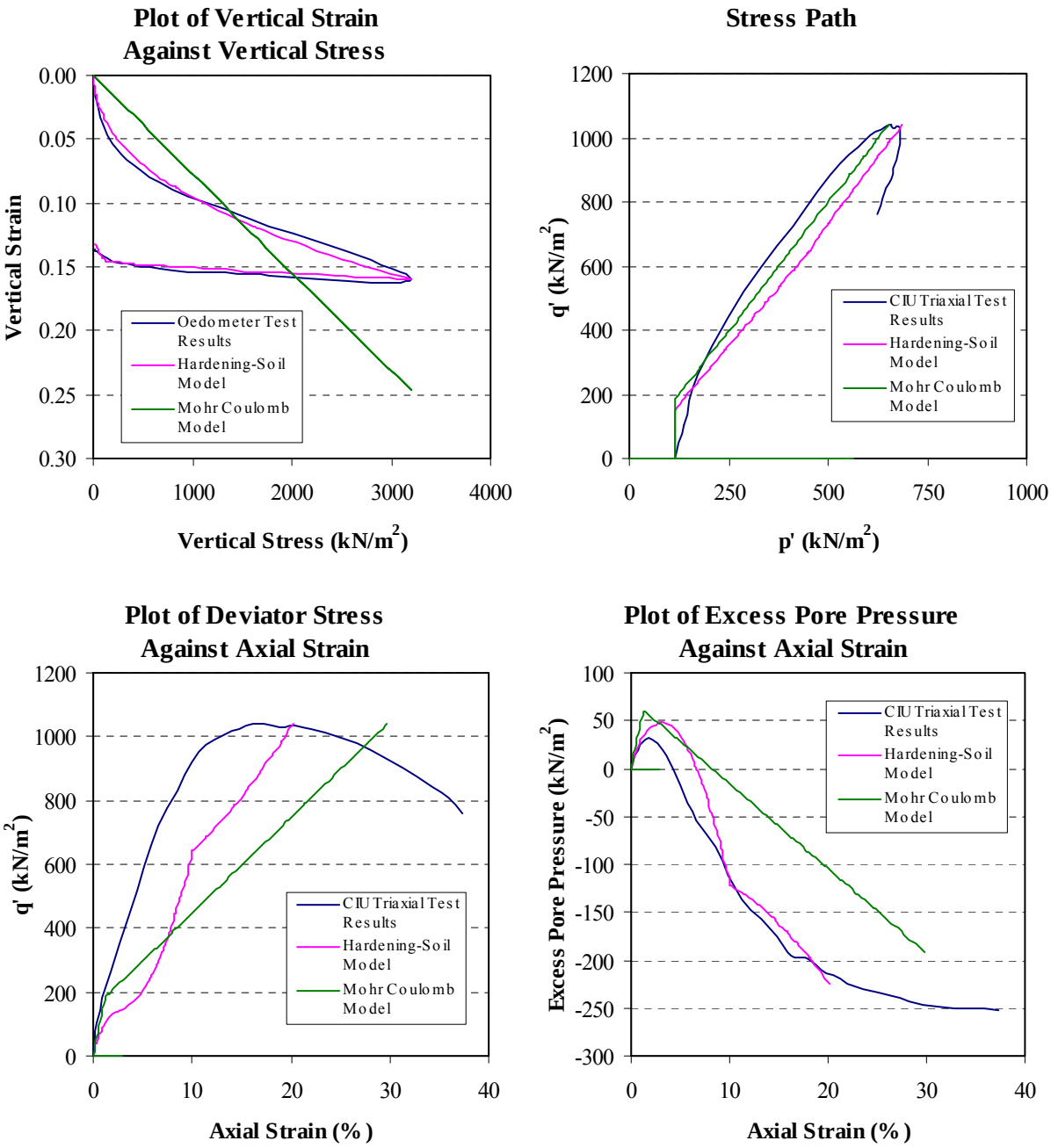

Figure 4.13 Simulation of oedometer and unconsolidated undrained triaxial test results of Sample 1

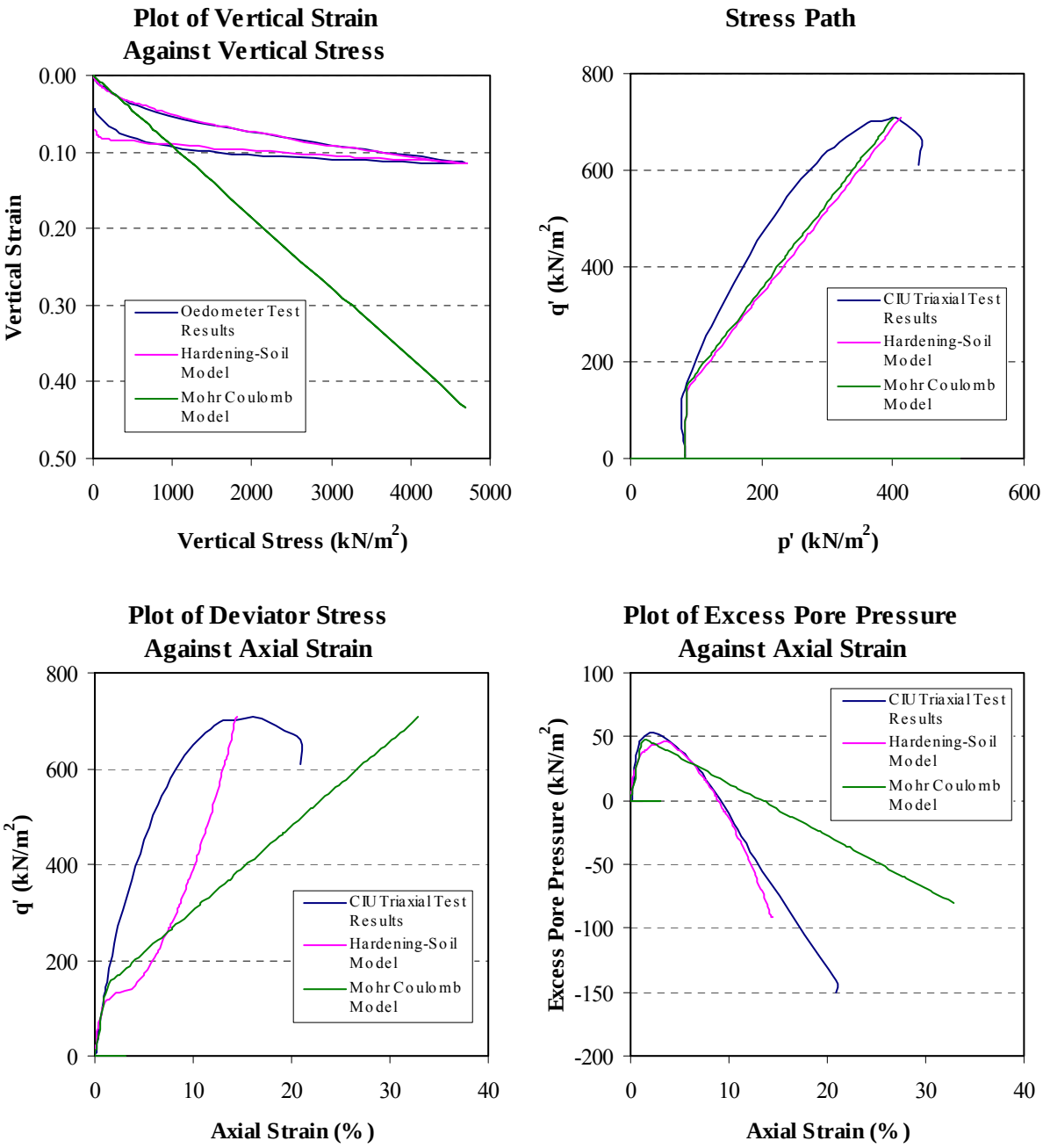

Figure 4.14 Simulation of oedometer and unconsolidated undrained triaxial test results of Sample 2

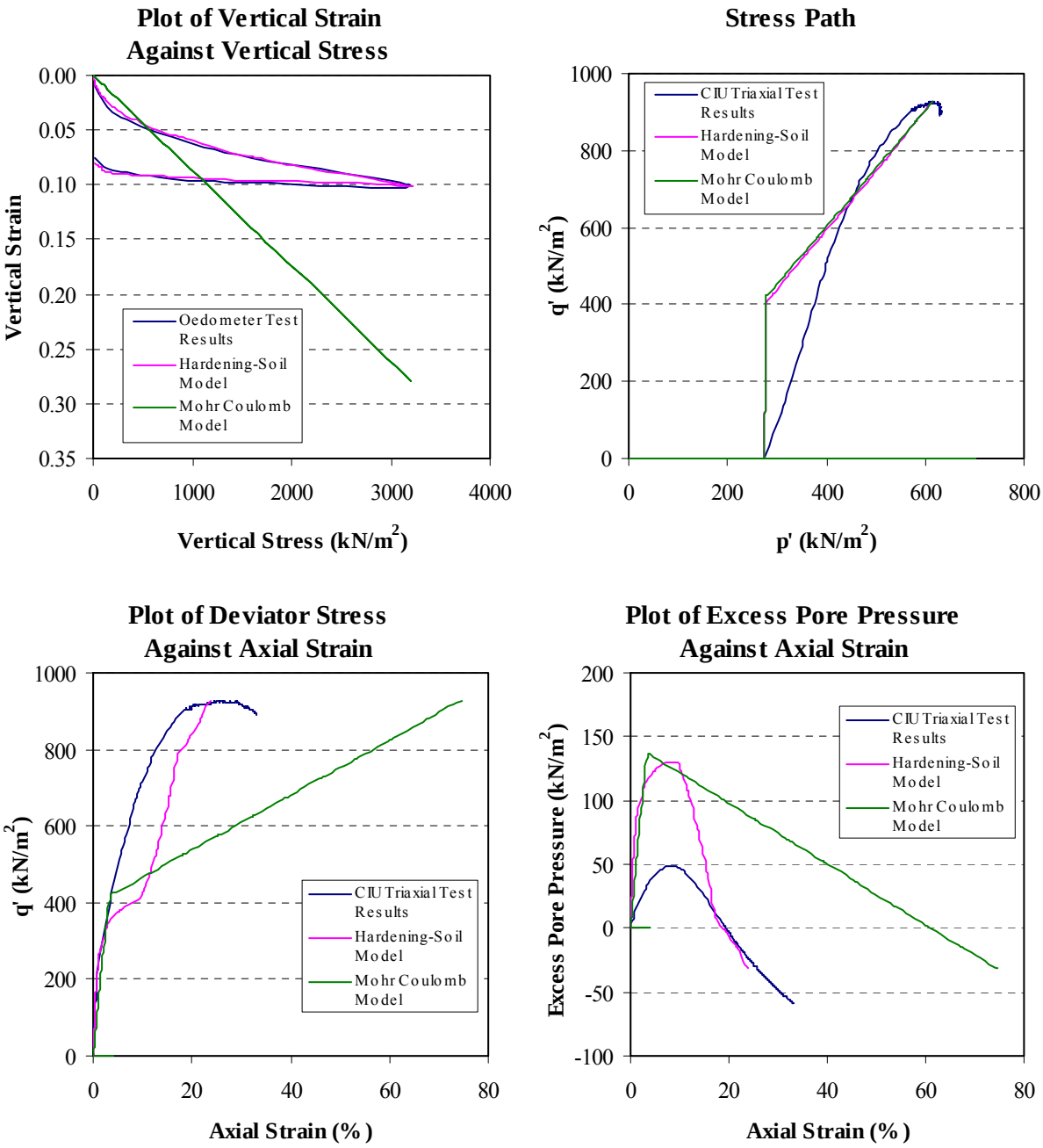

Figure 4.15 Simulation of oedometer and unconsolidated undrained triaxial test results of Sample 3

CHAPTER 5 PLAXFLOW

5.1 Introduction

PLAXFLOW is a newly released PLAXIS BV product for performing groundwater flow calculations. The stand-alone version of the PLAXFLOW program can consider steady state flow and transient flow with time-dependent boundary conditions. Sophisticated material models for saturated and unsaturated groundwater flow are incorporated into the PLAXFLOW program. PLAXFLOW is also compatible with PLAXIS for the deformation and stability analysis. Only two-dimensional plane strain groundwater flow computations can be performed when the PLAXFLOW program is first launched. However, with the release of new program updates, the PLAXFLOW program is capable of solving axisymmetrical groundwater flow problems. This is extremely useful as PLAXIS does not have the capability to calculate axisymmetrical groundwater flow for deformation and stability analysis. In this chapter, the material models and standardised material sets available in PLAXFLOW are briefly described and the performance of using PLAXFLOW to simulate axisymmetrical transient groundwater flow is assessed.

5.2 Material Models

Brinkgreve et al. (2003) summarised the material models for steady state, transient, saturated and unsaturated groundwater flow computations that are available in the PLAXFLOW program. Fully saturated soil behaviour can be analysed using the Saturated model. Both the Van Genuchten model and the Approximate Van Genuchten model are supported by the PLAXFLOW program

5.2.1 Van Genuchten Model

Van Geouchten (1980) developed an equation for the water content-pressure head relationship of soils. This relationship is continuous in nature and has a continuous slope. The unique form of Van Geouchten's equation allows one to develop closed-form analytical expressions to predict the hydraulic conductivity of unsaturated soils.

The degree of saturation of soils could be less than unity if air is trapped inside the soil voids. Van Geouchten (1980) believed that a residual saturation, S_{res}, would describe the pore water that remains in the voids of soils with high suction head and the degree of saturation of soils, S, is dependent on effective pressure head, ϕ_p, as given in Equation 5.1. The Van Genuchten model then relates the relative permeability of soil, k_{rel}, to the degree of saturation, S, through its effective saturation, S_e, in accordance to Equations 5.2 and 5.3. The effective permeability of soil, k, can then be obtained from its relative permeability using Equation 5.4.

$$S(\phi_p) = S_{res} + (S_{sat} - S_{res}) \left[1 + (g_a |\phi_p|)^{g_a}\right]^{\left(\frac{1-g_n}{g_n}\right)} \tag{5.1}$$

$$S_e = \frac{S - S_{res}}{S_{sat} - S_{res}} \tag{5.2}$$

$$k_{rel}(S) = (S_e)^{g_l} \left[1 - \left(1 - S_e\left(\frac{g_n}{g_n - 1}\right)\right)^{\left(\frac{g_n}{g_n - 1}\right)}\right]^2 \tag{5.3}$$

$$k = k_{rel}(S)\, k_{sat} \tag{5.4}$$

where S_{sat} and k_{sat} denote the actual degree of saturation for saturated soil and saturated permeability of soil, respectively. g_a, g_l and g_n are parameters of the Van Genuchten model.

5.2.2 Approximate Van Genuchten Model

Brinkgreve et al. (2003) reported that the Approximate Van Genuchten model is a linearised Van Genuchten model, which is numerically more stable than the original Van Genuchten model. Input parameters of the Approximate Van Genuchten model are approximately equivalent process parameters of the original Van Genuchten model. It is apparent from Equation 5.5 that the Approximate Van Genuchten model relates the degree of saturation to the effective pressure head, ϕ_p. The extent of the unsaturated zone under hydrostatic conditions is represented by the material-dependent pressure head parameter, ϕ_{ps}. The degree of saturation of soil is taken to be zero when the effective pressure head is less than the threshold value of ϕ_{ps} whereas the degree of saturation is unity under saturated soil conditions.

$$S(\phi_p) = \begin{cases} 1 & \text{if } \phi_p \geq 0 \\ 1 + \dfrac{\phi_p}{|\phi_{ps}|} & \text{if } \phi_{ps} \leq \phi_p \leq 0 \\ 0 & \text{if } \phi_p \leq \phi_{ps} \end{cases} \quad (5.5)$$

The Approximate Van Genuchten model made use of a log-linear relation of pressure head, as given in Equation 5.6, to describe the relative permeability in the transition zone of varying saturation. The pressure head at which the relative permeability is reduced to 10^{-4} is denoted by the model parameter, ϕ_{pk}. Under saturated condition, the permeability of soil is equal to the saturated permeability, which is taken to be constant.

$$k_{rel}(\phi_p) = \begin{cases} 1 & \text{if } \phi_p \geq 0 \\ 10^{\frac{4\phi_p}{|\phi_{pk}|}} & \text{if } \phi_{pk} \leq \phi_p \leq 0 \\ 10^{-4} & \text{if } \phi_p \leq \phi_{pk} \end{cases} \quad (5.6)$$

The pressure head parameter, ϕ_{ps}, of the Approximate Van Genuchten model is derived from the classical Van Genuchten model using Equation 5.7. The Approximate Van Genuchten model parameter, ϕ_{pk}, is equal to the pressure head at which the relative permeability of soil is 10^{-2} in the classical Van Genuchten model. The pressure head parameter, ϕ_{pk}, has a lower limit of –0.5m.

$$\phi_{ps} = \frac{1}{S_{\phi_p = -1.0m} - S_{sat}} \tag{5.7}$$

where $S_{\phi_p = -1.0m}$ is the degree of saturation in the original Van Genuchten model at which the effective pressure head, ϕ_p, equals to a value of –1.0m and S_{sat} refers to the degree of saturation under saturated conditions.

5.3 Material Sets Available in PLAXFLOW

The PLAXFLOW program provides predefined material sets for the Van Genuchten model and the Approximate Van Genuchten model. According to Brinkgreve et al. (2003), these material models, with predefined parameters, are categorized using international soil classification systems. In-situ soils can be identified using Hypres, USDA or Staring soil classification systems. User-defined material models are also available in the PLAXFLOW program. Default values of coefficient of permeability for the various soil classification, Ks, are available for both Van Genuchten model and Approximate Van Genuchten model. The coefficient of permeability can be changed to a suitable value representative of the soil considered.

5.3.1 Hypres Soil Classification System

The Hypres soil classification system is an international system that categorizes non-organic soils, according to the soil particle fractions, into coarse, medium, medium

fine, fine, very fine soils and organic soils. Brinkgreve et al. (2003) reported that the difference in hydraulic properties between Upper soils within 1 m below the ground surface and Lower soils is considered in the Hypes soil classification system. The standardised parameter sets for the Van Genuchten model and the Approximate Van Genuchten model are presented in Tables 5.1 and 5.2, respectively.

5.3.2 USDA Soil Classification System

Standardised material models are available for the USDA soil classification system. The USDA series is an international system that classifies soils into sand, loamy sand, sandy loam, loam, silt, silty loam, sandy clayey loam, clayey loam, silty clayey loam, sandy clay, silty clay and clay. The pre-defined parameter sets for the Van Genuchten model and the Approximate Van Genuchten model are listed in Tables 5.3 and 5.4, respectively.

5.3.3 Staring Soil Classification System

The Staring soil classification system is commonly used in the Netherlands. A distinction between Upper soils and Lower soils is made in the Staring soil classification system. The Upper soils stated in Table 5.5 include sand B1, B2, B3, B4, B5, B6, B7, B8, B9, clay B10, B11, B12, loam B13, B14, and peat B15, B16, B17, B18. The lower soils contain sand O1, O2, O3, O4, O5, O5, O6, O7, sandy clay O8, O9, O10, clay O11, O12, O13, loam O14, O15 and peat O16, O17, O18. The pre-defined parameter sets for the Van Genuchten model and the Approximate Van Genuchten model are summarised in Tables 5.5 and 5.6, respectively.

5.4 Verification of Axisymmetrical Groundwater Flow

The axisymmetric and transient features of the PLAXFLOW program can be verified by modelling a problem of radial flow to a well. Freeze and Cherry (1979) reported that theoretical solutions for predicting the response of ideal aquifers due to pumping are available. Theis (1935) made use of an analogy to heat-flow theory to derive a closed-form solution for evaluating the drawdown in hydraulic head in a horizontal confined aquifer. The drop in hydraulic head at any radial distance from a well at any time after pumping can be obtained from the Theis Solution as follows:

$$h_o - h = \frac{Q}{4\pi T}\int_u^\infty \frac{e^{-u}\,du}{u} \tag{5.8}$$

$$W(u) = \int_u^\infty \frac{e^{-u}\,du}{u} \tag{5.9}$$

$$u = \frac{r^2 S_A}{4T_A t} \tag{5.10}$$

where Q, T_A, S_A, r and t denote the pumping rate of well, transmissivity of aquifer, storativity of aquifer, distance from well axis and pumping time. W(u) is the well function representing the exponential integral.

The problem selected for the validation of axisymmetric and transient features of the PLAXFLOW program is obtained from GEO-SLOPE (1998). The drawdown in hydraulic head of an ideal aquifer is modelled by means of an axisymmetric geometry using the PLAXFLOW program. The aquifer is horizontal and confined between impermeable formations on the top and bottom. It has a constant thickness of 5 m and has a total hydraulic head of 16 m before pumping. A 0.3 m diameter single well that penetrates the entire aquifer is modelled in the finite element mesh. The pumping rate of the well is assumed to be constant at 0.125 m^3/s with respect to time. The ideal

aquifer has a transmissivity of 0.01 m^2/s and a storativity of 0.05. Thus, the permeability of the aquifer is 0.002 m/s. Fully saturated soil behaviour is modelled in the finite element computation using the Saturated material model. Figure 5.1 shows the finite element mesh of the ideal horizontal aquifer. The finite element mesh consists of 536 15-node triangular elements.

Transient analysis is performed with a first time increment of 10 seconds and the time increments increase with a factor of two, until the maximum time increment is 900 seconds is reached. The hydraulic head profile in the horizontal aquifer after 3970 seconds of well pumping is presented in Figure 5.2. Figure 5.3 shows a comparison between the numerical hydraulic heads and those derived from the Theis Solution at Sections X-X and Y-Y. Sections X-X and Y-Y are at radial distances of 4 m and 20 m from the pumping well, respectively. It is found that there is good agreement between the numerical results from the PLAXFLOW program and the Theis solution. Hence, it can be concluded that the PLAXFLOW program can perform axisymmetrical and transient groundwater flow computations with reasonable accuracy.

Table 5.1 Van Genuchten model parameters for Hypres Soil Classification System (Brinkgreve et al, 2003)

Soil Types	θ_r	θ_s	K_s (x 10^{-2} m/day)	g_a (cm^{-1})	g_l	g_n
Upper Soils						
Coarse	0.025	0.403	60.000	0.0383	1.2500	1.3774
Medium	0.010	0.439	12.061	0.0314	-2.3421	1.1804
Medium Fine	0.010	0.430	2.272	0.0083	-0.5884	1.2539
Fine	0.010	0.520	24.800	0.0367	-1.9772	1.1012
Very Fine	0.010	0.614	15.000	0.0265	2.5000	1.1033
Lower Soils						
Coarse	0.025	0.366	70.000	0.0430	1.2500	1.5206
Medium	0.010	0.392	10.755	0.0249	-0.7437	1.1689
Medium Fine	0.010	0.412	4.000	0.0082	0.5000	1.2179
Fine	0.010	0.481	8.500	0.0198	-3.7124	1.0861
Very Fine	0.010	0.538	8.235	0.0168	0.0001	1.0730
Organic	0.010	0.766	8.000	0.0130	0.4000	1.2039

Table 5.2 Approximate Van Genuchten model parameters for Hypres Soil Classification System (Brinkgreve et al, 2003)

Soil Types	ϕ_{ps} (m)	ϕ_{pk} (m)
Upper Soils		
Coarse	-2.37	-1.06
Medium	-4.66	-0.50
Medium Fine	-8.98	-1.20
Fine	-7.12	-0.50
Very Fine	-8.31	-0.73
Lower Soils		
Coarse	-1.82	-1.00
Medium	-5.60	-0.50
Medium Fine	-10.15	-1.73
Fine	-11.66	-0.50
Very Fine	-15.06	-0.50
Organic	-7.35	-0.97

Table 5.3 Van Genuchten model parameters for USDA Soil Classification System (Brinkgreve et al, 2003)

Soil Types	θ_r	θ_s	K_s (x 10^{-2} m/day)	g_a (cm^{-1})	g_l	g_n
Sand	0.045	0.430	712.80	0.145	0.5	2.68
Loamy Sand	0.057	0.410	350.20	0.124	0.5	2.28
Sandy Loam	0.065	0.410	106.10	0.075	0.5	1.89
Loam	0.078	0.430	24.96	0.036	0.5	1.56
Silt	0.034	0.460	6.00	0.016	0.5	1.37
Silty Loam	0.067	0.450	10.80	0.020	0.5	1.41
Sandy Clay Loam	0.100	0.390	31.44	0.059	0.5	1.48
Clayey Loam	0.095	0.410	6.24	0.019	0.5	1.31
Silty Clayey Loam	0.089	0.430	1.68	0.010	0.5	1.23
Sandy Clay	0.100	0.380	2.88	0.027	0.5	1.23
Silty Clay	0.070	0.360	0.48	0.005	0.5	1.09
Clay	0.068	0.380	4.80	0.008	0.5	1.09

Table 5.4 Approximate Van Genuchten model parameters for USDA Soil Classification System (Brinkgreve et al, 2003)

Soil Types	ϕ_{ps} (m)	ϕ_{pk} (m)
Sand	-1.01	-0.50
Loamy Sand	-1.04	-0.50
Sandy Loam	-1.20	-0.50
Loam	-1.87	-0.60
Silt	-4.00	-1.22
Silty Loam	-3.18	-1.02
Sandy Clay Loam	-1.72	-0.50
Clayey Loam	-4.05	-0.95
Silty Clayey Loam	-8.23	-1.48
Sandy Clay	-4.14	-0.55
Silty Clay	-31.95	-0.95
Clay	-21.42	-0.60

Table 5.5 Van Genuchten model parameters for Staring Soil Classification System (Brinkgreve et al, 2003)

Soil Types	θ_r	θ_s	K_s (m/s)	g_a (m^{-1})	g_l	g_n
Sand						
B1	0.02	0.43	2.71E-06	2.340	0.000	1.801
B2	0.02	0.42	1.45E-06	2.760	-1.060	1.491
B3	0.02	0.46	1.78E-06	1.440	-0.215	1.534
B4	0.02	0.46	3.38E-06	1.560	0.000	1.406
B5	0.01	0.36	6.12E-06	4.520	-0.359	1.933
B6	0.01	0.38	1.17E-05	2.220	-1.747	1.238
O1	0.01	0.36	1.76E-06	2.240	0.000	2.286
O2	0.02	0.38	1.47E-06	2.130	0.168	1.951
O3	0.01	0.34	1.26E-06	1.700	0.000	1.717
O4	0.01	0.35	1.14E-06	1.550	0.000	1.525
O5	0.01	0.32	2.89E-06	5.210	0.000	2.374
O6	0.01	0.33	3.93E-06	1.620	-1.330	1.311
O7	0.01	0.51	4.53E-06	1.230	-2.023	1.152
Silt						
B7	0.00	0.40	1.63E-06	1.940	-0.802	1.250
B8	0.01	0.43	2.73E-07	0.990	-2.244	1.288
B9	0.00	0.43	1.78E-07	0.650	-2.161	1.325
O8	0.00	0.47	1.05E-06	1.360	-0.803	1.342
O9	0.00	0.46	2.58E-07	0.940	-1.382	1.400
O10	0.01	0.48	2.45E-07	0.970	-1.879	1.257
Clay						
B10	0.01	0.43	8.10E-08	0.640	-3.884	1.210
B11	0.01	0.59	5.24E-07	1.950	-5.901	1.109
B12	0.01	0.54	6.22E-07	2.390	-5.681	1.094
O11	0.00	0.42	1.60E-06	1.910	-1.384	1.152
O12	0.01	0.56	1.18E-07	0.950	-4.295	1.158
O13	0.01	0.57	5.06E-07	1.940	-5.955	1.089
Loam						
B13	0.01	0.42	1.50E-06	0.840	-1.497	1.441
B14	0.01	0.42	9.26E-08	0.510	0.000	1.305
O14	0.01	0.38	1.75E-07	0.300	-0.292	1.729
O15	0.01	0.41	4.28E-07	0.710	0.912	1.298
Peat						
B15	0.01	0.53	9.41E-06	2.420	-1.476	1.280
B16	0.01	0.80	7.86E-07	1.760	-2.259	1.293
B17	0.00	0.72	5.16E-07	1.800	-0.350	1.140
B18	0.00	0.77	7.72E-07	1.970	-1.845	1.154
O16	0.00	0.89	1.24E-07	1.030	-1.411	1.376
O17	0.01	0.86	3.39E-07	1.230	-1.592	1.276
O18	0.01	0.57	3.99E-07	1.380	-1.204	1.323

Table 5.6 Approximate Van Genuchten model parameters for Staring Soil Classification System (Brinkgreve et al, 2003)

Soil Types	ϕ_{ps} (m)	ϕ_{pk} (m)
Sand		
B1	-1.87	-1.35
B2	-2.32	-0.79
B3	-3.37	-2.18
B4	-3.81	-2.36
B5	-1.31	-0.56
B6	-4.51	-0.70
O1	-1.48	-1.15
O2	-1.79	-1.51
O3	-2.46	-1.93
O4	-3.22	-2.30
O5	-1.11	-0.48
O6	-4.50	-1.18
O7	-9.76	-0.98
Silt		
B7	-4.72	-1.14
B8	-7.03	-1.46
B9	-9.61	-2.33
O8	-4.78	-1.74
O9	-5.89	-2.07
O10	-7.77	-1.59
Clay		
B10	-13.06	-1.47
B11	-9.51	-0.27
B12	-9.61	-0.21
O11	-7.20	-0.76
O12	-11.55	-0.82
O13	-11.45	-0.24
Loam		
B13	-6.19	-2.25
B14	-12.82	-7.09
O14	-20.68	-9.37
O15	-9.30	-14.08
Peat		
B15	-3.77	-0.73
B16	-4.45	-0.82
B17	-8.03	-1.19
B18	-6.98	-0.64
O16	-5.64	-1.86
O17	-6.06	-1.39
O18	-4.63	-1.45

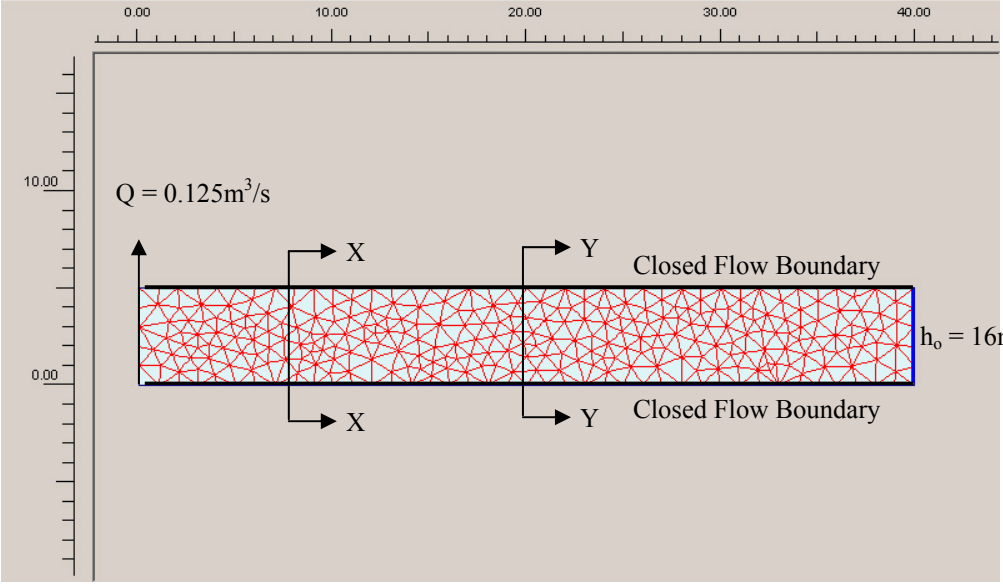

Figure 5.1 Finite element mesh of aquifer

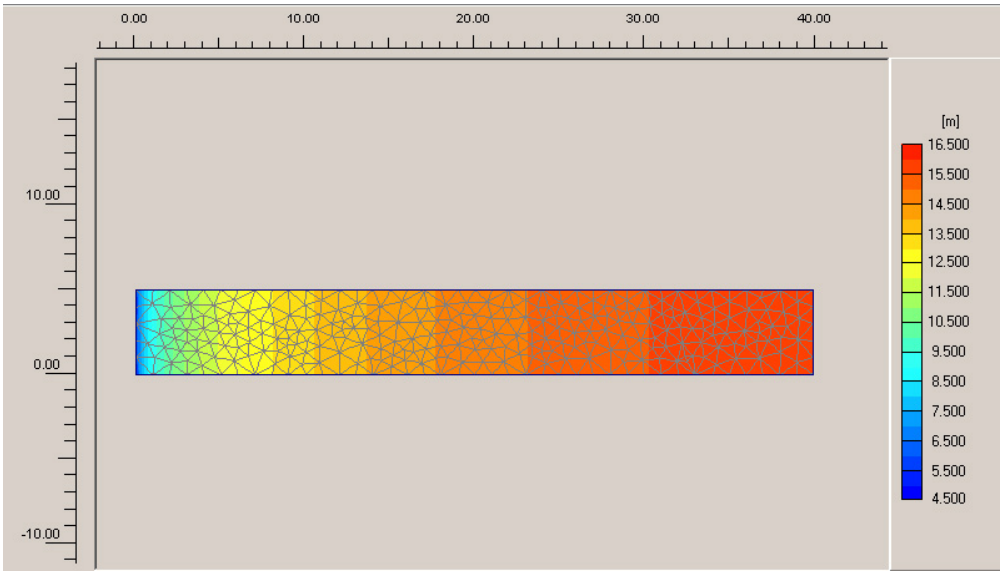

Figure 5.2 Hydraulic head in aquifer after 3970 seconds of pumping

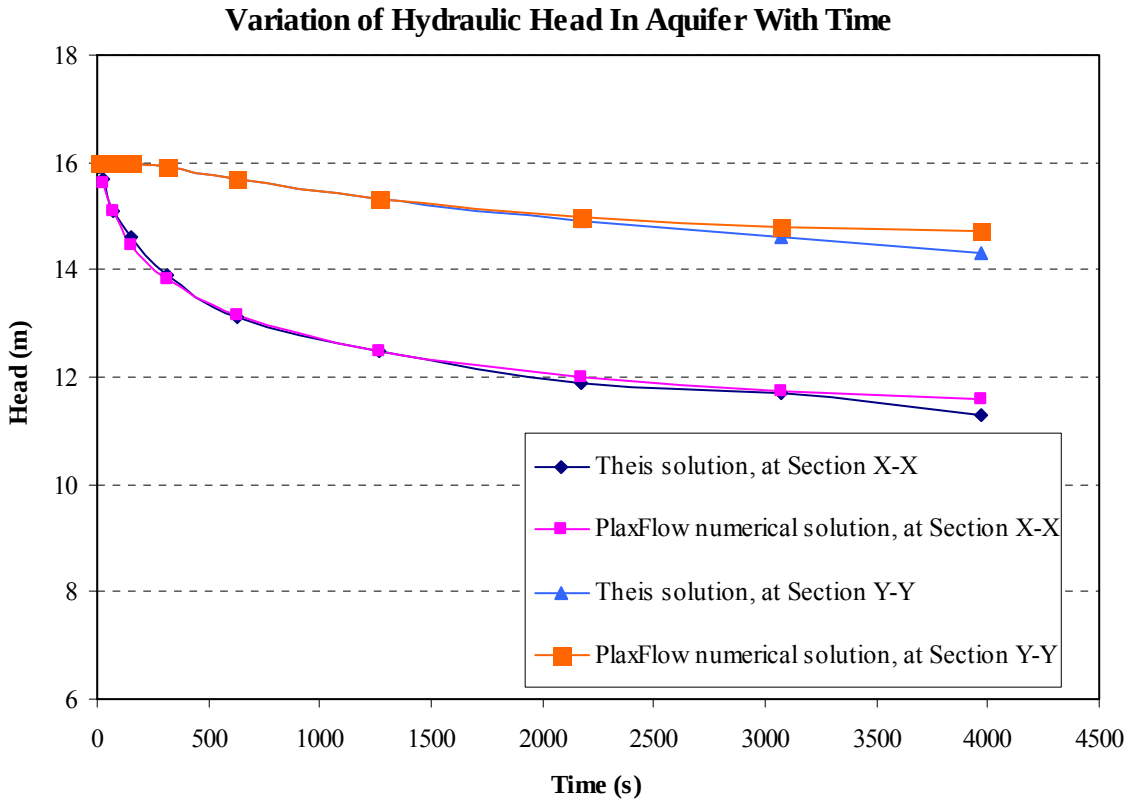

Figure 5.3 Comparison between the PLAXFLOW numerical solution and the Theis solution

CHAPTER 6 FINITE ELEMENT ANALYSIS

6.1 Introduction

Some Hardening-Soil model parameters that are representative of Old Alluvium soils have been determined in Chapter 4. With an understanding of the material models that are available for groundwater flow computations in the PLAXFLOW program, finite element analysis can be performed using the PLAXIS program to simulate the response of the excavation support system for the Influent Pumping Shaft 2 (IPS-2) of the Influent Pumping Station at Changi. A circular concrete diaphragm wall is adopted as the retaining system for the excavation of Influent Pumping Shaft 2 as presented in Chapter 3. Finite element modelling of the excavation is described in detail in this Chapter. Hardening-Soil model parameters for soils at the project site are estimated using the results of soil investigation works described in Chapter 3 and the author also refer to the published results of other researchers summarised in Chapter 2. The development of hoop strains, bending moments and displacements of the shaft wall during the excavation and construction process is carefully examined in this chapter. A convergence analysis is conducted to verify that the finite element solution has converged to an accurate solution. Some limitations of the finite element model are also discussed in this chapter.

6.2 Finite Element Model

As the diaphragm wall of Influent Pumping Shaft 2 is circular in plan and uniform soil stratification is assumed at the project site, the 70 m-deep excavation is considered to be axisymmetrical about the centreline of the excavated area. Hence, the axisymmetrical model of the PLAXIS program is used to simulate the excavation and

construction process. Deformations and stresses in any radial direction of an axisymmetrical finite element model are assumed to be identical. 15-node triangular elements are used to model the soil layers and other volume clusters. These elements provide a fourth order interpolation for displacements and the numerical integration makes use of twelve Gauss points.

The excavation is 40.2 m in diameter. The finite element mesh used in the analysis consists to 1552 15-node triangular elements as shown in Figure 6.1. This finite element mesh is created with reference to the soil stratification at the site, as shown in Figure 3.6, and the excavation support system illustrated in Figure 3.7. In order to improve the accuracy of the numerical solution, finer elements are used near the excavation in the geometry mesh where large changes in stress and movements are expected. It is mentioned in Chapter 2 that the width of the plastic zone determined by Britto and Kusakabe (1983) is approximately 0.4 times the excavation depth for undrained unsupported axisymmetrical excavations. Imamura et al. (2000) reported that the failure zone of shafts, up to 50 m in depth, is approximately 35% of the shaft diameter from the shaft lining. Hence, the side boundary of the geometry model is taken to be 160 m away from the retaining wall, which is more than two times the final excavated depth and is approximately four times its diameter, to avoid any undesirable interactions from fixities at the side boundary of the finite element mesh. A convergence study has been performed to ensure that the finite element solution provided by this geometry mesh has converged and it will be described in the later part of this chapter.

Figure 3.8 reveals that the excavation took 231 days to reach the final excavated depth of 70 m. Consolidation analysis is hence performed to simulate the time-dependent response of the excavation support system. As the development and dissipation of negative excess pore pressures in the soils with time is analysed, the progressive changes in the stresses and strains in the finite element model can be determined. Closed consolidation boundaries are defined at both the vertical boundaries and the bottom boundary of the finite element mesh to restrict water flow across the boundaries. These boundaries represent line of symmetry, impervious bottom soil layer of the finite element mesh and geometric boundaries where consolidation is unlikely to take place across. If these geometric boundaries are not closed, the excess pore pressure at the boundaries is zero and water can flow freely across the boundaries.

As the PLAXIS program cannot perform axisymmetrical groundwater flow calculations, the PLAXFLOW program is used in conjunction with the PLAXIS program to generate groundwater pressures for the finite element analyses, as elaborated in Chapter 5. At each phase of modelling, the PLAXFLOW program is launched using a command button in the PLAXIS program to generate pore pressures for the finite element mesh in PLAXIS. The PLAXIS program then make use of the pore pressures computed by PLAXFLOW for deformation and stability calculations. Apart from the parameters required for deformation and stability analyses in PLAXIS, parameters necessary for steady state, transient, saturated and unsaturated groundwater flow computations in PLAXFLOW can also be inputted in PLAXIS.

Closed flow boundaries are defined at the bottom boundary and the vertical side boundary representing the line of symmetry of the finite element mesh to restrict water

flow across the boundaries during groundwater calculations. Fully saturated soil behaviour of all the soil layers, except the Backfill and the Reclaimed Sand, is modelled in the finite element analysis using the Saturated material model. Groundwater pressures in the Backfill and the Reclaimed Sand are computed using the Approximate Van Genuchten model, adopting predefined material sets for Loamy Sand and Sand from the USDA soil classification system, respectively. All the above have been elaborated in Chapter 5.

Figure 3.6 shows the simplified soil profile at the site while Figure 3.7 presents the actual dimensions of Influent Pumping Shaft 2. The behaviour of soil layers is simulated using the Hardening-Soil constitutive model. The concrete diaphragm wall and internal concrete ring walls of Influent Pumping Shaft 2 are modelled as non-porous elastic materials. Both the shaft wall and the ring walls are modelled as volume clusters in the finite element mesh to account for their actual dimensions. In order to output the structural stresses in the shaft wall, a flexible plate element is placed in the middle of the wall. This flexible plate has a flexural stiffness and axial stiffness that are reduced by 10^7 times the actual stiffness of the shaft wall. Hence, the flexible plate will not affect the rigidity of the wall. A factor of 10^7 has to be applied to the structural forces generated by the flexible plate element to obtain the actual magnitude of the forces and moments acting on the circular shaft wall. This method of placing a flexible plate in a volume wall cluster to output structural forces is recommended by PLAXIS (1999).

Interfaces are used in the finite element mesh to simulate the soil-structure interaction between the excavation support system and the adjacent soil. In general, the wall

friction and cohesion of real soil-structure interaction is weaker than its adjacent soil. Hence, the wall friction and cohesion are modelled in the finite element mesh using an interface strength, R_{inter}, which relates the strength of the interface to the soil strength as follows:

$$c_i = R_{inter}\, c_{soil} \quad (6.1)$$

$$\tan \phi_i = R_{inter} \tan \phi_{soil} \quad (6.2)$$

where c_i, ϕ_i, c_{soil}, and ϕ_{soil} represent the cohesion and friction angle of the interface and the soil, respectively.

BS8002 recommends a value of 75% of design undrained soil strength for the mobilised wall friction. However, Tan (2000) suggested using wall interface strength in the range of 0.8 to 1.0 to simulate soil-structure interaction between concrete and sandy soils. Hence, in the present study, a value of 0.8 for the interface strength is adopted to model the contact between the concrete shaft wall and its adjacent soils, as suggested by Tan (2000).

6.3 Finite Element Analysis

As mentioned earlier, the excavation carried out for the Influent Pumping Shaft 2 is analysed using the consolidation analysis. Times taken for each excavation stage, installation of internal ring walls and time lags when there was no excavation are considered in the consolidation analysis. The time sequence of excavation and ring wall construction for Influent Pumping Shaft 2 is summarised in Table 6.1. There are eight excavation stages and seven stages of casting of ring walls. The internal ring walls are cast in various lifts in each installation stage. Details of the installation of ring walls have been described in Chapter 3. The time, from the commencement of the

excavation of Influent Pumping Shaft 2, at which the various lifts of ring walls are cast are summarised in Table 6.2. A uniform surcharge of 15 kN/m^2, specified by the excavation designer, is applied in the area of 10 m behind the diaphragm wall to account for loads that arises from construction equipment and materials.

In order to obtain representative soil parameters at the project site, references have been made to the site investigation works, publications on Old Alluvium soils by other researchers summarised in Chapter 2 and important relationships obtained from the finite element simulation of oedometer and consolidated undrained triaxial tests in Chapter 4. As mentioned in Chapter 3, standard penetration tests were performed in BH 1 and BH 2 and the horizontal permeability of Clayey Sand layer is determined. As consolidation finite element analysis requires effective stress parameters as inputs, the strength parameters recommended by Li and Wong (2001) serve as a basis for the strength parameters adopted in the finite element analysis. Over-consolidation ratios (OCR) of the Old Alluvium soils are computed using an approximate relationship proposed by Li and Wong (2001), as shown in Equation 2.2. This relationship correlates the over-consolidation ratio of Old Alluvium to their SPT N-value and effective in-situ overburden pressure.

Table 6.1 Excavation and construction sequence of IPS-2

Stage	Event	Reduced Level (m)		Time Taken (Days)	No of Days From Commencement of Excavation
		From	To		
1	Excavation of Backfill for the Lowering of General Ground Surface	105.0	103.0	-	-
2	Installation of Diaphragm Wall	102.0	29.5	-	0
3	1st Excavation	103.0	89.0	14	14
4	No Activity			19	33
5	Casting of 1st Ring Wall	102.0	90.5	18	51
6	No Activity			6	57
7	2nd Excavation	89.0	81.0	10	67
8	No Activity			7	74
9	Casting of 2nd Ring Wall	88.0	82.5	8	82
10	No Activity			2	84
11	3rd Excavation	81.0	71.4	7	91
12	No Activity			5	96
13	Casting of 3rd Ring Wall	80.0	73.0	8	104
14	No Activity			4	108
15	4th Excavation	71.4	63.4	8	116
16	No Activity			9	125
17	Casting of 4th Ring Wall	73.0	65.0	20	145
18	No Activity			3	148
19	5th Excavation	63.4	54.5	8	156
20	No Activity			4	160
21	Casting of 5th Ring Wall	63.0	56.0	8	168
22	No Activity			3	171
23	6th Excavation	54.5	47.1	8	179
24	No Activity			4	183
25	Casting of 6th Ring Wall	56.0	48.5	12	195
26	No Activity			2	197
27	7th Excavation	47.1	39.3	6	203
28	No Activity			5	208
29	Casting of 7th Ring Wall	48.5	41	14	222
30	No Activity			4	226
31	8th Excavation	39.3	33.0	5	231

Table 6.2 Date of casting of ring walls

Ring Wall	Lift	Reduced Level (m)		Day, From Commencement of Excavation
		From	To	
1st	5th	102.0	100.6	51
	4th	100.6	98.1	48
	3rd	98.1	95.6	44
	2nd	95.6	93.1	40
	1st	93.1	90.5	34
2nd	3rd	88.0	86.6	82
	2nd	86.6	84.6	79
	1st	84.6	82.5	75
3rd	3rd	80.0	78.1	104
	2nd	78.1	75.6	100
	1st	75.6	73.0	97
4th	4th	73.0	71.6	145
	3rd	71.6	70.1	137
	2nd	70.1	67.6	133
	1st	67.6	65.0	126
5th	3rd	63.0	61.1	168
	2nd	61.1	58.6	165
	1st	58.6	56.0	161
6th	4th	56.0	54.6	195
	3rd	54.6	53.6	190
	2nd	53.6	51.1	187
	1st	51.1	48.5	184
7th	4th	48.5	47.1	222
	3rd	47.1	46.1	216
	2nd	46.1	43.6	213
	1st	43.6	41.0	209

The undrained shear strength, c_u, of the various soil layers can deduced from their SPT N-values by using the correlations recommended by Orihara and Khoo (1998) and Li and Wong (2001). Their stiffness modulus can then be determined from correlations, which relate the undrained stiffness to their undrained shear strength, proposed by Dames and Moore (1983) and Sharma et al. (1999). The following correlations are adopted for the soils at the project site.

Table 6.3 Correlations used for determination of soil parameters

Soil Type	k, where c_u = k SPT N-values	$\frac{E_u}{c_u}$
Reclaimed Sand	5	225
Silty Sand 1	4	200
Clayey Sand	4	200
Silty Sand 2	4	200
Silty Sand 3	5.4	300

Once the undrained stiffness modulus of the soils is established, their effective stiffness modulus can be determined. The reference secant stiffness modulus, E_{50}^{ref}, can be calculated from the effective stiffness modulus of the soils using Equation 4.4. From the findings obtained in Chapter 4, equal value for the reference secant stiffness modulus, E_{50}^{ref}, and the reference tangential oedometer stiffness modulus, E_{oed}^{ref}, is adopted in the finite element analysis. The ratio of reference unloading stiffness modulus to reference secant stiffness modulus of Old Alluvium soils is found to fall in the range of 3.7 to 9.7, as listed in Table 4.3. Hence, the reference unloading stiffness modulus is taken to be four times of the reference secant stiffness modulus in the present study.

The permeabilities adopted for the various Old Alluvium soil layers fall within the range proposed by earlier researchers, as described in Chapter 2. In accordance to Sharma et al. (1999), the vertical permeability of Old Alluvium soils is assumed to be smaller than the horizontal permeability by a factor of 3. The stiffness of concrete shaft wall and ring walls are determined from their average cube strength, mentioned in Chapter 3, according to BS 8110 (1985a). The proposed soil parameters are listed in Table 6.4 and Table 6.5 while the structural properties of the diaphragm wall and ring

walls are summarised in Table 6.6. The reduced flexural stiffness and axial stiffness of the flexible plate in the diaphragm wall are given in Table 6.7.

Table 6.4 Proposed soil parameters I

Soil Type	γ_{unsat} (kN/m^2)	γ_{sat} (kN/m^2)	c'	ϕ'	ψ	k_h (m/s)	k_v (m/s)	OCR
Backfill	16.9	20.5	1	28	0	1.00E-7	1.00E-7	1.00
Reclaimed Sand	16.9	20.5	1	30	0	1.00E-5	1.00E-5	1.00
Silty Sand 1	17.3	20.7	6	35	5	1.00E-7	3.33E-8	7.63
Clayey Sand	17.4	20.8	8	36	6	5.83E-9	1.94E-9	4.44
Silty Sand 2	17.3	20.7	10	36	6	1.00E-9	3.33E-10	3.43
Silty Sand 3	17.3	20.7	20	36	6	1.00E-10	3.33E-11	2.03

Table 6.5 Proposed soil parameters II

Soil Type	E_{50}^{ref} (kN/m^2)	E_{oed}^{ref} (kN/m^2)	E_{ur}^{ref} (kN/m^2)	p^{ref} (kN/m^2)	m	ν_{ur}'	R_f
Backfill	10000	10000	10000	100	0.6	0.2	0.9
Reclaimed Sand	15700	15700	62800	100	0.5	0.2	0.9
Silty Sand 1	16700	16700	66800	100	0.6	0.2	0.9
Clayey Sand	15800	15800	63200	100	0.6	0.2	0.9
Silty Sand 2	16800	16800	67200	100	0.6	0.2	0.9
Silty Sand 3	35400	35400	141600	100	0.6	0.2	0.9

Table 6.6 Material properties of excavation support system

Wall Type	γ (kN/m^3)	E (kN/m^2)	ν
Diaphragm Wall	24	3.72E7	0.2
Ring Wall	24	3.54E7	0.2
Guide Wall	24	2.01E7	0.2

Table 6.7 Properties of flexible plate

Wall Type	EA (kN/m)	EI (kNm^2/m)	ν
Flexible Plate	4.47	0.54	0.2

Arrizumi et al. (1999) highlighted the importance of temperature in influencing the wall displacement and circumferential stresses. The temperature variation inside the third lift of the first stage of ring wall installation was monitored for 232.5 hours after casting. This lift of ring wall is located from a Reduced Level of 98.1 m to 95.6 m, with a depth of 2.5 m. Five thermocouple sensors are placed at centre of the section mid-height of the lift, as shown in Figure 6.2. The mean temperature inside the lift is obtained by averaging the readings from the five thermocouples. The variation of average temperature with time inside the lift is plotted in Figure 6.3. The influence of temperature variation in the ring walls is considered in the finite element analysis. Since only the temperature variation at the third lift of first stage installation of ring wall was monitored, the temperature changes at other lifts of ring walls are assumed to be similar to the measured temperature variation.

According to Mindess and Young (1981), fresh concrete is fluid-like in nature. Hydration of cement takes place and this results in the setting and hardening of concrete. Setting describes the onset of rigidity in fresh concrete while hardening is defined as the development of useful strength. Figure 6.4 illustrates the process of setting and hardening of concrete. Initial set is the state of concrete where it is beginning to stiffen considerably whereas final set is the state of concrete where it has hardened to a point at which it can sustain some load. A transitional period exists between the states of true fluidity and true rigidity.

Since the PLAXIS program cannot model thermal interactions, the author proposes a method of modelling the temperature effects of ring walls on the diaphragm wall. La Londe and Janes (1961) have mentioned that unrestrained concrete expands during an increase in temperature and contracts during a decrease in temperature. However, due to the rigidity of the circular shaft wall and high stiffness of Old Alluvium soils, expansion and contraction of internal ring walls are believed to be restricted by the diaphragm wall. Thus, stresses are applied on the ring walls by the diaphragm wall to prevent circumferential volumetric changes of the ring walls. The same amount of reaction stresses will be applied onto the diaphragm wall. Thus, the temperature effects of ring wall on the retaining wall can be represented by equivalent stresses acting on the diaphragm wall.

Formulas relating stresses and the corresponding changes in dimensions for axisymmetrical structures are provided by Young and Budynas (2002). Equation 6.3 is given by Young and Budynas (2002) to compute the change in radius of a cylindrical vessel induced by a uniform radial pressure. The change in radius of the ring wall due to temperature variations can be computed with the availability of the coefficient of thermal expansion of concrete from many design codes. The uniform radial pressure, which would have acted on the ring wall to cause the corresponding change in radius, can then be determined. Thus, this pressure would be applied by the shaft wall to prevent the free expansion and contraction of the internal ring wall. As a result, a reaction pressure of equal magnitude is applied on the shaft wall to model the thermal effects of the ring wall. Equation 6.4 has been derived to compute the equivalent radial stress, q_t, acting on the diaphragm wall due to a change in temperature in the ring wall.

$$\Delta R = \frac{q_t R^2}{Et} \tag{6.3}$$

$$q_t = \frac{\alpha_c \Delta T \, Et}{R} \qquad (6.4)$$

where α_c, ΔT, E, t, R and ΔR represent the coefficient of thermal expansion of concrete, change in temperature, stiffness of ring wall at a particular time after casting, wall thickness, radius and change in radius of ring wall, respectively.

The FIP (1984) suggested a recommended value of 10 x $10^{-6}/^{o}C$ for the coefficient of thermal expansion of concrete. Both BS 8110 (1985b) and AS 3600 (1994) reported that the coefficient of thermal expansion of concrete varies over a range of values and is dependent on the type of aggregate, cement paste and the degree of saturation of concrete. BS 8110 (1985b) and AS 3600 (1994) also mentioned that the coefficient of thermal expansion of concrete is approximately 2 x $10^{-6}/^{o}C$ lesser than partially dry concrete. These coefficients of thermal expansion of concrete are adopted in the computation of equivalent stresses acting on the diaphragm wall due to the temperature variation inside the ring wall.

Table 6.8 presents the equivalent thermal stresses computed using Equation 6.4. As fresh concrete is partially fluid-like in nature and has not gained strength during the first few hours of casting, the equivalent stresses are nearly zero, according to Equation 6.4, although the temperature inside the ring walls increases rapidly. Thermal stresses are only calculated after the concrete has gained rigidity, which is approximately 14 hours after casting. As cube strength tests for concrete ring walls were conducted at various days after casting by the builder of the Influent Pumping Station, the stiffness of ring walls at various times is determined and inputted into Equation 6.4 to compute the equivalent radial stress, q_t, acting on the diaphragm wall. Expansion of the internal ring walls results in the equivalent thermal stresses acting radially towards the retained

side of the excavation whereas contraction of ring walls bring about stresses which act radially towards the excavated side.

Table 6.8 Equivalent stresses acting on diaphragm wall

Day	Thermal Stresses (kN/m^2)
2	120
3	48
4	-51
5	-139
6	-236
7	-288
8	-323
9	-380
10	-402

6.4 Results and Observations

The instrumentation plan for Influent Pumping Shaft 2 (IPS-2) is shown in Figure 3.4. Strain gauges are installed at twelve elevations of three diaphragm wall panels of Influent Pumping Shaft 2 as shown in Figure 3.3. The three panels are S4, S12 and S20, respectively. Panel S20 is located near Influent Pumping Shaft 1 (IPS-1) while Panel S20 is closer to the Coarse Screen Shaft (CCS). These strain gauges are placed on the steel reinforcements of the shaft wall to monitor its hoop and flexural strains, which develop during the excavation and construction works. The development of hoop strains, bending moments and deflections of the diaphragm wall will be studied. Table 6.9 lists the positions of the strain gauges.

Comparisons between the predicted and measured hoop strains of the diaphragm wall of Influent Pumping Shaft 2 are shown in Figures 6.5 to 6.10. As there are some irregularities in the measured hoop strains during the first fourteen days of excavation

of Influent Pumping Shaft 2, measured hoop strains that are computed from the fourteenth day of excavation are compared with the numerical results. By adopting a convention that hoop compression of the circular shaft wall is denoted by negative values of hoop strains, an increase in negative values of the hoop strains means that the wall has developed greater compressive hoop strains.

Table 6.9 Location of strain gauges

Level of Strain Gauge	Reduced Level (m)	Depth from Final Ground Surface Level (m)	Position	Adjacent Soil Layer
A	99	4	Behind 4th lift of 1st Ring Wall	Reclaimed Sand
B	93	10	Behind 1st lift of 1st Ring Wall	Reclaimed Sand
C	87	16	Behind 3rd lift of 2nd Ring Wall	Silty Sand 1
D	82	21	Below 1st lift of 2nd Ring Wall	Clayey Sand
E	75	28	Behind 1st lift of 3rd Ring Wall	Silty Sand 2
F	69	34	Behind 2nd lift of 4th Ring Wall	Silty Sand 2
G	62	41	Behind 3rd lift of 5th Ring Wall	Silty Sand 2
H	57	46	Behind 1st lift of 5th Ring Wall	Silty Sand 3
I	51	52	Behind 1st lift of 6th Ring Wall	Silty Sand 3
J	45	58	Behind 2nd lift of 7th Ring Wall	Silty Sand 3
K	40	63	Below1st lift of 7th Ring Wall	Silty Sand 3
L	33	70	No Adjacent Ring Wall	Silty Sand 3

It is apparent from Figures 6.5 to 6.10 that the hoop strains recorded at the same elevation of the three panels, S4, S12 and S20, have different magnitudes. This could be due to deviation from the assumed soil profile as Old Alluvium soils are known to

be highly variable, vertically as well as laterally. The hoop strains recorded at the same elevations of the three panels show similar trends, despite of their different relative positions, to the two neighbouring shafts. It can be observed from the site measurements of hoop strains that they generally reflected the excavation process that was carried out above and at the vicinity of the elevation of the strain gauges. This phenomenon is best observed from the measured hoop strains at Level L. The strain gauge at Level L is located 33 m below the final ground surface level. It can be observed from Figure 6.10 that the wall developed negative compressive hoop strains significantly during the periods of time when the eight excavations stages above Level L are carried out. There are little changes in the hoop strains at Level L during the periods where there was no excavation.

The measured hoop strains at other elevations also reflected the excavation stages that are carried out above their elevations. Excavation stages that are conducted at greater depths below the strain gauge levels appeared to have diminishing effects on the development of hoop strains. Soil inside the excavated area, near strain gauge Level A and Level B, are removed during the first excavation stage. It is apparent from Figure 6.5 that the strain gauges at both Level A and Level B showed an increase in the compressive hoop strains between the first and second excavation stages. Strain gauge at Level A did not register an increase in hoop stains during the second excavation stage but an increase in hoop strains during the second excavation stage occurred at Level B.

Soils within the excavated area, adjacent to strain gauge at Level C, are removed during the second excavation. The measured strain gauge reflected the increase in hoop

strains due to the second excavation. However, it is evident in Figure 6.6 that the hoop strains at Level C increased significantly before the third excavation stage and they do not increase further due to the later excavation stages. Strain gauge at Level D has showed a significant increase in hoop compression between the second and third excavation stages and between the third and fourth excavation stages. It is observed from Figure 6.7 to Figure 6.10 that the compressive hoop strains at those elevations increased when excavation stages above their elevations were carried out. However, increase in hoop strains are also observed when no excavation activity was carried out and the hoop strains tend to stabilise during the later excavation stages.

Careful examination of measured hoop strains has shown that the shaft wall has gained compressive strains at other times, which do not correspond to the periods when excavations are carried out. The increases in hoop stress may be induced by the thermal effects of the ring wall. This phenomenon can be best illustrated by considering the hoop strains at Level A, Level B, Level G and Level H as these two pairs of strain gauges are installed behind the same segments of ring walls.

Strain gauges at Levels A and B are located behind the fourth lift and first lift of the first segment of ring wall respectively. It can be observed from Figure 6.5 that the hoop strain at Level A decreased sharply around the 41st, 45th and 49th day after the commencement of the excavation of Influent Pumping Shaft 2. This is followed by an increase in compressive hoop strain in the wall at Level A at the 49th day after the commencement of excavation. It is apparent that the hoop strain at Level B decreased suddenly around the 35th day before the hoop strain became more negative

significantly. These sudden decreases in hoop strains occurred soon, but not immediately, after the lifts of the first ring wall are cast.

Such changes in hoop strains may be due to temperature variation of the lifts of ring walls after they are cast as the second, third and fourth lifts of the first segment of ring wall are cast at the 40^{th}, 44^{th} and 48^{th} day respectively. It is postulated by the author that the rise in temperature in the concrete lifts due to hydration of Portland cement results in the tendency for the concrete to expand. As this expansion is restrained by the rigid diaphragm wall and stiff Old Alluvium soils, it induces equivalent stresses acting on the circular diaphragm wall as mentioned earlier. It is evident from Figures 6.5 to 6.10 that the decrease in hoop strains did not occur as soon as the lifts of ring wall were cast. This phenomenon could be due to the fluid-like nature of concrete after mixing and hence, the concrete has not set and attained structural strength to exert thermal forces on the diaphragm wall. The observation, which the increase in compressive hoop strains of the diaphragm wall at Level B occurred before the increase of hoop strains at Level A, further supports the author's proposal that the increase in compressive strains are manifestations of thermal effects of the ring wall as the lift adjacent to Level B is placed before the lift adjacent to Level A. These increases in compressive strains of the wall are due to the drop in temperature inside the ring wall, as shown in Figure 6.3.

Similar trends have been observed for the plots of hoop strains of the diaphragm wall at Levels G and H. Strain gauges at these levels are located behind the third lift and first lift of the fifth segment of ring wall respectively. The diaphragm wall developed compressive hoop strains significantly during the periods when the excavation stages

above the strain gauges are carried out. The lift adjacent to strain gauge at Level H is placed a few days before the placement of the lift near the strain gauge at Level G. An increase in compressive hoop strains of the diaphragm wall at Level H also occurred before the increase of hoop strains at Level G during the period of casting of lifts for the fifth segments of ring wall. Hence, the postulation of changes in hoop strains of the shaft wall due to thermal variation of internal ring walls appears reasonable.

The influence of temperature changes of ring walls on the shaft wall is modelled in the PLAXIS program using the method proposed by the author in the earlier part of this chapter. Figures 6.5 to 6.10 present the measured hoop strains and predicted hoop strains by the finite element analyses with temperature change considerations. It can be seen that the finite element analysis, which accounted for the thermal effects of ring walls, provides a better prediction of the hoop strain development as compared to the finite element analysis that does not consider the thermal effects. Although the strain gauge at Level D is 0.5 m below the second segment of ring wall and 3 m above the third segment of ring wall, the increase in compressive strains of the wall due to the temperature effects of installation of the ring walls can also be accounted for, as shown in Figure 6.6. If the temperature effects on ring wall on the shaft wall are not account for, the predicted hoop stresses will not be conservative and may result in an unsafe design for a circular shaft wall with internal ring walls that are cast in-situ.

Undrained and drained finite element analyses are performed to study the effects of consolidation on the response of the excavation support system. Comparisons between the undrained, consolidation and drained finite element computations on the development of hoop strains of the circular shaft wall are presented in Figures 6.11 to

6.14. Excavation of the Influent Pumping Shaft 2 can only be carried out to a depth of 54.55 m in the drained analysis as the soil in the finite element analysis has collapsed due to heaving of excavated area. Figure 6.15 shows the plastic points that would have occurred if this excavation were carried out in drained conditions. The soils beneath the excavated area fail in tension. It is observed from Figures 6.11 to 6.14 that the undrained hoop strains form the upper limits while the drained hoop strains form the lower limits of this excavation problem. The time-dependent consolidation effects are prominent as the numerical hoop strains become less compressive during the periods where no excavation is carried out and approach the drained solution. In other words, the circular shaft wall would experience a decrease in hoop compression due to consolidation effects, if failure were not reached. This consolidation-induced change in hoop compression strain can be observed in many of the measured and predicted hoop strain variations. However, the change in hoop strains is negligible when the wall is adjacent to soils with very low permeability, such as the Silty Sand 3 layer.

There were drifts in readings measured by some strain gauges, that were placed inside the diaphragm wall to measure flexural strains, at various days of the excavation and some of them had to be re-initialised from time to time. Hence, it is difficult to establish the trend of bending moment changes with excavation depth. The variations of measured and predicted bending moments of the diaphragm wall with depth at Day 57 and Day 84 of the excavation are plotted in Figure 6.16. It is apparent that there are significant differences between the measured and predicted bending moments. Both hogging and sagging moments are observed at many different elevations. Since bending moments are computed using strain gauges data, they are derived values.

Hence, they tend to be not as reliable as the hoop strain data as hoop strains are primary values that are obtained from the instruments directly.

Figure 6.17 shows the measured and predicted diaphragm wall deflections at Day 104 and Day 218 of the excavation at Influent Pumping Shaft 2. I1 and I3 are wall inclinometers. As deformations of the diaphragm wall were measured by insert-type inclinometers that assume the deflection at the bottom of the wall is zero, the predicted wall deflections are adjusted accordingly. It can be observed that the predicted wall deflections agree fairly well with the measured deflections.

6.5 Zone of Influence

The influence of the excavation of Influent Pumping Shaft 2 on the retained soil stresses at the final excavation depth is illustrated in Figure 6.18. The radial, vertical and circumferential stress in the soil continuum at Level D, Level G and Level L are considered. The stress variations are plotted in Figure 6.18. It can be observed that the radial stresses in the soil continuum decreases with decreasing radius from the shaft wall where the circumferential stress increases with decreasing radius from the shaft wall. The vertical stress tends to increase with decreasing radius, with the exception at Level D.

It is apparent from Figure 6.18 that the percentage changes in soil stresses increase with depth. The change in soil stresses is most significant within one diameter from the shaft wall. This zone of influence is higher than that proposed by Britto and Kusakabe (1982) and Imamura et al. (2000). It is mentioned in Chapter 3 that the nearest distance between the diaphragm walls of Influent Pumping Shaft 2 and Influent Pumping Shaft

1 is 18.4 m while the closest distance between diaphragm walls of Influent Pumping Shaft 2 and Coarse Screen Shaft is 23.8 m. It is apparent that the distances between the shaft walls are approximately one diameter of the shafts. Thus, excavations at Influent Pumping Shaft 1 and Coarse Screen Shaft would most probably be affected by the excavation at Influent Pumping Shaft 2.

6.6 Convergence Study

When a finite element mesh is refined repeatedly, the finite element solution would theoretically converge to the exact solution of the problem. There are a few types of refinement in checking the convergence of a finite element solution. They are the H-refinement, the P-refinement and the R-refinement. The H-refinement method requires the use of a finer mesh with more elements, P-refinement refers to the use of higher order elements in the geometry mesh and R-refinement refers to the rearrangement of nodes in the finite element mesh. P-refinement is not applicable in the present study as the higher-order 15-node element is used in the finite element model. Hence, H-refinement is performed to check the convergence of the results of finite element analysis. The number of elements in the finite element mesh is increased from 1552 to 3125. Figure 6.19 show a comparison of the time-dependent hoop strain development using the two mesh densities. It is evident that the finite element solution has converged and the coarser mesh with 1552 15-node elements is adequate in simulating the behaviour of the circular shaft.

6.7 Limitations of Finite Element Model

It is apparent from Figures 6.5 to 6.10 and Figures 6.16 to 6.17 that discrepancies between the measured and numerical results are present. Some assumptions have been made in the finite element modelling of the excavation and there are factors that cannot be considered in the finite element simulation. These assumptions and factors may influence the response of excavation of a vertical shaft and they are discussed in this section.

6.7.1 Soil Stratification

The simplified soil profile obtained from BH1 and BH2, illustrated in Figure 3.6, is considered to be representative of the soil stratification at the project site. Thickness of the various soil layers is assumed to be uniform in the finite element model. Literature review of earlier research carried out on Old alluvium confirms that it is a highly variable formation, in terms of its composition, weathering and geotechnical properties. Thus, the assumption of uniform thickness and adoption of same geotechnical properties, listed in Tables 6.4 and 6.4, for the entire soil layers might not be applicable for the modelled area of the project site. The thickness and geological properties of the various soil layers are likely to defer at different panels of the diaphragm wall of Influent Pumping Shaft 2. Although the finite element results agree reasonably well with the instrumented results, the variation of soil thickness and properties are likely to affect the development of stresses and deformations of the excavation support system and might contribute to the discrepancies between measured and predicted results.

6.7.2 Interaction Effects Between Shafts

Excavations at Coarse Screen Shaft and Influent Pumping Shaft 1 are carried out, 46 days and 118 days respectively, after the commencement of excavation at Influent Pumping Shaft 2. The excavation sequence of the shafts is presented together with the predicted and measured hoop strains in Figures 6.5 to 6.10. Due to the close proximity of the three shafts, the zones of influence due to excavation of the shafts are expected to overlap. Similar effects, as shown in Figure 6.18, are likely to occur during the excavations at Influent Pumping Shaft 1 and Coarse Screen Shaft. Hence, the radial soil stresses in between the three shafts might be further reduced and the vertical and circumferential soil stresses between the shafts might be further increased when excavations at Influent Pumping Shaft 1 and Coarse Screen Shaft were conducted. These changes in soil stresses and the corresponding changes in soil stiffness are likely to affect the development of structural forces and movements of Influent Pumping Shaft 2. The true extent and significance of interaction effects on the response of the three shafts can only be studied more accurately using a three-dimensional numerical software such as ABAQUS, CRISP and FLAC.

However, it can be observed from Figures 6.5 to 6.10 that the hoop strains measured by strain gauges at the same elevation of Influent Pumping Shaft 2 have similar trends, despite of their different positions relative to the neighbouring shafts. Panel S20 is located near Influent Pumping Shaft 1 while Panel S20 is closer to the Coarse Screen Shaft. It is apparent that changes in the measured hoop strains in the diaphragm wall of Influent Pumping Shaft 2, when the neighbouring excavations are carried out, seem to be negligible and are not as significant as the substantial development of hoop strains during its excavation and ring wall construction stages. This may be due to the

additional rigidity provided by internal ring walls as excavations at neighbouring shafts, to the depths where the strain gauges are located, are usually carried out after the ring walls at Influent Pumping Shaft 2 are constructed. The changes in soil stresses and stiffness due to the interaction of the shafts are likely to be distributed to both the diaphragm wall and internal ring walls such that the effects on the diaphragm wall is reduced.

Hence, although interaction effects of the shafts cannot be examined in the axisymmetrical finite element analysis, it is apparent that the adoption of such analysis in modelling the excavation and construction phases at Influent Pumping Shaft 2, together with the simulation of thermal effects, is adequate in predicting the major trends in the behaviour of this circular excavation supporting system.

6.7.3 Simulation of thermal effects

Discrepancies between the predicted and measured increase in compressive stresses induced by the temperature effects of ring wall are present. These discrepancies may be due to the usage of the assumed value for coefficient of thermal expansion of concrete. The coefficient of thermal expansion of concrete varies over a range of values and is dependent on the type of aggregate, cement paste and the degree of saturation of concrete. The temperature variation in the third lift of the first ring wall installation stage is adopted for all the lifts of other ring walls. The temperature inside each lift may vary as the thermal properties of concrete and insulating conditions changes. Thus, the actual thermal stresses acting on the diaphragm wall may not be similar to the stresses adopted, as shown in Table 6.8, which are derived based on the assumed coefficient of thermal expansion of concrete and temperature variation. As

the temperature variation of the third lift of the first ring wall installation stage was only monitored for the first 232.5 hours after casting, thermal stresses acting on the diaphragm wall after the first 232.5 hours after casting cannot be determined and included in the finite element analysis.

As temperature differences between the ring walls, diaphragm wall and the surrounding soils exist, there are complex thermodynamics transfers between the ring walls, diaphragm wall and surrounding soil. The complicated interactive effects of thermal transfer between the ring walls and diaphragm wall and between the diaphragm wall and soil cannot be accounted for in the finite element analysis. These phenomenons are likely to complicate the development of volumetric changes and hoop strains in the internal ring walls and diaphragm wall and result in the discrepancies between the numerical and measured results.

6.7.4 Shrinkage and Creep of Concrete

Shrinkage occurs in concrete and it results in a decrease of concrete volume with time. This reduction in volume occurs due to physico-chemical changes and changes in moisture content of the concrete and generally, it can be classified into drying shrinkage, autogenous shrinkage and carbonation shrinkage. Concrete also exhibit creep behaviour and its strain increases with time due to sustained stress. These effects of shrinkage and creep of concrete cannot be accounted for in the finite element modelling using PLAXIS and may affect the development of hoop strains and contribute to some discrepancies between the numerical and measured hoop strains.

6.7.5 Strain gauges

Vibrating wire strain gauges are spot welded to the surface of steel reinforcement in the diaphragm wall. Sensors are mounted atop of the strain gauges and readings are obtained from a data logger. Drifts and loss of calibration in strain gauges with time and temperature and inaccuracy of readings due to imperfect bonding and non-uniformity between the strain gauge and steel reinforcement are common problems occurring in these instruments and they are plausible causes of discrepancies between the numerical and the measured hoop strains.

6.8 Summary

The temperature variation due to hardening of internal concrete ring walls is found to be an important factor that influences the response of a circular vertical shaft, which has cast in-situ ring walls. A method to calculate equivalent stresses to model the thermal effects of ring walls has been proposed and successfully implemented. The predicted hoop strains and wall deflection agree fairly well to the measured hoop strains and deflections of the diaphragm wall. It is evident that the design of a circular vertical shaft with cast in-situ internal ring walls would not be conservative if the thermal effects of ring walls were not accounted for. The assumptions and limitations of the finite element model in simulating the behaviour of a circular excavation support system are also discussed.

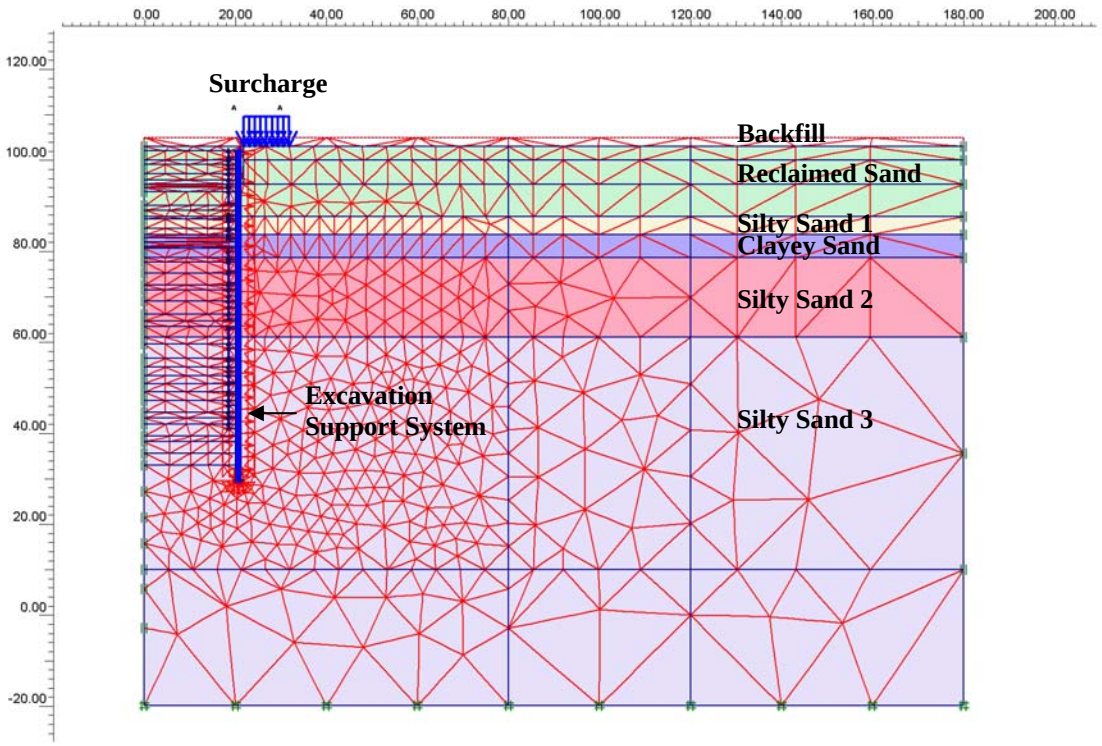

Figure 6.1 Finite element mesh for excavation at Influent Pumping Shaft 2 (1552 15-node triangular elements)

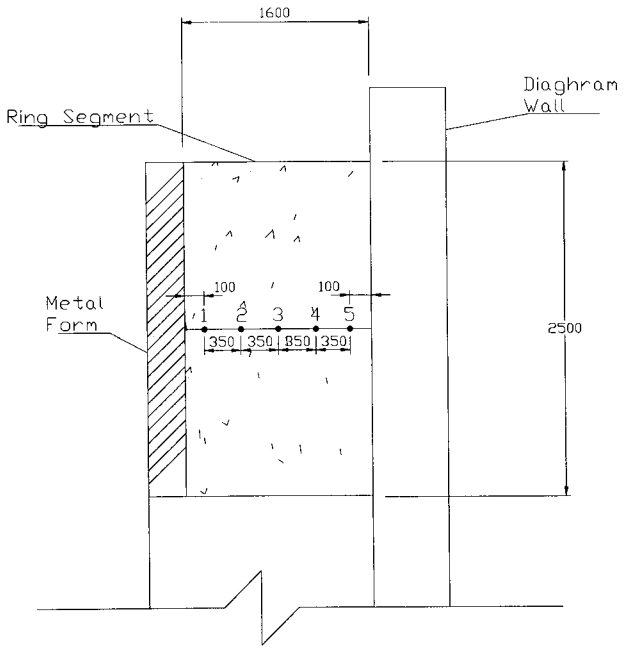

Figure 6.2 Location of thermocouple sensors in ring wall

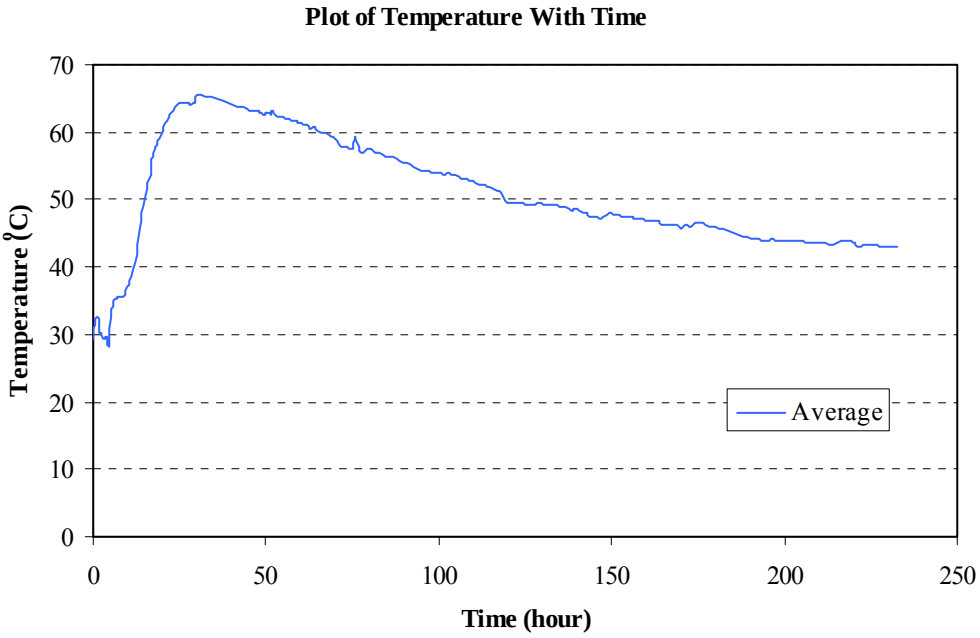

Figure 6.3 Average temperature variation inside ring wall

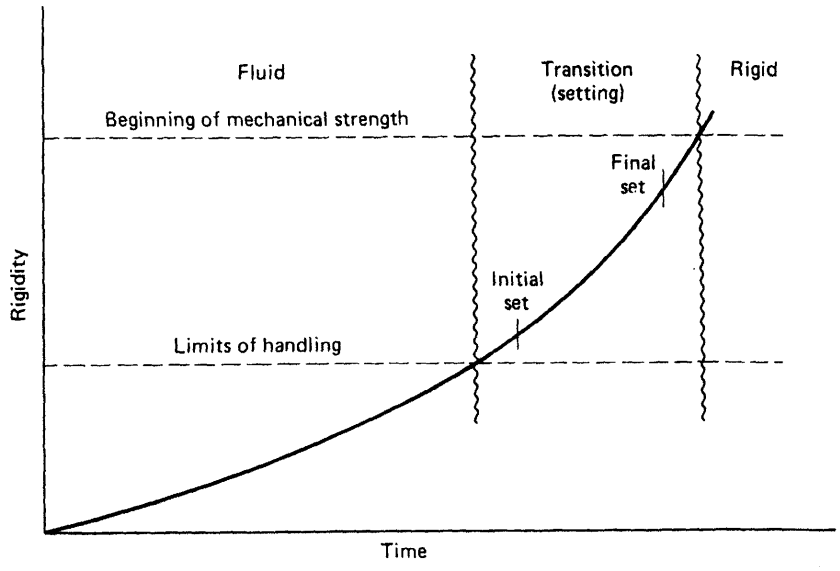

Figure 6.4 Process of setting and hardening of concrete (Mindess and Young, 1981)

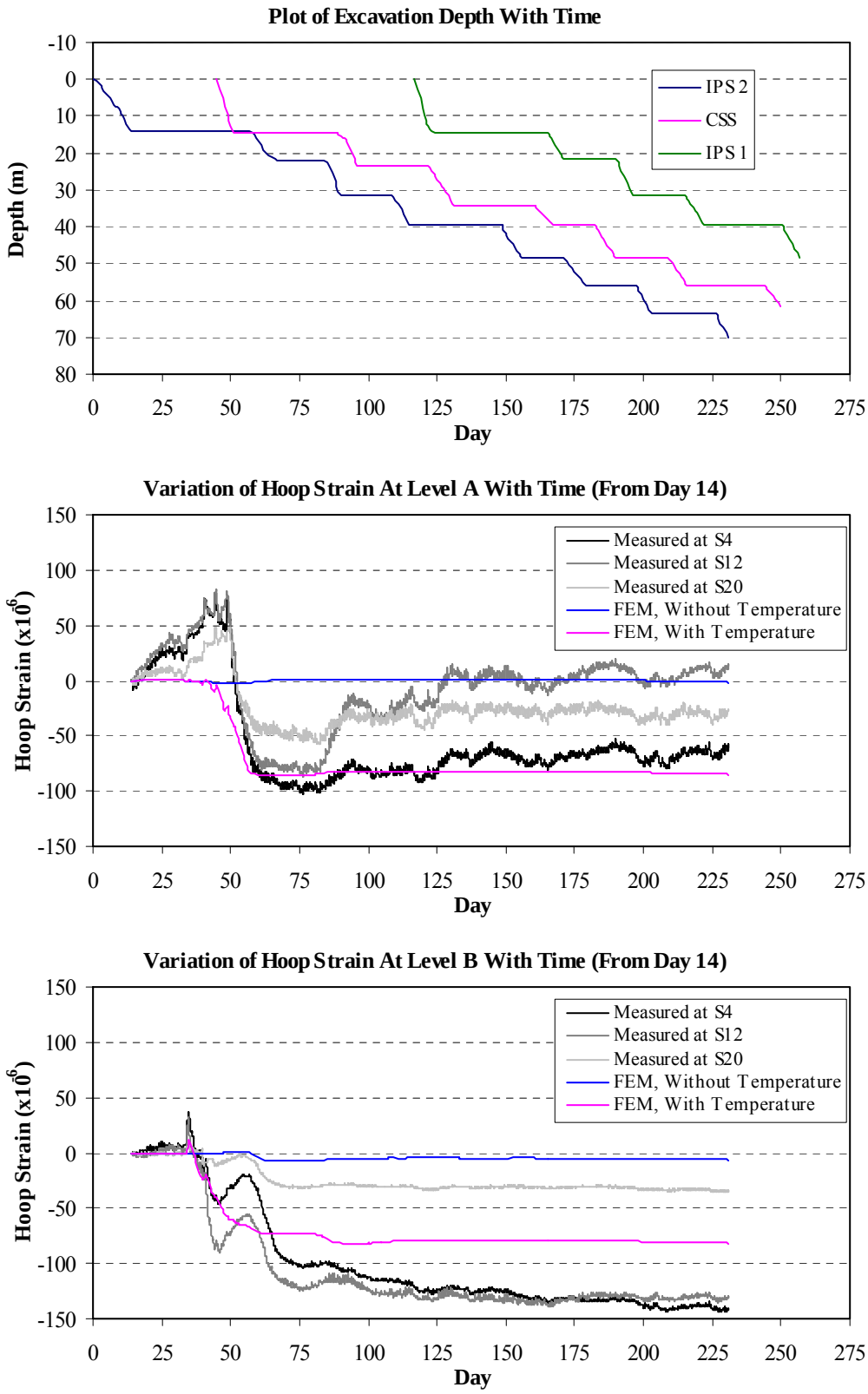

Figure 6.5 Comparison of measured and predicted hoop strains at Level A and Level B

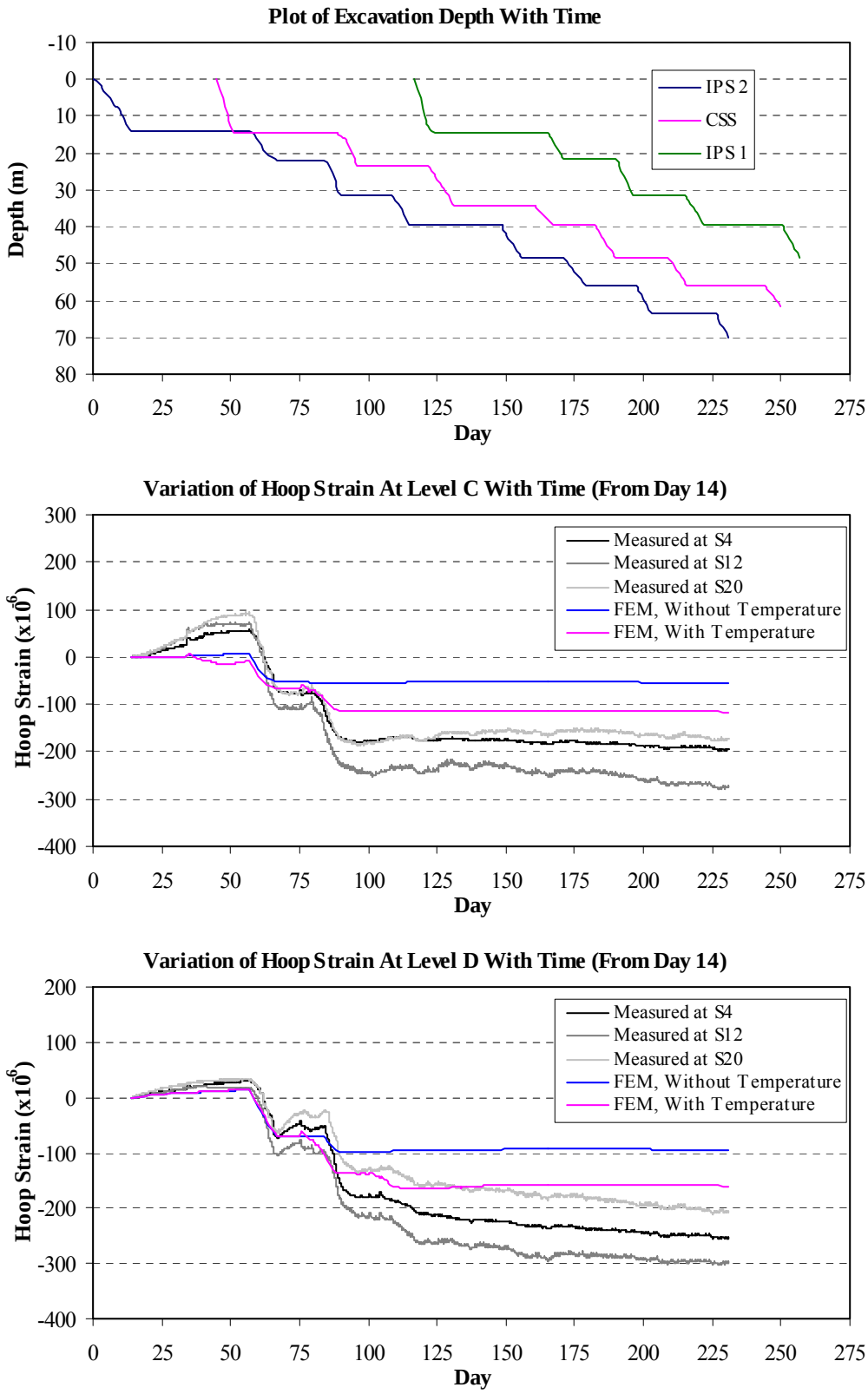

Figure 6.6 Comparison of measured and predicted hoop strains at Level C and Level D

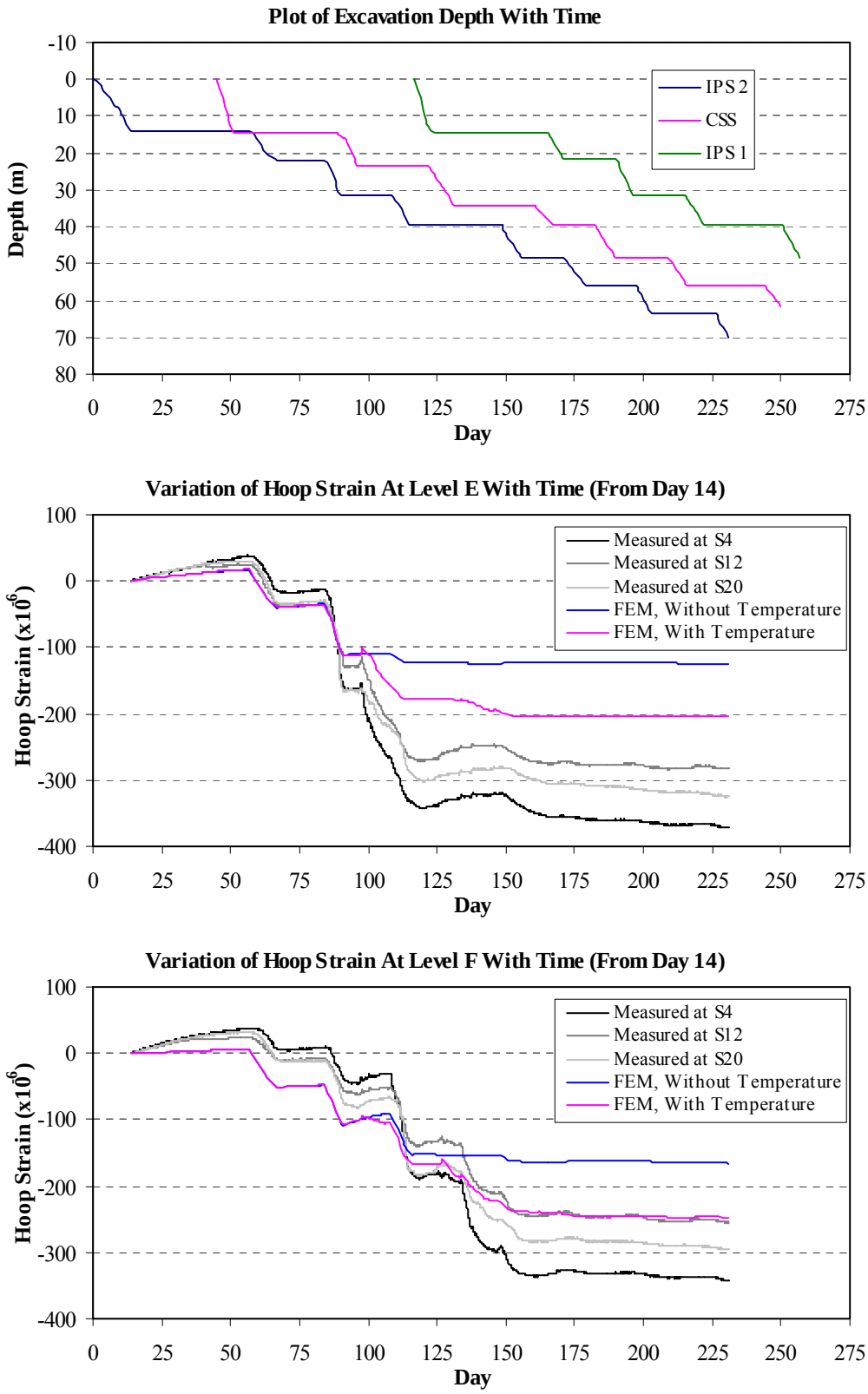

Figure 6.7 Comparison of measured and predicted hoop strains at Level E and Level F

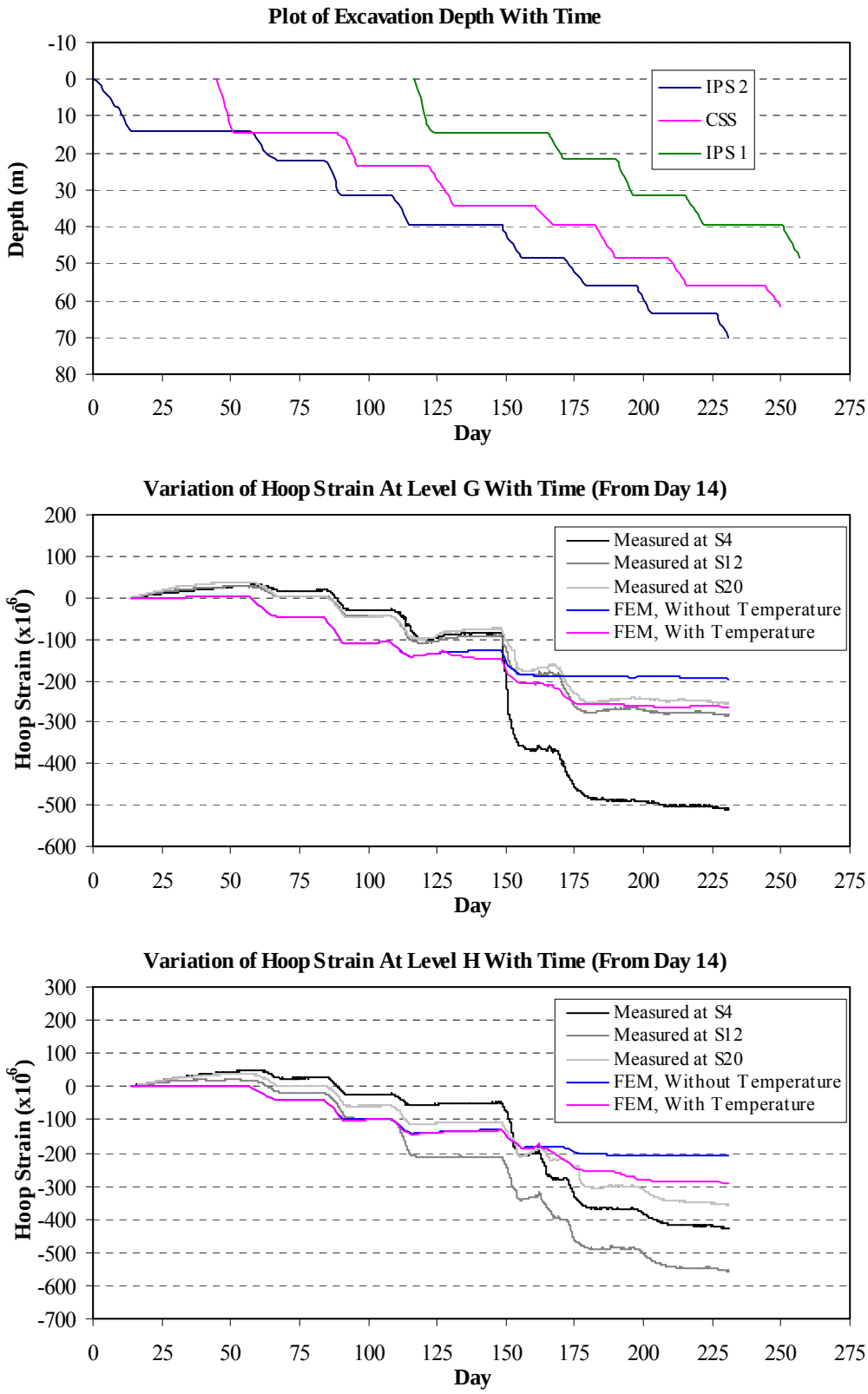

Figure 6.8 Comparison of measured and predicted hoop strains at Level G and Level H

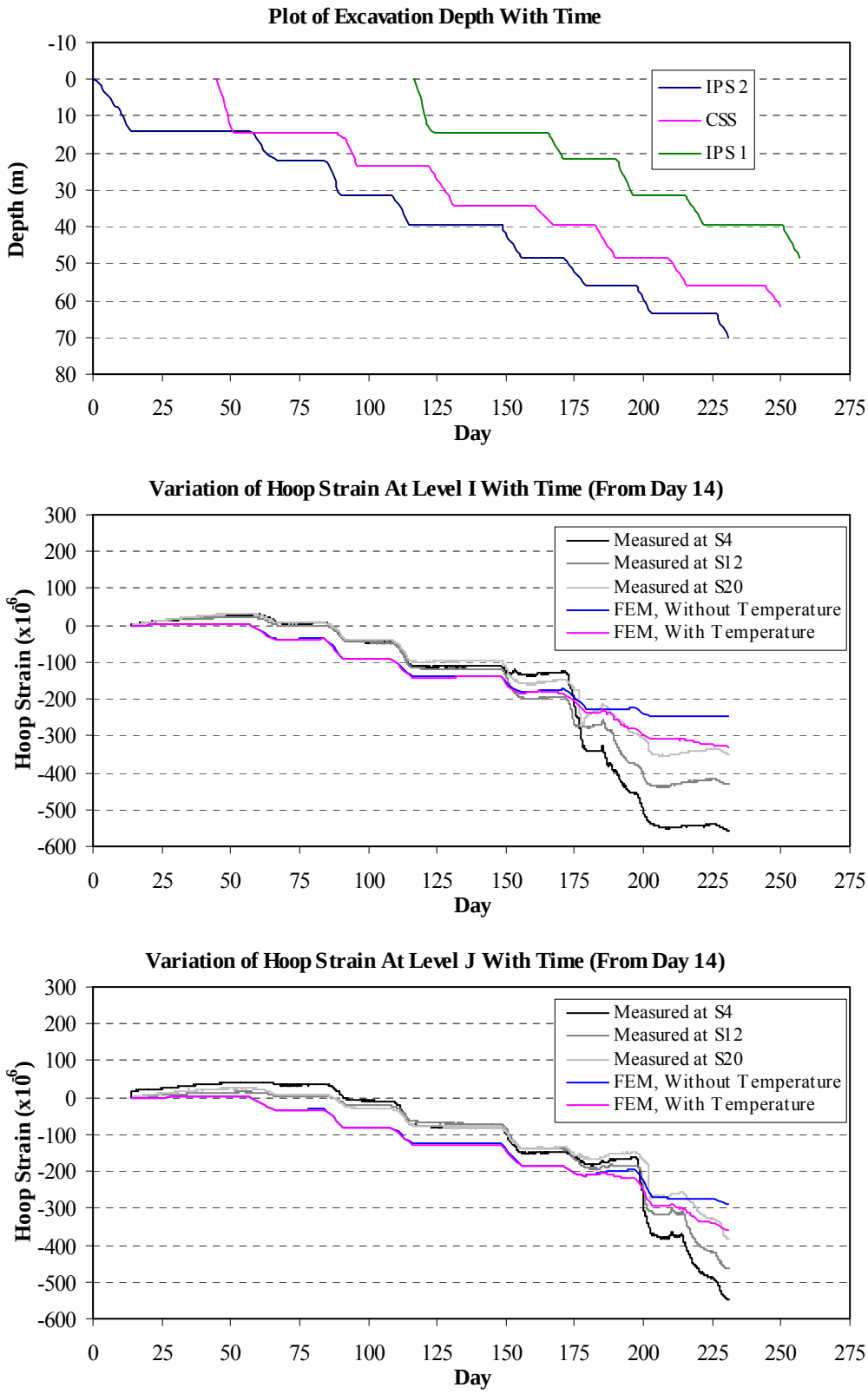

Figure 6.9 Comparison of measured and predicted hoop strains at Level I and Level J

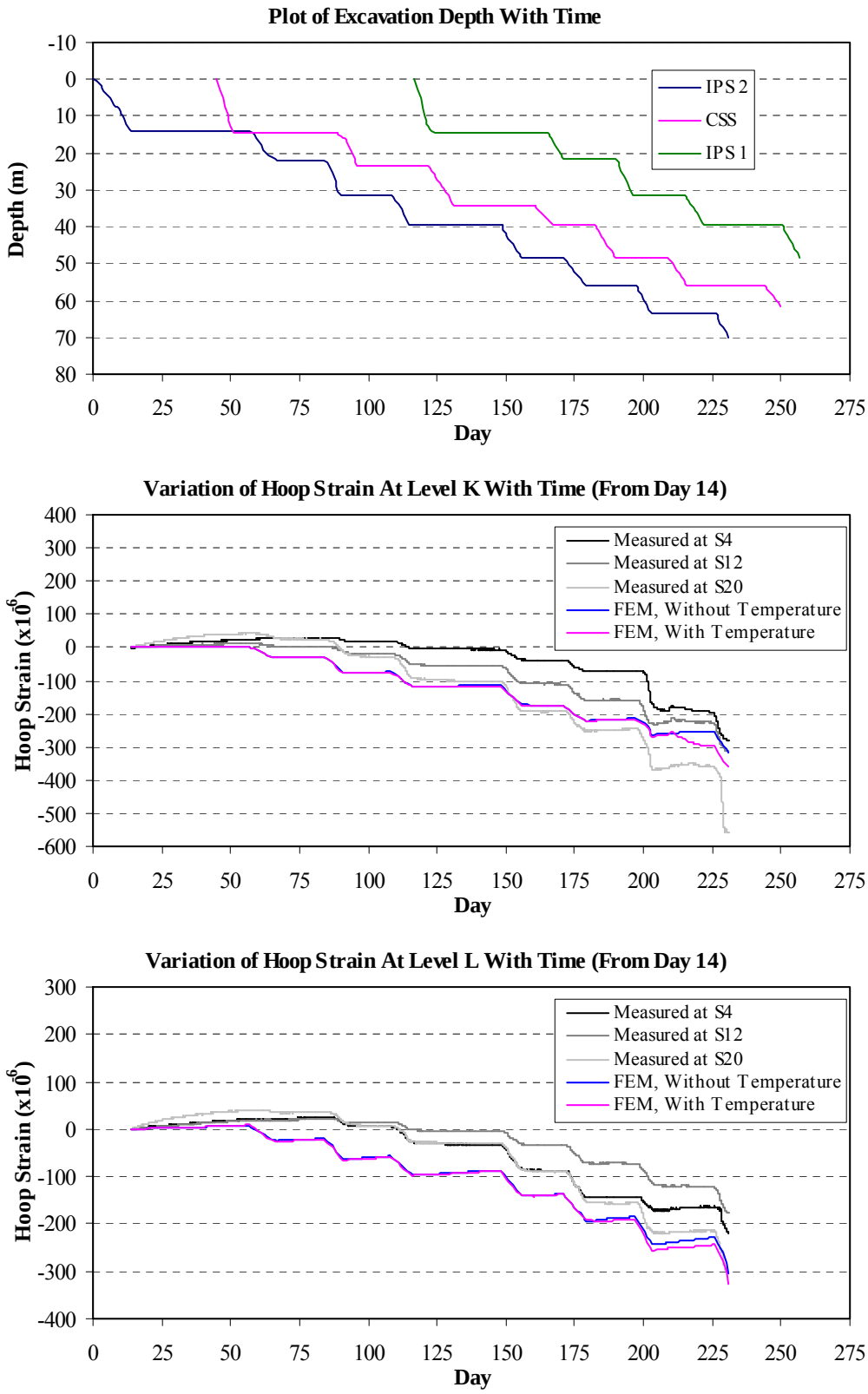

Figure 6.10 Comparison of measured and predicted hoop strains at Level K and Level L

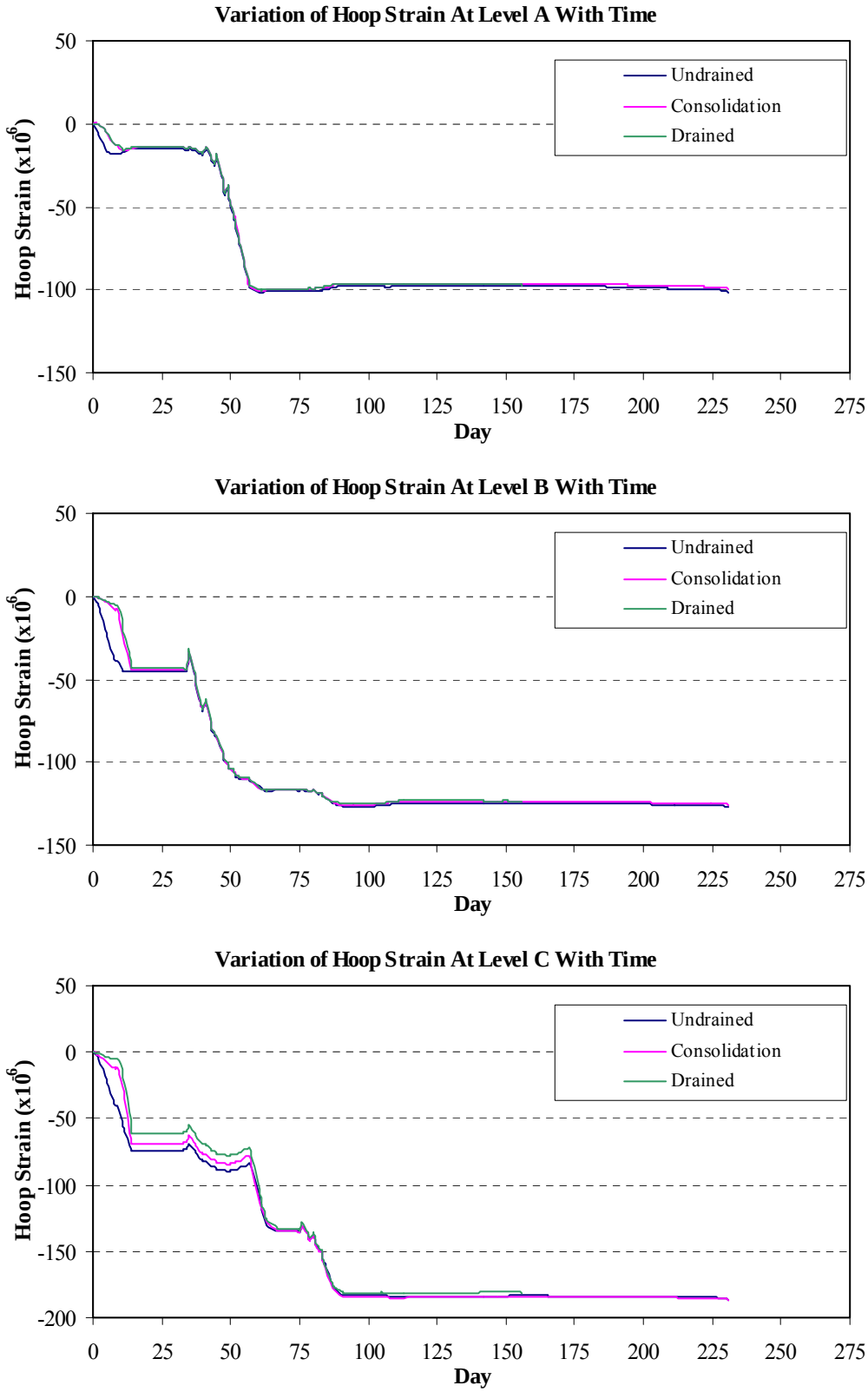

Figure 6.11 Comparison between undrained, consolidation and drained analysis on hoop strains at Level A, Level B and Level C

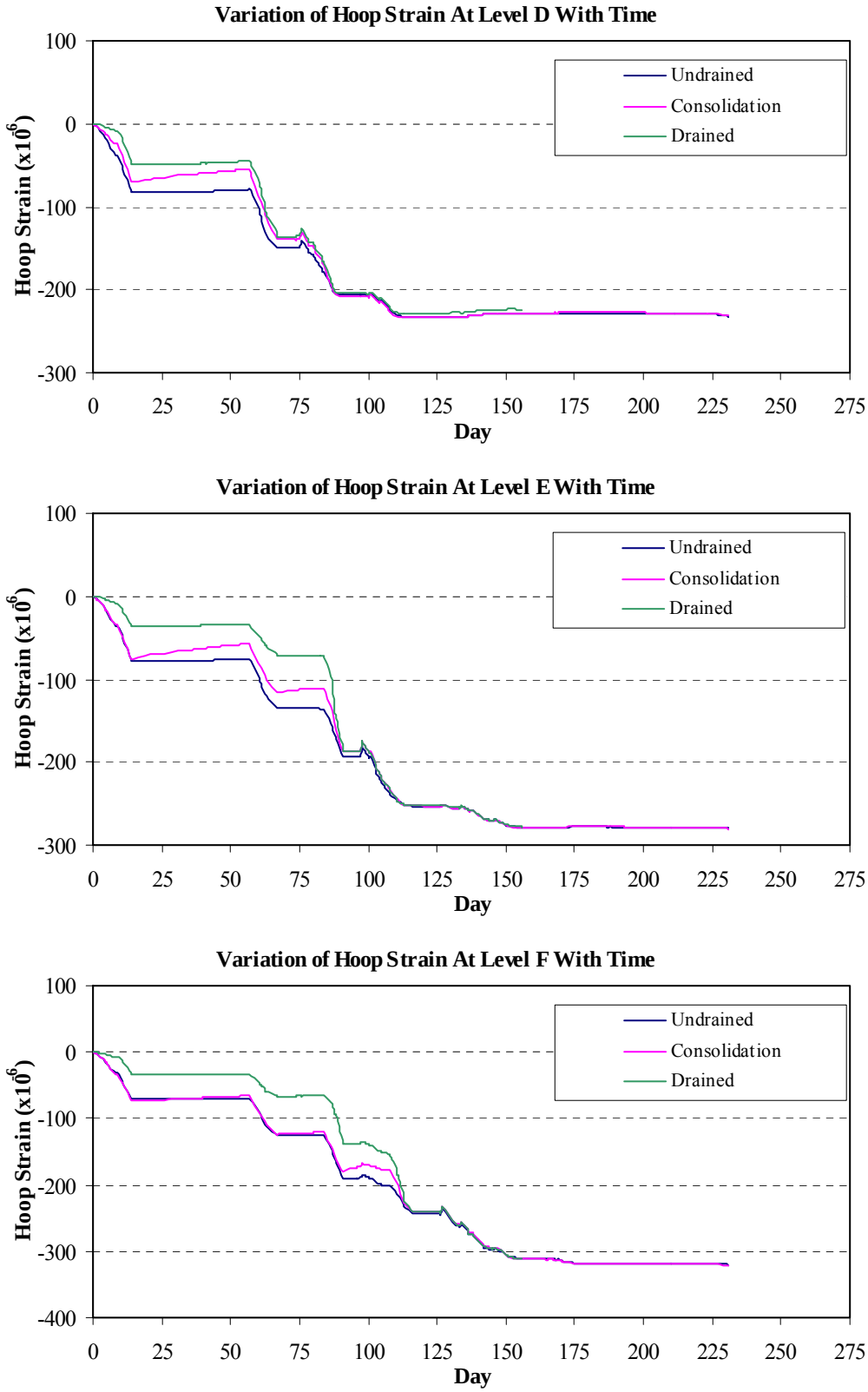

Figure 6.12 Comparison between undrained, consolidation and drained analysis on hoop strains at Level D, Level E and Level F

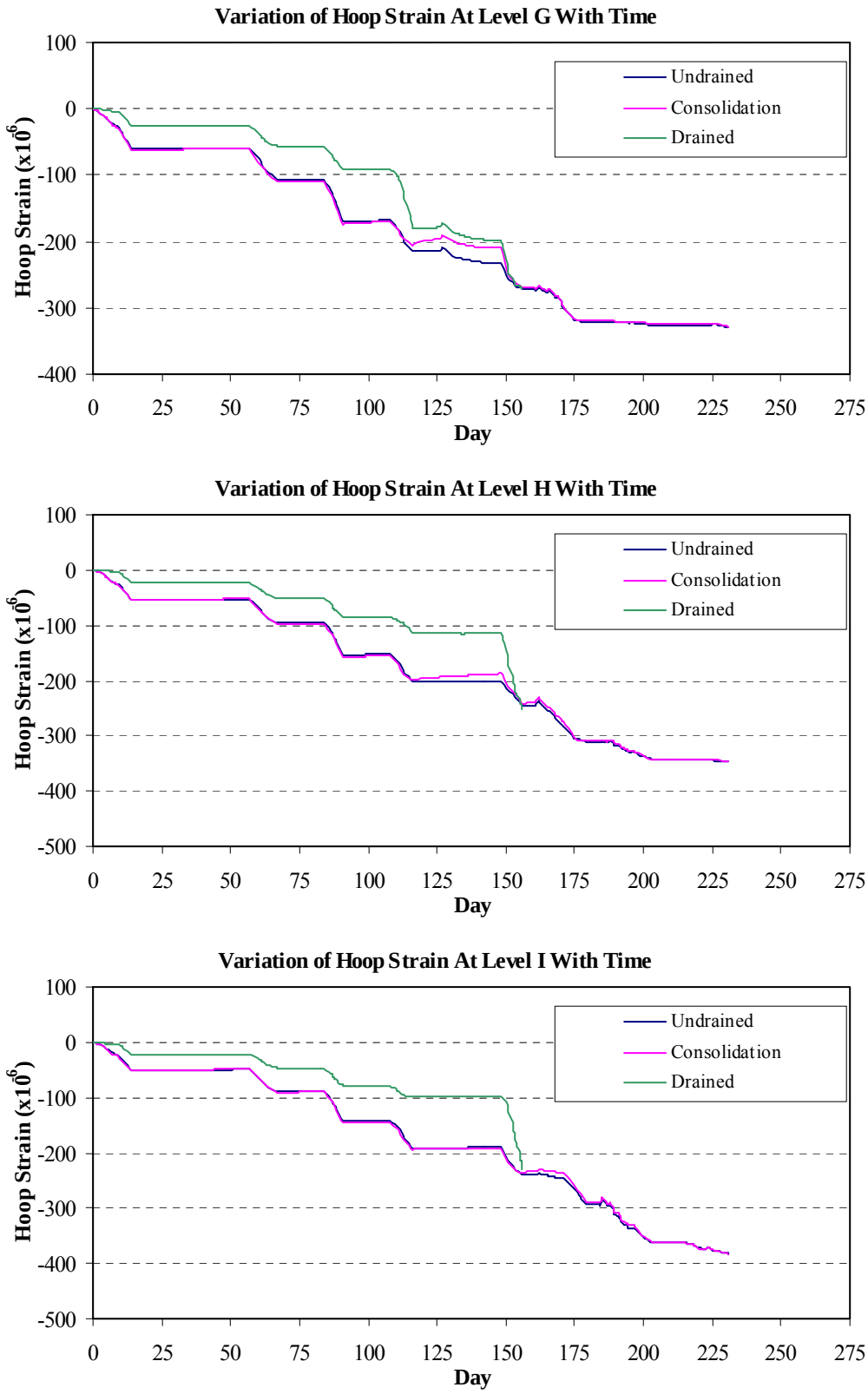

Figure 6.13 Comparison between undrained, consolidation and drained analysis on hoop strains at Level G, Level H and Level I

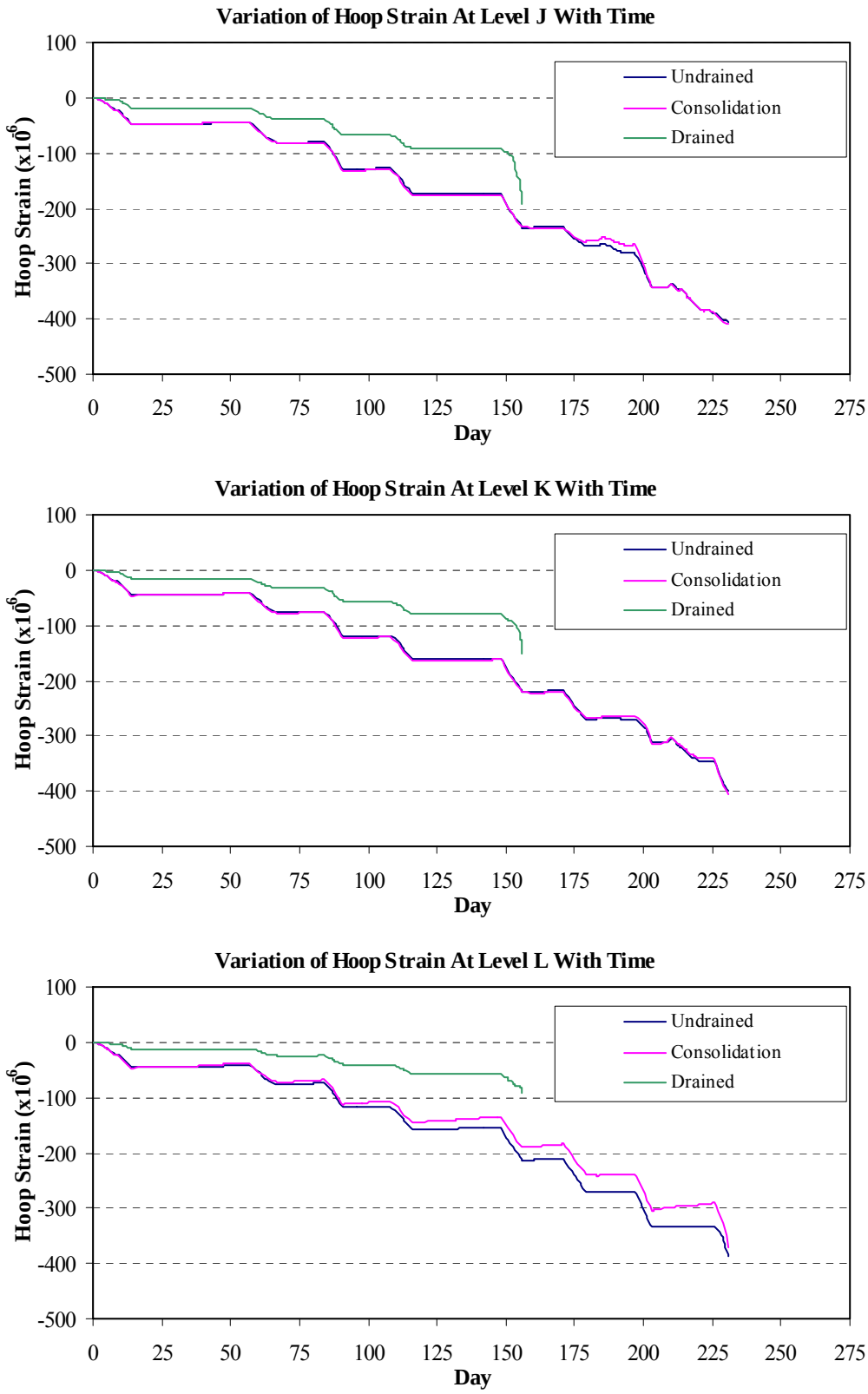

Figure 6.14 Comparison between undrained, consolidation and drained analysis on hoop strains at Level J, Level K and Level L

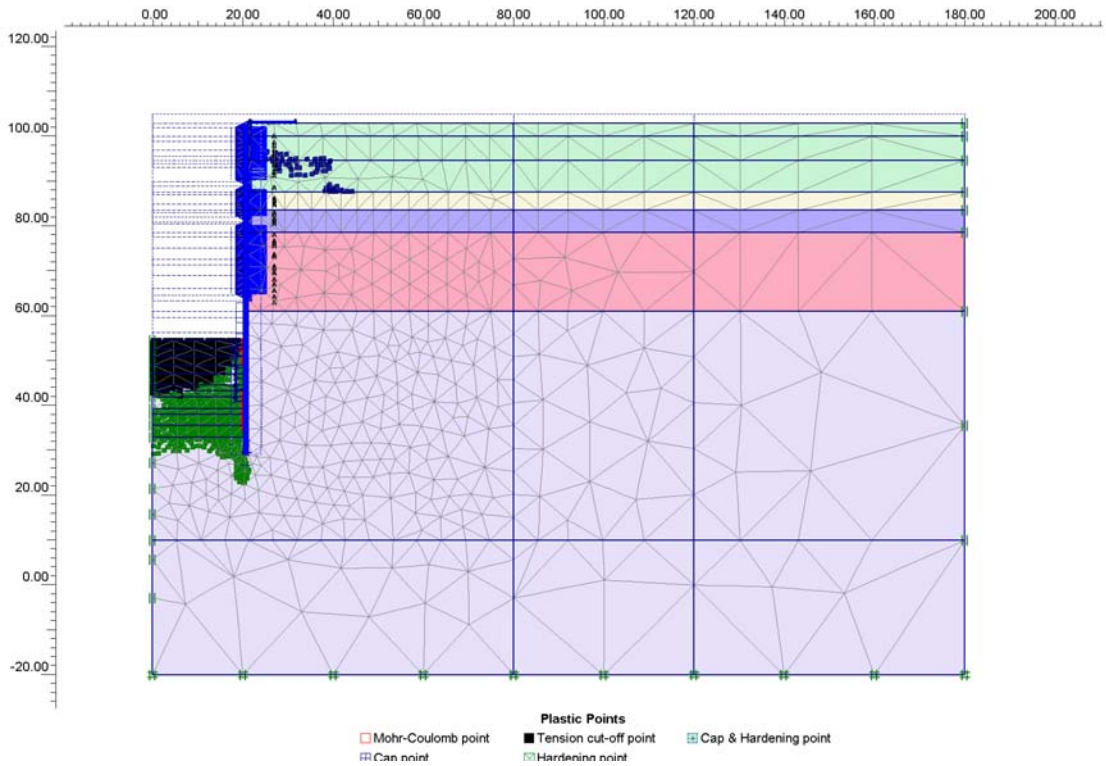

Figure 6.15 Plot of plastic points in drained analysis

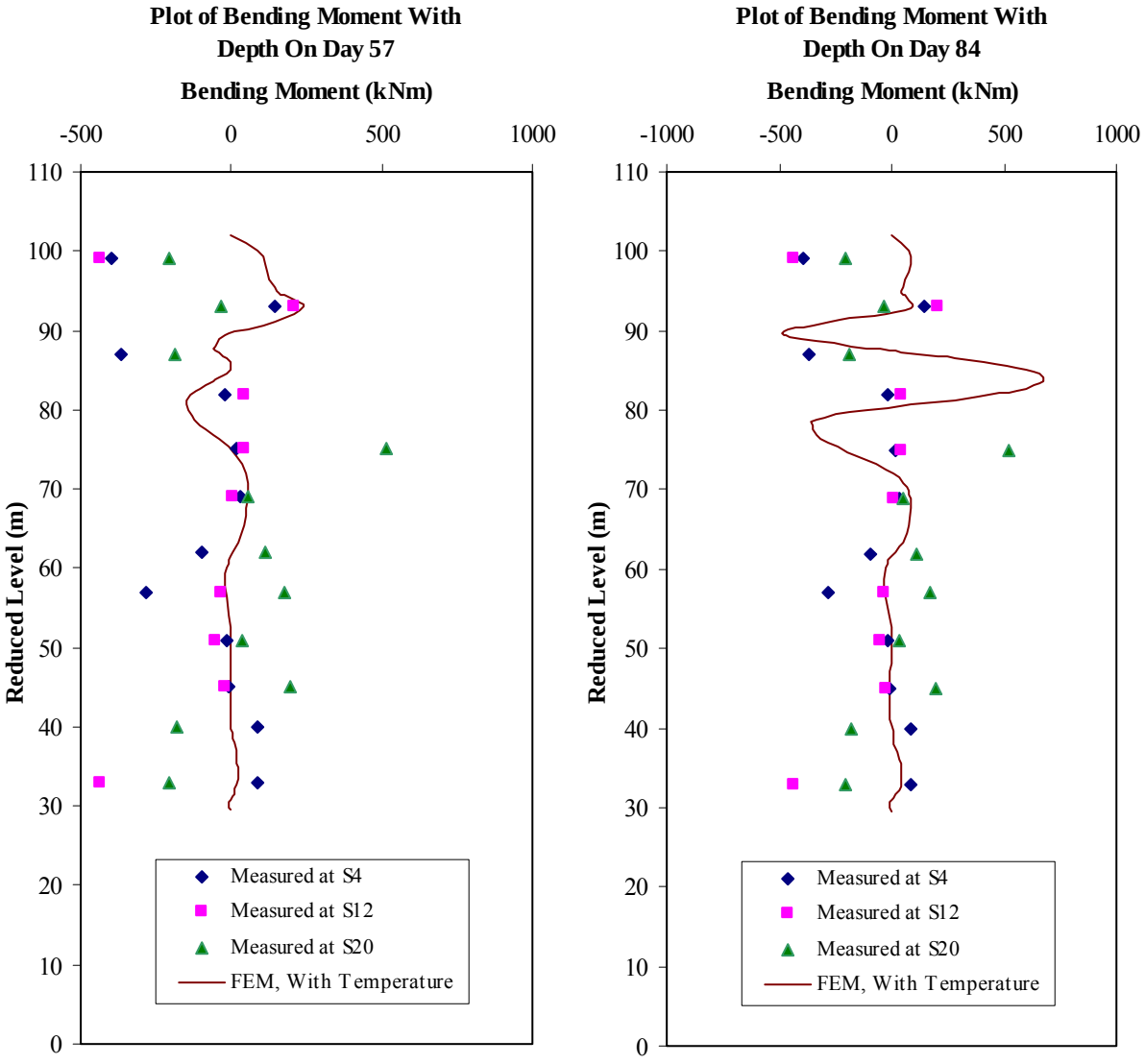

Figure 6.16 Measured and predicted bending moments of diaphragm wall

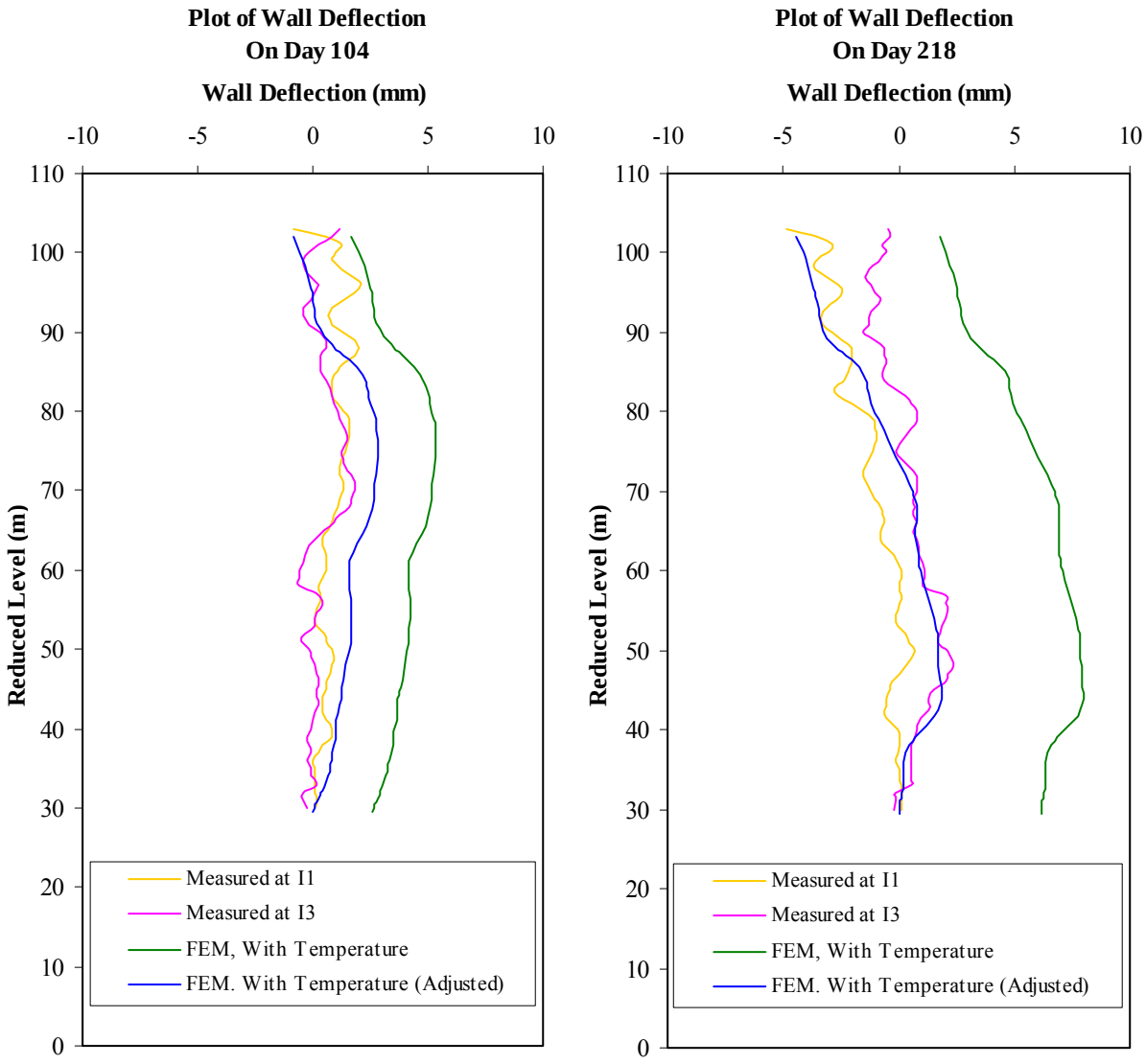

Figure 6.17 Measured and predicted deflections of diaphragm wall

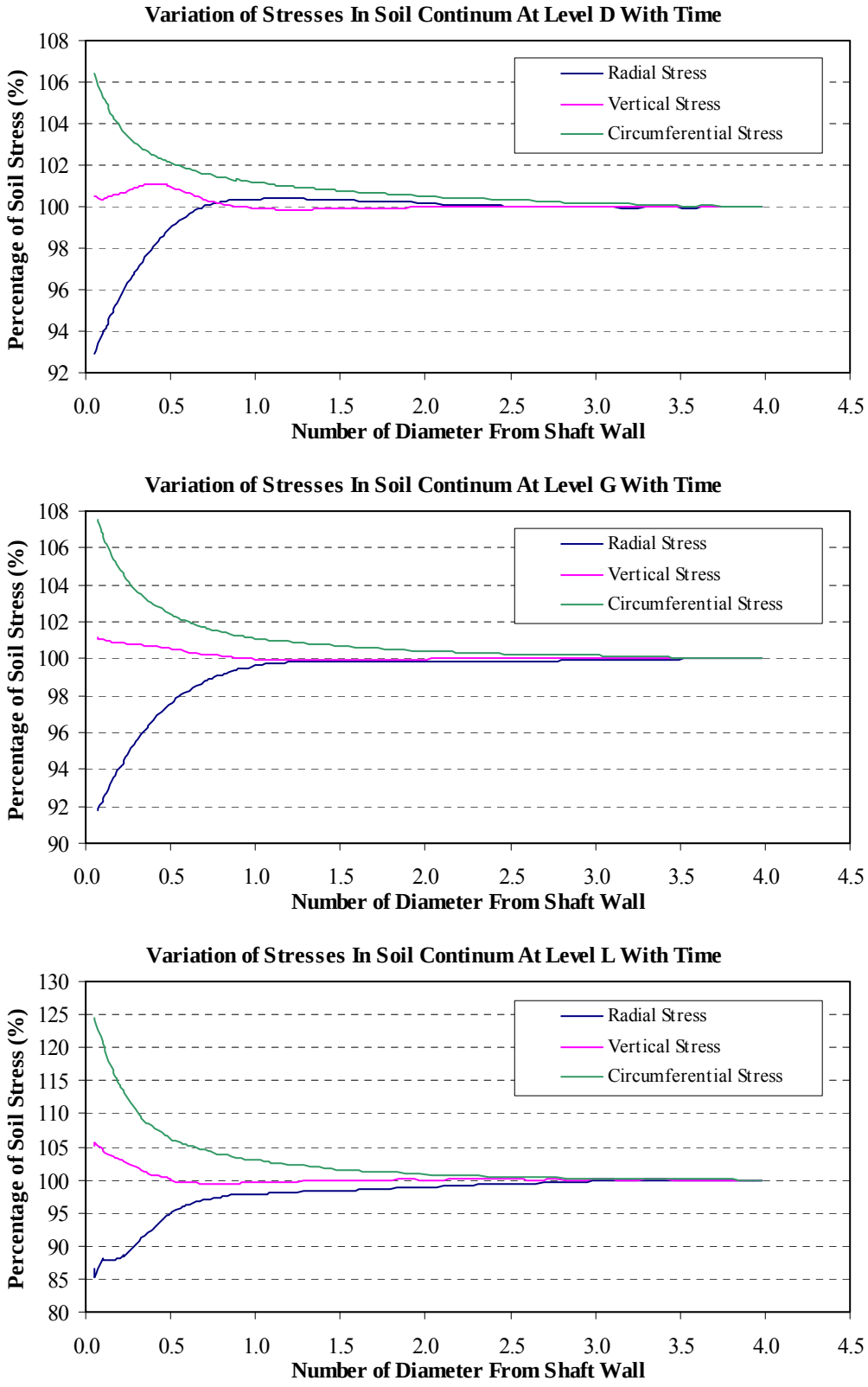

Figure 6.18 Variation of stresses in soil continuum at Level D, Level G and Level L

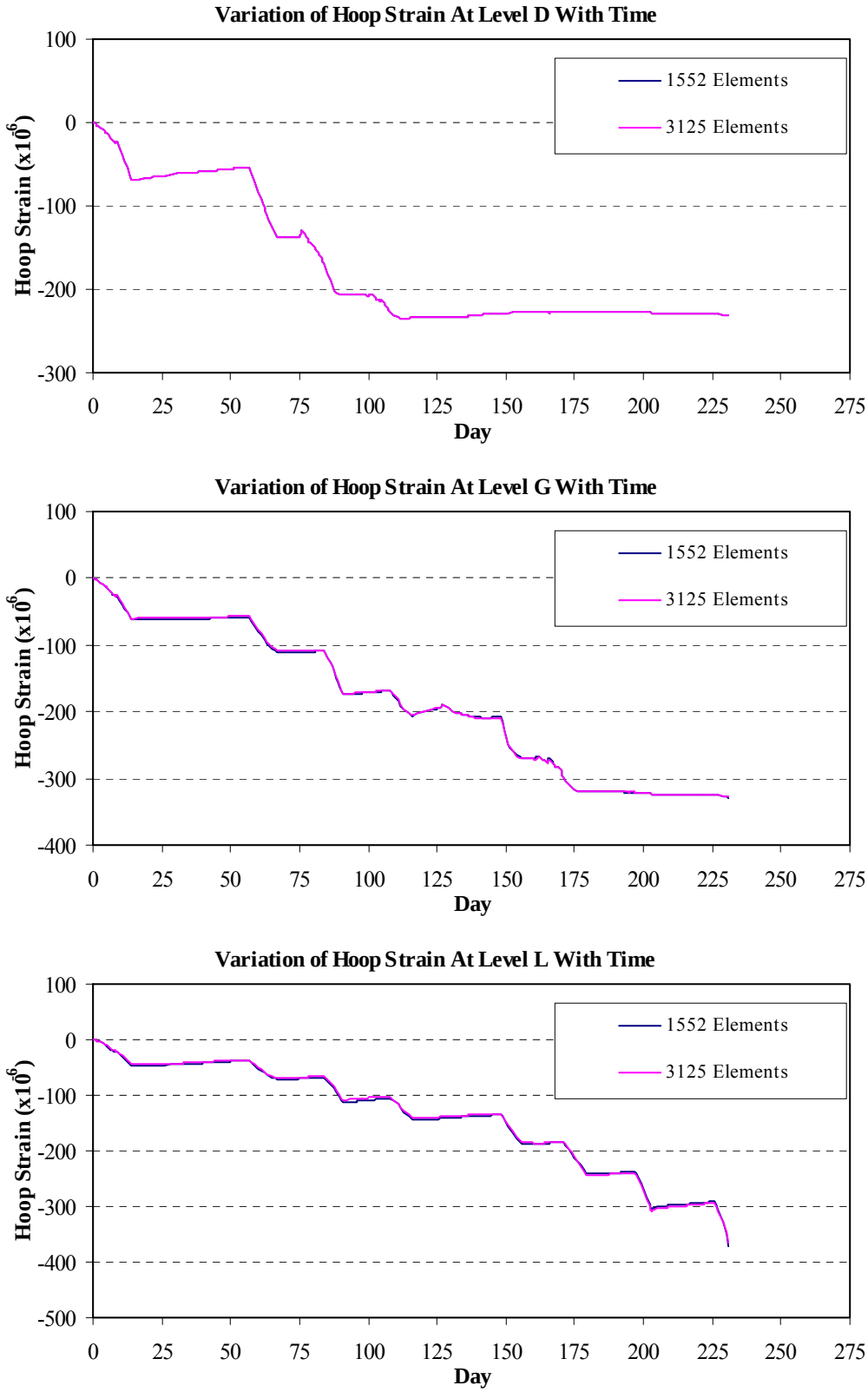

Figure 6.19 Influence of mesh density on hoop strains at Level D, Level G and Level L

CHAPTER 7 PARAMETRIC STUDIES

7.1 Introduction

Influences of various parameters on the behaviour of the circular excavation support system for Influent Pumping Shaft 2 are examined in this chapter. Various parameters are used as inputs in the finite element analysis described in Chapter 6. Many of these parameters, such as material and soil properties, cannot be determined with absolute accuracy. Old Alluvium soils are known to be highly variable, vertically as well as laterally. The actual construction process may not be identical to the process stipulated. Thus, it is beneficial to perform parametric studies to evaluate the responses of the circular shaft due to deviations from the assumed conditions. This understanding would aid in the design of similar circular shafts in Old Alluvium soils.

The parametric studies are performed by repeating the finite element analysis with different values of a particular parameter while keeping the magnitude of other input parameters unchanged. The influence of the parameters is assessed by comparing the changes in the maximum hoop force, maximum moment, maximum shear and maximum deflection of wall at the final excavated depth, as each parameter is varied through a range of values. The relative importance of the reference stiffness parameters of the Hardening-Soil Model is investigated. The influences of soil strength, soil stiffness, over-consolidation ratio and permeability of the soil strata on the response of the circular shaft are studied. Effects due to possible discrepancies in the grade of concrete used for the diaphragm wall and internal ring wall and the interface strength of the diaphragm wall are examined.

The maximum hoop force, F_z, moment, M, shear, V, and deflection, δ, of the cylindrical shaft wall obtained due to the varied parameter are expressed as a percentage of the maximum hoop force, F_{zo}, moment, M_o, shear, V_o, and wall deflection, δ_o, of the reference finite element analysis that made use of the basic soil parameters and material properties described in Chapter 6. Some multipliers are adopted to reflect the influences of the parameter under study. They are defined as follows:

a) E_{50}^{ref} Multiplier: Ratio of varied reference secant stiffness modulus to the basic reference secant stiffness modulus

b) E_{oed}^{ref} Multiplier: Ratio of varied reference tangential oedometer stiffness modulus to the basic reference tangential oedometer stiffness modulus

c) E_{ur}^{ref} Multiplier: Ratio of varied reference unloading stiffness modulus to the basic reference unloading stiffness modulus

d) Soil Stiffness Multiplier: Ratio of varied reference soil stiffness to the basic reference soil stiffness

e) OCR Multiplier: Ratio of varied over-consolidation ratio (OCR) to the basic over-consolidation ratio of soil

f) Permeability Multiplier: Ratio of varied coefficient of permeability to the basic coefficient of permeability of soil

7.2 Influence of Soil Strength

The strength of soil would affect the failure and strains of the soil continuum. Hence, the influence of soil strength in the design of the circular shaft is studied by varying the effective angles of friction of the various soil strata at the project site. The effective angles of friction are varied within $\pm 4^{o}$ of the basic effective angles of friction listed in Table 6.4. The influences of effective angles of friction on the structural forces and wall deflection are illustrated in Figure 7.1.

It is evident that the effective angle of friction of Silty Sand 3 layer is the most dominating factor that influences the maximum hoop force and maximum deflection of the wall. The maximum hoop force and wall deflection decrease as the soil strength of the Silty Sand 3 layer increases. The magnitude of maximum hoop force and wall deflection varies within ±6% of the reference maximum hoop force and wall deflection calculated based on the basic effective angles of friction. The effective angles of friction of the other soil layers have negligible effects on the development of maximum hoop force and wall deflection. It can be seen from Figure 7.1 that the magnitude of maximum hoop force and wall deflection, as the effective angles of friction of all soil layers are varied together, does not deviate significantly from the value of maximum hoop force and wall deflection where only the effective angle of friction of the Silty Sand 3 is studied. Thus, effective angle of friction of the Silty Sand 3 layer is the most important factor on the development of maximum hoop force and maximum deflection of the circular shaft wall.

The magnitude of maximum moment and shear acting on the circular shaft wall decreases as the effective angles of all soil layers, except the Reclaimed Sand layer, are

increased independently. The effective angle of the Silty Sand 1 layer is most influential to the shear development of the wall as the shear can defer by as much as 15% from the reference value. The magnitude of shear force, as the effective angles of friction of all soil layers are varied together, does not deviate significantly from the shear forces where only the effective angle of friction of the Silty Sand 1 is varied.

7.3 Effect of Hardening-Soil Stiffness Modulus

The soil stiffness parameters of the Hardening-Soil model consist of the reference secant stiffness modulus, E_{50}^{ref}, the reference tangential oedometer stiffness modulus, E_{oed}^{ref}, and the reference unloading stiffness modulus, E_{ur}^{ref}. The soil stiffness parameters of all the soil layers at the project site are varied independent of each other at between 70% and 130% of the reference soil modulus in this study.

The effect of the reference secant stiffness modulus on the behaviour of the circular excavation support system is shown in Figure 7.2. When the reference secant stiffness modulus, E_{50}^{ref}, is varied, the maximum hoop force, maximum moment, maximum shear and maximum deflection developed in the circular shaft wall vary within ±1% of the maximum structural forces and wall deflection obtained from the reference finite element analysis where the basic input parameters are used. Similar observations can be deduced from Figure 7.3 where the effects of the reference tangential oedometer stiffness modulus, E_{oed}^{ref}, are studied.

The influence of the reference unloading stiffness modulus, E_{ur}^{ref}, is shown in Figure 7.4, where it is evident that the reference unloading stiffness modulus, E_{ur}^{ref}, is the most important soil stiffness parameter of the Hardening-Soil model as compared to

the reference secant stiffness modulus, E_{50}^{ref}, and the reference tangential oedometer stiffness modulus, E_{oed}^{ref}, in this circular shaft excavation. It is consistent to the findings reported by Yong et al (1989) and Tan and Tan (2004). They recommended the use of unloading soil stiffness for excavation design. Thus, engineers should be more critical in selecting a value for the reference unloading stiffness modulus in the design of an excavation support system. A decrease in the reference unloading stiffness modulus, E_{ur}^{ref}, generally results in an increase in the maximum hoop force, maximum moment, maximum shear and maximum wall deflection, as shown in Figure 7.4.

7.4 Influence of Soil Stiffness

The reference secant stiffness modulus, E_{50}^{ref}, the reference tangential oedometer stiffness modulus, E_{oed}^{ref}, and the reference unloading stiffness modulus, E_{ur}^{ref}, of the various soil layers are varied together between 70% and 130% of the basic soil stiffness parameters in this study. The influence of these soil stiffness parameters of the individual soil strata are plotted in Figure 7.5.

The soil stiffness parameters of the Silty Sand 3 layer is also found to be most crucial to the development of maximum hoop force and maximum wall deflection, in comparison to other soil layers. The maximum hoop force and wall deflection decrease with an increase in soil stiffness of the Silty Sand 3 layer. The magnitude of maximum hoop force and wall deflection varies within ±4% of the reference maximum hoop force and wall deflection. It can be observed from Figure 7.5 that the soil stiffness parameters of other soil layers have little effects on the maximum hoop force and wall deflection. The maximum moment and shear forces in the circular shaft wall decrease

as the soil stiffness parameters of all the soil layers increase. The individual effects of the various soil layers at the site are less consistent, as shown in Figure 7.5.

7.5 Influence of Over-Consolidation Ratio

The over-consolidation ratio (OCR) adopted for the Old Alluvium soils at the project site are calculated based on an approximate relation proposed by Li and Wong (2001). It would affect the state of stress generated in the soil continuum of a finite element model, as the effective horizontal soil stresses are determined from the over-consolidation ratio. Effects due to deviations from the assumed over-consolidation ratios are analysed by varying the over-consolidation ratios within 60% to 140% of the adopted values listed in Table 6.4. The influence of over-consolidation ratios of the soil strata is illustrated in Figure 7.6.

It can be deduced from Figure 7.6 that the over-consolidation ratio of the Silty Sand 3 layer controls the development of maximum hoop force and maximum wall deflection. The maximum hoop force and wall deflection increase together with an increase in over-consolidation ratio of the Silty Sand 3 layer. The magnitude of maximum hoop force and wall deflection varies within ±8% of the reference maximum hoop force and wall deflection, as the over-consolidation ratio of the Silty Sand 3 layer is varied. The over-consolidation ratios of other Old Alluvium soil layers have insignificant effects on the maximum hoop force and wall deflection as compared to that of the Silty Sand 3 layer.

The maximum moment and shear acting on the circular shaft wall increase with an increase in over-consolidation ratio. The over-consolidation ratio of the Silty Sand 1

layer is most critical to the development of shear forces while the over-consolidation ratio of both the Silty Sand 1 layer and the Clayey Sand layer affect the bending moment of the shaft wall more significantly than the over-consolidation ratio of other soil layers. It can be observed from Figure 7.6 that an increase in over-consolidation ratio results in a greater percentage increase in the maximum moment and shear than the hoop force and wall deflection.

7.6 Influence of Soil Permeability

Consolidation analysis accounts for the time-dependent dissipation of excess pore pressures. Thus, the influence of the coefficient of permeability of the soil strata is investigated in this section. The coefficients of permeability are increased up to 100 times the proposed soil permeabilities presented in Table 6.4. The ratios between vertical and horizontal coefficients of permeability of the various soil layers assumed in Chapter 6 remains unchanged in the present study. The effects due to soil permeability on the structural forces and deflection of the circular diaphragm wall are shown in Figure 7.7.

It can be observed that the maximum hoop force and wall deflection decrease as the coefficient of permeability increases. An increase in hoop force and wall deflection is evident when the coefficient of permeability further increases to 100 times of their reference soil permeabilities. Figure 7.7 shows a reverse trend for the maximum moment and shear as the coefficients of permeability are varied. The maximum moment and shear increase as the coefficient of permeability increases by 10 to 20 times the reference soil permeabilities and their magnitudes decrease as the coefficient of permeability are further increased to 100 times of their reference soil permeabilities.

Figure 7.8 shows the influence of coefficient of permeability of the variation of hoop strains at three elevations of the circular shaft wall with time. Level D, Level G, and Level L are located at 21 m, 41 m and 70 m below the final ground surface level, respectively. Generally, higher soil permeability results in lower hoop strains as it is mentioned in Chapter 6 that the drained condition provides the lower limits of hoop strains while the undrained condition gives the upper limits of hoop strains, if the soil has not approached failure. Thus, if the soils have higher permeabilities, they would be closer to the drained condition and result in smaller hoop strains of the circular shaft. This phenomenon leads to the trend of decreasing maximum hoop force when the coefficients of permeability increase up to 10 to 20 times of the reference soil permeabilities in this parametric study.

Figure 7.9 and Figure 7.10 present state of stress in the soil continuum where a permeability multiplier of 1 and 100 are adopted. It is observed that more hardening points are present at the base of the excavation in soils with higher permeability Hardening point is a stress point whose stress state corresponds to the maximum mobilised friction angle that has previously been reached. Thus, failure is imminent when the permeability multiplier is further increased and it is manifested in an increase in compressive hoop strains or hoop force when the final stages of excavation are carried out. As the magnitude of the maximum moment and shear decreases with further increase in permeability, the measurement of hoop strains of a circular shaft would serve as a critical guide to alert the engineers on possible deviations of the stability of the excavation due to the usage non-representative soil permeability during the design stage. It is interesting to note the hoop strains experienced by upper elevations of the wall do not further increase during the last few excavation stages

when the drained condition is approached. Hence, it is very important to install strain gauges near the bottom of the excavation for the instrumentation works to be meaningful.

7.7 Influence of Interface Strength

The effects of the interface strength of the circular diaphragm wall, R_{inter}, on the structural forces and wall deflection are studied and plotted in Figure 7.11. The interface strength, R_{inter}, is varied from 0.6 to 1.0. It can be observed that the maximum hoop force, maximum shear and maximum wall deflection decrease with an increase of interface strength. In other words, the hoop force, shear and wall deflection can be reduced with an increase with the wall adhesion and wall friction. However, the moment acting on the retaining wall increases with an increase of wall adhesion and wall friction.

7.8 Influence of Grade of Concrete of Circular Shaft Wall

As the modulus of elasticity of concrete is highly dependant on the strength of the concrete, the influence of the grade of concrete used for the diaphragm wall of Influent Pumping Shaft 2 on the response of the circular excavation support system is examined. The grade of concrete used in this parametric study varies from Grade-35 to Grade-90 and the corresponding modulus of elasticity of the diaphragm wall is varied accordingly in the finite element analysis. It is apparent from Figure 7.12 that the maximum hoop force and moment experienced by the circular shaft wall increase with an increase in the strength of concrete. The maximum hoop force and moment are deduced by 7.4% and 3.5% respectively when a grade-30 concrete wall is adopted as the excavation support system. However, a decrease of wall stiffness will result in an

increase of wall deflection of approximately 30% of the reference maximum wall deflection when a grade-30 concrete wall is installed at the site. There are no significant changes in the maximum shear force in the wall as the grade of concrete is varied. Maximum hoop stresses acting on the shaft wall are expressed as percentage of the grade of concrete as shown in Figure 7.13 and it is evident that this percentage increases as the cube strength of for concrete diaphragm wall decreases and the hoop stresses on lower grade concrete walls will exceed to allowable limits for their structural stability.

7.9 Influence of Grade of Concrete of Ring Wall

As internal concrete ring walls are cast against the diaphragm wall, the influence of the strength of ring walls is also studied to provide insights on its role in affecting the performance of the circular excavation support system. The grade of concrete of the ring walls used in this parametric study varies from Grade-35 to Grade-90 and the corresponding modulus of elasticity of the ring wall is changed accordingly in the finite element analysis. Figure 7.14 shows the responses of the diaphragm wall due to the different grades of concrete of its internal ring walls.

The maximum hoop force, maximum moment and maximum wall deflection of the circular diaphragm wall decrease in magnitude when a higher grade concrete is adopted for the ring walls. However, the maximum shear in the diaphragm wall increases when the strength of concrete of the ring walls is increased. It is evident from Figure 7.14 that the structural forces and deflections of the diaphragm wall only varies within ±3% from those structural forces and deflection obtained from the reference case where the basic input parameters are used.

7.10 Summary

The reference unloading stiffness modulus, E_{ur}^{ref}, is the most important soil stiffness parameter of the Hardening-Soil model for an excavation problem. For a given grade of concrete for a circular shaft wall, the effects of various parameters on the maximum hoop force and maximum wall deflection, when the parameters are varied, are found to be similar as hoop forces are developed due to wall compression, which manifests as wall deflections. Increase in the strength and stiffness of the soils would lead to a decrease in wall displacements and hoop forces whereas increase in the over-consolidation ratio of soil would result in higher wall displacements and hoop forces. However, the development of maximum shear and moment in the excavation support system is less straightforward.

It is apparent that the soil parameters of Silty Sand 3 layer is found to be most critical to the development of hoop force and wall deflection of the circular diaphragm wall whereas the parameters of Silty Sand 1 and Clayey Sand layers are more influential to the development of moment and shear acting on the diaphragm wall. The consolidation phenomenon would affect the behaviour of the excavation support significantly and the study of the influence of soil permeability has highlighted the importance of the measurement of hoop strains in a circular shaft wall, which can serve as a guide for examine the performance of the retaining structure.

The study of the influence of the grade of concrete of the circular shaft wall shows that adopting a stiffer concrete shaft wall would aid in the control of soil movements effectively. The use of a higher grade concrete for the ring wall would also help to reduce the maximum wall deflection although the reduction would not be as significant

as using a higher grade concrete for the circular shaft wall. Hoop forces and moments in the shaft wall increase when a higher-grade concrete is used for the diaphragm wall but the allowable limits for structural stability of concrete may be exceeded when using lower grade concrete. Using a higher-grade concrete for the ring wall would lead to a slight decrease in the hoop forces and moments in the shaft wall. Thus, it may serve as a rectification method to prevent structural failure of the shaft wall if it is under-designed by sharing some structural loads.

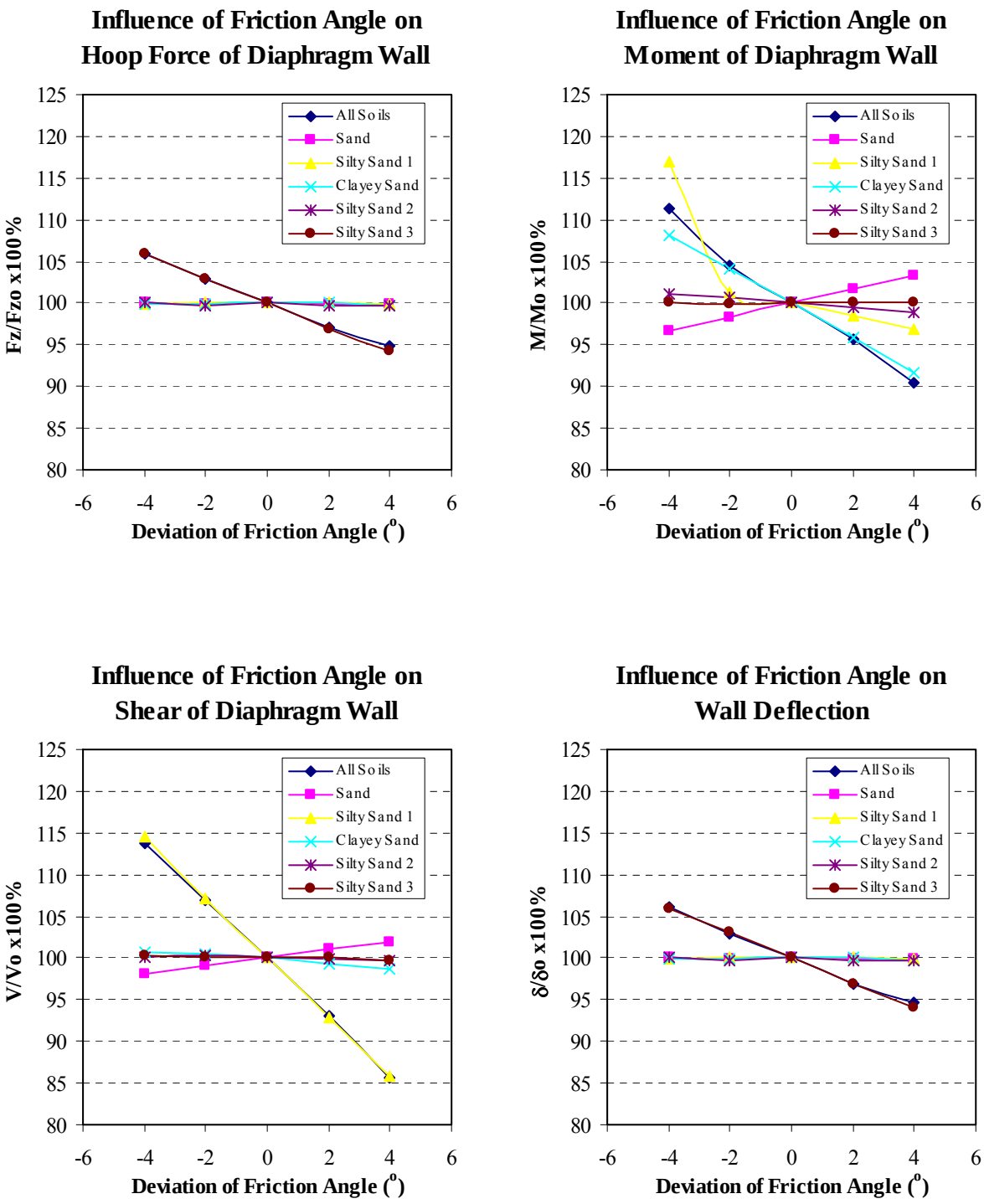

Figure 7.1 Influence of effective angle of friction of soil

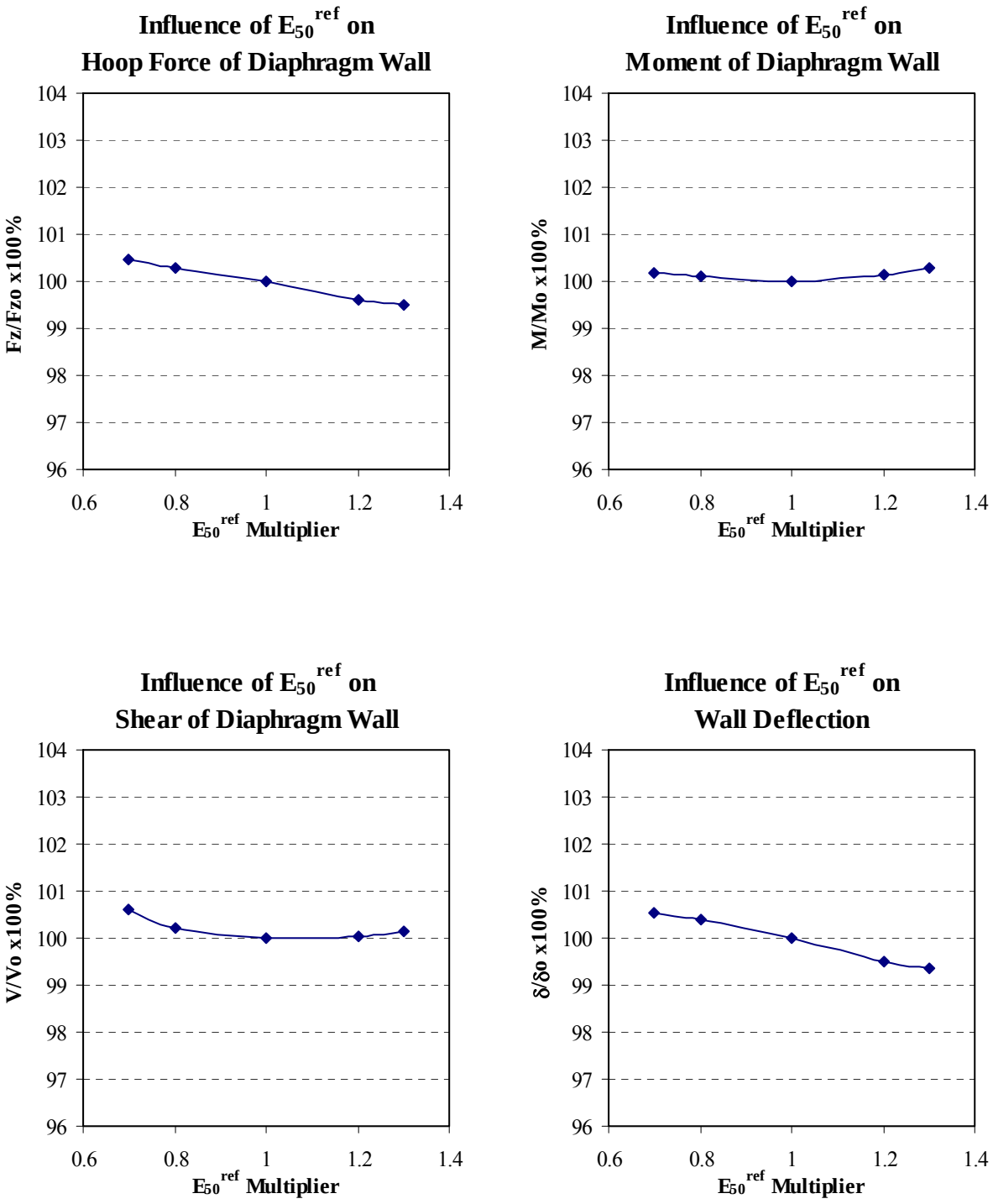

Figure 7.2 Influence of reference secant stiffness modulus

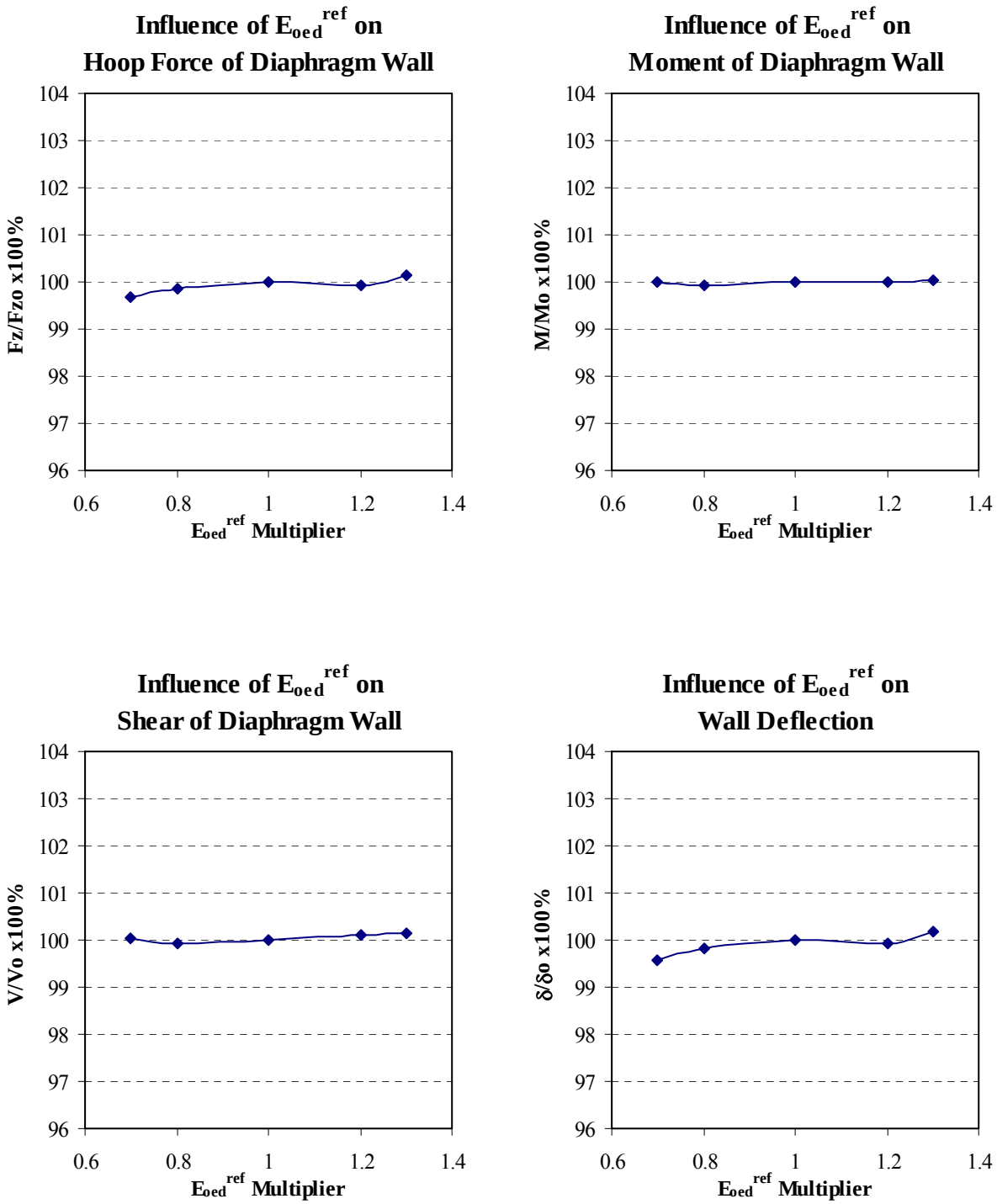

Figure 7.3 Influence of reference tangential oedometer stiffness modulus

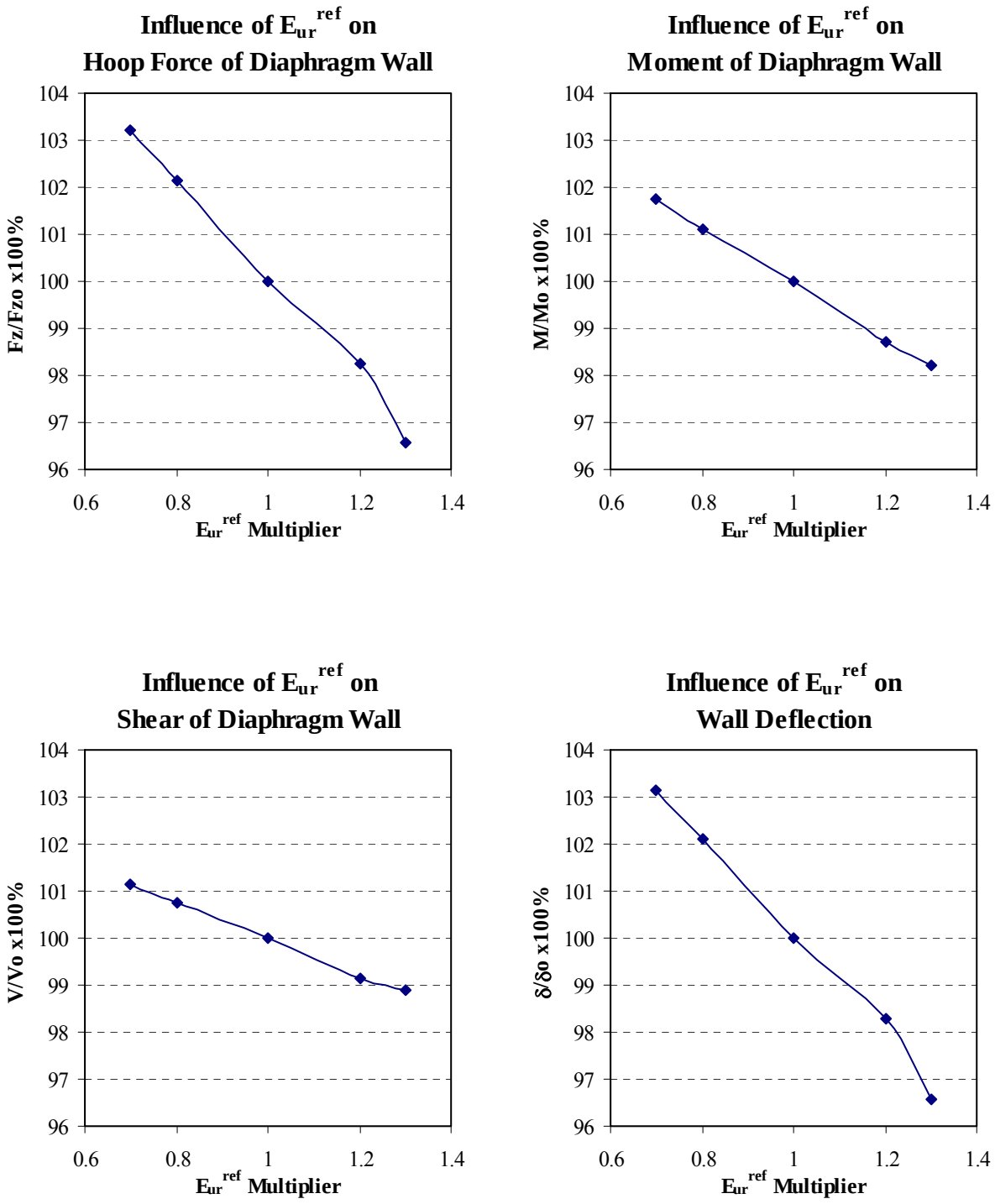

Figure 7.4 Influence of reference unloading stiffness modulus

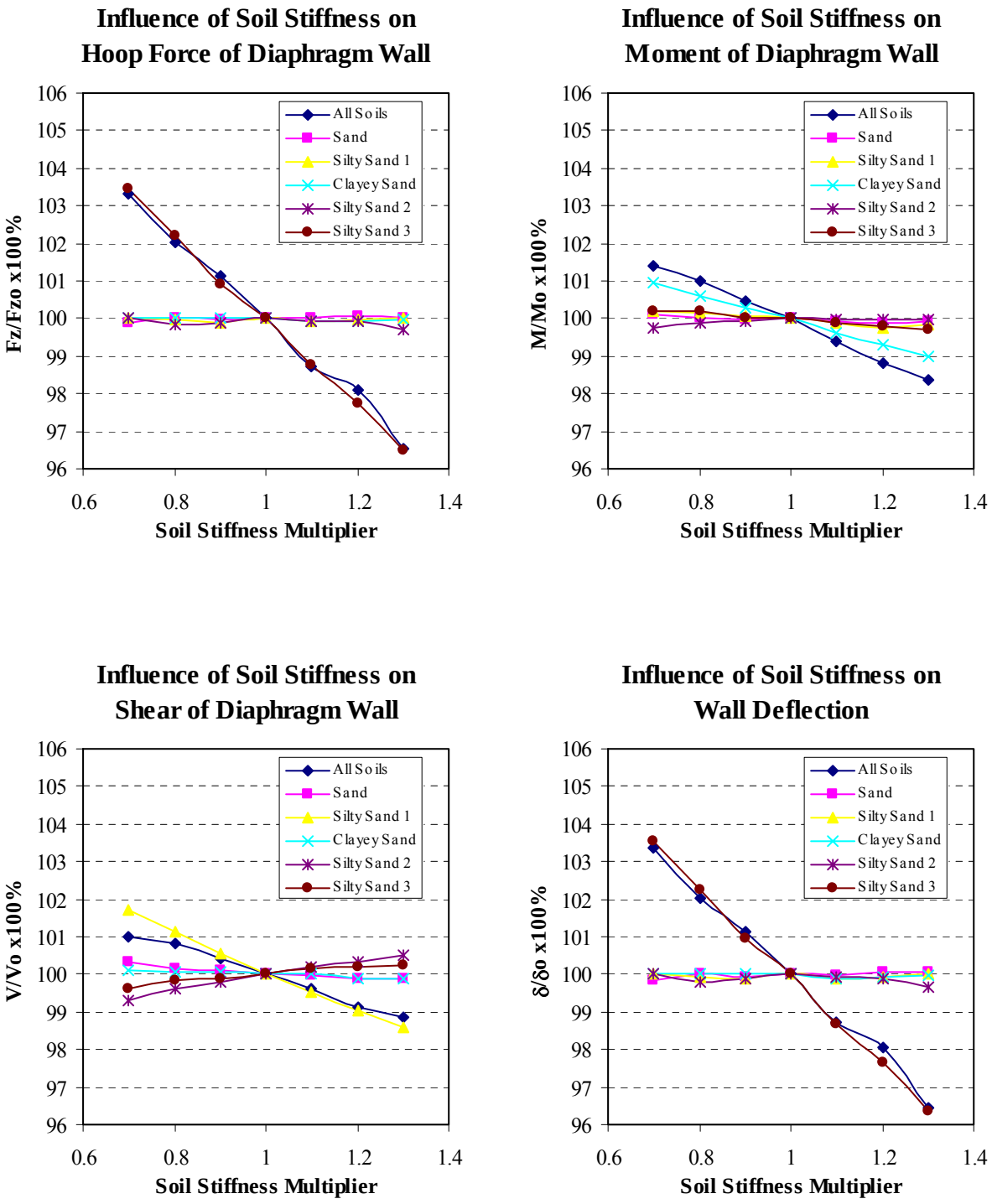

Figure 7.5 Influence of soil stiffness

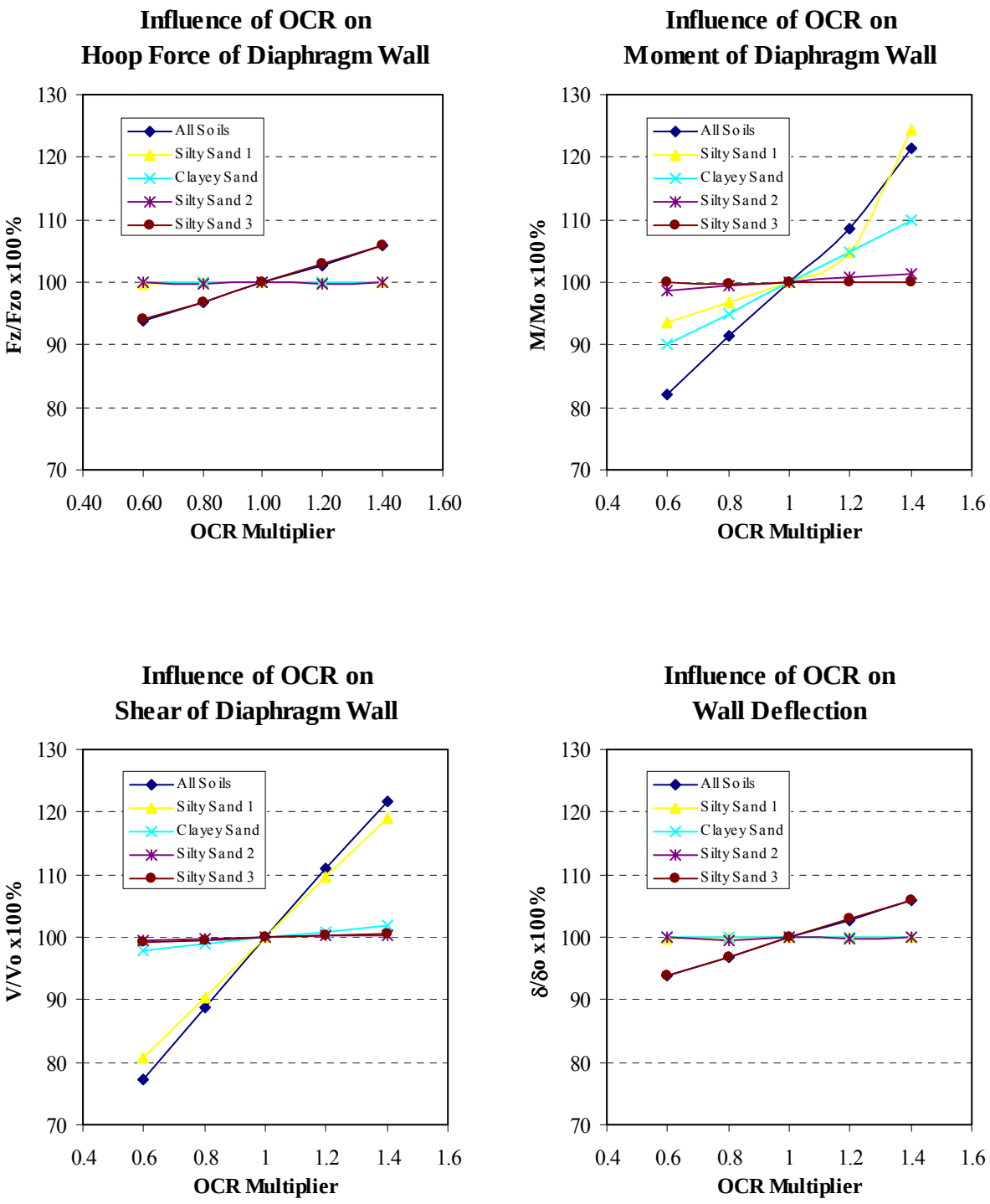

Figure 7.6 Influence of over-consolidation ratio of Old Alluvium soils

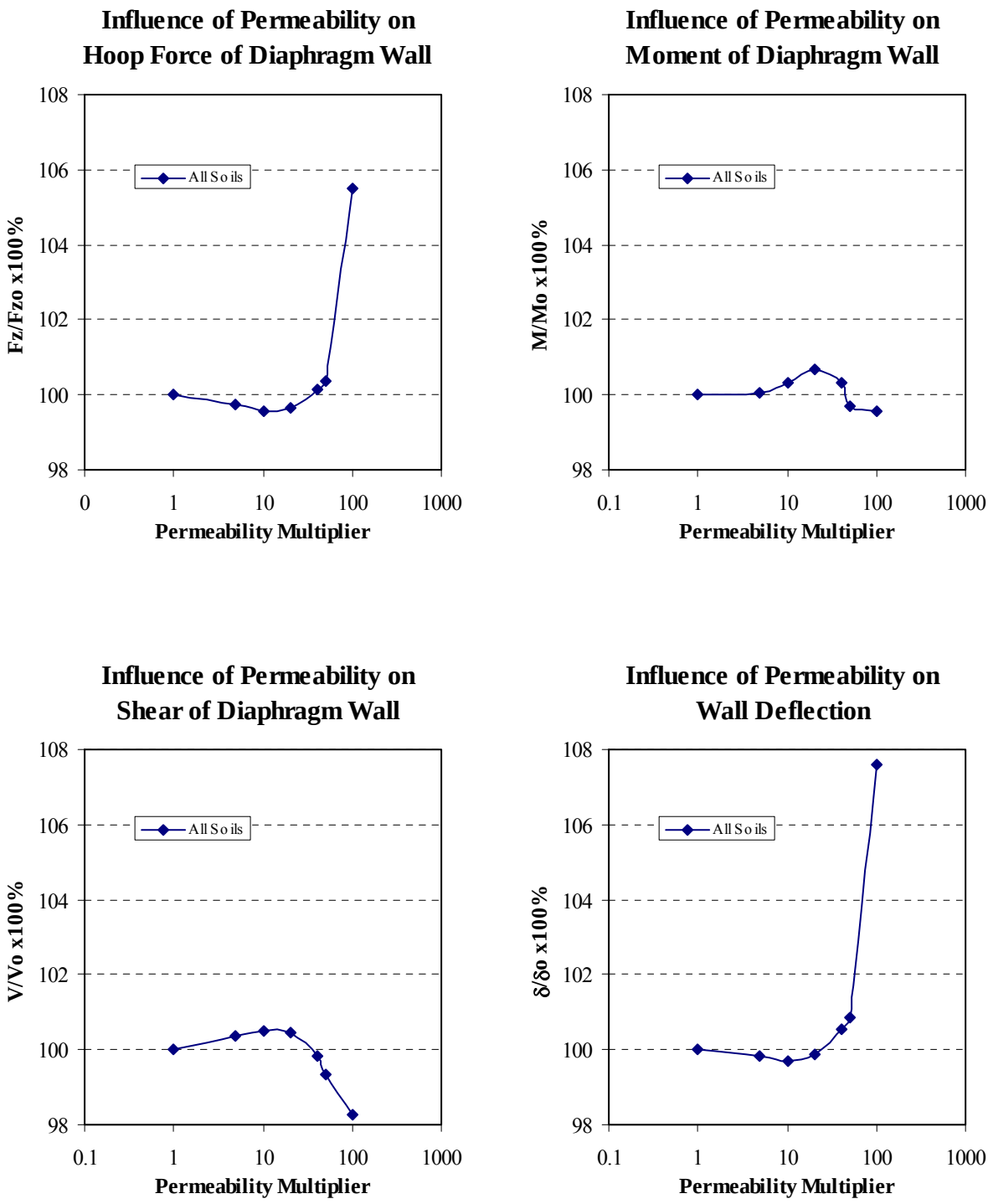

Figure 7.7 Influence of soil permeability

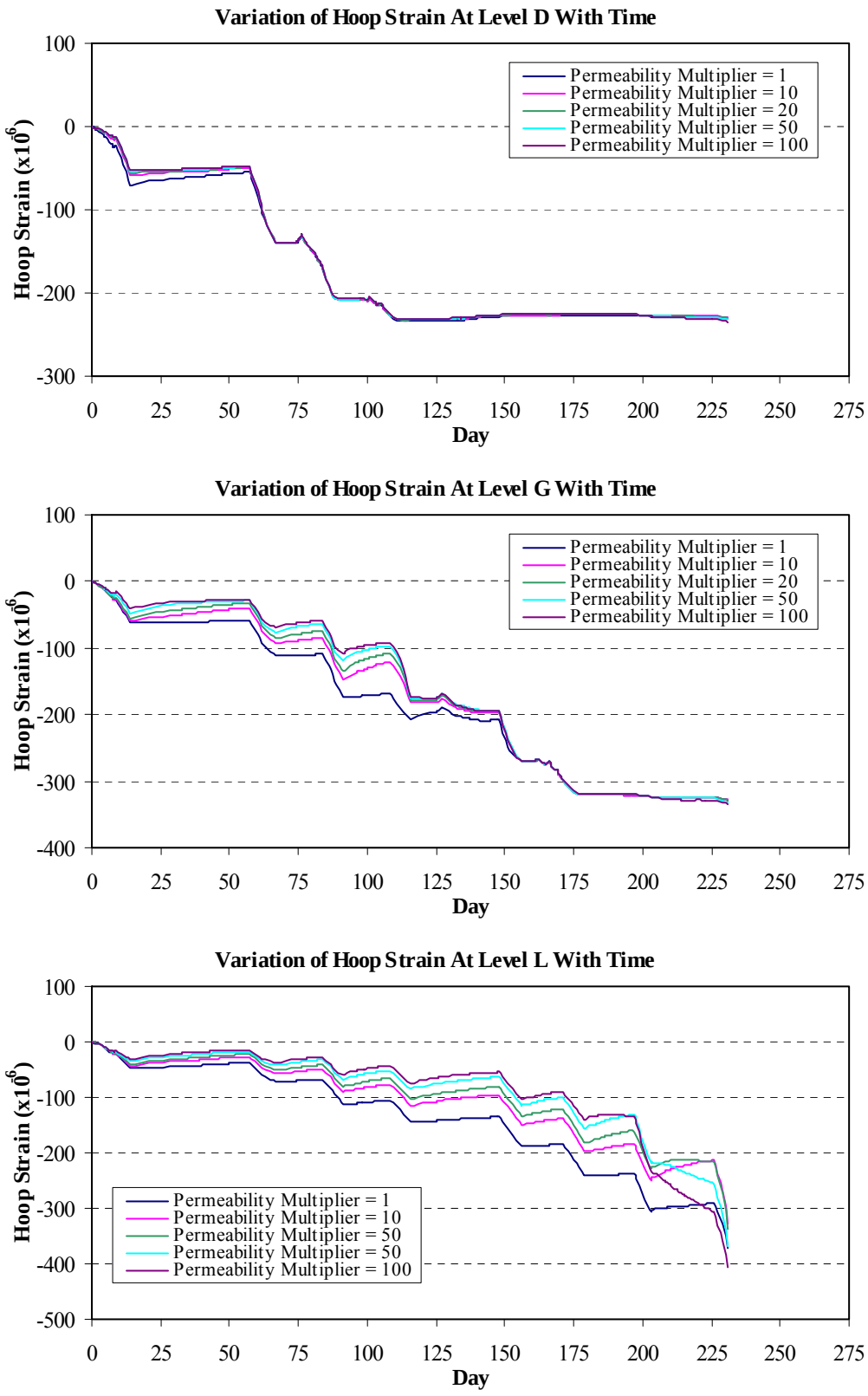

Figure 7.8 Influence of permeability on the variation of hoop strains with time

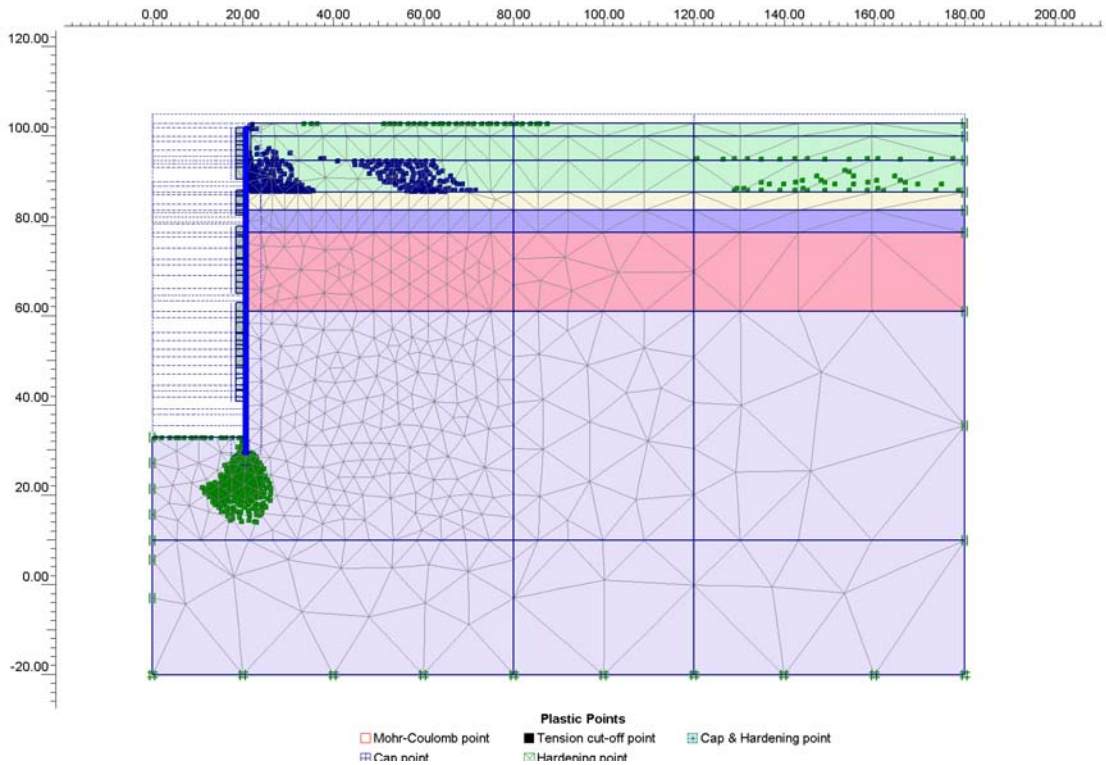

Figure 7.9 Plot of plastic points where permeability multiplier = 1

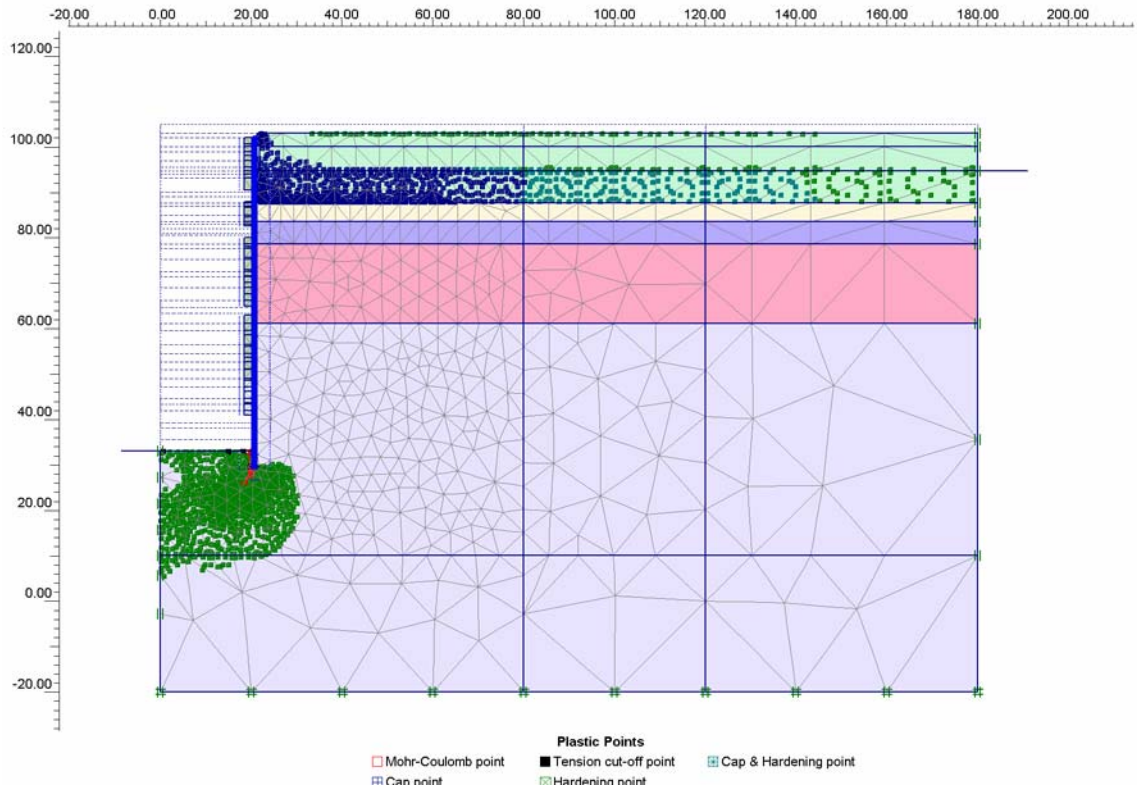

Figure 7.10 Plot of plastic points where permeability multiplier = 100

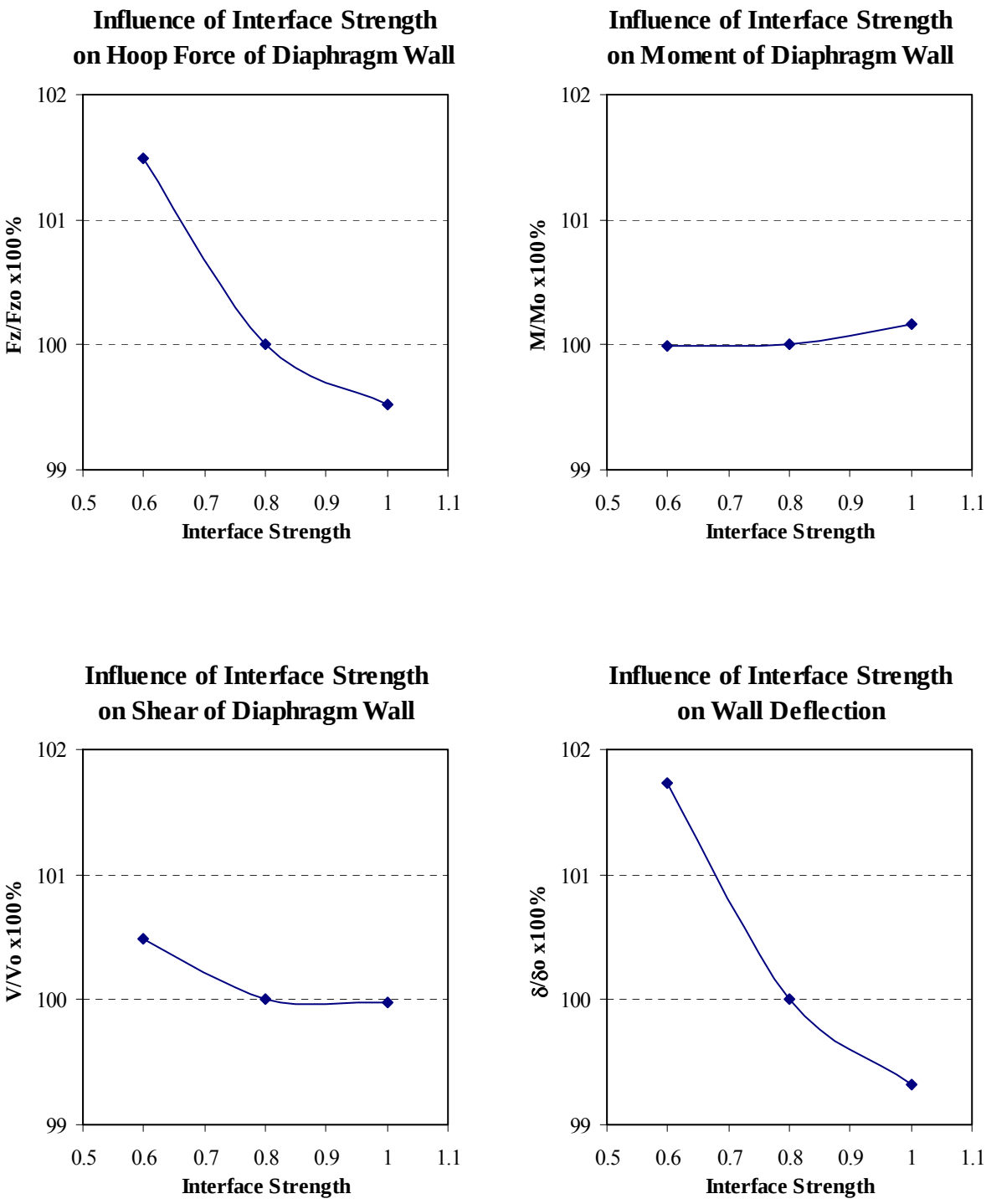

Figure 7.11 Influence of interface strength

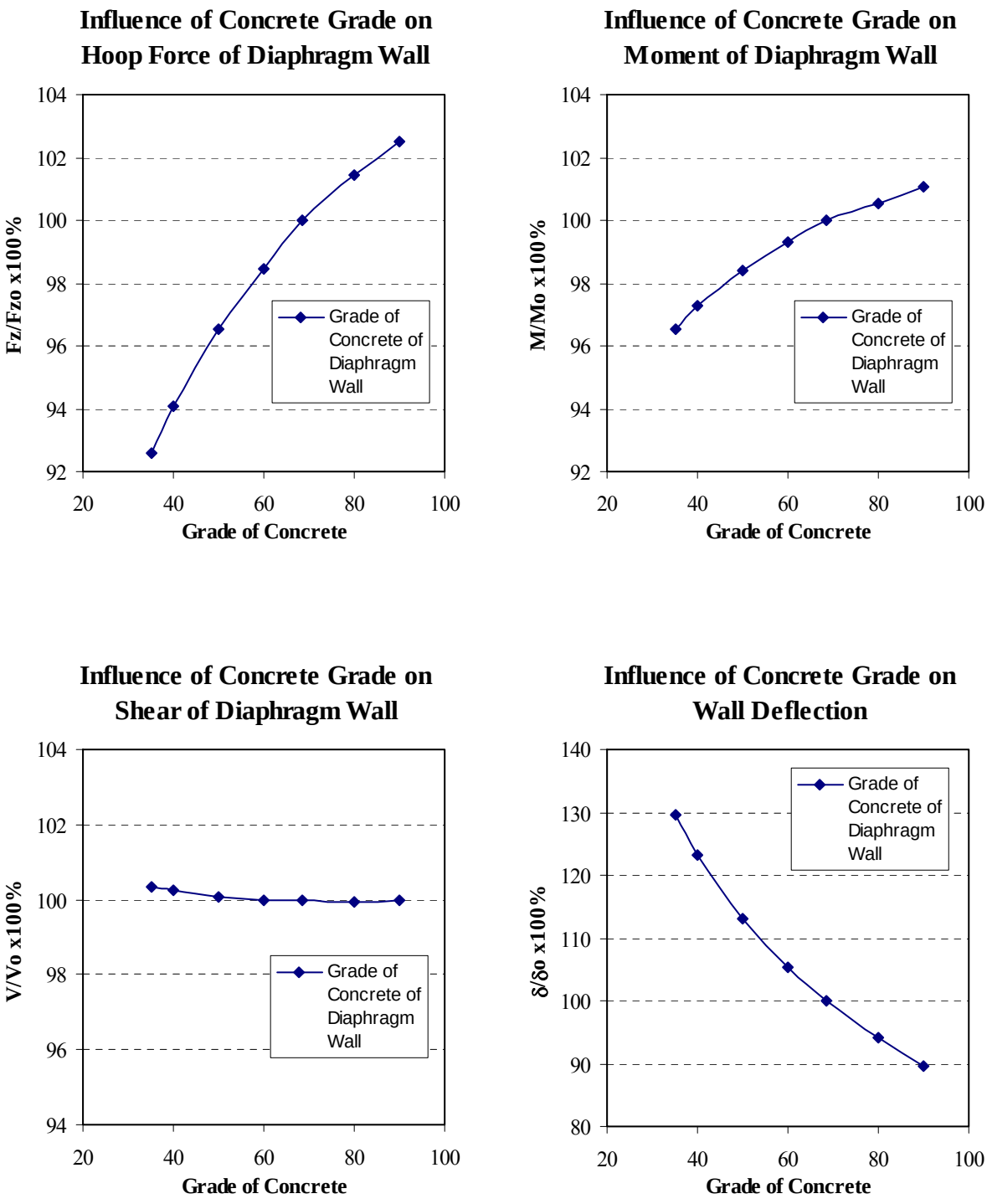

Figure 7.12 Influence of grade of concrete of diaphragm wall

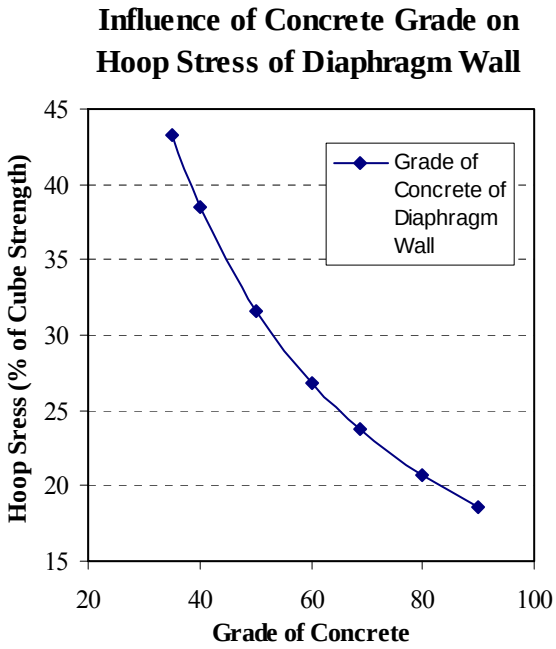

Figure 7.13 Influence of grade of concrete of hoop stress of diaphragm wall

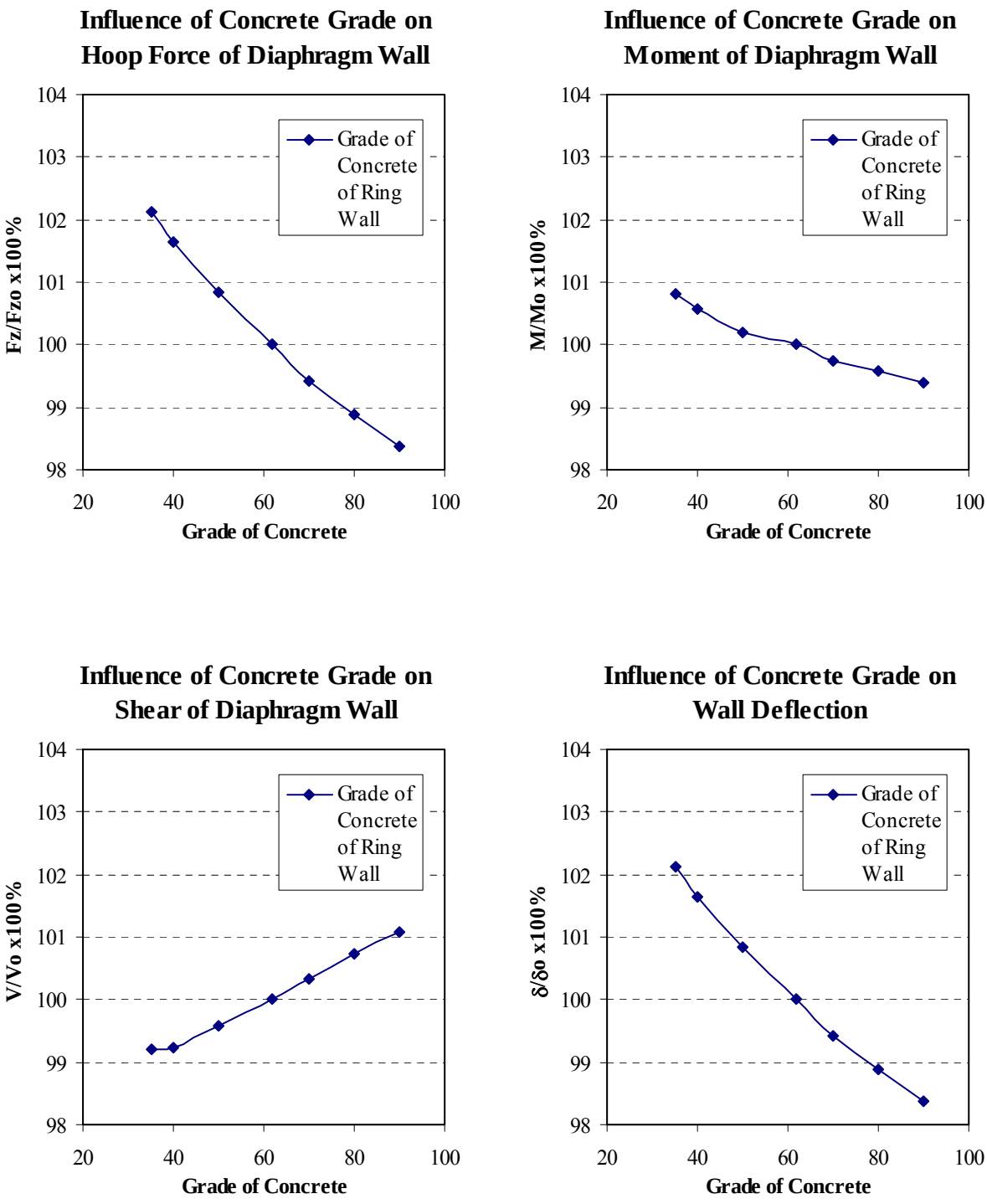

Figure 7.14 Influence of grade of concrete of ring wall

CHAPTER 8 CONCLUSION

8.1 Concluding Remarks

The finite element approach of solving geotechnical problems requires the use of appropriate constitutive models to simulate the behaviour of the soil continuum and structures as close to reality as possible. The Hardening-Soil model is an advanced constitutive model that is formulated in the framework of classical theory of plasticity and is able to account for both shear hardening and compression hardening. The stress dependency of soil stiffness is considered in the Hardening-Soil model. Hence, this constitutive model is employed to simulate the behaviour of Old Alluvium soils at the Influent Pumping Station project site. A study on the model parameters of the Hardening-Soil model is performed to obtain representative soil parameters for the constitutive model.

Schanz and Bonnier (1997) proposed a method for determining the reference tangential oedometer stiffness modulus, E_{oed}^{ref}, and the power for stress-dependency of stiffness, m, of the Hardening-Soil model using one-dimensional oedometer test results. This method is critically assessed by the author. Derivation of the equations for computing the reference tangential oedometer stiffness modulus, E_{oed}^{ref}, and the power for stress-dependency of stiffness, m, is carried out independently by the author. It is found that Schanz and Bonnier (1997) made an assumption of zero effective cohesion in their derivation. One-dimensional oedometer element tests are also simulated using the PLAXIS program to validate the method proposed by Schanz and Bonnier (1997). It can be concluded from the finite element study that this method can provide reasonable estimation of the power for stress-dependency of stiffness and the reference tangential

oedometer stiffness modulus for cohesionless soils with a power for stress-dependency of stiffness that ranges from 0.5 to 0.7. It is found that the use of a higher reference pressure in this method aids in enhancing the accuracy of determining the reference tangential oedometer stiffness of cohesionless soils. The inapplicability of this method for cohesive soils is also confirmed by the finite element study.

Results of laboratory oedometer and triaxial tests conducted on Old Alluvium soil are simulated using the Hardening Soil model to obtain some representative soil parameters for Old Alluvium. It is evident that the use of equal value for the reference secant stiffness modulus, E_{50}^{ref}, and the reference tangential oedometer stiffness modulus, E_{oed}^{ref}, is appropriate for Old Alluvium soils. The ratio of the reference unloading stiffness modulus to the reference secant stiffness modulus of Old Alluvium soils is found to be highly variable.

The time-dependent response of the cylindrical excavation support system for the Influent Pumping Shaft 2 (IPS-2) of the Changi Water Reclamation Plant has been successfully simulated using the PLAXIS program after obtaining insights on the model parameters of the Hardening-Soil model. It is observed from the measured hoop strains that the hoop strain at a particular elevation of the circular shaft wall would reflect the excavation stages above its elevation and at some depth below it. Excavation at greater depth appears to have little influence on the development of hoop strains above it.

It can be observed that the hoop strains of the shaft wall are also affected by temperature variation of its internal ring walls and the author has proposed a simplified

method of modelling the thermal effects by applying equivalent stresses on the circular shaft wall. A finite element analysis with the modelling of thermal effects acting on the diaphragm wall would yield a better prediction of the measured hoop strains as compared to a finite element analyses that does not account for those stresses. As significant compressive hoop stresses are generated due to thermal effects, the modelling of equivalent stresses would produce a more suitable conservative design of a circular excavation support system that consists of cast in-situ internal ring walls. The zone of influence of this excavation is found to be approximately one diameter from the shaft wall.

The influences of various parameters on the behaviour of the circular excavation support system are examined to obtain greater understanding in the design of a circular shaft. The soil parameters of Silty Sand 3 layer is found to be most influential in the development of hoop forces and wall deflections of the circular shaft whereas the parameters of Silty Sand 1 and Clayey Sand layers are more influential in the development of moments and shears acting on the shafts. Coefficient of permeability is an important parameter that is often neglected by design engineers and it affects the rate of consolidation. As Old Alluvium is highly variable, it is recommended that more field permeability tests to be conducted if a circular excavation is to be carried in Old Alluvium. It is also advisable to measure the hoops strains of the wall near the excavated depth, as it would serve as the design check on the assumed coefficient of permeability and other input parameters. The use of circumferential bracings, in the form of internal ring walls, may served as a rectification method to prevent structural failure of the shaft wall if it is under-designed. The movement of the wall is most effectively reduced by adopting a higher grade of concrete for a stiffer shaft wall.

This research sought to use a finite element program to simulate the response of the circular excavation support system for Influent Pumping Shaft 2 and to examine the influence of various key parameters on such circular excavations in Old Alluvium. With the proposal of representative Hardening-Soil model parameters for Old Alluvium soils and a simplified method to account of thermal effects of ring walls on the shaft wall, the behaviour of the circular excavation support system is reflected reasonably well and the above objectives have been achieved.

8.2 Recommendations For Further Research

It has been established that the circular excavation at Influent Pumping Shaft 2 caused significant stress changes in its adjacent soils, up to a distance of one shaft diameter. As the Coarse Screen Shaft and Influent Pumping Shaft 1 are located within one diameter of the excavation, the performance of these two shafts would be affected by the excavation at Influent Pumping Shaft 2. Although an axisymmetrical model is found to be adequate in predicting the major trends in the behaviour of Influent Pumping Shaft 2 during its construction period, the neighbouring excavations may influence its performance. Hence, a three-dimensional study of the interaction effects of the three shafts using numerical software, such as ABAQUS, CRISP and FLAC, is recommended for further study to understand the interactive behaviour of the shafts. The complicated interactive thermal effects between the ring walls, diaphragm wall and surrounding soils may be studied using a more advanced numerical software.

REFERENCES

1. Abel, J.F., Dowis, E. and Richards, P. Concrete Shaft Lining Design. 20th U.S. Symposium on Rock Mechanics, 4-6 June 1979, Austin, Texas, pg 627-633.

2. Aleva, G.J.J., Bon, E.H., Bossin, J.J. and Sluiter, W.J. A Contribution to the Geology of the Part of Indonesian Tin Belt: The Sea Areas Between Singkep and Bangka Islands and Around Karaimata Islands. Bulletin of Geological Society of Malaysia, No. 6, pg 257-272. 1973.

3. Alexander, F.E.S. Report on the Availability on Singapore and the Surrounding Islands. Singapore. 1950.

4. Ariizumi, K, Kumagai, T. and Kashiwagi, A. Behaviour of Large-Scale Cylindrical Earth Retaining Wall. International Symposium on Geotechnical Aspects of Underground Construction in Soft Ground, 19-21 July 1999, Tokyo, Japan, pg 481-486.

5. Berezantzev, V. G. Earth Pressure on the Cylindrical Retaining Walls. Brussels Conference on Earth Pressure Problems, Volume 2, 1958, Brussels, Belgium, pg 21-27.

6. Bloodworth, A.G. and Houlsby, G.T. Three Dimensional Analysis of Building Settlement Caused By Shaft Construction. International Symposium on

Geotechnical Aspects of Underground Construction in Soft Ground, 19-21 July 1999, Tokyo, Japan, pg 607-612.

7. Brinkgreve, R. B. J. PLAXIS: Finite Element Code for Soil and Rock Analysis (Version 8), A. A. Balkema Publishers, Netherlands. 2002.

8. Brinkgreve, R. B. J., Al-Khoury, R. and Van Esch, J. M. PLAXIS: PLAXFLOW – Version 1, A. A. Balkema Publishers, Netherlands. 2003.

9. British Standard Institution. BS 8002: 1994 : Code of Practice For Earth Retaining Structures. 1994.

10. British Standard Institution. BS 8110-1: 1985 Structural Use of Concrete – Part 1: Code of Practice For Design and Construction. 1985a.

11. British Standard Institution. BS 8110-2: 1985 Structural Use of Concrete – Part 2: Code of Practice For Special Circumstances. 1985b.

12. Britto, A. M. and Kusakabe, O. Stabiliy of Unsupported Axisymmetric Excavations in Soft Clay. Geotechnique, Vol. 3, pg 261-270. 1982.

13. Britto, A. M. and Kusakabe, O. Stabiliy of Axisymmetric Excavations in Clays. Journal of Geotechnical Engineering, Vol. 109, No. 5, pg 666-681. 1983.

14. Britto, A. M. and Kusakabe, O. On The Stability of Supported Excavations. Canadian Geotechnical Journal, Volume 21, pg 338-348. 1984.

15. Burton, C.K. The Older Alluvium of Johore and Singapore. Journal of Tropical Geography, Vol. 18, pg 30-42. 1964.

16. Chen, F. C. and Chen Y. F. The Deep Excavation of 50m Depth Cylindrical Inground Storage Tank. 3rd Asian Young Geotechnical Engineers Conference, Geotechnical Engineering in Asia: 2000 and Beyond, 14-16 May 1997, Singapore, pg 141-150.

17. Chu, J., Goh, P. P., Pek, S. C. and Wong, I. H. Engineering Properties of the Old Alluvium Soil. Underground Singapore 2003, 27-28 November 2003, Singapore, pg 285-295.

18. Dames and Moore. Mass Rapid Transit System, Singapore: Detailed Geotechnical Study – Interpretive Report. Provisional Mass Rapid Transit Authority, Singapore. 1983.

19. Dutro, J. J. T., Dietrich, R. V. and R. M. Foose. AGI Data Sheets for Geology in the Field, Laboratory, and Office, 2nd Edition, American Geological Institute, Falls Church, VA. 1982.

20. Federation Internationale De La Precontrainte. Practical Design of Reinforced And Prestressed Concrete Structures Based On The CEB-FIP Code (MC78), T. Telford, London. 1984.

21. Freeze, R.A. and Cherry, J.A. Groundwater. Prentice Hall, United States of America. 1976.

22. Fujii, T., Hagiwara, T. and Kusakabe, O. Active Failure Mechanism of a Deep Circular Shaft in Dry Sand. International Symposium on Geotechnical Aspects of Underground Construction in Soft Ground, 15-17 April 1996, London, UK, pg 137-142.

23. Fujii, T., Ueno, K., Hagiwara, T. and Taguchi, A. Experiment and Analysis of Earth Pressure on an Axisymmetric Shaft in Sand. International Conference Centrifuge 94, 31 August – 2 September 1994, Singapore, pg 791-796.

24. GEO-SLOPE. User's Guide: SEEP/W For Finite Element Seepage Analysis. GEO-SLOPE International Ltd., Canada. 1998.

25. Gupta, A., Rahman, A., Wong, P.P. and Pitts, J. The Old Alluvium of Singapore and the Extinct Drainage System to the South China Sea. Earth Surface Processes and Landforms, Vol. 12, pg 259-275. 1987.

26. Hagiwara, T., Ugai, K., Fujii, T. and Ishibashi, M. Numerical Simulation of Centrifugal Model Tests on Earth Pressure of A Deep Shaft in Dry Sand By

Elasto-Plastic FEM. 8th International Conference on Computer Methods and Advances in Geomechanics, Volume 2, 22-28 May 1994, Morgantown, West Virginia, USA, pg 1731-1736.

27. Hulme, T.W. and Burchell, A.J. Tunnelling Projects in Singapore: An Overview. Tunnelling and Underground Space Technology, Vol 14, No 4, pg 409-418. 1999.

28. Imamura, S., Nomoto, T., Fujii, T., Hagiwara, T. and Kusakabe, O. Earth Pressures Acting on a Deep Shaft and the Movements of Adjacent Ground in Sand. International Symposium on Geotechnical Aspects of Underground Construction in Soft Ground, 19-21 July 1999, Tokyo, Japan, pg 647-652.

29. Janbu, J. Soil Compressibility as Determined by Oedometer and Triaxial Tests. European Conference on Soil Mechanics and Foundation Engineering, Vol 1, 1963, Wiesbaden, pg 19-25.

30. Kondner, R. L. and Zelasko, J. S. A Hyperbolic Stress Strain Formulation for Sand. 2nd Pan American Conference on Soil Mechanics and Foundation Engineering, 1963, Brazil, pg 289-394.

31. Lade, P.V., Jessberger, H. L., Makowski, E. and Jordan, P. Modeling of Deep Shafts in Centrifuge Tests. 10th International Conference on Soil Mechanics and Foundation Engineering, Vol 1, 15-19 June 1981, Stockholm, pg 683-691.

32. Lambe, T.W. Braced Excavation. Proceedings of Speciality Conference on Performance of Earth-Supported Structures, 1970, Ithaca, New York, pg 149-218.

33. Li, W. Deep Excavation in the Old Alluvium in Singapore. First Year Report, School of CSE, Nanyang Technological University, Singapore. 1999.

34. Li, W.W. and Wong, K. S. Geotechnical Properties of Old Alluvium in Singapore. Journal of The Institution of Engineers, Singapore, Vol. 41, No. 3, pg 10-20. 2001.

35. La Londe, W. S. and Janes. M. F. Concrete Engineering Handbook, 1st Edition, McGraw-Hill, New York. 1961

36. Mikhail, R. A., Kucker, M.S., Fischer, G.R., Robinson, R. A. and Godlewski, P. M. Earth Pressures on Deep Shafts. North American Tunnelling 2000, 6-11 June 2000, Boston, Massachusetts, USA, pg 563-571.

37. Mindess, S. and Young, J. F. Concrete, Prentice Hall, New Jersey. 1981.

38. Naval Facilities Engineering Command. Design Manual 7.01: Soil Mechanics. USA. 1986.

39 Orihara, K. and Khoo, K. S. Engineering Properties of Old Alluvium in Singapore and Its Parameters for Bored Pile and Excavation Design. 13th

Southeast Asian Geotechnical Conference, 16-20 November 1998, Taipei, Taiwan, pg 545-550.

40. Panet, M. and Guenot, A. Analysis of Convergence Behind The Face of A Tunnel. 3rd International Symposium on Tunnelling' 82, 1982, pg 197-204.

41. Pfeiffer, D. Investigations For Groundwater, Singapore Islands, Eastern End. No. 2 (Final Report), U.N. E.C.A.F.E. Natural Resources Division, Mineral Resources Section, Sala Santitham, Thailand. 1972.

42. Pitts, J. A Review of Geology and Engineering Geology in Singapore. Quarterly Journal of Engineering Geology, Vol. 17, pg 93-101. 1984.

43. Pitts, J. An Indirect Method of Determining Magnitudes of Erosion Using the c/p' ratio. Earth Surface Processes and Landforms, Vol. 11, pg 107-110. 1986.

44. PLAXIS. PLAXIS Bulletin, No 7. PLAXIS BV. 1999.

45. Poh, K.B., Buttling, S. and Hwang, R. Some MRT Experiences of the Soils and Geology of Singapore. Singapore Mass Rapid Transit Conference, 6-9 April 1987, Singapore, pg 177-191.

46. Powderham, A.J. Design and Construction of Deep Circular Cofferdam in Collapsed Ground. International Symposium on Geotechnical Aspects of

Underground Construction in Soft Ground, 19-21 July 1999, Tokyo, Japan, pg 567-572.

47. Prater, E.G. An Examination of Some Theories of Earth Pressure on Shaft Linings. Canadian Geotechnical Journal, Volume 14, pg 91-106. 1977.

48. PWD. Geology of the Republic of Singapore. Public Works Department, Singapore. 1976.

49. Roark, R.J. and Young, W. C. Formulas for Stress and Strains, 5th Edition, McGraw-Hill, New York. 1975.

50. Rowe, P. W. The Stress-dilatancy Relation for Static Equilibrium of an Assembly of Particles in Contact. Proceedings of the Royal Society of London, Vol 269, pg 500-527. 1962.

51. Rowe, P. W. Theoretical Meaning and Observed Values of Deformation Parameters for Soil. Proceedings of Roscoe Memorial Symposium, 29-31 March 1971, Cambridge University, pg 143-194.

52. Schanz, T. and Bonnier, P.G. Verification of a Soil Model with Predicted Behaviour of A Sheet Pile Wall. 9th International Conference on Computer Methods and Advances in Geomechanics, 2-7 November 1997, Wuhan, China, pg 953-959.

53. Schanz, T. and Vermeer, P.A. Angles of Friction and Dilatancy of Sand. Geotechnique, Volume 46, No 1, pg 145-151. 1996.

54. Schanz, T. and Vermeer, P.A. On The Stiffness of Sand. Pre-Failure Deformation Behaviour of Geomaterials, Thomas Telford, London. 1998.

55. Schanz, T., Vermeer, P.A. and Bonnier, P.G. The Hardening Soil Model: Formulation and Verification. International Symposium Beyond 2000 in Computational Geotechnics: 10 Years of PLAXIS, 18-20 March 1999, Amsterdam, The Netherlands, pg 281-296.

56. Sharma, J.S., Chu, J. and Zhao, J. Geological and Geotechnical Features of Singapore: An Overview. Tunnelling and Underground Space Technology, Vol. 14, No. 4, pg 419-431. 1991.

57. Sokolovski, V.V. Statics of Earthy Medium. 1954.

58. Standards Association of Australia. AS 3600-1994 Concrete Structures, Standards Association of Australia, Homebush, N.S.W. 1994.

59. Tan, B. T. and Weele, B.V. Design and Construction of Sewer Tunnels Under The Deep Tunnel Sewerage System. International Conference of Tunnels and Underground Structures, 26-29 November, 2000, Singapore, pg 235-240.

60. Tan, S. A. Course notes. HDB Short course: Use of PLAXIS for Geotechnical FEM Analysis. 2000.

61. Tan, S. A. and Tan, R. Y. Numerical Study of Two Braced Excavations in Singapore Marine Clay. Journal of The Southeast Asian Geotechnical Society, Vol 35, No 1, pg 9-27. 2004.

62. Tan, S.B., Lee, K.W. and Loy, W.C. Engineering Geology of The Old Alluvium in Singapore. 6th Southeast Asia Conference on Soil Engineering, 19-23 May 1980, Taipei, Taiwan, pg 673-384.

63. Terzaghi, K. Theoretical Soil Mechanics. John Wiley and Sons, Inc, New York. 1943.

64. Theis, C.V. The Relation Between The Lowering of The Piezometric Surface And The Rate And Duration of Discharge of A Well Using Groundwater Storage. Transactions of American Geophysical Union, 2, pg 519-524. 1935.

65. Ueno, K., Yokoyama, Y., Ohi, A., Fujii, T. Earth Pressures Acting on Flexible Circular Shafts in Sand. International Symposium on Geotechnical Aspects of Underground Construction in Soft Ground, 15-17 April 1996, London, UK, pg 237-242.

66. Vermeer, P.A. Hardening Soil Model. First Asian Course for Experienced PLAXIS Users, 31 July – 2 August 2003, Singapore.

67. Westergaard, H. M. Plastic State of Stress Around a Deep Well. Journal of Boston Society of Civil Engineers, Volume 27, pg 1-5. 1940.

68. Wong, R. C. K. and Kaiser P. K. Design and Performance Evaluation of Vertical Shafts: Rational Shaft Design Method and Verification of Design Method. Canadian Geotechnical Journal, Volume 25, pg 320-337. 1988.

69. Xanthakos, P. P. Slurry Walls as Structural Systems, 2nd Edition, McGraw-Hill, New York. 1994

70. Yong, K.Y., Lee, F.H., Parnploy, U., and Lee, S. L. Elasto-Plastic Consolidation Analysis for Strutted Excavation in Clay. Computers and Geotechnics, Vol. 8, pg 311-328. 1989.

71. Young, W. C. and Budynas, R. G. Formulas for Stress and Strains, 7th Edition, McGraw-Hill, New York. 2002.

Appendix A

The author's derivation of Schanz and Bonnier's (1997) equations for determining Hardening-Soil model parameters is presented as follows:

$$E_{oed} = E_{oed}^{ref} \left(\frac{c' \cos\phi' + \sigma_1' \sin\phi'}{c' \cos\phi' + p^{ref} \sin\phi'} \right)^m$$

$$E_{oed} = E_{oed}^{ref} \left(\frac{c' \cot\phi' + \sigma_1'}{c' \cot\phi' + p^{ref}} \right)^m$$

For c' = 0,

$$E_{oed} = E_{oed}^{ref} \left(\frac{\sigma_1'}{p^{ref}} \right)^m$$

$$\frac{d\sigma_1'}{d\varepsilon_1} = E_{oed}^{ref} \left(\frac{\sigma_1'}{p^{ref}} \right)^m$$

$$\frac{d\varepsilon_1}{d\sigma_1'} = \frac{1}{E_{oed}^{ref}} \left(\frac{p^{ref}}{\sigma_1'} \right)^m$$

$$\int d\varepsilon_1 = \int \frac{1}{E_{oed}^{ref}} \left(\frac{p^{ref}}{\sigma_1'} \right)^m d\sigma_1'$$

$$\varepsilon_1 + c1 = \frac{1}{E_{oed}^{ref}} \left(p^{ref}\right)^m \left(\frac{\sigma_1'^{1-m}}{1-m} \right) + c2$$

where c1 and c2 are integration constants

When $\sigma_1' = 0$, $\varepsilon_1 = 0$

$c1 = c2$

Thus,

$$\varepsilon_1 = \frac{1}{(1-m)E_{oed}^{ref}} \left(p^{ref}\right)^m \left(\sigma_1'\right)^{1-m}$$

$$= \frac{1}{(1-m)E_{oed}^{ref}} \left(p^{ref}\right)^{m-1} p^{ref} \left(\sigma_1'\right)^{1-m}$$

$$= \frac{p^{ref}}{(1-m)E_{oed}^{ref}} \left(\frac{\sigma_1'}{p^{ref}}\right)^{1-m}$$

$$\ln \varepsilon_z = \ln \left(\frac{p^{ref}}{(1-m)E_{oed}^{ref}}\right) + (1\text{-}m) \ln \left(\frac{\sigma_1'}{p^{ref}}\right)$$

When plotting ln ε against $\ln \left(\frac{\sigma_1'}{p^{ref}}\right)$,

$$\ln \varepsilon_z = A \ln \left(\frac{\sigma_1'}{p^{ref}}\right) + B$$

A = Gradient

$= 1 - m$

m = 1 - A

B = Intercept

$$= \ln \left(\frac{p^{ref}}{(1-m)E_{oed}^{ref}}\right)$$

$$e^B = \left(\frac{p^{ref}}{(1-m)E_{oed}^{ref}}\right)$$

$$E_{oed}^{ref} = \left(\frac{p^{ref}}{(1-m)\, e^{B}} \right)$$

$$= \frac{1}{A} \frac{p^{ref}}{e^{B}}$$

Appendix B

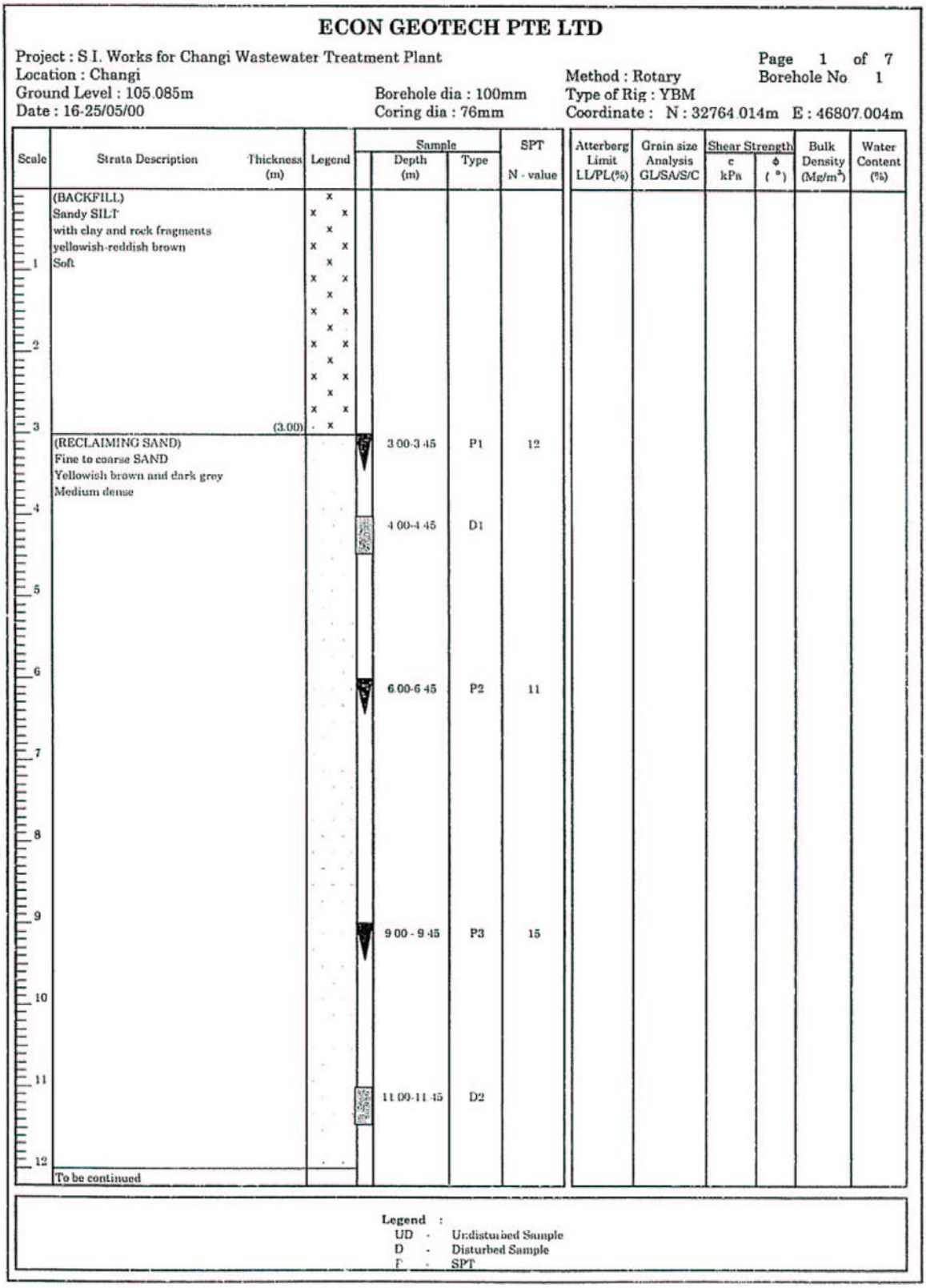

ECON GEOTECH PTE LTD

Project : S I. Works for Changi Wastewater Treatment Plant — Page 1 of 7
Location : Changi — Method : Rotary — Borehole No 1
Ground Level : 105.085m — Borehole dia : 100mm — Type of Rig : YBM
Date : 16-25/05/00 — Coring dia : 76mm — Coordinate : N : 32764.014m E : 46807.004m

Scale	Strata Description	Thickness (m)	Legend	Sample Depth (m)	Sample Type	SPT N - value	Atterberg Limit LL/PL(%)	Grain size Analysis GL/SA/S/C	Shear Strength c kPa	Shear Strength ϕ (°)	Bulk Density (Mg/m³)	Water Content (%)
1	(BACKFILL) Sandy SILT with clay and rock fragments yellowish-reddish brown Soft											
2												
3		(3.00)										
4	(RECLAIMING SAND) Fine to coarse SAND Yellowish brown and dark grey Medium dense			3.00-3.45	P1	12						
5				4.00-4.45	D1							
6				6.00-6.45	P2	11						
7												
8												
9				9.00 - 9.45	P3	15						
10												
11				11.00-11.45	D2							
12	To be continued											

Legend :
UD - Undisturbed Sample
D - Disturbed Sample
P - SPT

ECON GEOTECH PTE LTD

Project : S.I. Works for Changi Wastewater Treatment Plant
Location : Changi
Ground Level : 105.085m
Date : 16-25/05/00

Borehole dia : 100mm
Coring dia : 76mm

Method : Rotary
Type of Rig : YBM
Coordinate : N : 32764.014m E : 46807.004m

Borehole No 1

Scale	Strata Description	Thickness (m)	Legend	Sample Depth (m)	Sample Type	SPT N - value	Atterberg Limit LL/PL(%)	Grain size Analysis GL/SA/S/C	Shear Strength c kPa	Shear Strength ϕ (°)	Bulk Density (Mg/m^3)	Water Content (%)
13	(Reclaiming SAND) Fine to coarse SAND Yellowish brown and dark grey Medium dense			12.0-12.45	P4	18						
14												
15				15.00-15.45	P5	20						
16												
17		(14.00)										
	Silty fine to coarse SAND Yellowish brown Very dense			17.00-17.45	P6	51						
18												
19				19.00-19.45	P7	63						
20												
21		(4.00)										
	Clayey f-c SAND Yellowish brown and bluish grey Medium dense			21.00-21.45	P8	24						
22												
23	Very dense			23.00-23.45	P9	54						
24	To be continued											

Legend :
UD - Undisturbed Sample
D - Disturbed Sample
P - SPT

ECON GEOTECH PTE LTD

Project : S I. Works for Changi Wastewater Treatment Plant
Location : Changi
Ground Level : 105.085m
Date : 16-25/05/00

Borehole dia : 100mm
Coring dia : 76mm

Method : Rotary
Type of Rig : YBM
Coordinate : N : 32764.014m E : 46807.004m

Scale	Strata Description	Thickness (m)	Legend	Sample Depth (m)	Sample Type	SPT N - value	Atterberg Limit LL/PL(%)	Grain size Analysis GL/SA/S/C	Shear Strength c kPa	Shear Strength ϕ (°)	Bulk Density (Mg/m³)	Water Content (%)
25	Clayey fine to coarse SAND Reddish-yellowish brown Very dense			25.00-25.45	P10	53						
26												
27	Dense			27.00-27.45	P11	42						
28												
29		(8.00)										
	Silty fine to coarse SAND Bluish grey and greenish grey Very dense			29.00-29.45	P12	61						
30												
31	Dense to very dense			31.00-31.45	P13	50						
32												
33	Very dense			33.00-33.45	P14	54						
34												
35				35.00-35.45	P15	65						
36												
	To be continued											

Legend :
UD - Undisturbed Sample
D - Disturbed Sample
P - SPT

ECON GEOTECH PTE LTD

Project : S.I. Works for Changi Wastewater Treatment Plant
Location : Changi
Ground Level : 105.085m
Date : 16-25/05/00

Borehole dia : 100mm
Coring dia : 76mm

Method : Rotary
Type of Rig : YBM
Coordinate : N : 32764.014m E : 46807.004m

Borehole No 1

Scale	Strata Description	Thickness (m)	Legend	Sample Depth (m)	Sample Type	SPT N - value	Atterberg Limit LL/PL(%)	Grain size Analysis GL/SA/S/C	Shear Strength c kPa	Shear Strength ϕ (°)	Bulk Density (Mg/m³)	Water Content (%)
37	Silty fine to coarse SAND Bluish grey Very dense	(8.00)										
38	Silty CLAY Pinkish grey and bluish grey Hard			37.00-37.45	P16	46						
39		(2.00)										
40	Silty fine to coarse SAND Greenish grey and reddish brown Dense			39.00-39.45	P17	48						
41	Dense to very dense			41.00-41.45	P18	50						
42												
43	Very dense			43.00-43.45	P19	65						
44												
45				45.00-45.45	P20	61						
46												
47				47.00-47.45	P21	54						
48	To be continued											

Legend :
UD - Undisturbed Sample
D - Disturbed Sample
P - SPT

ECON GEOTECH PTE LTD

Project : S.I. Works for Changi Wastewater Treatment Plant
Location : Changi
Ground Level : 105.085m
Date : 16-25/05/00

Borehole dia : 100mm
Coring dia : 76mm

Method : Rotary
Type of Rig : YBM
Coordinate : N : 32764.014m E : 46807.004m

Scale	Strata Description	Thickness (m)	Legend	Sample Depth (m)	Sample Type	SPT N - value	Atterberg Limit LL/PL(%)	Grain size Analysis GL/SA/S/C	Shear Strength c kPa	Shear Strength ϕ (°)	Bulk Density (Mg/m³)	Water Content (%)
49	Silty fine to coarse SAND greenish grey Dense to very dense			49.00-49.45	P22	50						
50												
51	Yellowish brown Very dense			51.00-51.45	P23	52						
52												
53				53.00-53.45	P24	54						
54												
55				55.00-55.45	P25	63						
56												
57				57.00-57.45	P26	59						
58												
59				59.00-59.45	P27	78						
60	To be continued											

ECON GEOTECH PTE LTD

Project : S.I. Works for Changi Wastewater Treatment Plant
Location : Changi
Ground Level : 105.085m
Date : 16-25/05/00

Borehole dia : 100mm
Coring dia : 76mm

Method : Rotary
Type of Rig : YBM
Coordinate : N : 32764.014m E : 46807.004m

Scale	Strata Description	Thickness (m)	Legend	Sample Depth (m)	Sample Type	SPT N - value	Atterberg Limit LL/PL(%)	Grain size Analysis GL/SA/S/C	Shear Strength c kPa	Shear Strength ϕ (°)	Bulk Density (Mg/m³)	Water Content (%)
61	Silty fine to coarse SAND Greenish grey Dense			61.00-61.45	P28	47						
63	Very dense			63.45	P29	65						
65	Bluish grey and yellowish brown Dense			65.00-65.45	P30	43						
67	Very dense			67.00-67.45	P31	62						
69				69.00-69.45	P32	64						
71				71.00-71.45	P33	61						
72	To be continued											

Groundwater Observation(during drilling operation)*

17/05/2000	19:00	4.80m	20/05/2000	8:00	3.90m	22/05/2000	8:00	4.00m
19/05/2000	8:00	5.50m	20/05/2000	18:00	4.80m	22/05/2000	19:00	5.10m
19/05/2000	19:00	6.00m						

* The depth of water measured during drilling operation should not be used as groundwater ta

ECON GEOTECH PTE LTD

Project : S.I. Works for Changi Wastewater Treatment Plant
Location : Changi
Ground Level : 105.085m
Date : 16-25/05/00

Borehole dia : 100mm
Coring dia : 76mm

Method : Rotary
Type of Rig : YBM
Coordinate : N : 32764.014m E : 46807.004m

Borehole No. 1

Scale	Strata Description	Thickness (m)	Legend	Sample Depth (m)	Sample Type	SPT N - value	Atterberg Limit LL/PL(%)	Grain size Analysis GL/SA/S/C	Shear Strength c kPa	Shear Strength ϕ (°)	Bulk Density (Mg/m³)	Water Content (%)
73	Silty fine to coarse SAND Greenish grey Very dense			73.00-73.45	P34	54						
74												
75				75.00-75.45	P35	71						
		(36.45)										
76	Borehole terminated at 75.45 as instructed Borehole backfilled with cement grouting											
77												
78												
79												
80												
81												
82												
83												
84												

Ground water Observation (during drilling operation)*

23/05/2000	8:00	4.70m	24/05/2000	19:00	5.70m	26/05/2000	8:00	4.50m
23/05/2000	19:00	5.00m	2505/2000	8:00	3.70m	26/05/2001	18:00	4.70m
24/05/2000	8:00	5.40m	25/05/2000	19:00	4.80m			

* The depth of water mensured during drilling operation should not be used as groundwater table

ECON GEOTECH PTE LTD

Project : S.I. Works for Changi Wastewater Treatment Plant
Location : Changi
Ground Level : 105.100m
Date : 16-25/05/00

Borehole dia : 100mm
Coring dia : 76mm

Method : Rotary
Type of Rig : YBM
Coordinate : N : 32817.016m E : 46840.007m

Borehole No 2

Scale	Strata Description	Thickness (m)	Legend	Sample Depth (m)	Sample Type	SPT N - value	Atterberg Limit LL/PL(%)	Grain size Analysis GL/SA/S/C	Shear Strength c kPa	Shear Strength ϕ (°)	Bulk Density (Mg/m^3)	Water Content (%)
1	(BACKFILL)											
	Sandy SILT											
	with clay and rock fragments											
	yellowish-reddish brown											
	Soft											
		(1.30)										
	(Reclaiming SAND)											
2	Silty fine to coarse SAND											
	Dark grey											
	Loose											
3				3.00-3.45	P1	8						
4				4.00-4.45	D1							
5												
6												
	Light brown			6.00-6.45	P2	7						
7												
8												
9				9.00 - 9.45	P3	9						
	With some shell fragments											
10												
11				11.00-11.45	D2							
12												
	To be continued											

Legend :
UD - Undisturbed Sample
D - Disturbed Sample
P - SPT

ECON GEOTECH PTE LTD

Project : S.I. Works for Changi Wastewater Treatment Plant
Location : Changi
Ground Level : 105.100m
Date : 16-25/05/00

Borehole dia : 100mm
Coring dia : 76mm

Method : Rotary
Type of Rig : YBM
Coordinate : N : 32817.016m E : 46840.007m

Borehole No 2

Scale	Strata Description	Thickness (m)	Legend	Sample Depth (m)	Sample Type	SPT N - value	Atterberg Limit LL/PL(%)	Grain size Analysis GL/SA/S/C	Shear Strength c kPa	Shear Strength ϕ (°)	Bulk Density (Mg/m³)	Water Content (%)
13	(Reclaiming SAND) Fine to coarse SAND Dark grey Medium dense			12.0-12.45	P4	12						
14												
15				15.00-15.45	P5	12						
16												
17												
18		(16.70)										
	Silty fine to coarse SAND whitish grey Very dense			18.00-18.45	P6	54						
19												
20		(2.00)										
	Clayey fine to coarse SAND Whitish grey and yellowish brown Very dence			20.00-20.45	P7	52						
21												
22		(2.00)										
	Silty CLAY Yellowish brown and bluish grey Very stiff			22.0-22.45	P8	20						
23												
24		(2.00)										
	To be continued											

Legend :
UD - Undisturbed Sample
D - Disturbed Sample
P - SPT

ECON GEOTECH PTE LTD

Project : S.I. Works for Changi Wastewater Treatment Plant
Location : Changi
Ground Level : 105.100m
Date : 16-25/05/00

Borehole dia : 100mm
Coring dia : 76mm

Method : Rotary
Type of Rig : YBM
Coordinate : N : 32817.016m E : 46840.007m

Scale	Strata Description	Thickness (m)	Legend	Sample Depth (m)	Sample Type	SPT N - value	Atterberg Limit LL/PL(%)	Grain size Analysis GL/SA/S/C	Shear Strength c kPa	Shear Strength ϕ (°)	Bulk Density (Mg/m³)	Water Content (%)
25	Silty fine to coarse SAND Yellowish brown Dense			24.00-24.45	P9	33						
26	Greenish yellow Medium dense			26.00-26.45	P10	28						
27												
28	Greenish grey Very dense			28.00-28.45	P11	51						
29												
30	Medium dense to dense			30.00-30.45	P12	30						
31												
32	Dense			32.00-32.45	P13	38						
33												
34	Reddish-yellowish brown Very dense			34.00-34.45	P14	59						
35												
36												
	To be continued											

Legend :
UD - Undisturbed Sample
D - Disturbed Sample
P - SPT

ECON GEOTECH PTE LTD

Project : S.I. Works for Changi Wastewater Treatment Plant
Location : Changi
Ground Level : 105.100m
Date : 16-25/05/00

Borehole dia : 100mm
Coring dia : 76mm

Method : Rotary
Type of Rig : YBM
Coordinate : N : 32817.016m E : 46840.007m

Scale	Strata Description	Thickness (m)	Legend	Sample Depth (m)	Sample Type	SPT N - value	Atterberg Limit LL/PL(%)	Grain size Analysis GL/SA/S/C	Shear Strength c kPa	Shear Strength ϕ (°)	Bulk Density (Mg/m³)	Water Content (%)
37	Silty fine to coarse SAND Reddish-yellowish brown Dense			36.00-36.45	P15	45						
38	Yellowish dark brown and bluish grey Dense to very dense			38.00-38.45	P16	50						
40	Bluish grey Very dense			40.00-40.45	P17	66						
42		(18.00)										
42	Clayey SILT With sand Yellowish dark brown and bluish grey Hard			42.00-42.45	P18	78						
44		(2.00)										
44	Silty fine to coarse SAND Greenish grey Very dense			44.0-44.45	P19	56						
46				46.00-46.45	P20	34						
48	To be continued											

Legend :
UD - Undisturbed Sample
D - Disturbed Sample
P - SPT

ECON GEOTECH PTE LTD

Project : S.I. Works for Changi Wastewater Treatment Plant
Location : Changi
Ground Level : 105.100m
Date : 16-25/05/00

Borehole dia : 100mm
Coring dia : 76mm

Method : Rotary
Type of Rig : YBM
Coordinate : N : 32817.016m E : 46840.007m

Scale	Strata Description	Thickness (m)	Legend	Sample Depth (m)	Sample Type	SPT N - value	Atterberg Limit LL/PL(%)	Grain size Analysis GL/SA/S/C	Shear Strength c kPa	Shear Strength ϕ (°)	Bulk Density (Mg/m^3)	Water Content (%)
	Silty fine to coarse SAND greenish grey Dense			48.00-48.45	P21	35						
49												
50	Bluish grey Medium dense			50.00-50.45	P22	25						
51												
52	Yellowish brown and bluish grey Very dense			52.00-52.45	P23	56						
53												
54	Greenish grey Dense			54.00-54.45	P24	39						
55												
56	Very dense			56.00-56.45	P25	64						
57												
58	Greenish grey and dark brown Dense			58.00-58.45	P26	44						
59												
60		(16.00)										
	To be continued											

ECON GEOTECH PTE LTD

Project : S.I. Works for Changi Wastewater Treatment Plant
Location : Changi
Ground Level : 105.100m
Date : 16-25/05/00

Borehole dia : 100mm
Coring dia : 76mm

Method : Rotary
Type of Rig : YBM
Coordinate : N : 32817.016m E : 46840.007m

Borehole No. 2

Scale	Strata Description	Thickness (m)	Legend	Sample Depth (m)	Sample Type	SPT N - value	Atterberg Limit LL/PL(%)	Grain size Analysis GL/SA/S/C	Shear Strength c kPa	Shear Strength ϕ (°)	Bulk Density (Mg/m^3)	Water Content (%)
61	Clayey SILT Yellowish dark brown and bluish grey Hard			60.00-60.45	P27	50						
62		(2.00)										
63	Silty fine to coarse SAND Bluish grey Dense			62.00-62.45	P28	42						
64				64.00-64.45	P29	35						
65												
66	Very dense			66.00-66.45	P30	95						
67												
68				68.00-68.45	P31	65						
69												
70	Greenish grey			70.00-70.45	P32	73						
71												
72	To be continued											

Groundwater Observation(during drilling operation)*

16/05/2000	18:40	1.80m	19/05/2000	3:00	5.20m	20/05/2000	18:00	5.20m
17/05/2000	8:10	1.90m	19/05/2000	19:00	5.90m	22/05/2000	8:00	1.00m
17/05/2000	19:00	3.80m	20/05/2000	8:00	4.70m	22/05/2000	19:00	5.40m

* The depth of water measured during drilling operation should not be used as groundwater ta

ECON GEOTECH PTE LTD

Project : S.I. Works for Changi Wastewater Treatment Plant
Location : Changi
Ground Level : 105.100m
Date : 16-25/05/00

Borehole dia : 100mm
Coring dia : 76mm

Method : Rotary
Type of Rig : YBM
Coordinate : N : 32817.016m E : 46840.007m

Borehole No 2

Scale	Strata Description	Thickness (m)	Legend	Sample Depth (m)	Sample Type	SPT N - value	Atterberg Limit LL/PL(%)	Grain size Analysis GL/SA/S/C	Shear Strength c kPa	Shear Strength ϕ (°)	Bulk Density (Mg/m³)	Water Content (%)
73	Silty fine to coarse SAND Greenish grey Very dense			72.00-72.45	P33	69						
74												
75	Bluish grey	(13.45)		75.00-75.45	P34	73						
76	Borehole terminated at 75.45 as instructed Borehole backfilled with cement grouting											
77												
78												
79												
80												
81												
82												
83												
84												

Ground water Observation (during drilling operation)*

23/05/2000	8:00		24/05/2000	19:00	5.00m
23/05/2000	19:00	4.50m	25/05/2000	8:00	4.60m
24/05/2000	8:00		25/05/2000	19:00	4.00m

* The depth of water measured during drilling operation should not be used as groundwater table